

University of Technology Sydney
Faculty of Engineering and Information Technology
School of Civil and Environmental Engineering

Investigation of Composite Façade Mullions

By

Sihao (Susan) Huang

BEngSc, Tonji University, China, 1991

MEngSc, University of New South Wales, Australia, 1997

MIEAust, CPEng, Chartered Professional Engineer, The institute of Engineers Australia

NPER, National Professional Engineers Register

Submitted in fulfilment of the requirements for the degree of

Doctor of Philosophy

May 2014

CERTIFICATE OF AUTHORSHIP/ORGINALITY

I certify that the work in this thesis has not previously been submitted for a degree nor has it been submitted as part of requirements for a degree except as fully acknowledged within the text.

I also certify that the thesis has been written by me. Any help that I have received in my research work and the preparation of the thesis itself has been acknowledged. In addition, I certify that all information sources and literature used are indicated in the thesis.

Production Note:
Signature removed prior to publication.

Sihao (Susan) Huang

May 2014

Acknowledgement

I would like to take this opportunity to express my sincere gratitude to my principal supervisor, Professor Bijan Samali, for his encouragement, support, understanding and immense knowledge. Professor Samali brought me into the research world and patiently guided me through my PhD study and helped me with the thesis writing. I could not have imagined to have finished my research without his help.

I would like to also show my greatest appreciation to my co-supervisor, Associate professor Jianchun Li for his tremendous support, guidance, enthusiasm and patience which helped me through the most challenging period of my research. It was a great pleasure to be able to have routine technical discussions with him. His expertise helped me to achieve a higher research standard.

My sincere thanks also go to my sponsor, Permasteelisa Group and its Sydney Research Director, Dr Marc Zobec, who provided me funding and direction for this research project. It was a big motivation to me knowing that my research was recognized and needed by the industry.

At last, I would like to thank my family: my husband Xiaodong Wang and son Douglas Wang as well as my parents for their continuous support, patience and understanding through my study.

Table of Contents

CERTIFICATE OF AUTHORSHIP/ORGINALITY	I
<i>Acknowledgement</i>	II
List of Figures.....	VII
List of Tables.....	XIII
List of Notations	XIV
<i>Abstract</i>	XVII
1. Introduction.....	2
1.1 Scope and limitations.....	6
1.2 Thesis layout.....	7
2. Literature review	10
2.1 Introduction	10
2.2 Past studies on composite façade mullion.....	11
2.3 Study of material properties of aluminium and polyamide.....	14
2.4 Studies involving Interfacial modelling.....	17
2.5 Sandwich theory	25
2.6 Sandwich beam under bending.....	26
2.7 Summary and conclusions.....	31
3. Experimental investigation of a typical thermal break façade mullion section.....	34
3.1 Introduction	34
3.2 Typical Section of thermal break façade mullion under investigation	35
3.3 Quasi-static shear and transverse tensile tests at various temperatures	36
3.3.1 Shear tests.....	37
3.3.1.1 Test setup	37
3.3.1.2 Failure modes and typical results.....	41
3.3.2 Transverse tensile tests	45
3.3.2.1 Test setup	45

3.3.2.2	Failure modes and typical results	48
3.4	High strain rate shear and transverse tensile tests at room temperature	52
3.4.1	Shear tests.....	53
3.4.2	Section transverse tensile tests under high strain rate loadings.....	55
3.4.3	Test results and discussion	57
3.5	Four-point bending beam tests at room temperature under quasi-static loadings	61
3.5.1	Test setup.....	61
3.5.2	Failure mechanism and typical results	64
3.6	Summary and conclusions.....	69
4.	Numerical investigation of the typical thermal break façade section	72
4.1	Introduction	72
4.2	Material modelling.....	73
4.2.1	Aluminium material modelling	73
4.2.2	Polyamide material property	79
4.3	Investigation of the influence of element types.....	82
4.4	Interaction between aluminium profile and polyamide insert.....	89
4.5	Numerical investigation of the section shear capacity.....	100
4.5.1	Model setup	100
4.5.2	Typical results	107
4.6	Numerical investigation of section transverse tensile capacity	112
4.6.1	Model setup	112
4.6.2	Typical results	119
4.7	Numerical investigation of façade beam in four point bending	124
4.7.1	FE Model setup – model geometry, boundary conditions and mesh assignment.....	124
4.7.2	Proposed partitioned multi-phase beam failure model	130
4.7.3	Typical results	135

4.8	Summary and conclusions.....	140
5.	Comparison of experimental and numerical investigations	144
5.1	Introduction	144
5.2	Comparison of shear test results and FE modelling	145
5.3	Comparison of tensile test results and FE modelling	148
5.4	Comparison of beam test results and FE modelling	157
5.4.1	Comparison of deformed shapes	157
5.4.2	Comparison of load vs mid-span displacement.....	159
5.4.3	Comparison of strain distribution diagrams.....	162
5.4.4	Comparison of moment-curvature relationship.....	166
5.5	Summary and conclusion	174
6.	Numerical investigation of other profiles with similar connection details	178
6.1	Introduction	178
6.2	Numerical investigation of the section shear capacity.....	179
6.2.1	Section geometry	179
6.2.2	Model setup	180
6.2.3	Typical results	186
6.3	Numerical investigation of the section transverse tensile capacity	190
6.3.1	Model setup.....	190
6.3.2	Typical results	195
6.4	Numerical investigation of four-point beam bending.....	200
6.4.1	Model setup	200
6.4.2	Typical results and discussions	211
6.5	Summary and conclusions.....	215
7.	Proposed frame work for analytical solution based on sandwich theory	218
7.1	Introduction	218
7.2	Analytical formulations.....	221

7.2.1	Superposition approach.....	221
7.2.2	Basic assumptions.....	222
7.2.3	Sub-structure I.....	223
7.2.4	Sub-structure II.....	240
7.2.5	Overall structure behaviour.....	249
7.3	Equivalent section.....	250
7.4	Summary and conclusions.....	253
8.	Summary, conclusions and recommended future works.....	256
8.1	Summary and conclusions.....	256
8.2	Recommended future works.....	260
Appendix – Polyamide Material Properties in transverse direction.....		262
Bibliography:.....		263

List of Figures

Figure 1.1	Images of modern curtain walls	3
Figure 3.1	Section details.....	36
Figure 3.2	Shear test setup sketch and photo at room temperature.....	38
Figure 3.3	Test setup inside temperature chamber.....	40
Figure 3.4	High/Low temperature test setup.....	40
Figure 3.5	Shear test failure mode – Polyamide slipped away	41
Figure 3.6	Shear strength vs test temperatures	43
Figure 3.7	Characteristic shear strength vs temperature.....	43
Figure 3.8	Elasticity constant vs temperature.....	44
Figure 3.9	Load-slip relationship at room temperature	45
Figure 3.10	Tension test setup sketch and photo at room temperature.....	46
Figure 3.11	Tension test setup full view	47
Figure 3.12	Test setup inside temperature chamber	48
Figure 3.13	Tensile test failure modes.....	49
Figure 3.14	Tensile strength vs test temperatures	51
Figure 3.15	Characteristic tensile strength vs temperature	51
Figure 3.16	Test set-out on Schenck testing machine	54
Figure 3.17	Failure mode – Polyamide slippage	55
Figure 3.18	High strain rate tensile test setup on shake table	56
Figure 3.19	Tensile failure modes	57
Figure 3.20	Shear strength vs strain rates	58
Figure 3.21	Elasticity constant vs strain rates	58
Figure 3.22	Tensile strength vs strain rates.....	59
Figure 3.23	Test setup diagram	62
Figure 3.24	Full view of test setup	63
Figure 3.25	Strain gauge layout.....	64
Figure 3.26	Typical deformation of test specimen	65
Figure 3.27	Strain distribution diagrams along cross-section at dip load.....	66
Figure 3.28	Failure mechanism	67
Figure 3.29	Illustration of failure mechanism of this façade beam	68
Figure 3.30	Typical load vs mid-span displacement for beam types	69
Figure 4.1	Stress-strain diagram of Ramberg-Osgood model in general form.....	74

Figure 4.2	Stress-strain relationship of aluminium alloy 6063T6.....	76
Figure 4.3	True stress – true strain relationship of aluminium alloy 6063T6.....	79
Figure 4.4	Stress-Strain relationship of PA66 in longitudinal direction	80
Figure 4.5	Stress-Strain relationship of PA66 in transverse direction	81
Figure 4.6	True stress - true strain relationship of PA66 in longitudinal direction....	81
Figure 4.7	True stress - true strain relationship of PA66 in transverse direction.....	82
Figure 4.8	Trial model geometrical details	85
Figure 4.9	Boundary condition and theoretical reaction force diagram	85
Figure 4.10	Enlarged contact surface detail	91
Figure 4.11	Proposed model of progressive failure mechanism at aluminium and polyamide contact surfaces	93
Figure 4.12	Frictional behaviour between two contact bodies	95
Figure 4.13	Section geometry details.....	100
Figure 4.14	Partition assignment	101
Figure 4.15	Master-slave assignment.....	103
Figure 4.16	FE model details and comparison with test setup.....	104
Figure 4.17	Mesh assignment of part 1 (AL1) from different view angles	105
Figure 4.18	Mesh assignment of part 2 (AL2) from different view angles	105
Figure 4.19	Mesh assignment of part 3 (PA) from different view angles.....	106
Figure 4.20	Mesh assignment of the assembled whole section.....	106
Figure 4.21	Deformed shape	107
Figure 4.22	Load vs slippage of connection from FE model	110
Figure 4.23	Comparison of Stresses at along and cross direction at maximum loading	111
Figure 4.24	Partition assignments of AL2 in front and side views	113
Figure 4.25	Interaction assignment.....	115
Figure 4.26	FE model setup details and comparison with test setup.....	116
Figure 4.27	Mesh assignment of part 1 (AL1) from different view angles	117
Figure 4.28	Mesh assignment of part 2 (AL2) from different view angles	117
Figure 4.29	Mesh assignment of part 3 (PA) from different view angles.....	118
Figure 4.30	Mesh assignment of the assembled whole section.....	118
Figure 4.31	Deformed shape	119
Figure 4.32	Load vs displacement from FE model.....	120

Figure 4.33	Normal stress plot along Y-axis.....	121
Figure 4.34	Normal stress plot along X and Z axis	122
Figure 4.35	Details of simplified section	125
Figure 4.36	Model setup diagram.....	127
Figure 4.37	Symmetrical boundary assignments.....	127
Figure 4.38	Mesh assignment of part 1 (AL1) from different view angles	128
Figure 4.39	Mesh assignment of part 2 (AL2) from different view angles	128
Figure 4.40	Mesh assignment of part 3 (PA) from different view angles	129
Figure 4.41	Mesh assignment of assembled whole section	129
Figure 4.42	Partition assignment of top aluminium part (AL1) and polyamide (PA)..	130
Figure 4.43	Partition assignment of bottom aluminium part (AL2).....	130
Figure 4.44	Proposed progressive beam failure model.....	132
Figure 4.45	Interaction assignment.....	133
Figure 4.46	Deformed shape and displacement contour along 2-axis (vertical displacement).....	135
Figure 4.47	Displacement contour along 3-axis (horizontal displacement)	135
Figure 4.48	Load vs mid-span displacement for all models	136
Figure 4.49	Shear stress contour from model D.....	139
Figure 4.50	Bending stress contour from model D.....	139
Figure 5.1	Comparison of deformed shapes	145
Figure 5.2	Random slippage at connections	146
Figure 5.3	Relationship of load – slippage of connection comparison	147
Figure 5.4	Comparison of deformed shape.....	149
Figure 5.5	Load-displacement relationships from test data.....	150
Figure 5.6	Revised load-displacement relationships from test data.....	151
Figure 5.7	Load-displacement relationships – comparison of test and FE model ...	152
Figure 5.8	Comparison of load-displacement relationship under different boundary conditions	154
Figure 5.9	Load-displacement relationships – comparison of test and modified FE model	156
Figure 5.10	Comparison of bending deformation	157
Figure 5.11	Comparison of connection failure.....	158

Figure 5.12	Load vs mid-span displacement graph – Type B beam.....	159
Figure 5.13	Load vs mid-span displacement graph – Type C beam.....	160
Figure 5.14	Load vs mid-span displacement graph – Type D beam	160
Figure 5.15	Load vs mid-span displacement graph – Type E beam.....	161
Figure 5.16	Mid-span strain distribution diagrams at critical loading stages – Type B beam.....	162
Figure 5.17	Mid-span strain distribution diagrams at critical loading stages – Type C beam.....	163
Figure 5.18	Mid-span strain distribution diagrams at critical loading stages – Type D beam.....	164
Figure 5.19	Mid-span strain distribution diagrams at critical loading stages – Type E beam.....	165
Figure 5.20	Illustration of a bent segment.....	167
Figure 5.21	Load vs bottom curvature at mid-span location – Type B beam	169
Figure 5.22	Load vs bottom curvature at mid-span location – Type C beam	170
Figure 5.23	Load vs bottom curvature at mid-span location – Type D beam.....	170
Figure 5.24	Load vs bottom curvature at mid-span location – Type E beam	171
Figure 5.25	Strain distribution diagrams in the location of combined bending and shear forces – all beam types.....	172
Figure 5.26	Comparison of typical strain distribution diagrams at dip load between regions under pure bending and under combined bending and shear forces.....	173
Figure 6.1	Geometry of the asymmetrical mullion section under study.....	179
Figure 6.2	Partition assignment.....	180
Figure 6.3	Master-slave assignment	182
Figure 6.4	Boundary conditions and applied displacement	183
Figure 6.5	Mesh assignment of part AL1 from different view angles	184
Figure 6.6	Mesh assignment of part AL2 from different view angles	184
Figure 6.7	Mesh assignment of polyamide part PA from different view angles	185
Figure 6.8	Mesh assignment of the assembled whole section	185
Figure 6.9	Deformed shape.....	186
Figure 6.10	Load vs slippage of connection.....	189
Figure 6.11	Partition assignment of internal and external aluminium parts	190

Figure 6.12	Interaction assignment.....	192
Figure 6.13	Displacement and boundary conditions	192
Figure 6.14	Mesh assignment of the internal aluminium part from different view angles	193
Figure 6.15	Mesh assignment of polyamide part from different view angles.....	193
Figure 6.16	Mesh assignment of the external aluminium part from different view angles	194
Figure 6.17	Mesh assignment of the assembled whole section.....	194
Figure 6.18	Deformed shape from different view angles	195
Figure 6.19	Enlarged details of failure mode.....	196
Figure 6.20	Load vs displacement diagram	197
Figure 6.21	Details of simplified section	201
Figure 6.22	Model setup diagram.....	202
Figure 6.23	Assignment of lateral support.....	203
Figure 6.24	Mesh assignment of internal aluminium part	204
Figure 6.25	Mesh assignment of polyamide part	205
Figure 6.26	Mesh assignment of external aluminium part.....	205
Figure 6.27	Mesh assignment of the whole section.....	205
Figure 6.28	Interaction assignment.....	207
Figure 6.29	Load vs mid-span displacement – Trial 1.....	208
Figure 6.30	Load vs mid-span displacement – comparison of trial models.....	209
Figure 6.31	Deformed shape and displacement contour along 2-axis (vertical displacement).....	211
Figure 6.32	Displacement contour along 3-axis (horizontal displacement)	211
Figure 6.33	Strain distribution diagrams at mid-span location	213
Figure 6.34	Load vs curvatures at various locations of the mid-span cross-section	214
Figure 7.1	Illustration of superposition loadings	221
Figure 7.2	Geometry and free body diagram of overall sub-structure I.....	223
Figure 7.3	Loads and internal forces on skins and core of sub-structure I.....	224
Figure 7.4	Deformation diagram of sub-structure I	226
Figure 7.5	Loading diagram of four-point bending.....	233
Figure 7.6	Shear force diagram.....	233

Figure 7.7	Bending moment diagram	233
Figure 7.8	Peeling stress in the core	239
Figure 7.9	Free body diagram of overall sub-structure II.....	241
Figure 7.10	Loads and internal forces on skins and core of sub-structure II	242
Figure 7.11	Deformation diagram of sub-structure II.....	243
Figure 7.12	Geometry of the typical thermal break façade section	251
Figure 7.13	Geometry of equivalent solid section.....	252

List of Tables

Table 3.1	Beam specimen types and quantity	62
Table 4.1	Stress and strain conversion	78
Table 4.2	Comparison of deformed shapes	86
Table 4.3	Comparison of bending stresses	88
Table 4.4	Frictional coefficient assignment for the proposed progressive failure model	94
Table 4.5	Contact shear stresses at top connection	108
Table 4.6	Contact shear stresses at bottom connection	109
Table 4.7	FE model type and span details	127
Table 4.8	Detailed dimension of partition	131
Table 4.9	Assignment of displacement and friction co-efficient	134
Table 4.10	Contact stress along Z-axis at top connection	137
Table 4.11	Contact stress along Z-axis at bottom connection	138
Table 5.1	Boundary conditions	153
Table 6.1	Contact shear stresses at the connection between internal aluminium part and polyamide	187
Table 6.2	Contact stresses at the connection between external aluminium part and polyamide	188
Table 6.3	Contact stresses at connection between internal aluminium part and polyamide	198
Table 6.4	Contact stresses at connection between external aluminium part and polyamide	199
Table 6.5	Assignment of displacement and friction co-efficient	210

List of Notations

A_c	Total areas of polyamide inserts
A_t and A_b	Area of top and bottom skins, respectively
b	The width of beam
c	Elasticity constant (N/mm^2) – Chapter 3
c	Height of core – Chapter 7
c_0	Elasticity constant under quasi-static loading
c_t and c_b	Distance from neutral axis to the centroidal axis of top and bottom skins, respectively
d_t and d_b	Height of top and bottom skin
D_1 to D_4	Integration constants which will be determined by boundary conditions
E	Young's modulus of the material
E_c	Young's modulus of core material
EI	Flexural stiffness of the beam
f_e	Conventional elastic limit
F_k	Force needed to maintain relative motion between two bodies
F_{max}	Maximum shear/tensile load (N)
F_s	Force just sufficient to prevent the relative motion
G_c	Shear modulus of the core.
I_t and I_b	Second moment of inertia of top and bottom skin
l	Length of the test specimen (mm)
M	Applied bending moment
M_T^I	Total bending moment existing at the section
M_{xx}^i	Bending moments at top and bottom skins ($i = t, b$)
NA	Neutral axis of the section
N_T^I	Axial force existing at the section
N_{xx}^i	Axial forces at top and bottom skins ($i = t, b$)

n	Exponent characterizing the degree of hardening of the curve
P	Force normal to the interface between the two sliding bodies
P^{II}	Concentrated load P applied on sub-structure II
P_t^I and P_b^I	Concentrated load P applied on sub-structure I at top and bottom skin
P_t^T and P_b^T	Concentrated load P applied on the whole structure at top and bottom skin
p^{II}	Vertical peeling stress at the interface between core and skins
p_t^I and p_b^I	Vertical normal stress at top and bottom contact layers, respectively.
Q	Tensile strength (N/mm)
Q_T^I	Total shear force existing at the section
Q_{mean}	Mean value of the measured values of transverse tensile strength at the test temperature
Q_{xx}^i	Shear forces at top and bottom skins ($i = t, b$)
q^{II}	UDL applied on sub-structure II
q_t^I and q_b^I	UDL applied on sub-structure I at top and bottom skin
q_t^T and q_b^T	UDL applied on the whole structure at top and bottom skin
T	Shear strength (N/mm)
T_{mean}	Mean value of the measured values of shear strength at the test temperature
u_t^0 and u_b^0	Horizontal displacement at the neutral axis of top and bottom skin,
w^I	Vertical displacement of the skins and core for sub-structure I.
w_c^{II}	Displacement of core of sub-structure II
x_1 and x_2	Distance equal to one-third of span length and
$\varepsilon_{0,e}$	Residual strain corresponding to the stress f_e
ε^{pl}	True plastic strain
ε^t	True total strain
σ_v^c	Normal compressive stress in vertical direction in the core

ΔF	Increase of the shear load (N)
$\Delta\delta$	represents the corresponding displacement of ΔF (mm)
\dot{C}	Elasticity constant under a specific strain rate loading
γ	Coefficient relating to the type of profile
ρ	Radius of curvature
σ	True stress
s	Estimated standard deviation
γ	Shear strain of the core.

Abstract

Modern curtain wall systems are typically designed with extruded aluminium members. As a load bearing vertical element of the curtain wall system, mullions are also made of aluminium extrusions with glass fibre reinforced polyamide acting as a thermal break joining the external and internal extrusions together. This research is focused on the behaviour of this type of thermal break composite façade mullions under quasi-static loadings.

Literature survey was carried out. Past research works on of the thermal break façade mullions was studied, as well as the current European standard specifying the performance requirement, proof and test for the thermal break profiles. Sandwich theory was studied and laid as a foundation of this research. Literature regarding material properties of aluminium and polyamide; interfacial action between aluminium and polyamide and composite beam bending were investigated and appropriate methodologies were adopted.

To investigate the behaviour of the thermal break façade mullions, a typical mullion section was studied. This is a symmetrical composite section made of external and internal aluminium extrusions and joined by a glass fibre reinforced polyamide core. Experimental investigations were carried out to find the section shear and tensile capacity as well as the connectivity constant. The section capacity tests were performed at various temperatures under quasi-static loadings to investigate the temperature effect. Experiments under high strain rate loading have been performed at room temperature to find the relationship between section shear and tensile capacity and loading rates. As the mullions usually work as a simply supported beam under wind, temperature and earthquake loads, bending behaviour is necessary to be investigated. Experiments of four-point bending were performed on this façade section. Specimens of three for four sets of span length each were tested at room temperature under quasi-static loadings.

Numerical simulations for the section shear and tensile tests, as well as four-point bending tests were carried out. Interfacial actions between aluminium and polyamide were modelled based on Coulomb's friction theory. Two new failure models – “Proposed progressive failure model” and “Proposed partitioned multi-phase beam failure model” were developed and applied to section shear capacity model and beam bending models to simulate the interface failure. ABAQUS software was chosen to

perform the simulations. The FE modelling results were compared with the experimental results in detail.

The results of experimental investigations on section capacities at various temperatures concluded that the section shear and tensile capacity as well as connectivity constant increased with decreased temperature. Experiments under high strain rate loads showed the section shear and tensile capacity was not sensitive to strain rate. However, the connectivity constant showed a clear trend of strain rate sensitivity.

Comparisons between experimental results and the numerical results were made. Failure modes observed from the shear and tensile experiments were repeated by the FE shear and tensile models. Load vs slippage graph obtained from shear model matched the experimental one very well. The load-displacement graph generated by the FE tensile model with equivalent material properties agreed well with the experimental one.

Results obtained from the FE beam models correlated to the experimental results very well. Load vs mid-span displacement graphs produced from both experiments and the FE models showed consistent peak loading capacity. The three-stage progressive failure mode observed from the experiments was reproduced by the FE models. Mid-span strain distribution diagrams at elastic range, generated by the FE models, were compared with the experimental ones as well. It was found that the FE model results were relatively consistent with the experimental ones. However, further improvements can be made in future studies. The relationship between moment and curvature at mid-span bottom extreme fibre obtained from the FE models confirmed consistency with experimental results.

A proposed frame work for an analytical solution of four-point bending of this type of composite thermal break façade profile in the elastic range was presented in this thesis. Based on the sandwich theory and superposition approach, formulations were derived to work out deflection and stresses, including peeling stresses between aluminium skins and polyamide core. Due to limited time and scope, the analytical solution has not been verified by experimental and numerical works in this research. It is recommended that experimental and numerical investigations be carried out to verify the analytical solutions and apply them to the industry applications in future studies.

Another asymmetrical thermal break profile was also investigated numerically. Finite element models of the section shear and tensile capacity were established by ABAQUS

software. The proposed progressive failure model was successfully applied to simulate the failure mechanism in the shear model. A four-point bending beam model was built in ABAQUS software with the proposed partitioned multi-phase beam failure model, effectively simulating the interface failure mechanism. The FE models generated similar trends as the typical section models, especially shear and tensile capacity models. However, variations in the beam model were observed. Further experimental investigations are required to confirm the phenomenon revealed by the numerical investigation in future studies.

Further research on the thermal break façade mullions can be extended to further investigation of strain rate sensitivity of section shear and tensile strength by performing large quantities of experiments and numerical simulations under high strain rate loadings. Future studies to carry out experimental and numerical investigations to verify the analytical solution and extended into industrial applications are highly recommended as well. Future studies involving experimental investigation of the asymmetrical thermal break sections to confirm the behaviour shown by the FE modelling is also valuable to provide further insight.

This page is left blank intentionally

Chapter 1

Introduction

1. Introduction

The façade of a building is important from an architectural design point of view as it provides transparency and illumination, weatherproofing, thermal isolation, load distribution and sound insulation. The building façade has been gradually transformed from ancient masonry/stone to the modern curtain walls due to the development of technology.

Prior to the middle of the nineteenth century, buildings were constructed with the exterior walls of the building (bearing walls, typically masonry) supporting the load of the entire structure. The development and widespread use of structural steel and later reinforced concrete allowed relatively small size columns to support large loads and the exterior walls of buildings were no longer required for structural support. This development paved the way to the increased use of glass as an exterior façade and the birth of modern day curtain walls.

The first true curtain walls were built by the Ottoman Empire in the 18th century, where large glass panels were framed with wood. Oriel Chambers in Liverpool, England, was the world's first metal framed glass curtain walled building built in 1864, followed by 16 York Street, Liverpool, in 1866. The extensive glass walls of both buildings allowed light to penetrate further into the building utilizing more floor spaces and reduced lighting costs in short winter months.

The majority of early metal framed curtain walls were made with steel mullions and the plate glass was attached to the mullions with asbestos or fibreglass modified glazing compound. Later, silicone sealants or glazing tape were substituted. It is not until 1970s that aluminium extrusions for mullions were widely used. Aluminium offers the unique advantage of being able to be easily extruded into nearly any shape required for design and aesthetic purposes. Today, the design complexity and shapes available are nearly limitless. Custom made shapes can be designed and manufactured with relative ease. This enables almost every architectural imagination to be realised. Characterised façade made of aluminium curtain walls give building its own character. A few examples are shown in Figure 1.1.



Large glass panel curtain wall



Curtain wall façade with human image

Figure 1.1 Images of modern curtain walls

The function of façade is not only the architectural appearance of the building but also provides enclosure to the building. It separates the interior environment of the building from external heat, water and wind. A curtain wall is usually an aluminium-framed wall, containing in-fills of glass, metal panels, or thin stone. The frame is attached to the building structure at floor levels and does not carry the floor or roof loads of the building. The wind, earthquake and gravity loads of the curtain wall are transferred to the building structure. The aluminium frame system comprises mullions and spandrel beams. Curtain wall mullions are the vertical load bearing elements while spandrel beams are the horizontal framing elements supported by the mullions.

To obtain energy efficiency, the curtain wall mullions comprise aluminium extrusions joined by thermal breaks. Thermal breaks are barriers between exterior and interior aluminium extrusions which are usually made of low heat conductive material, typically glass-fibre reinforced polyamide. The glass-fibre reinforced polyamide is mechanically locked into the aluminium extrusions to provide thermal isolation. The advantage of energy efficiency makes the composite thermal break profiles as the most popular curtain wall/window mullion type currently.

Although the thermal break composite façade sections are the most widely used mullion sections, only limited analytical research on these composite façade profiles has been carried out. As a major building component, it is necessary to carry out further research to understand the behaviour of the thermal break façade mullion section to help façade

industry. The goal of this research is, therefore, to obtain a full understanding of the behaviour of the façade section.

In order to gain a thorough understanding, experimental and numerical investigations were carried out. Analytical formulations were derived to evaluate bending capacity of thermal break façade mullions.

As the thermal break façade composite section has exterior and interior aluminium extrusions and thermal break joining them together, it can be simplified as a sandwich structure as suggested in the early studies (Feldmeier 1987) and (Heinrich, Schmid & Stiell 1980). However, unlike the conventional sandwich structures, the bonding between skins and core of a thermally broken composite façade section is not achieved by laminate as typical sandwich structures, e.g. woven glass fibre-epoxy face sheets and a PVC foam core in (Steeves & Fleck 2004b), fibre reinforced composite structure mentioned in (Johnson & Holzapfel 2006), (Johnson, Pickett & Rozycki 2001) or honey comb sandwich panels (Kee Paik, Thayamballi & Sung Kim 1999).

The aluminium profiles and polyamide core are actually crimped together. During manufacturing process, the glass fibre reinforced polyamide was rolled into pre-knurled aluminium profile. The bonding between aluminium and polyamide insert has been achieved by pre-knurling the aluminium intake during manufacture. Glass-fibre reinforced polyamide is then rolled into and forms a mechanical interlock between these two materials.

This normal pressure is then transferred from the aluminium profile to polyamide insert. Friction is also generated during rolling process which helps develop shear connection. The connectivity depends on the shear resistance at aluminium profile and polyamide thermal break.

High pressure is often generated during rolling process. It deforms the aluminium extrusions and transfers the pressure to polyamide inserts. This helps to form friction between aluminium and polyamide. However, the pressure transmitted during rolling is not constant and cannot be controlled as it also depends on the knurled shape on the aluminium profile. The sharpness and newness of the knurled wheels decide the knurling shape but are often wearing off during process. Therefore, the knurling shape is hard to keep constant. This results in possible large variation of shear resistance/friction force at the connection.

Due to the existence of possible fluctuation in connectivity caused by manufacturing process, it is, therefore, important to do experimental investigation to understand the behaviour of such thermal break mullions. In this study, comprehensive laboratory tests were carried out to investigate section shear and tensile capacities of a typical symmetrical thermal break façade mullion section in accordance with EN14024:2004 (Standard 2004). Experimental investigation was carried out at various temperatures and various loading rates. These experiments provide first hand information regarding how the section capacities vary with temperature changes and whether the section capacities are strain rate sensitive.

As the façade mullion is usually designed as a simply supported beam spanning between the floors, it supports the loadings that are laterally applied on the glass panels, such as wind, earthquake, thermal and blast loading as well. To understand the bending behaviour of the mullion section, experiments using four-point bending for four different spanned beams of the same typical thermal break section at room temperature under quasi-static loadings were carried out. A total of twelve beam specimens, three per each span, were tested. Comprehensive data were collected for the displacements along the beam span and strain data at the mid-span along the cross-section. These experimental data provided insight into how the thermal break façade behaves under bending.

To gain further understanding of the behaviour of the thermal break façade mullion section, Finite Element models for the typical thermal break façade mullion section, used for experimental investigation, were created by ABAQUS software version 6.11 to simulate the experiments and obtain further details. FE models to investigate section shear capacity as well as transverse tensile capacity were demonstrated. To simulate the interfacial action between the aluminium skins and polyamide core, frictional interaction was introduced. A proposed progressive failure model was proposed to simulate the failure modes from the shear tests. In terms of the FE tensile model, the numerical simulation was performed to show the failure of the section. The failure modes of both FE models presented similarity to the experiments. Typical analysis results, including contact stresses between the interfaces, were plotted and confirmed the validity of the proposed progressive failure model.

Beam models of four-point bending were also created by using ABAQUS software. Four beam models were built to match the spans of beam specimens. Frictional interaction was also adopted to simulate the interfacial action between the skins and the core. To model the failure mechanism, a proposed partitioned multi-phase beam failure model was created and successfully applied to the beam models. FE beam models demonstrated similar failure modes as the experimental ones.

Comparisons between the FE model results and the experimental ones were made for shear and transverse tensile capacity models as well as the beam models. A good correlation between the FE models and experiments were observed for all models.

An asymmetrical thermal break façade mullion section was also investigated numerically. FE models were created to determine shear and transverse tensile capacity as well as bending capacity. The proposed progressive failure model and the proposed partitioned multi-phase failure model were applied. Results proved that the two proposed failure models are applicable to analyse this asymmetrical section.

A proposed frame work for analytical solution was set out based on sandwich theory which was employed in the early studies of the thermal break sections. With superposition approach, the analytical frame work eliminated the dependence on the input of experimental investigation. A series of formulas were derived to determine the beam bending capacity. The derived formulation established a base to set up design tables for various thermal break sections.

The details of the experimental and numerical investigations of the typical thermal break façade mullion section as well as the analytical frame work are discussed in the relevant chapters. The numerical investigation of a custom made asymmetrical thermal break section is also presented.

1.1 Scope and limitations

This research is focused on experimental and numerical investigations of a typical thermal break façade section. The objective is to explore the complexity and multiplicity of the thermal break section as this research is the first comprehensive study in its kind.

The experimental investigation mainly involved quasi-static experiments for both section capacity tests as well as beam tests although a series of high strain rate section

capacity tests, involving a small quantities of specimens, were also carried out to explore the strain rate sensitivity of section shear and tensile capacity. Future study is recommended to continue the research on strain rate sensitivity of the thermal break composite mullion sections to draw sensible conclusions.

Drop tests to evaluate the behaviour of the thermal break section have been excluded from the scope of this study as the results of field tests performed by industrial partner confirmed that high strain rate was not relevant to the façade composite section. Strain rate study regarding the dynamic wind and earthquake loadings are also excluded as the focus of this research is on the section behaviour under quasi-static loadings.

The numerical investigations on section capacities and beam capacity have been carried out. Material properties of aluminium alloy and glass fibre reinforced polyamide under room temperature were adopted. The temperature effect has not been included in the scope either. To investigate the temperature effect in the FE models, the material properties at high/low temperatures are required. Due to lack of testing facilities and funding, both material properties of aluminium and polyamide were unable to be obtained. Therefore, considering temperature effects in the FE model has been classified as part of a future study,

As this research has been planned to study the typical thermal break section under quasi-static loading by experimental and numerical investigation, analytical formulation to calculate the capacity of the thermal break section has been initiated but not verified. The frame work of analytical solution, based on sandwich theory proposed in this thesis, is in its early stages. To develop a series of formulations and design tables requires further experimental and numerical investigations of various types of thermal break sections. Comprehensive data from different profile types are required to prove the validity of design formulas and create design charts. Therefore, future studies will be required to continue this research.

1.2 Thesis layout

This thesis comprises eight chapters. The first chapter is the Introduction, followed by literature review of past studies, material properties of aluminium and polyamide, interfacial modelling, sandwich theory and sandwich beam under bending presented in Chapter 2.

Chapters 3 and 4 details the experimental and numerical investigation of a typical thermal break façade section. Comparison of experimental and FE model results was carried out in Chapter 5. Another thermal break façade profile is investigated through FE modelling and is explained in Chapter 6.

Chapter 7 proposes a frame work for analytical solutions based on sandwich theory. Formulation based on superposition approach was initiated to lay the foundation for further analytical studies.

The final chapter is the Conclusions. The conclusion chapter wraps up the whole thesis.

Chapter 2

Literature Review

2. Literature review

2.1 Introduction

As a composite section, a typical thermal break façade mullion section comprises two aluminium skins and a core made of glass fibre reinforced polyamide. The behaviour of the composite section may differ to the homogeneous section. To understand the behaviour of composite sections, literature studies were carried out.

Regarding to this thermal break composite façade section, limited research resource could be found. One of them was Feldmeier and Schmid's technical paper (Franz Feldmeier 1988). The other one was the European standard EN14024:2004 (Standard 2004). Both of them are based on the classical sandwich theory.

Based on the past studies, the strength of the composite section is related to the material properties of skin and core materials as well as the connectivity between skin and core. Literature studies about material properties of aluminium alloy and glass fibre reinforced polyamide were also carried out. To understand the interfacial action between the contact surfaces of aluminium and polyamide, literature on interfacial modelling of sandwich structures was studied.

As a load bearing component of façade system, the thermal break façade mullion is usually supported between floor to floor by floor structure. The mullion can be simplified to a simply supported beam under bending. The literature regarding sandwich beam bending was therefore investigated. The literature mentioned in this chapter provided valuable reference to this research.

2.2 Past studies on composite façade mullion

Aluminium framed wall and window systems can be back dated to the 1930's. It was rapidly developed after the World War II. Until 1990's, it accounted for approximately 65% of the commercial market (Nik Vigener 2011a; Nik Vigener 2011b). As aluminium is a highly heat conductive material, thermal breaks made of plastic were introduced to be placed between inward-facing and outward-facing of mullions to provide thermal isolation. Now, a typical mullion section in the building industry is the one comprising an external and internal extruded aluminium section with thermal breaks made of glass fibre reinforced polyamide joining the two together (Cooke 2007).

With the introduction of glass fibre reinforced polyamide thermal break, the typical mullion section is no longer a homogeneous section but a composite section. However, structural effects of thermal breaks were ignored in the design at the early stages (Cooke 2007). Thus, the prediction of deflection of mullions was inaccurate then.

To help the designers to understand the behaviour of the mullion and take composite action into consideration, Feldmeier and Schmid wrote a three-part paper (Franz Feldmeier 1988). In the first part, they developed a series of formulas to work out effective stiffness of the composite section based on the sandwich theory by Stamm and Witte (Stamm & Witte 1974). They assumed the connection between plastic and aluminium is ideal rigid; the composite action relies on the shear flow and the composite connection is elastic. Based on these assumptions, they took Hooke's law as a base for stress and strain relationship, i.e. stress and strain maintain a linear relationship when the deformation of aluminium and plastic are small. As the Young's modulus of plastic is relatively low comparing to that of aluminium, they suggested ignoring the normal stresses in the plastic and therefore the aluminium has the strength to force the plastic to bend parallel to it. Distortions were also neglected as well as the rotation of vertical axis of the profile cross-section. A composite parameter λ was introduced to measure the degree of composite effect. It ranges from zero to one. When λ equals to zero, the connectivity between aluminium and plastic is non-existent. However, the connection is assumed fully rigid when λ equals to one. The rigidity of the connection lies in between these two limits. By adopting sandwich theory, they were able to work out the relationship between deflection and bending moment and the relationship between angle of rotation of deformed element and shear force. And therefore, they derived the equation for calculating the effective second moment of

inertia of the composite section as well as equations for calculating bending capacity and deflection.

In part 2, they explained the rules set by German national and international regulations regarding the stability of metal-plastic composite profile and provided a calculation example under temperature and wind loads. Laboratory tests to determine shear strength and shear stiffness; transverse tensile strength and creep and ageing behaviour were discussed as well.

Part 3 focused on the application and justification of pre-dimensioning diagram. With the methodology stated in parts 1 and 2, they provided working example to do preliminary design of the metal-plastic composite section.

Sixteen years after Feldmeier and Schmid's work (Franz Feldmeier 1988), European standard of EN14024 was published in 2004 (Standard 2004). EN14024 is not a replacement for any previous standards. It was published to deal with the performance of metal profiles with thermal barrier (break). It specified the mechanical performance; requirements; proof and tests for the assessment of metal-plastic profiles. This standard was limited to the thermal barrier profiles designed for windows, window walls and curtain walls, but did not apply to the thermal barriers made only of metal profiles connected with metal pins and screws. It also separated the assessment between windows, doors and related components from profiles in facades. This standard set up two categories based on the design span and three types of mechanical design systems for the assessment of mechanical resistance and deflection.

EN14024 specified the general requirements of assessment for the three types of systems and also specified the test procedure to assess the thermal barrier material independently of the shape of the thermal barrier and of the profile design. Requirements for strength and deformation were listed in Table 1 for each category and system.

Laboratory tests to assess the suitability of thermal barrier material; transverse tensile strength; shear strength and elasticity constant and ageing of the profile were specified in this standard. Testing environment including testing temperatures, specimen size, test setup and procedure were defined. Elevation method and formulas for determining tensile strength, shear strength and elasticity constant were given in the code.

Method of calculating static proof was detailed in Annexure A and B for category CW (category designated for constituent parts of curtain walls with spans greater than 2.25m) for all three mechanical systems. For category W (category designated for windows, doors and secondary constituent parts of curtain walls), the calculation of mechanical resistance was not required by this standard. However, deflection calculation was necessary. When calculating deflection, formulas provided by Annexure C to calculate effective second moment of inertia of the profile shall be adopted. These formulas were based on the effect of the elastic connection and consistent with the formulas given in (Franz Feldmeier 1988). A composite parameter λ defined by the formula similar to the one in (Franz Feldmeier 1988) was also used in the calculations in this standard.

Other studies such as the early paper by Schmid with others Heinrich, Stiell and Rosenheim in 1980 (Heinrich, Schmid & Stiell 1980) provided a static calculation method to work out the load versus displacement relationship by taking the composite action into consideration. They defined the connectivity by spring stiffness. Their study was also limited to the elastic range with linear stress and strain distribution along the cross-section assumed.

Overall, the past studies, including the current design standards are limited to the elastic analysis. The connection between aluminium and polyamide is assumed as elastic with small deformation. However, loadings such as wind and earthquake applied to the thermal break profile façade mullion could be much larger in the actual serviceability design. The connection may not be classified as an elastic connection. Therefore, it is necessary to carry out the study of the thermal break profile into plastic range. The objective of this research is to extend the study of this composite connection further into the plastic range.

2.3 Study of material properties of aluminium and polyamide

As the thermal break composite façade section comprises external and internal aluminium section and glass fibre reinforced polyamide thermal break, its load bearing capacity depends mainly on the material properties of aluminium and polyamide. It is, therefore, necessary to study the material properties of these two materials.

European standard Eurocode 9 (EN 1999-1-1:2007): Design of aluminium structures (Institution 2007), part 1-1: general structural rules, was studied to understand the requirements for resistance, serviceability, durability and fire resistance of aluminium structures. Its Chapter 3 gave material properties of all types of wrought aluminium alloys as well as cast aluminium alloys. The material properties include 0.2% proof strength, ultimate strength, minimum elongation and reduction factors, etc. It also gave the values of modulus of elasticity, shear modulus, Poisson's ratio, coefficient of linear thermal expansion and unit mass for the aluminium alloys. Its Annexure E provided two idealised material models to describe stress-strain relationship of aluminium alloys. These models are piecewise models and continuous models. In piecewise models, they are separated by bi-linear and three-linear models. The continuous models were also separated into two:

1. Continuous models in the form of $\sigma = \sigma(\varepsilon)$
2. Continuous models in the form of $\varepsilon = \varepsilon(\sigma)$

Formulas to define the characterization of stress-strain relationships were given and divided into three regions in the form of $\sigma = \sigma(\varepsilon)$. In terms of the continuous models in the form of $\varepsilon = \varepsilon(\sigma)$, Ramberg-Osgood model was discussed and formulas were derived to calculate the stress-strain relationships. An upper bound limit of elongation was given based on the experimental data. This standard provides comprehensive information and guidelines to calculate the material properties of aluminium alloys.

Further study into the continuous material model of aluminium alloys were carried out. Ramberg-Osgood material model was investigated. Ramberg and Osgood derived a simple formula to describe the stress-strain relationship of aluminium alloys using three parameters: Young's modulus and two secant yield strengths. Their work was first published in the Technical Note No. 902 of National Advisory Committee for Aeronautics, USA (Ramberg & Osgood 1943). In their article, they derived a series of

dimensionless charts based on a formula to determine the stress-strain curves when these three parameters were given.

Ramberg-Osgood continuous material model was adopted into the study by Welco, Paulsen and Brobak : The behaviour of thin-walled aluminium alloy profiles in rotary draw bending – a comparison between numerical and experimental results (Welo, Paulsen & Brobak 1994). Their work involved elasto-plastic finite element analysis of a rotary draw bending process using eight – node brick elements and contact elements. Their objective was to predict bendability and elastic spring back in industrial bending by using numerical simulation. Based on Ramberg-Osgood continuous material model, they worked out stress-strain relationship of aluminium alloy AA6063 and applied it into their FE model. The simulated behaviour matched well with the experimental behaviour with the help of applying accurate description of material model.

Gardner and Ashraf initiated a new design method in their paper titled “structural design for non-linear metallic materials” (Gardner & Ashraf 2006). They stated that many common metallic materials, such as aluminium alloys, stainless steel and some high strength steels, displayed sufficient non-linearity. They concluded that using bi-linear behaviour to describe these non-linear metallic materials would lead to inaccuracies and conservatisms for these materials. The new derived method, based on Ramberg-Osgood continuous material model, utilized a more accurate material model and a continuous measure of section deformation capacity to provide more rational and efficient design.

Unlike aluminium material, no material model for glass fibre reinforced polyamide has been established. Material properties are obtained by experiments. Curtis, Bader and Bailey (Curtis, Bader & Bailey 1978) carried out experiments to investigate the crack form and strength of polyamide thermoplastic reinforced with glass and carbon fibres. In their paper, they described the experimental procedure adopted and published their results. Discussion and comparison of strain, modulus and strength were made between polyamide with different fibre volume fractions and different fibre length.

Six years later, N. Sato, Kurauchi and S. Sato (Sato et al. 1984) studied the fracture mechanism of short glass fibre reinforced polyamide thermoplastic. They found that there were three stages in the failure. Their studies were also based on experimental investigation. Other studies such as Akay and O'Regan (Akay & O'Regan 1995) and Fu, et al. (Fu et al. 2000) studied fracture behaviour of glass fibre reinforced polyamide

mouldings and tensile properties of short-glass-fibre- and short-carbon-fibre-reinforced polypropylene composites based on experimental investigation as well.

Mouhmid, et al. (Mouhmid et al. 2006) investigated the influence of glass fibre content, temperature and strain rate on the mechanical behaviour of a short glass fibre reinforced polyamide 6.6. They described the test setup, specimen size and test environment. They carried out discussion on the test results and concluded that the studied composite material was a strain rate, temperature and fibre volume fraction dependant material.

Based on limited literature available on glass fibre reinforced polyamide, experimental investigation of the material properties are necessary in this study. Therefore, relevant standards were studied. To understand the general principles of setting up experiments, International Standard ISO 527-1 (Standardization 1993a) was studied. This standard provided guidelines for determining the tensile properties of plastics and plastic composites under defined conditions. It specified general principles, apparatus requirements, specimen requirements and preparation. It also specified test conditions and required test procedure as well. Evaluation methods for test results were provided to calculate stress, strain, modulus and Poisson's ratio. Test report requirements and typical stress-strain curves were provided at the end of the standard.

To be able to make specimens comply to the requirements of ISO 527-1, International Standard ISO 527-2 (Standardization 1993b) was studied. This standard specified the shape of specimen and detailed dimensions of the standard specimens. It also specified the detailed dimensions of alternative small specimens.

In summary, Ramberg-Osgood continuous material model was suggested by the above journal papers and European standard. It provides an accurate approach for non-linear metallic materials, such as aluminium alloys. Stress-strain relationships of aluminium alloys can be worked out by adopting the formulas provided by Annexure E of Eurocode 9 (Institution 2007). Since there is no material model established for glass fibre reinforced polyamide, its material properties need to be obtained through experiments.

2.4 Studies involving Interfacial modelling

As a composite section, the thermal break façade mullion section is made of two aluminium parts joined by the glass fibre reinforced polyamide. The connectivity between the aluminium and polyamide plays a considerable role in section capacity. To understand the interaction between the two materials, literature studies were carried out.

Back in 1968, Adekola (Adekola 1968) studied the partial interaction of elements of composite beams made of steel and concrete. The connection between steel and concrete was assumed elastic. He proposed a theory of interaction taking both slip and uplifting into account. His theory was based on the simple bending theory but ignoring shear lag effects. He assumed each element of a composite member is behaving separately and the longitudinal stress distribution over the depth of the entire composite section is not necessarily collinear. However, he assumed the curvatures of the interacting elements were equal. He also assumed that the rate of change of the axial force was directly proportional to slip and uplift force was directly proportional to differential deflection. With these assumptions, he formulated differential equations to analyse the relation between uplift and axial forces in the regions of positive uplift as well as the regions of negative uplift where frictional effects were incorporated.

Twelve years later, Yasunori, Sumio and Kajita studied steel-concrete composite beams by nonlinear finite element analysis (Yasunori, Sumio & Kajita 1981). Their nonlinear analysis was based the assumptions of:

1. The distribution of strain is linear throughout both depths of the steel beam and concrete slab.
2. Shear connectors act as continuous media along the length of the composite beam elements.
3. The steel beam and concrete slab deflect equally at all points along the beam element, i.e. equal curvatures at any cross-section.

Based on a cracked concrete slab, they worked out a series of formulas to analyse the composite beam by FE modelling. In this paper, they compared the numerical results with experimental ones and obtained good agreement.

Studying interaction in composite sections was carried out in details in 1986. Contact interaction between two (or more) three dimensional bodies was studied by Chaudhary and Bathe (Chaudhary & Bathe 1986). They derived a solution method and calculation

sequence algorithm to analyse the contact between two contact bodies. They assumed the region of contact was unknown prior to analysis and large changes in the contact area were possible. The changes in the contact area were possibly relative sliding with Coulomb friction or separation after contact. The developed contact forces on the two bodies were assumed to be statically equivalent to each other and the support reactions were in equilibrium with the externally applied forces, inertia forces and the contact forces for each body. They employed a Lagrange multiplier technique to enforce the conditions of sticking and sliding contact between the two bodies. Their solution and algorithm was able to be applied on multi-body contact problems for both static and dynamic analysis.

Based on Coulomb friction theory, a static frictional model was studied by Chang, Etsion and Bogoy (Chang, Etsion & Bogoy 1988). They studied frictional forces required to shear off the interface bonds of contacting metallic rough surfaces. During their calculation, they took the prestress condition of contacting asperities into consideration. The contact surfaces were modelled by a collection of spherical asperities with Gaussian height distribution. Contrary to the classic law of friction, they concluded the static friction coefficient was affected by material properties and surface topography and was actually dependant on the external loading.

Blau also studied the significance and use of the friction coefficient (Blau 2001) in 2001. He reviewed the measurement and use of static and kinetic friction coefficients. He also discussed the usefulness of the friction coefficients and described the sources of frictional resistances in terms of shear localization. Similarly, Urbakh, et. al. (Urbakh et al. 2004) also discussed the friction, adhesion and lubrication in their paper. They provided modern views of the friction and its application.

Cao and Evans (Cao & Evans 1989) studied the debonding and interface fracture resistance of composite elements containing biomaterial interfaces. They carried out experimental investigations regarding a symmetric double cantilever beam, an asymmetric cantilever beam, a four-point flexural beam and a composite cylinder. Their experimental investigation revealed that the critical strain energy release rate increased with increase in phase angle, especially when the crack opening became small. Their experimental results were consistent with the proposed simple contact zone model.

Further research was conducted concerning contact between an unidirectional glass fibre/epoxy composite beam and supporting rollers by Cui and Wisnom (Cui & Wisnom 1992). They applied contact elements supplied by ABAQUS software to calculate the actual contact stresses and contact length at the supporting rollers under three- or four-point beam bending. They concluded their FE modelling results gave more realistic stress distributions than those based on assumed load distributions. If the material were assumed to be linear elastic, large parts of the beam followed the classical beam theory in both three-point and four-point bending specimens. However, the shear stresses locally in the vicinity of the rollers were higher than the maximum shear stress given by classical beam theory. If the material were assumed nonlinear, then the classical beam theory would not be valid.

Damage analysis of interface was carried out by Ladeveze and Corigliano (Allix, Ladevéze & Corigliano 1995) in their paper titled “Damage analysis of interlaminar fracture specimens”. They analysed delamination specimens within the framework of a damage meso-modelling of composite. They used a stacking sequence of homogeneous layers and interlaminar interfaces to model a laminate. Small displacements and strain hypotheses were considered when modelling the interface delamination. The interface was assumed to be damageable in order to simulate the delamination phenomenon. When considering the propagation of a pre-existing crack, the main parameters for the interface model identification were the critical energy release rates. Finite element scheme was used to model two beams connected by a damageable interface. Comparison of results between simulation and testing showed the proposed modelling has capacity for a complete simulation of delamination using relatively little experimental data.

Padhi, et, al. (Padhi et al.) studied laminated composite plates in bending. They developed and implemented a progressive failure methodology for composite plates. They used several failure criteria to predict the failure mechanisms. They also studied the effect of aspect ratio on the strength and stiffness of the composite plates. Finite element software ABAQUS was used to analyse the plate bending. Non-linear strain-displacement relations which contain large strain and large rotation were used in the analysis. The predictions of the model correlate well with the experimental results for different aspect ratios.

Corigliano, Rizzi and Papa (Corigliano, Rizzi & Papa 2000) also studied a composite sandwich by numerical and experimental investigation. Their paper presented the results of an experimental and numerical study on the mechanical behaviour of a synthetic-foam/glass-fibre composite sandwich. It focused on the experimental testing of this sandwich composite panels and its separate components as well as numerical FE simulation of the sandwich panels under three- and four-point bending tests. They described the uniaxial tensile and compressive tests, flatwise tension tests, three- and four-point bending (TPB and FPB) tests. FE model strategy was described and ABAQUS software was employed to carry out the numerical simulation. To simulate the core collapse, skin collapse or delamination, they proposed a simplified procedure for the simulation of the progressive damage in the core, in the skins or in the line of elements near the interface between the extra-skin and the core. This simplified procedure consisted of a local stiffness release at the Gauss point level, implemented through a user subroutine. When a threshold value of a scalar failure index was reached in a single Gauss point, the tensile elastic modulus E was annihilated locally; the contribution of that Gauss point to the element stiffness matrix was then brought to zero. In the numerical calculations, a Rankine criterion was assumed for the simulation of damage in the core and the skins, while a control on the maximum shear stress was adopted for the strip of elements at the boundary core/lower skin for the simulation of skin debonding. This procedure was based on the assumption of elastic/perfectly brittle behaviour. In the simulations, the core was considered as homogeneous and isotropic, same for the skin. The critical value of shear stress for the simulations of skin debonding was adopted from the test results. The numerical analyses were conducted under the assumption of plane strain. Four node plane strain elements were used for the mesh. The loading and support rollers are simulated as rigid bodies. Comparison between test results and FE model were made in the paper. Load/displacement plot obtained by activating the rupture criterion in the core for TPB model was compared with the test results. All the comparisons showed good correlation between test and FE model.

Johnson, Pickett and Rozycki (Johnson, Pickett & Rozycki 2001) proposed numerical methods to predict impact damage in composite structures. They adopted the continuum damage mechanics (CDM) model for simulating the delamination failure of fabric-reinforced composites. The stacked shell elements were assigned with a contact

interface condition. Different failure modes were discussed and FE code PAM-CRASH was implemented. Testing results were compared with the FE results. In the FE model, ply layers were tied together using a “sliding interface” with an interface traction-displacement law. The computational model gave a good approximation for delamination stresses and failure.

Continuing the above study, Johnson worked together with Holzapfel and described the progress made on material modelling and numerical simulation of fibre reinforced composite shell structures subjected to high velocity impacts in their paper titled “Influence of delamination on impact damage in composite structures” (Johnson & Holzapfel 2006). The continuum damage mechanics (CDM) model for fabric reinforced composites was applied to model both in-ply damage and delamination failure during impact loading. Failure at the interface was modelled by degrading stresses using two interface damage parameters corresponding to interfacial tension and shear failures. Their numerical approach for delamination modelling was based on stacked shell elements with contact interface conditions. Shell elements representing a sub-laminate were mechanically tied together with nodal constraints via contact interfaces, which might separate when the interface failure condition is reached. Composite failure modellings were separated into two – delamination model and ply failure model. By applying CDM principles to an elastic interface, damage evolution equations were derived for through-thickness tensile and interlaminar shear damage. Tensile failure mode, shear fracture mode and mixed tensile and shear mode were discussed to derive the functions of delamination fracture, respectively. These functions were implemented into the computational code. Ply failure model was modelled by layered shell elements with a tied interface which might fail by delamination. Shell elements were assigned as homogeneous orthotropic elastic or elastic-plastic material property. Constitutive laws for orthotropic elastic material with internal damage parameters were derived. Damage evolution equations were derived as well. Pam-crash code was implemented. Therefore, each ply was represented by one layer of shell elements and the individual ply layers were tied together by using a “sliding interface” with an interface traction-displacement law. This approach gave a good approximation for delamination stresses and failure, with the advantage that the critical integration time step was larger since it depended on the area size of the shell elements. Impact simulation was made to simulate high

velocity impact of cylindrical shells. Comparison between computational results and tests showed good correlation.

Another paper regarding the failure mechanisms of sandwich beams by Steeves and Fleck (Steeves & Fleck 2004b) was studied. In the paper, they illustrated the four failure modes of a woven glass fibre-epoxy facing with PVC foam core sandwich beam. They adopted Allen's formula (Allen 1969) to obtain the stiffness of the beam and strength under three-point bending for each failure mode. They tested the material properties of PVC foam core and woven glass-epoxy face sheet and also designed and tested nine sets of three-point bending tests. Each set had its own geometry. ABAQUS software was used to analyse the sandwich beam response. The beam was modelled using plane strain elements. A refined mesh near the contacts between the beam and loading rollers was used. Contact between the sandwich beam and the three rigid circular rollers were handled by a contact algorithm within ABAQUS. To be able to achieve numerical convergence, coulomb friction coefficient of $\mu=0.01$ was adopted. The face sheets were treated as isotropic, elastic-ideally plastic with Poisson's ratio of 0.18. The contact between face sheets and core was not mentioned in this paper. However, they admitted the FE analysis did not take into account the progressive development of macroscopic shear cracks within the core, therefore, failure was predicted at a cross-head displacement of about half the observed value. Core shear failure was defined as the point where the maximum shear strain in the core attained the critical value of 15%. Comparison between test results, FE model and analytical prediction were performed. The FE simulation was able to capture the structural response of the sandwich beams up to the point of core or face failure.

A static friction model to predict the static friction for elastic-plastic contact of rough surfaces was presented by Kogut and Etsion (Kogut & Etsion 2004). Their proposed model incorporated the results of accurate finite element analyses for the elastic-plastic contact, adhesion and sliding inception of a single asperity in a statistical representation of surface roughness. They found that the strong effect of the external forces and nominal contact areas on the static friction coefficient was in contrast to the classical laws of friction. They concluded the main factors affecting the static friction coefficient were the dimensionless parameters of plasticity index and adhesion parameter. They also recommended that the effect of adhesion on the static friction was negligible at the plasticity index values larger than 2. They concluded that the classical laws of friction

were limiting cases of the present more general solution and were adequate only for high plasticity index and negligible adhesion. They pointed out some potential limitations of the proposed model and possible improvements. A comparison of their results with those obtained from approximate CEB friction model was made. Substantial differences were discovered. The CEB friction model showed severe underestimation of the static friction coefficient.

Cheng, Lee and Lu (Cheng, Lee & Lu 2006) proposed an FE analysis approach to evaluate equivalent elastic properties of complicated sandwich structures. They simplified the 3-D sandwich structure to an equivalent 2-D orthotropic thick plate continuum. They adopted small-deflection theory developed by Libove and Batdorf to analyse the truss-core sandwich panel. They used shell elements to model the top and bottom faces as well as the web. Instead of contact elements, they used rigid elements to model the connection between web and facings. They also adopted full-rigid elements to secure four side cross-sections. Comparison of their computed results with existing solutions was made in this paper. They also applied this method to a composite laminated circular-core sandwich panel to demonstrate the versatility of the proposed FE approach for complicated sandwich structures with good accuracy.

Recent studies, such as by Foo, Seah and Chai (Foo, Seah & Chai 2008) were carried out on numerical investigation of aluminium sandwich panels subjected to low-velocity impact loads. They used ABAQUS software to model a three-dimensional honeycomb sandwich plate and a rigid impactor. Three material models for aluminium alloys were considered for parametric study, which were elastic perfectly plastic, bilinear and Ramberg-Osgood strain hardening models. The different material models were proven to affect the impact response. They assumed the adhesive bonding between the face sheet and the core was perfect. Therefore, surface based tie constraint was assigned to connect the face sheet and core in FE modelling. They also adopted the penalty contact method in general contact algorithm provided by ABAQUS software to simulate the contact between the impactor and the top face sheet. To simplify the problem, frictional response during contact between the impactor and the structure was neglected. Friction between the clamp plates and face sheets was also ignored. They compared the numerical results with the experimental ones. They concluded the numerical model has the capability to predict the impact event adequately.

Programming technique of modelling sandwich structures can be learned from the paper by Hu, et al. (Hu et al. 2008). In this paper, they adopted an Arlequin based multi-scale method to study problems related to the mechanical behaviour of sandwich structures. They concentrated on a free clamped sandwich beam with vertical load applied on its free edge. They tested several coupling operators to assess the usefulness of the proposed approach. The purpose of their numerical simulations was to provide preliminary evaluation of the various coupling operators and the discrepancies between local and global models in the gluing zone.

A three-dimensional quasi-static contact problem with Coulomb friction was studied by Haslinger et al. (Haslinger et al. 2012). They focused on the full discretization of 3D quasi-static contact problems with Coulomb friction and a solution dependent on coefficient of friction. They used a three-step finite difference to work out time discretization. Based on the method of finite element approximation, which was based on T-FETI domain decomposition method, of the Tresca problems, they derived an explicit form of the static contact problem with Coulomb friction solved at each time level. Their numerical experiments showed the efficiency of the proposed method.

Recent study of interfacial relationship assignment can be obtained in the paper by Li, Li and Jiang (Li, Li & Jiang 2012). They studied composite frame structures consisting of high-strength concrete columns confined by continuous compound spiral ties and steel beams. Although their research related to the composite action at beam-column joint, interaction and load assignment methods were useful. They used ABAQUS software to model the joint between steel beam and concrete column. They assumed that no relative slip would occur between the steel beam and concrete. Therefore, they assigned tie constraint to connect them together. In terms of applying loadings, they assigned displacement loading for lateral load. They assigned displacement boundary conditions to define the applied lateral displacement to the frame structure.

In summary, the above works provide comprehensive information about the interfacial assignment for sandwich structures and other composite structures. Early literature was based on the elastic connection. Although some recent literatures considered the non-linear behaviour, they relied on the interface material failure rather than the failure of interfacial relationship, such as the occurrence of slip. In addition, the papers related to the friction theory provided further information and application.

2.5 Sandwich theory

As a composite thermal break façade section, sandwich theory was adopted as a base in the past studies presented in Section 2.2. Sandwich theory was mainly developed after the World War II (Straalen 2000). Early works were done by Reissner, Libove, Batdorf, Hoff and Mindlin which was collected by Plantema (Plantema 1966). It was followed by Allen (Allen 1969) and Stamm and Witte (Stamm & Witte 1974). The recent interpretation of this theory was by Zenkert (Zenkert 1995). This study was based on the sandwich theory interpreted by Allen and Zenkert.

Allen's book titled "Analysis and design of structural sandwich panels" was studied. Chapter two called "Sandwich Beams" was the main focus. In this chapter, Allen studied a sandwich beam consisted of two thin skins/faces and a thick core. All three layers were assumed firmly bonded together and the face material was much stiffer than the core material. He also assumed the materials of face and core were isotropic. Based on ordinary beam theory, he derived the shear stress distribution for the above sandwich beam. For the weak core, he assumed the core makes no contribution to the flexural rigidity of the sandwich, EI , and the shear stress is constant through the depth of the core while the faces behave as flexible membranes. The weak core was named as antiplane core.

He also studied sandwich beam with antiplane core and thick faces. He found the faces had significant local bending stiffness and no longer behaved as flexible membranes. The faces may be said to undergo local bending when it bends about its own centroidal axis rather than about the centroidal axis of the complete sandwich. He assumed that a face may also undergo purely extensional deformation when it was subjected to a uniform tensile or compressive stress. The contribution of the local bending stiffness of the faces to the bending stiffness of the entire sandwich was represented by the first term on the right-hand side of Eqn. 2.2 in Allen's book. He concluded that the local bending stiffness of the faces has an effect on the shear deformation of the core. The faces reduced the shear deflection at the expense of introducing additional bending moments and shear forces into the faces.

Allen gave formulas for deflection calculation of the different types of sandwich beams under various loading and boundary conditions based on the theory he developed.

A more recent book dealing with sandwich structures is Zenkert's "An introduction to sandwich construction" (Zenkert 1995). Chapter three of this book discussed the fundamentals of the sandwich beam theory. Based on early sandwich theory developed by Allen and others, he derived formulas for stress and deflection calculation of symmetrical thin faced sandwich beam as well as dissimilar faced sandwich beam. In Chapter 4, Zenkert explained the foundations of bending, buckling and free vibration of sandwich beam. Unlike the previous theory by Allen, et al, his theory included the effect of transverse shear deformation. He also provided formulas to calculate normal stresses and shear stresses as well as moment and curvature. In addition, he discussed the effect of thick faces and the effect of rigid core. Working examples of sandwich beams under various loading and boundary conditions were also provided in this chapter.

Overall, the sandwich theory developed by Allen, et al provided a solid base for studying the composite façade mullion profiles. The recent implementation from Zenkert improved the theory with consideration of transverse shear deformation of the core.

2.6 Sandwich beam under bending

Literature regarding the investigation of sandwich beams under bending was studied to gain knowledge in performing analytical, numerical and experimental investigations.

Monforton and Ibrahim (Monforton & Ibrahim 1977) carried out analytical investigation on sandwich plates. They derived an approximate formula to analyse sandwich plates comprised an orthotropic core and two unequal thickness anisotropic face plates.

Kemmochi and Uemura (K.Kemmochi 1980) studied a sandwich beam composed of soft core under four-point bending. They carried out analytical investigation and proposed a multilayer-builtup theory to analyse this sandwich beam. They took bending stiffness of face and core as well as the relative displacement between both faces into account. They adopted photoelastic measurement in their experimental investigation. The stress distribution obtained by the multilayer-builtup theory had good agreement with the experimental results.

Gordaninejad and Bert (Gordaninejad & Bert 1989) proposed a new sandwich theory by including transverse shear deformation in the facings and stretching action in the core. They compared the results of deflection and maximum shear stress with the ones obtained from classical sandwich theory. Their theory covered bi-modular material (different modulus in tension and compression) and ordinary material. They carried out both analytical and numerical comparison of the two theories. They concluded that the classical sandwich theory was not conservative in predicting deflection and maximum shear stresses.

Frostig and Baruch (Frostig & Baruch 1990) studied the behaviour of sandwich beams with transversely flexible core using a superposition approach. They proposed an analysis which could determine the transverse normal stresses at the interface layers between the skin and core in the regions of concentrated loads which were applied at the skins only. They also studied the main parameters affecting the overall behaviour and especially the peeling and the shear stresses between the skins and the core. In addition, they carried out numerical investigation based on the proposed principles to perform parametric study of some typical sandwich beams.

Further to the above study, Frostig et al. (Frostig & Shenhar 1995) investigated an asymmetrical sandwich beam with transversely flexible core. They developed the analytical method stated in (Frostig & Baruch 1990) further into the asymmetrical section and the loading condition was extended into any location, i.e. at upper or lower skins or at both. They studied the behaviours of the sandwich beam with and without the shear effects of the core. Their analytical methodology enhanced the physical insight into the beam behaviour at bending.

Frostig (Y 1992) extended his analytical investigation of sandwich beam with transversely flexible core into the failure mechanism. He studied the delaminated behaviour of this type of sandwich beam. Based on the similar assumption of small deformations, elastic behaviour, ordinary beam bending theory to the skins and ignoring shear strains in the core as the above papers, he derived a series of mathematical formulas with various boundary and loading conditions. He also provided numerical examples based on his methods. His high order analysis theory explored the behaviour of a general delaminated sandwich beam, defined the peeling stresses at the skin-core

interfaces as well as at the crack tips. His high-order theory was further discussed in other paper with his co-workers (Y. Frostig 1992).

Experimental investigation regarding the failure mechanisms for sandwich beams under bending was carried out by Cui, Wisnom and Jones (Frostig 1992). They tested two short beams made of sixteen plies and thirty-two plies of unidirectional glass fibre/epoxy under three and four point bending. They measured the inter-laminar shear strength and compared the results calculated by classical beam theory. They concluded that classical beam theory could not be applied to short beam specimen if the material shear response was non-linear.

Again, Frostig and shenhar (Shenhar, Frostig & Altus 1996) analytically investigated the bending behaviour of a sandwich beam with soft core and asymmetrical skins. The sandwich beam studied was a general one. The skins could be made of different materials, different geometries and different boundary conditions and could be either symmetrical or asymmetrical. They developed an analysis using variational principles to model the core as two-dimensional elastic medium and the skins as one-dimensional composite laminated beams. Their analysis included high-order effects using closed-form solutions for any type of sandwich construction and for any type of loading and boundary conditions. Local effects were also considered. Stresses and displacements along the beam and through the height of the core could be determined by their analytical methods.

One year later, Shenhar, Frostig and Altus (Sadighi & Saadati 2010) adopted a high-order analysis to define the stresses and failure mechanisms in the skin and the core of a sandwich beam with a compressible core under three point bending. Their analysis was general which could be used in beams with any type of skins and any type of boundary conditions. They determined the failure patterns with the aid of the analytical description of the longitudinal stresses in the skins and the principle stresses through the thickness of the core. The analytical methodology provided was able to indicate possible failure patterns and locations.

Around a decade ago, Daniel and Abot (Daniel & Abot 2000) studied the flexural behaviour of a composite sandwich beam. They carried out experimental investigations for a sandwich beam made of unidirectional eight-ply carbon/epoxy laminates and an aluminium honeycomb core. This sandwich beam was tested under three- and four-

point bending loads. Strain data were recorded in face sheets by strain gauges while strains in the honeycomb core were recorded by using moire technique. They found the beam face sheets show a softening non-linearity on the compression side and a stiffening non-linearity on the tension side. A linear variation in strain through the thickness was determined in both core and face sheets. The bending stiffness of the core can be neglected. In the case of pure bending, failure took place on the compression face of the beam. When shear was present, failure of the sandwich beam was governed by shear strength of the core. Simple analytical models by assuming the face sheets to behave like membranes and neglecting the contribution of the core, but accounting for the non-linear behaviour of the face sheets, were discussed. Results generated by analytical models were in good agreement with experimental ones.

Mines and Alias (Mines & Alias 2002) carried out experimental and numerical investigations on a polymer sandwich beam under three-point bending. They used ABAQUS software to perform a two-dimensional finite element simulation. They adopted material models to simulate the progressive failure. They considered skin failure model and foam core crush model. They adopted a feature of non-linear finite element analysis which used the incremental analysis as the structure deformed. They assigned maximum number of increments of 100 to fully model the progressive nature of the damage. They also considered volumetric effects when assigning foam crush model to the core. To avoid numerical instabilities due to large scale deformation in the core and material non-linearities, control parameters provided by the software were used. The numerical simulation highlighted the progressive damage of the beam.

Sokolinsky, et al. (Sokolinsky et al. 2003) also carried out analytical and experimental investigation of a sandwich beam made of aluminium face sheets and PVC foam core under four-point bending. They used three analytical methods, namely, classical sandwich theory, linear, and geometrically non-linear high-order sandwich panel theory (HSAPT), to analyse this sandwich beam. They found that the results generated by both linear and nonlinear HASPT were in excellent agreement. However, they concluded the classical sandwich theory underestimated the vertical displacements and failed to accurately predict the bending deformation.

Steeves and Fleck (Steeves & Fleck 2004a) developed analytical strength formulas to predict the collapse strength of sandwich beams with composite faces and polymer core

under three-point bending. They established an indentation model for elastic faces and an elastic-plastic core. They also worked out failure patterns and revealed the operative collapse mode as a function of geometry of sandwich beam.

Lagunegrand et al. (Lagunegrand et al. 2006) carried out experimental investigation of a laminated sandwich beam under four-point bending. They provided detailed setup of the experiment and results. The purpose of their test was to check the assumptions of defining an average stress criterion for the delamination initiation.

Belouettar, et al. (Belouettar et al. 2009) also studied the behaviour of a composite honeycomb sandwich beam under four-point bending. They focused on the experimental investigation of two types of composite beams. The sandwich beams were made of aluminium faces and either aluminium core or aramide fibre core. They carried out static and fatigue tests to investigate the flexural behaviour of both sandwich beams under these loads. They demonstrated the failure modes of the sandwich beams under static loads as well as fatigue loads. They also gave description of damage formation process from fatigue test results.

Sadighi and Saadati (Monforton & Ibrahim 1977) carried out analytical investigation of an unequal faced sandwich beam with flexible core. They used high-order theory to estimate core compression and face stresses and predicted damage modes. They compared their analytical results with some experimental results. They concluded that classical theory was not capable of predicting failure loads for unequal faced sandwich beam.

In summary, the literature studied was spanning over four decades. Most of them were based on the classical sandwich theory, but offered an enhancement. They provided useful methodology and formulations to carry out analytical investigations, especially the works done by Frostig and his co-workers. Although all these works were limited to the elastic calculations, they are useful source for this research.

2.7 Summary and conclusions

Extensive literature reviews were carried out regarding the behaviour of composite sections. Past studies of thermal break composite mullion sections provided useful formulation to calculate section strength and connectivity between face and core in elastic range. European standards provide guidelines and information for experimental setup, result evaluation and static proof loading. Literature about material properties provided the necessary information on elastic-plastic behaviour of aluminium alloy and test method of polyamide.

In terms of the interfacial action between face and core, comprehensive literature was studied. Frictional behaviour was assigned by some researchers to describe the interface behaviour. The finite element modelling techniques were also provided by the literature as well. Testing methods learnt from these studies provided useful information to this research.

Classical sandwich theory was studied. Analytical investigations regarding sandwich beams under bending were studied extensively. Enhancement to the classical sandwich theory was explored through the literature review process.

In conclusion, the literature studied provided a solid foundation for this research. Classical sandwich theory and its enhancements built a base for analytical investigations. Interfacial action assignment and finite element modelling techniques including assignment of elastic-plastic material behaviour were learnt. Guidelines and instructions on performing experimental investigations were also obtained from the relevant literature.

This page is left blank intentionally

Chapter 3

Experimental Investigation of a Typical Thermal Break Façade Mullion Section

3. Experimental investigation of a typical thermal break façade mullion section

3.1 Introduction

A thermal break façade mullion is usually made of aluminium profiles joined by a low heat conductive material – glass fibre reinforced polyamide in modern curtain wall system. The glass fibre reinforced polyamide is crimped into the connection which joins the aluminium profiles together. As both aluminium profiles and polyamide thermal barrier make the façade mullion a composite section, the load capacity of this mullion section relies not only on the material property but also on the connection. The deformed shapes and failure mechanism of this type of section are therefore more complicated than normal isotropic sections.

Adding to the uncertainty of the section capacity is the manufacturing process. During manufacture, the glass fibre reinforced polyamide was rolled into pre-knurled aluminium profile. The bonding between aluminium and polyamide bar has been done with steel rollers which deforms the aluminium with high pressure loadings. This normal pressure is then transferred from the aluminium profile to polyamide bar. Friction is also generated during rolling process which helps develop shear connection. The friction and normal pressure depend largely on the manufacturer and vary a lot. The complicated nature of the section geometry and uncertainty of connectivity at joints created by the manufacturing process make it important to carry out laboratory tests to gain first-hand information on the section characteristics.

Working as an exterior load bearing element, the thermal break façade mullion section is exposed to the weather. It has to withstand thermal loads, especially in winter and summer. It is, therefore, important to investigate the section capacity under various temperatures.

Apart from temperature load, facade mullions are also designed against other lateral loads, such as wind, earthquake and blast loads. Wind and earthquake loads are treated as equivalent static loadings conventionally while blast load is a dynamic load. Recently, design to withstand blast loads becomes increasingly important to façade design. As the curtain wall is at the exterior of the building, it is the first line of defence against blast loads. Accidental gas/chemical explosions and increasing terrorist attacks put blast design as one of the priorities, especially after 9/11 terrorist attack on the Twin Towers

of World Trade Centre in New York, USA in 2001 and suicide bomb attack on London Metro in 2005. These extreme events alert the designers worldwide to include blast load as one of the essential load cases for curtain wall design rather than a trivial one, particularly for landmark buildings.

In general, air blast pressures, impulse and durations vary from case to case. These pressures applied onto the curtain walls are not static but do occur at very short durations. The highly intense short duration transient blast loads can be categorized as high strain rate loads during design and associated research.

This chapter will focus on a comprehensive laboratory tests to determine section load capacity at various temperatures under quasi-static loadings, section capacity at room temperature under high strain rate loadings and four-point beam bending tests at room temperature under quasi-static loadings. Test results show the section capacity is sensitive to the temperature. Section capacity increases with decreasing temperature. However, section capacity does not show clear signs of strain rate sensitivity. Future study is recommended to confirm this conclusion. Beam tests also confirmed high ductility of this type of mullion section.

3.2 Typical Section of thermal break façade mullion under investigation

A typical composite façade section with thermal break was studied in this research. This typical facade mullion section was introduced by the sponsor - Permasteelisa group, who is a worldwide leading façade contractor. This façade section is comprised two external aluminium portions/skins and a polyamide core in the middle. The aluminium portions are made of aluminium alloy 6063-T6 and the core is made of polyamide 66 with 25% glass fibre. Details of the cross-section and photo are shown in Figure 3.1 below.

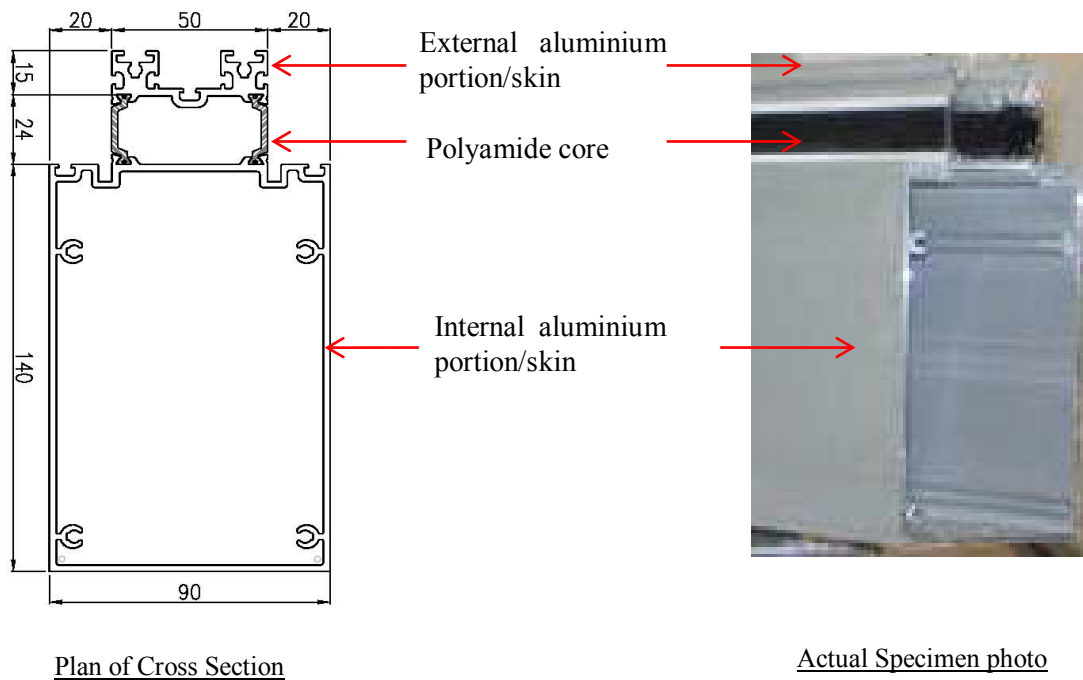


Figure 3.1 Section details

3.3 Quasi-static shear and transverse tensile tests at various temperatures

In order to get first-hand information on the section load capacity of this composite section, shear strength tests and transverse tensile strength tests were carried out. In the absence of any appropriate Australian Standard, European Standard EN14024:2004 (Standard 2004) was adopted to specify the requirements for assessment of the strength of this thermal break profile. This standard provides guidance and specification on the tests to determine the characteristic values of mechanical properties of the thermal break profile for curtain walls, doors and windows.

Considering a major load bearing component of curtain wall, the thermal break profile mullion provides effective thermal isolation. It has to withstand thermal loads, especially in winter and summer. It is, therefore, important to investigate the section capacity under various temperatures. EN14024 has taken temperature into account and specified three testing temperatures, which is low temperature (-20 ± 2) °C, room temperature (23 ± 2) °C and high temperature (80 ± 3) °C.

Shimadzu Hydraulic Universal Testing Machine, model REH 50/50 tonne at UTS, was chosen to perform all the tests under quasi-static loadings for this profile. This testing

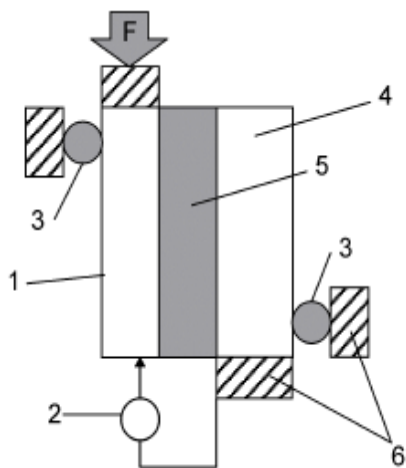
machine was operated under displacement control and the displacement rate was controlled in the range of 1mm/min to 5mm/min as per standard's requirement. Maximum loading was set to 20kN.

3.3.1 Shear tests

To obtain characteristic shear strength data, shear capacity tests were conducted to the requirements of EN14024. Ten specimens were tested at high, low and room temperatures. The length of each specimen was 100mm with tolerance of ± 1 mm. Test setup at all three temperature environments are explained in the following sections.

3.3.1.1 Test setup

For room temperature tests, shear deformation was measured directly on the specimen by a Linear Variable Differential Transformer (LVDT) and recorded with corresponding applied loading. The specimens were supported on a specially designed jig and guided laterally. Both vertical and lateral supports were welded on a 20mm thick steel plate and bolted onto the machine platform. As steel plate was bolted onto the bottom aluminium portion to restrict any rotation and lateral movement, a load pad was placed on the top aluminium portion outside the connection. The setup sketch and photo under room temperature is shown in Figure 3.2. The specimens were tested at the rate of 3mm/min to the maximum load or 2mm displacement if it slips according to the standard. The purpose of the shear tests was to test the connectivity between aluminium and polyamide.



Notation:

1. Test specimen
2. LVDT (displacement gauge)
3. Guide
4. Metal portion
5. Thermal barrier
6. Rigid support

Test Setup Sketch to EN14024

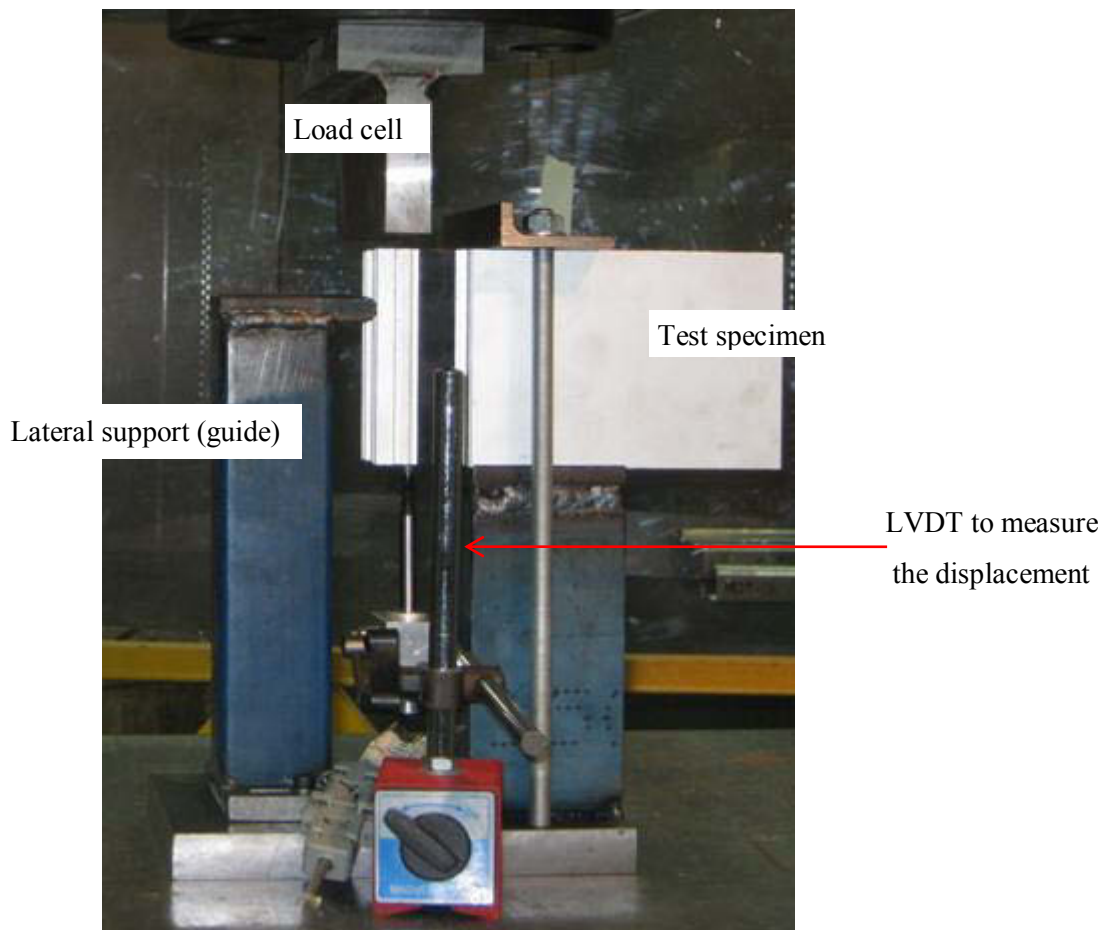


Figure 3.2 Shear test setup sketch and photo at room temperature

A temperature chamber was used to test specimens at high/low temperatures. It is relatively easy to do tests at high temperature (80 ± 3) °C as the temperature chamber can heat up itself and retain the inside temperature constant during tests. However, to

achieve the required low temperature (-20 ± 2) °C, liquid nitrogen in the Dewar was used to create low temperature testing condition. A plastic tube connecting nitrogen gas cylinder and the temperature chamber was placed in the liquid nitrogen Dewar to cool the gas. Cold nitrogen gas was blown into the chamber to generate low temperature of (-20 ± 2) °C inside and maintain the temperature at this level during testing. A thermocouple was attached to the specimen during test to confirm the temperature inside the chamber.

To be able to fit the test jig into the temperature chamber, test jigs were modified slightly. The bottom portion of aluminium was cut to fit into the temperature chamber and the loading pad was changed to a cylinder. Test specimens and jigs were pre-heated in an oven to (80) °C for high temperature tests, while they were stored in a freezer at (-20) °C with the test jigs for low temperature tests.

Unfortunately, the LVDT is designed to work only at room temperature. Hence, displacements couldn't be measured directly under the specimen inside the temperature chamber at high/low temperature tests. However, the crosshead displacement was measured by another LVDT attached to it. This displacement measurement provides a reasonable correlation with the displacement measured directly under the specimen. A series of verification tests were conducted prior to high/low temperature tests and the consistency between results were confirmed.

Test rate was set to 3 mm/min, the same as room temperature tests. Tests were performed to the maximum load. Test setup at high/low temperatures is shown in Figure 3.3 and Figure 3.4.

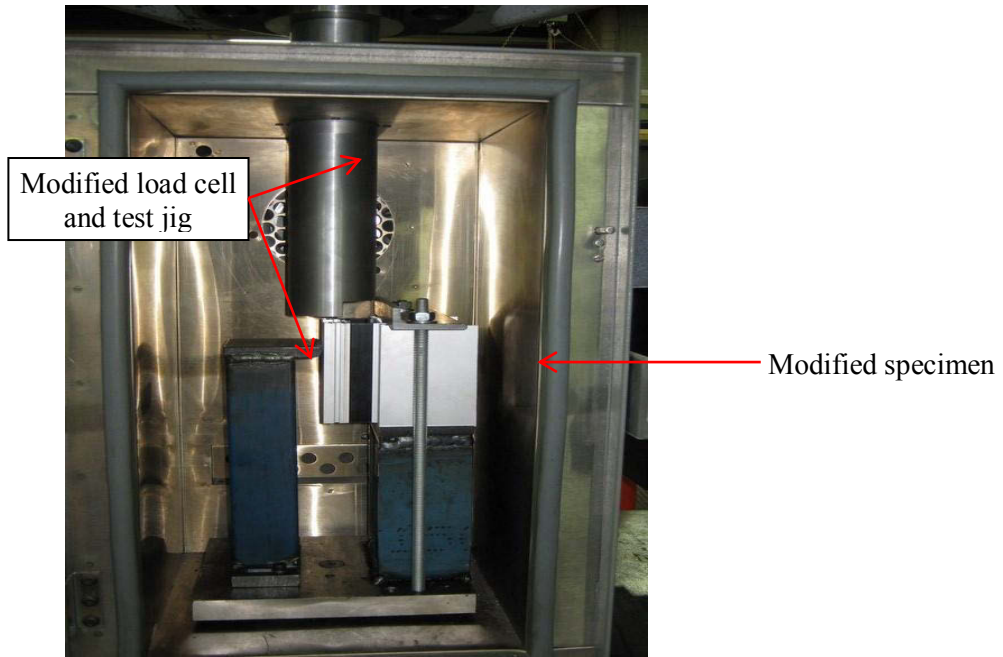


Figure 3.3 Test setup inside temperature chamber



Thermocouple - attached to the specimen inside the chamber to verify test temperature

Freezing nitrogen gas blown through tube to cool the chamber down

High temperature test setup

Low temperature test setup

Figure 3.4 High/Low temperature test setup

3.3.1.2 Failure modes and typical results

Failure mode of the shear tests at room, low and high temperatures are comparable, which is polyamide slipping away from the connection. The failed connections can be either top/ bottom or front/back connections as shown in Figure 3.5.

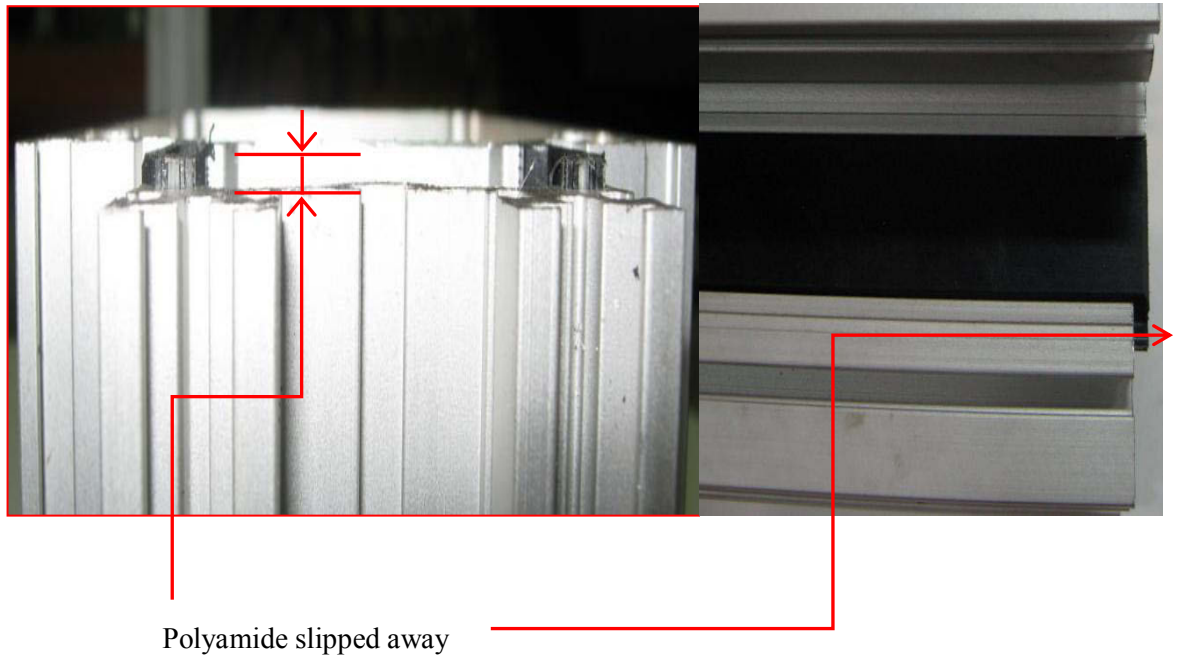


Figure 3.5 Shear test failure mode – Polyamide slipped away

Test results were evaluated by the methodology provided by EN14024:2004(Standard 2004).

Shear strength T (N/mm) for each test specimen shall be calculated as

$$T = \frac{F_{max}}{l} \quad [3.1]$$

where,

T represents the shear strength (N/mm)

F_{max} represents the maximum shear load (N)

l represents the length of the test specimen (mm)

Characteristic transverse shear strength shall be determined from the mean value of the test results calculated from [3.1] as 5% quantiles based on a logarithmic normal distribution with 75% confidence, which can be written as

$$T_c = T_{mean} - 2.02s \quad [3.2]$$

where,

T_{mean} represents the mean value of the measured values of shear strength at the test temperature

s represents the corresponding estimated standard deviation

The elasticity constant shall be obtained from the increment of deformation under load (slope of stress-strain curve) after the onset of the deformation. It shall be calculated by the following equation.

$$c = \frac{\Delta F}{\Delta \delta l} \quad [3.3]$$

where,

c represents the elasticity constant (N/mm²)

ΔF represents the increase of the shear load after the beginning of deformation (N)

$\Delta \delta$ represents the corresponding displacement of ΔF (mm)

l represents the length of the test specimen (mm)

Shear strength, characteristic shear strength and elasticity constant calculated by the above method are plotted against temperatures in the graphs below.

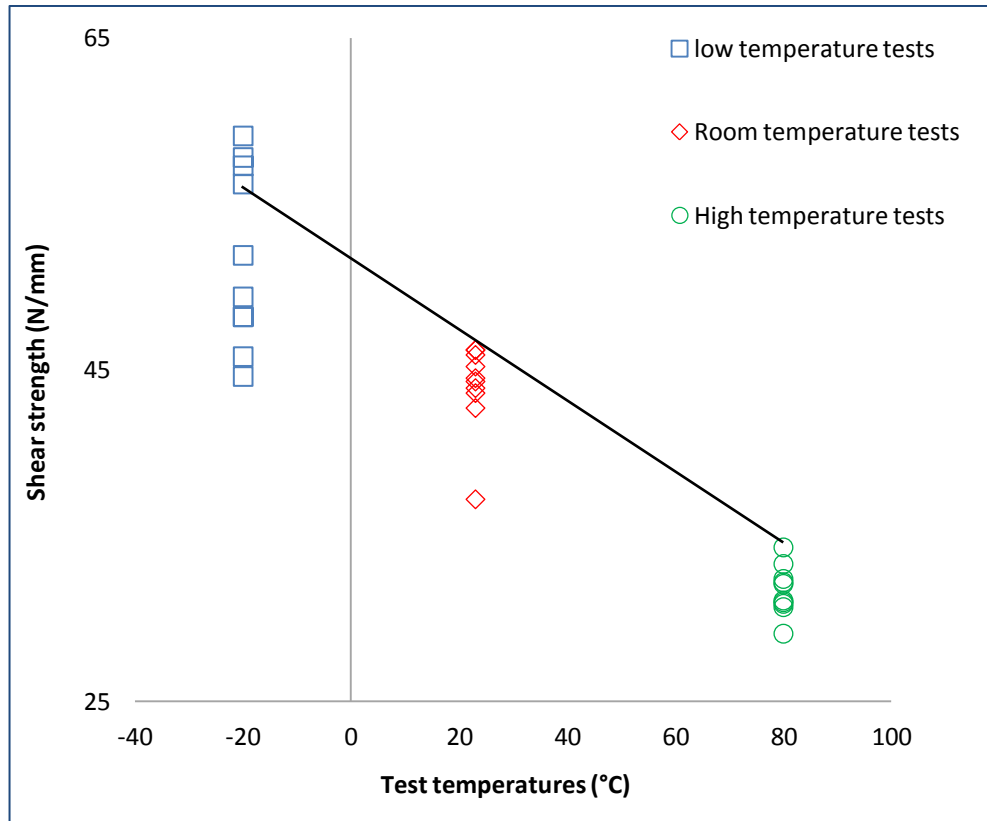


Figure 3.6 Shear strength vs test temperatures

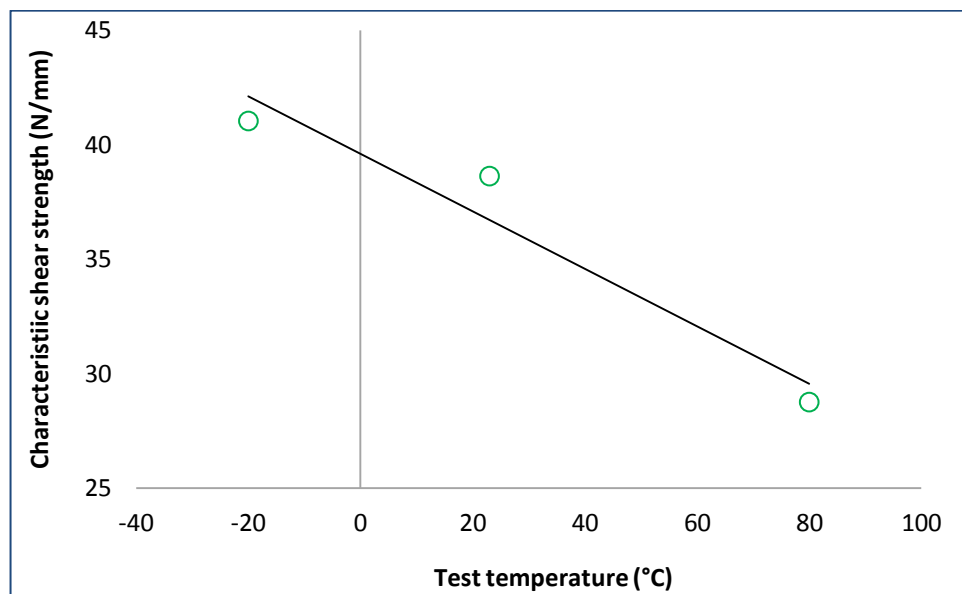


Figure 3.7 Characteristic shear strength vs temperature

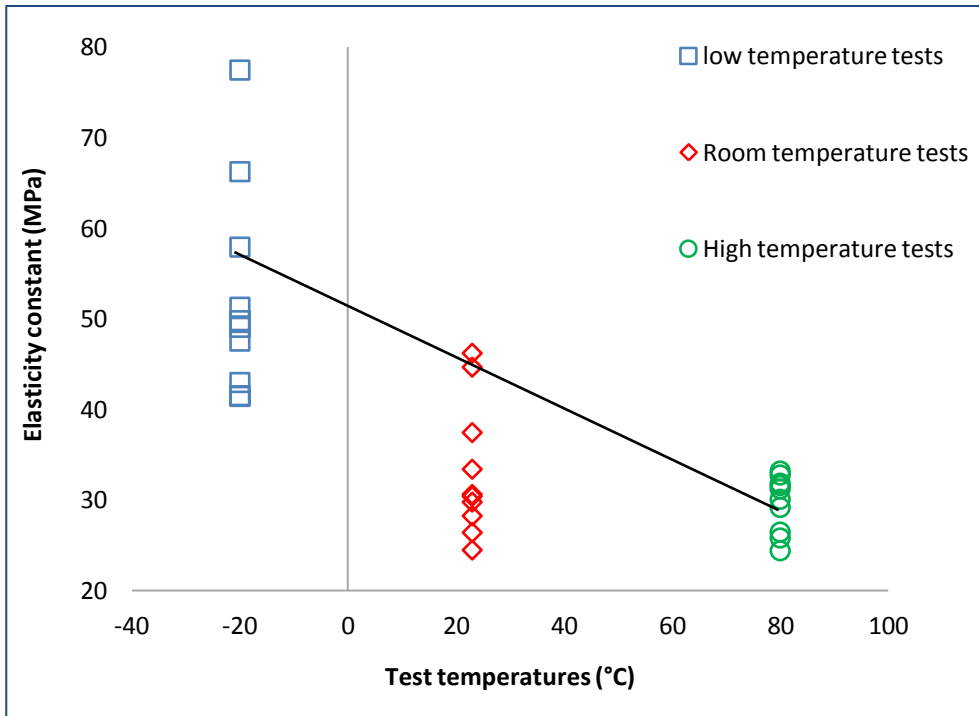


Figure 3.8 Elasticity constant vs temperature

The above graphs show the section shear strength, characteristic shear strength and elasticity constant decrease while temperature increases. The variation of the shear strength and elasticity constant between the specimens is large. The largest variation occurred in the low temperature test results; however the results from high temperature tests show the least difference.

This discrepancy in strength as well as for connectivity is largely due to the manufacturing process. The aluminium profile is pre-knurled in the connection to increase shear friction between the two materials. To have a good shear resistance, the sharpness of thumbwheel is critical to create a good knurled profile. In addition, optimum machine setting for rolling process is responsible for applying normal force and therefore generate good shear connection between aluminium and polyamide. As the sharpness of thumbwheel will reduce gradually during process, the knurled surface is impossible to stay uniform. Therefore, the shear friction force created by this process varies a lot. This explains the reason of the variation of shear strength and connectivity. This variation can also be seen from load vs displacement (slip) graph. A slip vs load graph which includes all room temperature tests is shown in Figure 3.9 below.

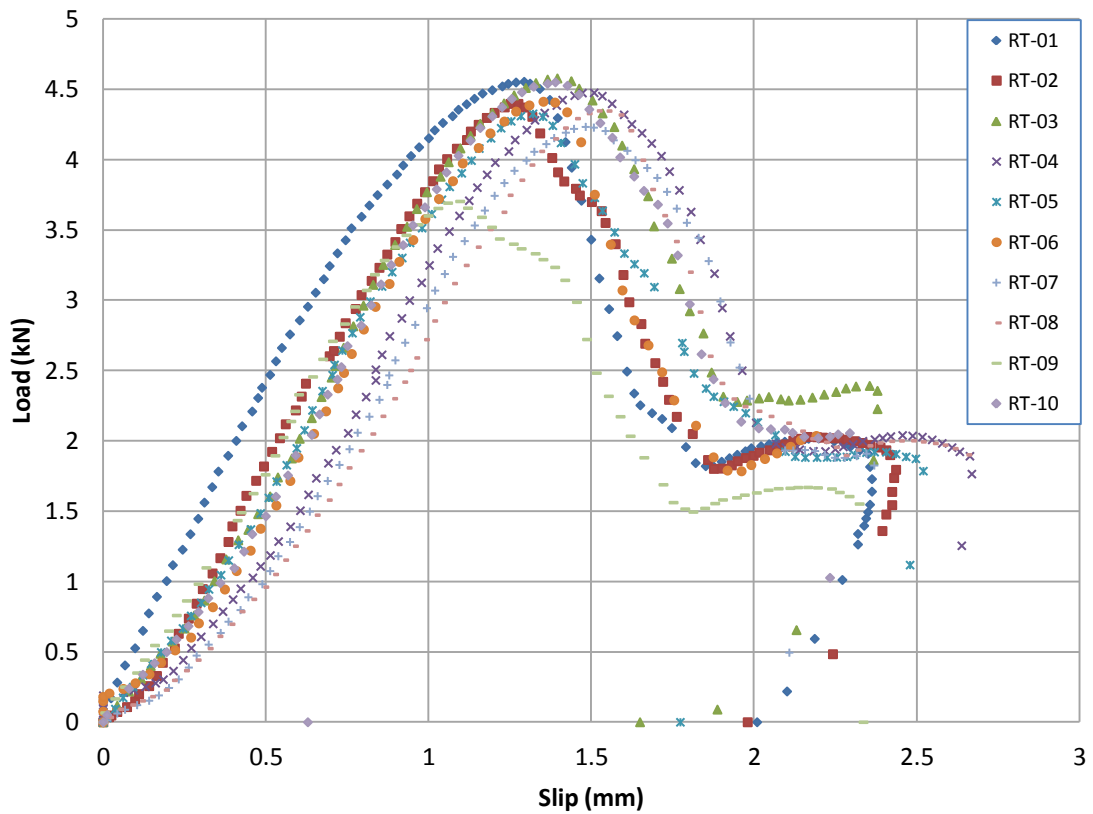


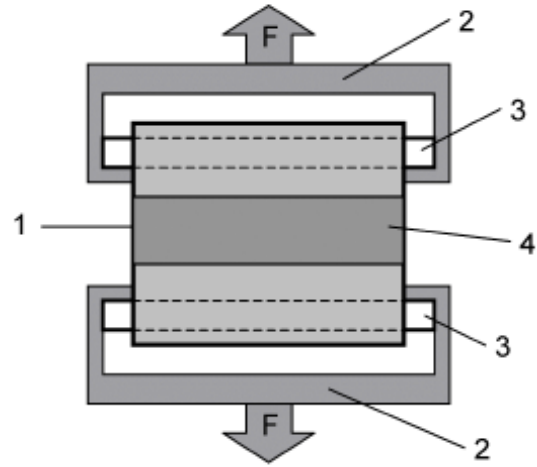
Figure 3.9 Load-slip relationship at room temperature

3.3.2 Transverse tensile tests

To obtain transverse tensile capacity data for the composite profile, ten specimens were tested at room temperature as well as high/low temperatures. The standard length of specimens was 100mm according to the standard. Test setup and typical results are discussed in the sections below.

3.3.2.1 Test setup

Testing jig was made according to EN14024:2004 Figure 4. Specimen was fixed at top and bottom along the centreline so that it could be loaded symmetrically. Steel brackets and steel bolts were used to connect the specimen to the testing machine. Unlike the shear tests, the specimen was fixed between the two cross heads. Test setup sketch and photo are shown in Figure 3.10 and Figure 3.11.



Notation:

- 1 Test specimen
- 2 Steel bracket
- 3 Guide
- 4 Thermal barrier

Figure 3.10 Tension test setup sketch and photo at room temperature



Figure 3.11 Tension test setup full view

Testing rate was controlled at 4mm/min, and the maximum loading was set to 20kN. During the tests, all specimens experienced large deformation. Tests were continued until the connection between polyamide and aluminium failed, i.e. polyamide was pulled away from aluminium, or polyamide was torn apart. Cross head displacement was measured by a LVDT attached to the testing platform with corresponding loadings including maximum load recorded by a data taker. The recorded displacement and loading data were output in the spread sheet format and used in the analysis.

To test specimens at high/low temperatures, the same temperature chamber used in the shear tests was acquired to create the designated temperature environment. Specimens and jigs were pre-heated in the oven to (80) °C for high temperature tests, while they were stored in the freezer at (-20) °C with the test jigs for low temperature tests.

Same testing jigs used at the room temperature tests were installed in the chamber as shown in Figure 3.12. The temperature chamber was heated and the temperature inside

was maintained at (80 ± 3) °C during high temperature tests while nitrogen gas cooled by liquid nitrogen in the Dewar was pumped into the temperature chamber to create desired low temperature at (-20 ± 2) °C and maintained it throughout the tests. The same setup used in the low temperature shear tests, shown in Figure 3.4, were employed in the low temperature tensile tests.



Figure 3.12 Test setup inside temperature chamber

3.3.2.2 Failure modes and typical results

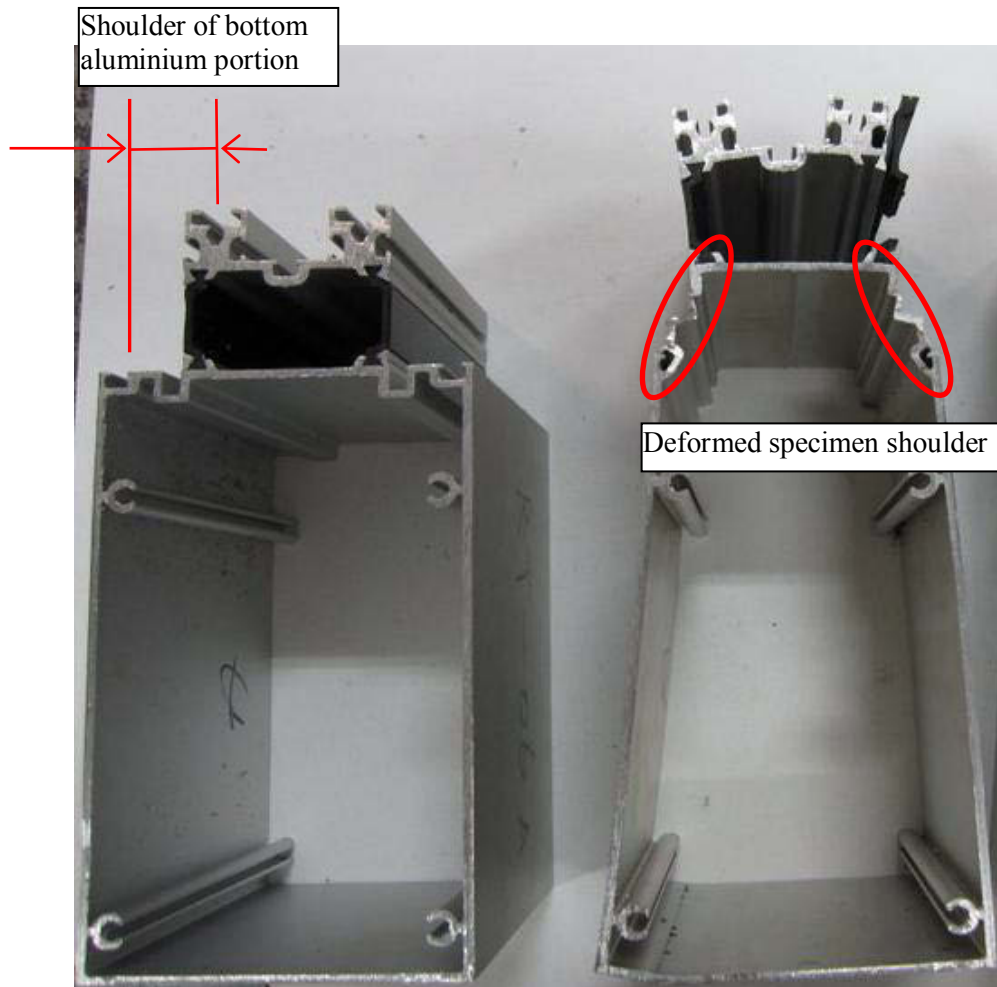
By observation, the failure modes were similar for all the tests performed at various temperatures. The polyamide was torn apart in some cases while the connection between polyamide and aluminium failed in other cases. Comparing with the specimen before test, the failed specimen shows excessive deformation at bottom aluminium portion. The shoulder of this portion rotated about 60° to stand almost vertically. Some portions of profile shoulder were pulled open while others were pressed close. The top aluminium portion was bent as if there was a point load pushing it up at the centreline. The whole section was stretched by about 20-30mm. Details of the failure modes are shown in Figure 3.13.



Polyamide torn apart



Polyamide pulled away from connection



Specimen before test

Specimen at failure

Figure 3.13 Tensile test failure modes

Tensile test results were also evaluated by the method illustrated in EN14024(Standard 2004) and presented below.

Transverse tensile strength Q (N/mm) for each test specimen shall be calculated as

$$Q = \frac{F_{max}}{l} \quad [3.4]$$

where,

Q represents the tensile strength (N/mm)

F_{max} represents the maximum tensile load (N)

l represents the length of the test specimen (mm)

Characteristic transverse tensile strength shall be determined on the mean value of the test results calculated from [3.4] as 5% quantiles based on a logarithmic normal distribution with 75% confidence, which can be written as

$$Q_c = Q_{mean} - 2.02s \quad [3.5]$$

where,

Q_{mean} represents the mean value of the measured values of transverse tensile strength at the test temperature

s represents the corresponding estimated standard deviation

Tensile strength and characteristic tensile strength are calculated from test data by adopting the above equations and plotted against temperatures below.

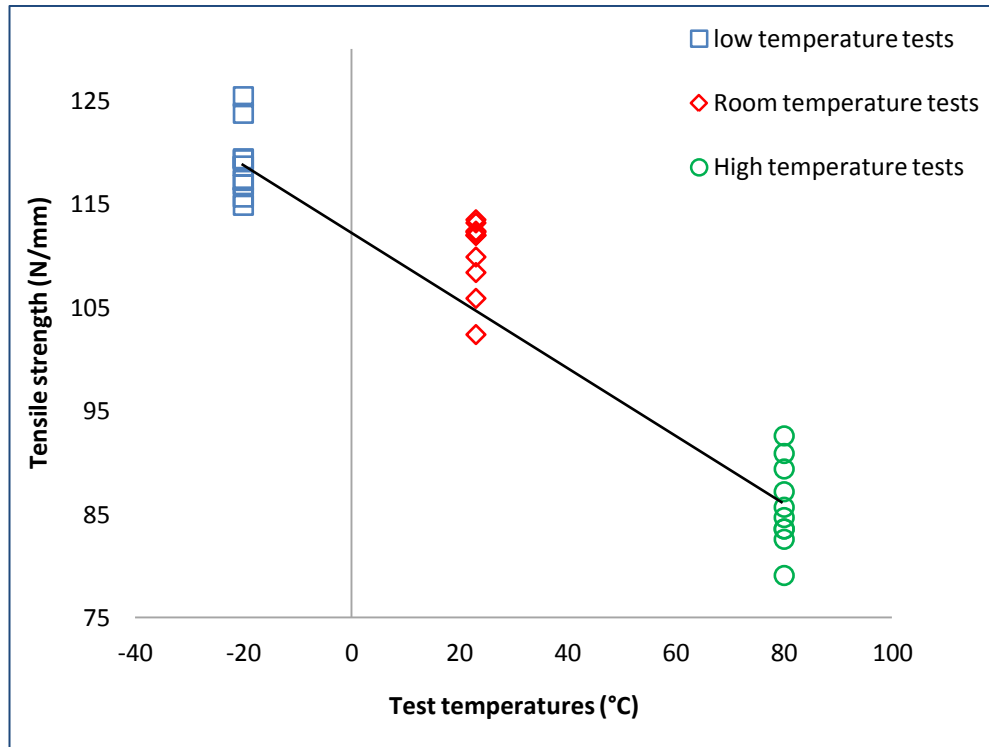


Figure 3.14 Tensile strength vs test temperatures

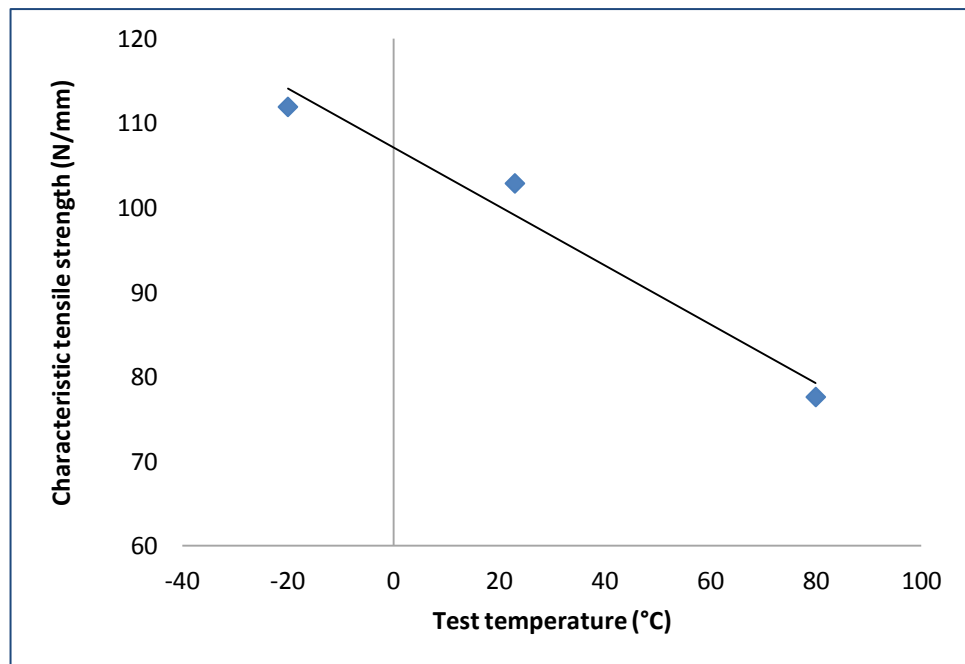


Figure 3.15 Characteristic tensile strength vs temperature

Similar to the shear strength, tensile strength as well as the characteristic tensile strength decreases as the temperature increases. The tensile strength varies more in high temperature tests than in low temperature tests which is in contrast to the shear strength.

However, the variation of strength between the specimens is not as large as shear strength tests.

3.4 High strain rate shear and transverse tensile tests at room temperature

As façade provides enclosure to buildings, its capacity of withstanding blast loading is also as important as withstanding other static loadings. In general, air blast pressures, impulse and durations vary from incidence to incidence. The pressures applied onto the curtain walls are not static but do occur at very short durations. The highly intense short duration transient blast loads can be categorized as high strain rate loads during design and research. As the major loading bearing element of façade system, it is therefore necessary to find out mullion section capacity under high strain rate loads for blast application.

To understand the magnitude of critical strain rates during blast, a series of field tests and numerical analysis were completed by the research arm of Permasteelisa Group recently. A number of trial runs for the façade with various glass thickness and loadings (pressures and impulses) were studied. Their research also included the glass status, which assumed the glass panel was intact or some layer broken. They have concluded that the strain rate varies linearly with the displacement and ductility factor in bending of the façade mullion. The strain rate is also related to the span of the mullion. The most critical strain rate concluded by their research varies from 0.05-1 strain/sec.

As this research was sponsored by Permasteelisa Group, we worked closely with their research arm. The critical strain rate of 0.05-1 strain/sec for mullion section was adopted here. Shear and tensile capacity tests at room temperature were carried out at the strain rate of 0.05/s, 0.1/s, 0.5/s and 1/s. The strain rate of 2/s was only performed for the tensile test. High strain rate load as an independent load case is studied only at room temperature in this research. Details of the tests are discussed in the following sections.

3.4.1 Shear tests

Shear strength tests of full section under high strain rate were carried out on Schenck machine at room temperature. Schenck machine is designed to do vibration and high speed tests. The highest design speed is 100mm/s. Due to the age of the machine (about 40 years old), it was recommended to reduce the achievable speed to 60mm/s.

As targeted testing strain rates are 0.05/s, 0.1/s, 0.5/s and 1/s, the length of the specimen had to be reduced to 60mm to achieve 1/s at 60mm/s loading speed. Since the standard specimen length specified by EN14024:2004 is 100mm, verification tests were carried out to prove the 60mm specimen had comparable characteristic values. Five specimens of 60mm in length were tested using Shimadzu machine at the speed of 3mm/min at room temperature. Comparing the test results with the 100mm long specimens, the difference of elasticity constant c between them was about 5%. This is within the acceptable range. Thus, the 60mm long specimens were used to test section shear capacity at above strain rates on Schenck machine.

The same test jig used in quasi-static tests was fixed on the actuator of the Schenck machine by bolts and fitted well. A small LVDT was placed under the section to measure the displacement directly. To avoid loading onto the polyamide thermal break, a steel block was placed on the top aluminium portion under the loading pad to direct the force onto the aluminium portion only and kept it away from connection. Testing setup is shown in Figure 3.16 below.

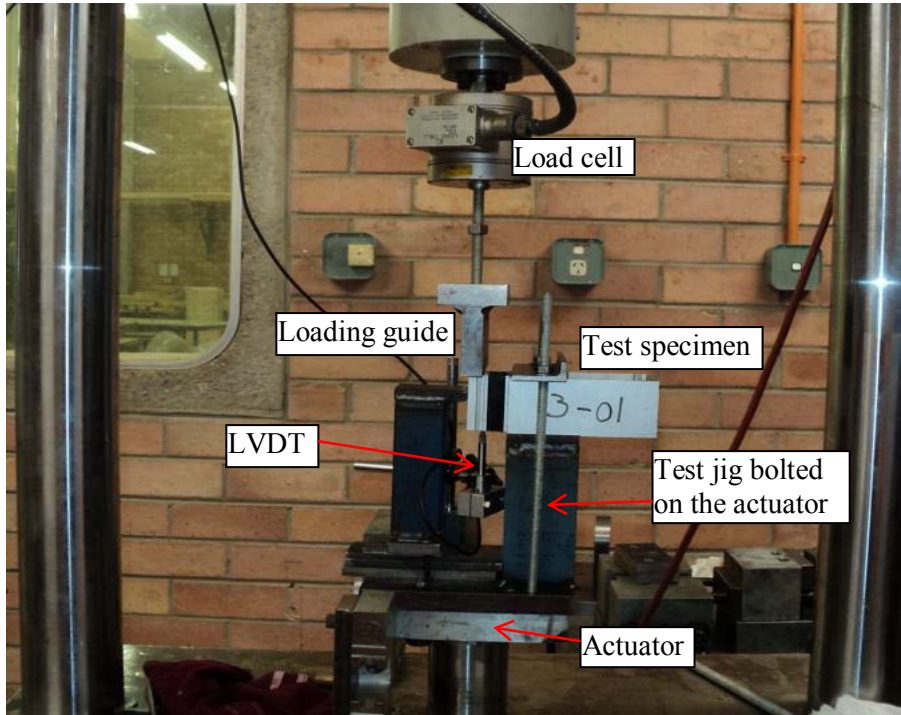


Figure 3.16 Test set-out on Schenck testing machine

Dynamic loading function was set as “ramp up”, which sets loading to increase linearly with time. Once the assigned speed was reached, the loading speed was kept constant. To achieve the desired constant loading speed from beginning of the test, loading pad was placed above the specimen at about 10-15mm to give enough time and distance to reach the desired testing speed.

Every test result was checked right after the test to verify the actual test speed. Unfortunately, the first two specimens of the 3mm/s tests and 60mm/s tests didn't achieve the required speed and there were no more spare specimens left. The test results of the 3mm/s and 60mm/s tests had to rely on the remaining three specimen's test results.

Failure mode of these dynamic tests is similar to the quasi-static test ones. The polyamide thermal break slipped from the connection. Photo of the failure mode is shown below.

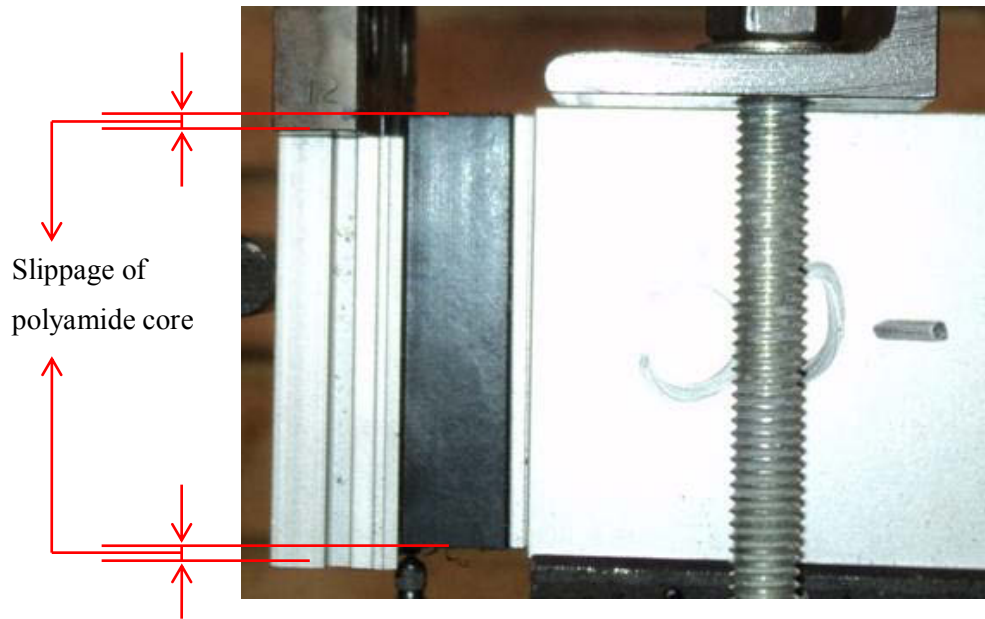


Figure 3.17 Failure mode – Polyamide slippage

3.4.2 Section transverse tensile tests under high strain rate loadings

Transverse tensile tests were done on the shake table at the strain rate of 0.05/s, 0.1/s, 0.5/s, 1/s and 2/s. Standard 100mm long specimens were tested to provide consistency to the quasi-static tests.

As the shake table is designed to simulate ground motions during earthquakes, it is capable of providing velocities up to the speed of 200mm/s. Special jig (steel beam welded on the plate) was fixed onto the concrete floor by chemical anchor bolts at one end. The other end was connected to a dynamic load cell by steel end plate and bolts. Therefore, the dynamic load cell was supported at the end while it was bolted to the tensile jig used in quasi-static tests to measure the applied load during testing at the other end. The tensile jig was bolted through a steel rod and supported by steel plate and end block which were welded on a large steel plate and bolted on the shake table.

Specimens were placed in the tensile jig horizontally. Since the table needs time and distance to accelerate to the required speed, a “slack” was designed in the system to provide this required distance before the specimen was pulled. Therefore, the specimen can be tested at the specified speed. The test setup is shown in Figure 3.18 below.

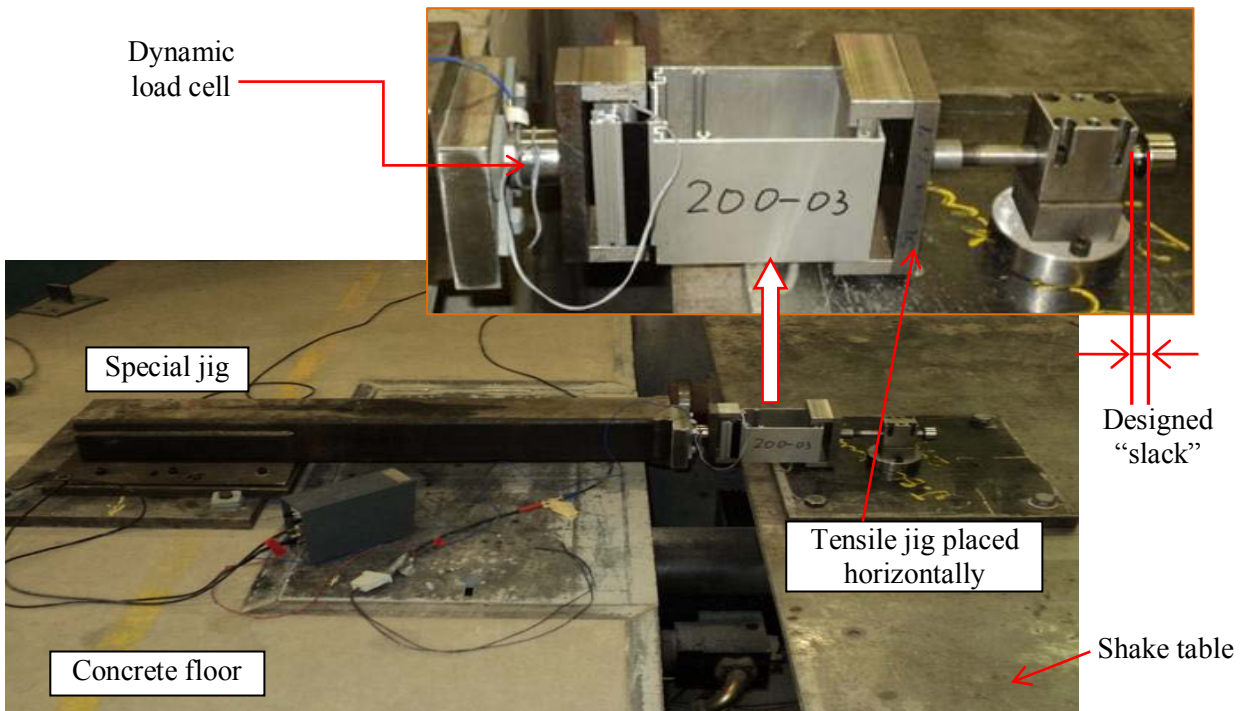


Figure 3.18 High strain rate tensile test setup on shake table

A triangular load function was adopted. However, only half of the loading cycle is relevant to these tests. Commanded displacement vs time graph was compared with actual table displacement vs time graph to make sure the shake table was reaching specified speed before tests commenced. A single channel quarter bridge dynamic amplifier was used with MTS Adaptive controller to record the load and table displacement at every 0.0005 second.

Five specimens were tested under each strain rate. Failure modes are similar to the quasi-static tests. Polyamide was pulled out of the connection for some specimens while it was broken for the others. Pictures of tested specimens are shown in Figure 3.19.

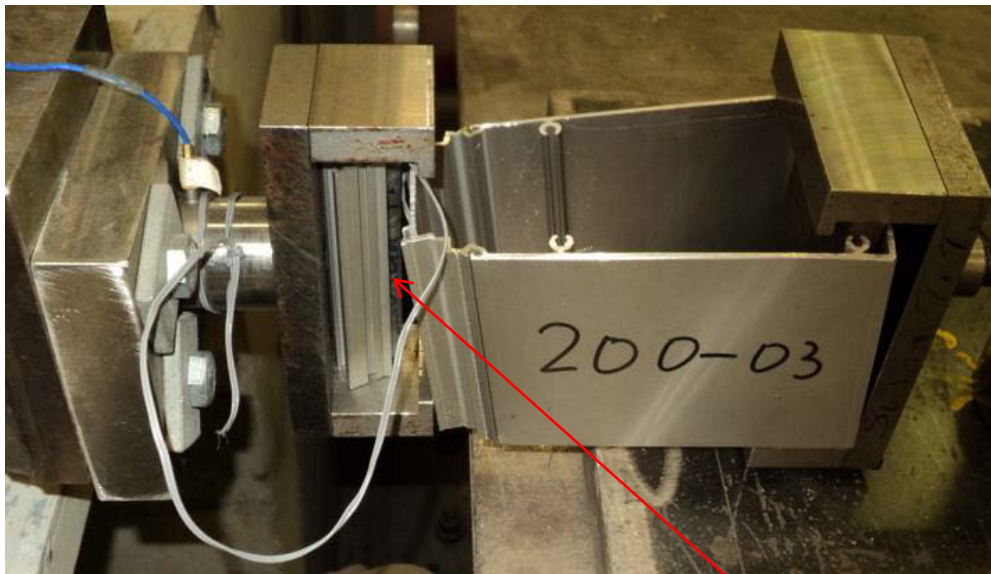


Figure 3.19 Tensile failure modes

3.4.3 Test results and discussion

Both dynamic shear and tensile test results were analysed based on the methodology adopted from EN 14024 (Standard 2004) listed above. As there were only five specimens for each test, mean values of these tests were also taken into consideration during analysis. Test data together with calculated characteristic strength are plotted in Figures Figure 3.20 to Figure 3.22.

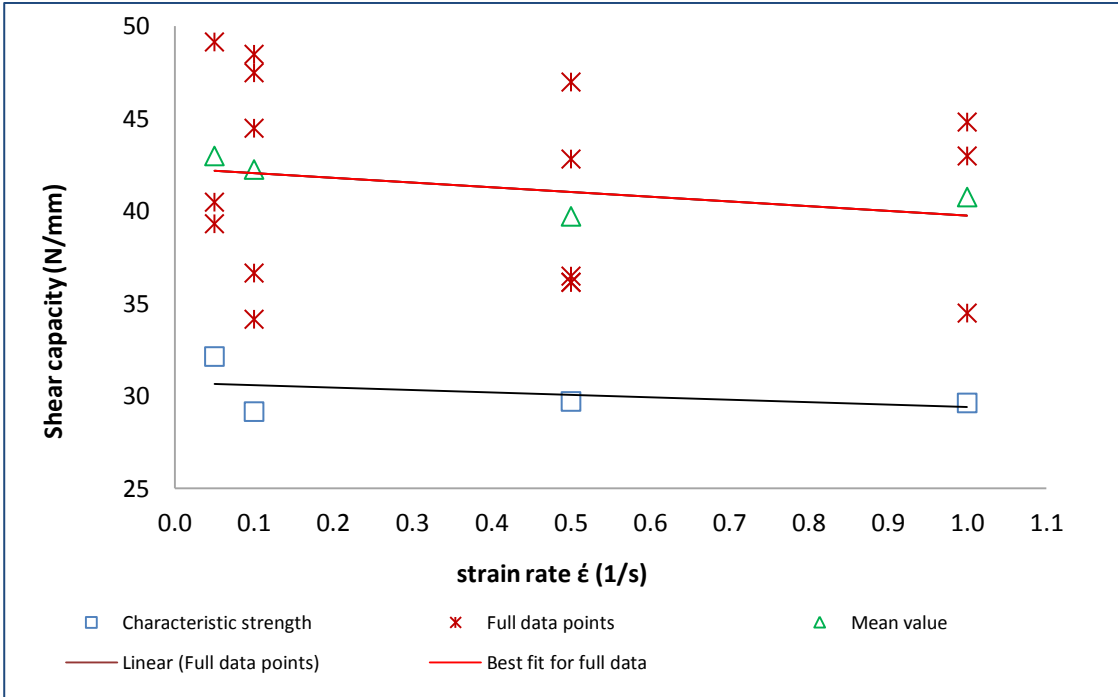


Figure 3.20 Shear strength vs strain rates

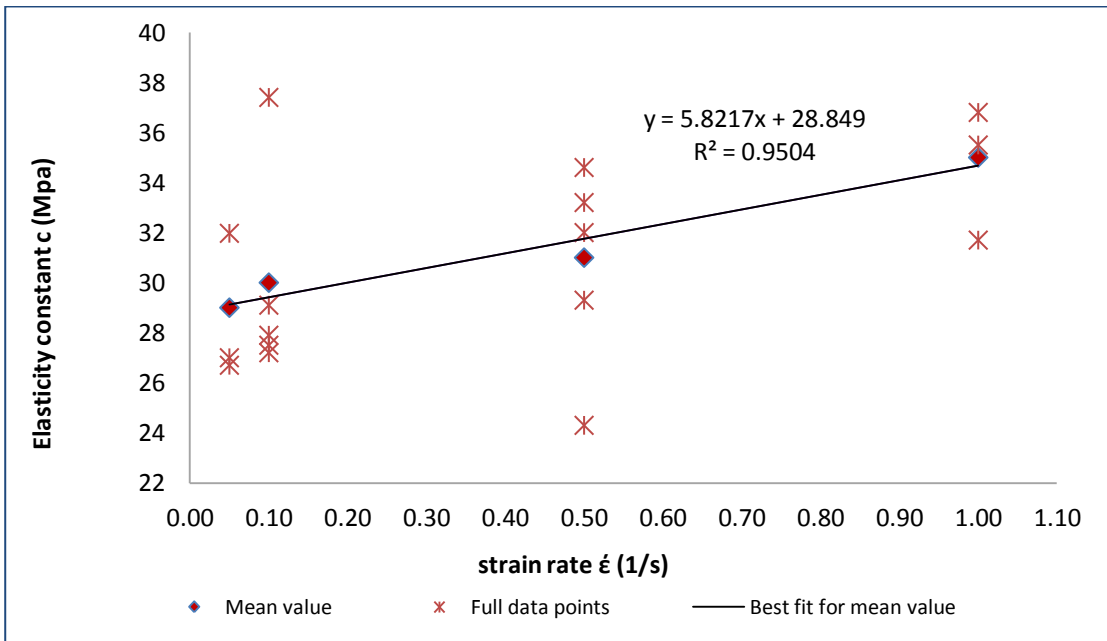


Figure 3.21 Elasticity constant vs strain rates

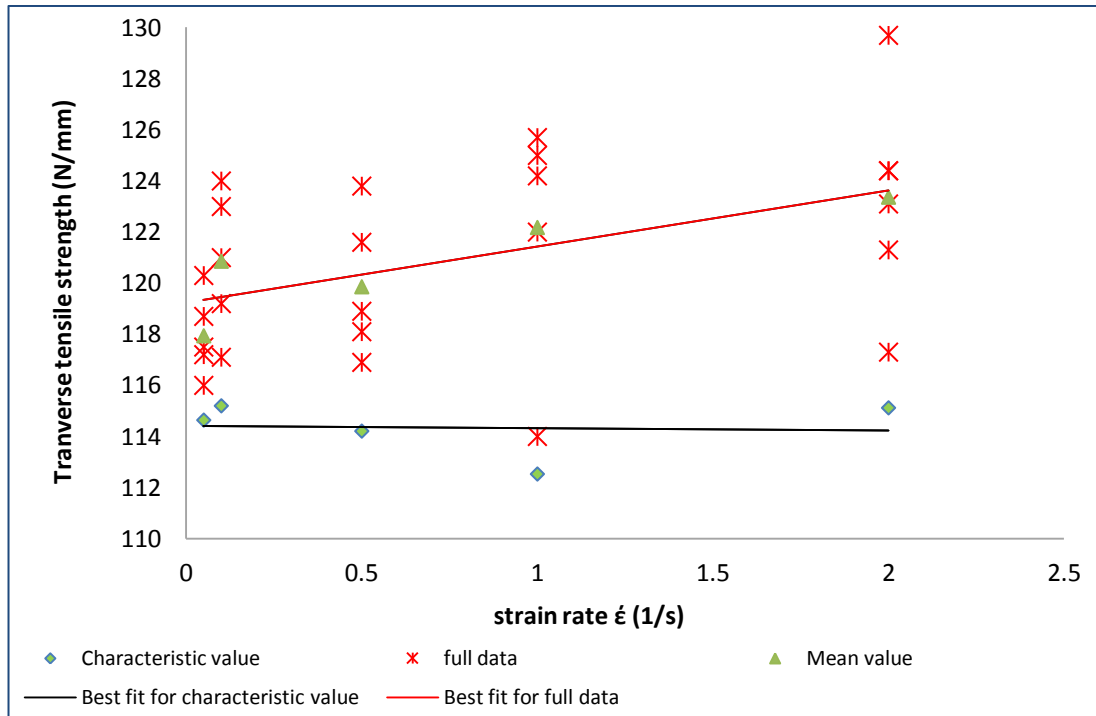


Figure 3.22 Tensile strength vs strain rates

From Figure 3.20, the shear strength shows no sensitivity to the strain rate as the best fit for both characteristic strength and full data are almost flat. Contrary to the shear strength, the indicator of the connectivity of the composite section - the elasticity constant ‘c’ increases with the strain rate as shown in Figure 3.21 above. The relationship between ‘c’ and strain rate $\dot{\epsilon}$ can be interpreted as a linear function,

$$\dot{c} = \gamma\dot{\epsilon} + c_0 \quad [3.6]$$

Where,

\dot{c} represents the elasticity constant under a specific strain rate loading

γ represents the coefficient relating to the type of profile

c_0 represents the elasticity constant under quasi-static loading

Similar to the shear strength, Figure 3.22 shows the best fit for the full data point which increases with the increasing strain rate. However, the best fit for the characteristic strength values which derived from the full data is flat. It is, therefore concluded that the tensile strength of this section is not strain rate sensitive.

The above graphs compare the results within high strain rate tests, where the strain rates vary from 0.05/s to 2/s. These comparisons are for the tests carried out on the same machine. Since quasi-static tensile and shear tests were performed on Shimadzu

machine while dynamic tests were completed on Schenck and shake table, it is not possible to compare exactly the results of quasi-static test with dynamic test results due to different machine manufacturers and tolerances. However, it is still reasonable to compare the general trend of the high strain rate test results with quasi-static results.

The shear strength obtained from high strain rate tests was generally lower than the value from quasi-static tests based on the results in Figure 3.20. The highest characteristic shear strength obtained from the high strain rate tests is 32.15N/mm, which is taken from 0.05 strain/s tests. It is about 17% lower than the results from quasi-static tests.

Contrary to shear strength, transverse tensile strength obtained from high strain rate tests was generally higher than the quasi-static test results. For example, the characteristic transverse tensile strength of 2 strain/s tests yielded 12% higher values than quasi-static test result based on results in Figure 3.22. However, comparing the results between high strain rate tests, it is hard to conclude that the transverse tensile strength increases with strain rate.

The high strain rate test results of elasticity constant shown in Figure 3.21 clearly presents a relationship with strain rate. However, the values obtained from quasi-static tests are slightly higher than the high strain rate test results.

Hence, further study is recommended to confirm the elasticity constant c is strain rate sensitive since the values obtained from quasi-static tests is slightly higher than the high strain rate test results. Firm conclusions shall be based on large quantity of tests to be done as the connection has large variations among the specimens during rolling and knurling process during manufacturing.

In conclusion, full section shear and transverse tensile strength is not sensitive to strain rate while elasticity constant ' c ' shows signs of strain rate sensitivity in high strain rate tests.

3.5 Four-point bending beam tests at room temperature under quasi-static loadings

The above sections investigated the shear and tensile load carrying capacity of this typical composite façade mullion section. As a major load bearing element in the curtain wall system, façade mullion is running vertically to resist uniformly applied lateral loads, such as earthquake, wind and thermal loads, etc. It is usually simply supported at both ends by structural slabs at floor levels. The applied lateral loads generate bending and shear forces on the mullion.

In order to thoroughly understand the behaviour of this façade mullion section, four-point bending tests were proposed. Since a simply supported beam under uniformly distributed loads is subjected to bending and shear forces, it only provides a bending plus shear combined loading situation. However, a simply supported beam under two equally spaced concentrated loads (four-point bending) generates not only combined bending and shear behaviour but also pure bending behaviour at middle portion of the beam between the two applied loads. It explores more loading patterns and therefore, it was chosen for the laboratory tests.

3.5.1 Test setup

All four-point bending beam tests were performed on Shimadzu Hydraulic Universal Testing Machine, model REH 50/50 tonne. Tests were done to displacement control. Displacement rate was set at 3mm/min. Four sets of beam specimens containing three specimens each were supplied by the sponsor – Permasteelisa Group. Specimen lengths were 2.5m, 3m, 3.5m and 4m. Specimens were supported by rollers at both ends. Two pairs of loading pads were placed on the shoulders of the section at one-third of the span to apply symmetrical loadings onto the specimen. The loading pads were fitted with a small roller to avoid load concentration and local buckling. Four Linear Variable Differential Transformers (LVDTs) were attached to the bottom of specimens at equal spacing of one-eighth of the span length. Due to the height limitation of the testing machine, LVDTs could not be fitted under the beam specimens. Light metal pads were glued under the bottom of specimens and protruding outside to allow LVDTs to be attached under to measure the displacement at these locations. Seven strain gauges were placed on one side face of the specimens at mid-span. Two reference strain gauges were

placed at 100mm on either side away from the mid-span. The specimens were categorized into four types which are listed in Table 3.1 below.

Table 3.1 Beam specimen types and quantity

Beam Specimen Type	L (mm)	Specimen Numbers
B	2120	3
C	2620	3
D	3120	3
E	3640	3

The test set-up diagram and photo are shown in Figure 3.23 and Figure 3.24 below.

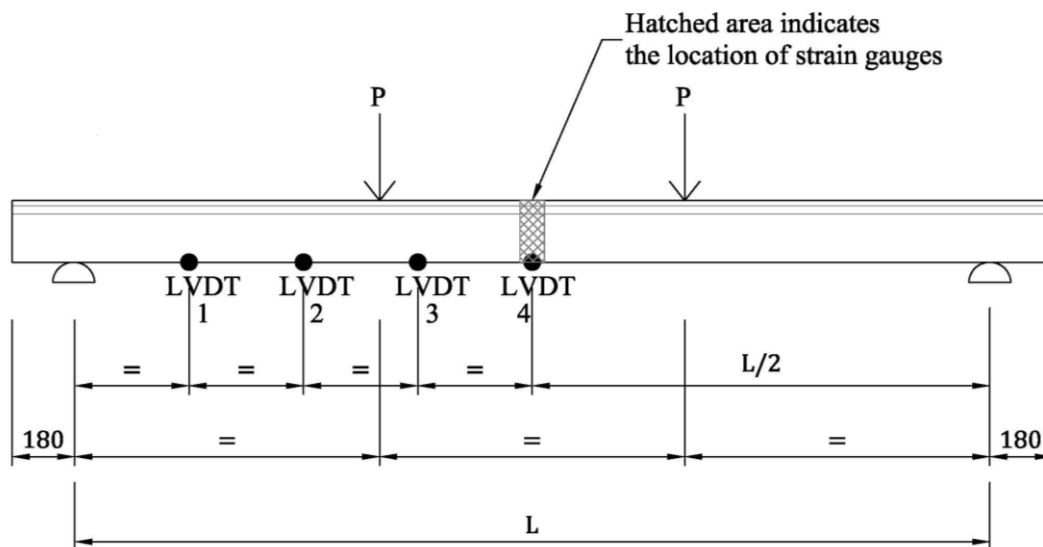


Figure 3.23 Test setup diagram

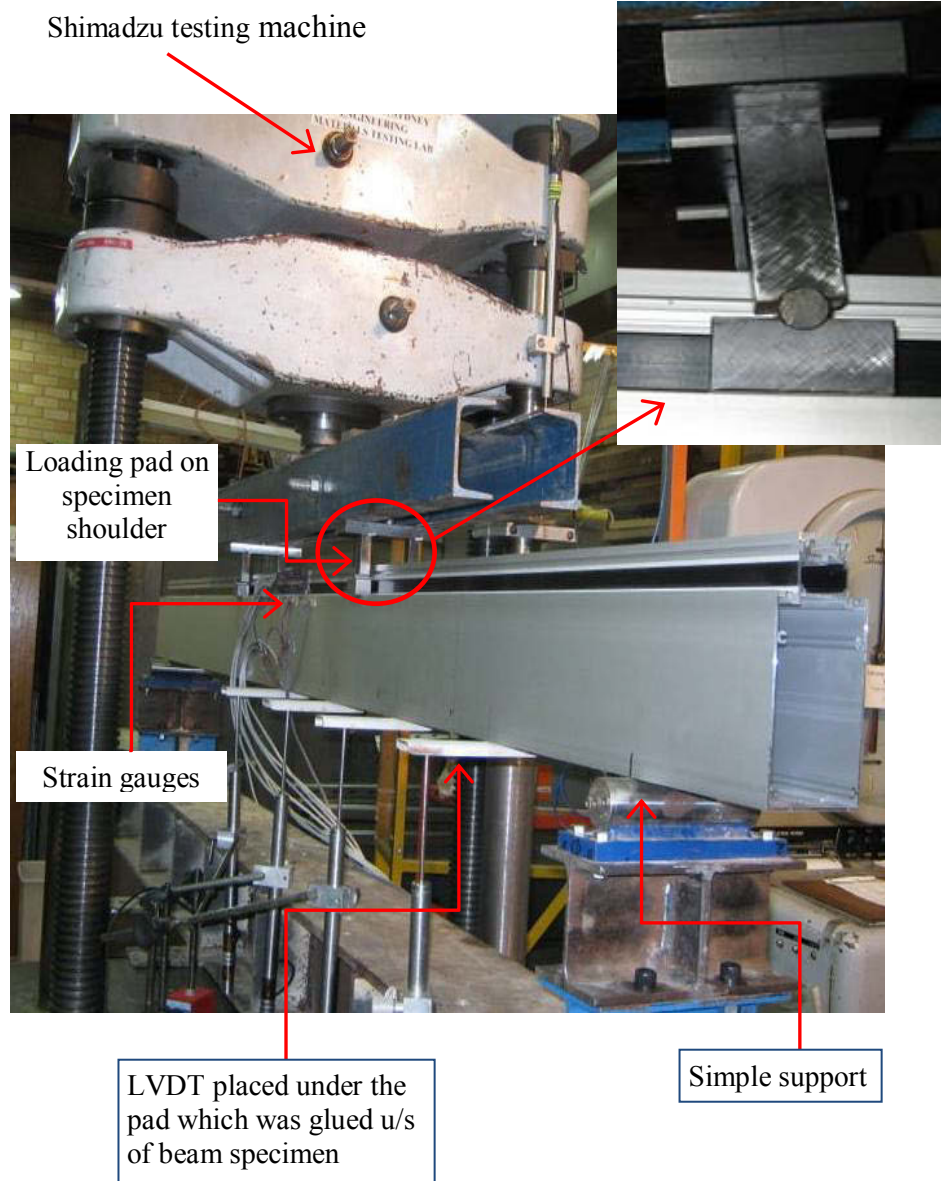
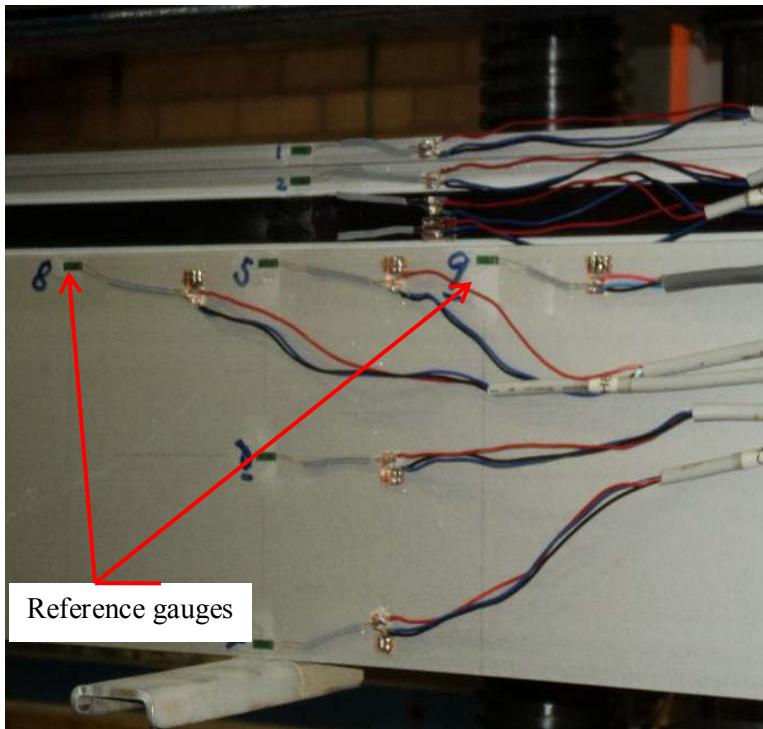
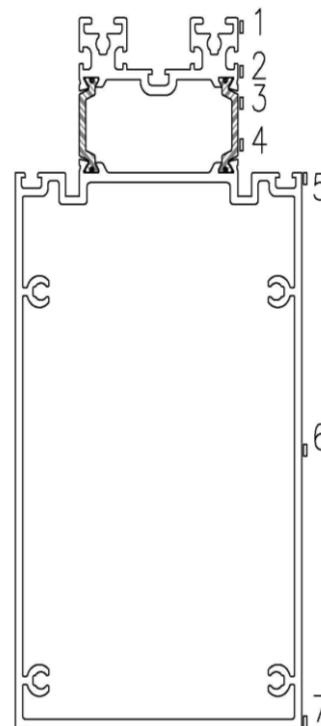


Figure 3.24 Full view of test setup

Since the geometrical details of the top aluminium profile are complicated, there is limited space available to fit strain gauges. Therefore, backing size of 3mm wide strain gauge type FLA-5-23-1L made by Tokyo Sokki KenKyujo Co., Ltd. was chosen. Detailed strain gauge layout is shown in Figure 3.25.



Layout photo



Layout diagram

Figure 3.25 Strain gauge layout

3.5.2 Failure mechanism and typical results

During testing, specimens bent gradually as the load increased. Top aluminium profile started slipping away from the polyamide core from the peak load. After the major slippage occurred, the load dropped and then picked up to reach the level between peak and dip loads then slowly increased towards the end of the test. The failure of composite action between top and bottom parts of the beam resulted in the dip load. This phenomenon was consistent throughout all bending tests, which can be called a three-stage progressive failure mode. All specimens went through large deformations as shown in Figure 3.26. LVDTs placed under the specimens to measure the displacement along the beam had to be removed in the latter stage of the test as the displacement was larger than the capacity of these LVDTs, which is limited to 80mm. The capacity of the LVDT attached on the cross-head can reach 120mm. Once the cross-head displacement reached 120mm, the test was stopped. None of the specimens could be tested to their maximum strength. The aim of these tests was to understand the behaviour of the

specimens under serviceability limit state as the glass panels have limited tolerance to the deformation of mullions. Therefore, glass panels usually crack before the mullions reach ultimate strength. Hence, the ultimate strength capacity of mullion does not govern the design.



Deformed shape of test specimen

Top connection slipped

Figure 3.26 Typical deformation of test specimen

Figure 3.26 above shows the top connection between polyamide and aluminium has slipped while the bottom connection was intact. The top aluminium portion was longer than the polyamide and bottom aluminium portions. This phenomenon indicates that the top aluminium portion has failed and lost connection to the bottom part of the section. As the strains at mid-span of the beam were measured during testing, strain distribution was plotted to investigate the behaviour of the whole cross-section under loading. The strain distribution of all beams at dip load after slip is plotted in Figure 3.27 below.

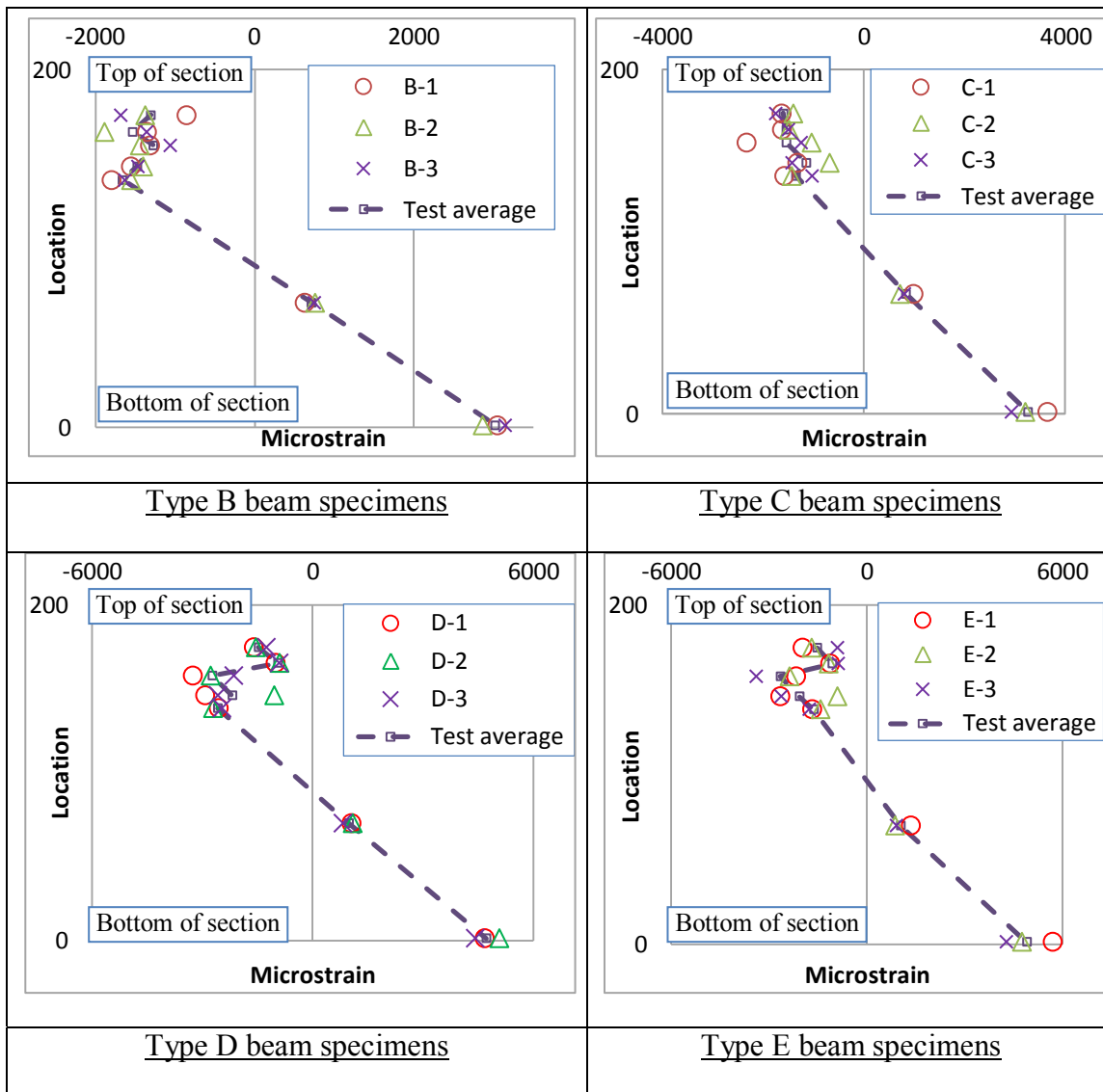


Figure 3.27 Strain distribution diagrams along cross-section at dip load

Figure 3.27 shows the strain distribution was not linearly distributed along the section at the dip load after slip. The strains at the top aluminium part had no correlation to the other parts at all. It worked as an independent part under pure compression. However, the bottom part of polyamide and bottom aluminium portion were acting together and bent along the centroidal axis of the combined section. The value of compressive strains of the top aluminium part was much smaller than the polyamide and top of bottom aluminium part. As the displacement is proportional to the strain, therefore, differential horizontal movement occurred between top aluminium part and the combined section of polyamide and bottom aluminium part. The top part shrank less than the combined

bottom parts and therefore it was longer. The above observation of the beam failure mechanism can be summarized into three loading stages.

1. Stage 1 – section was fully engaged and had full composite action.
2. Stage 2 – slip occurred at top connection between top aluminium part and polyamide part after reaching the peak load and load carrying capacity dropped.
3. Stage 3 – the top aluminium part acted independently and under pure compression while the polyamide and bottom aluminium part bent along their combined centroidal axis. The top aluminium part only rested on the combined polyamide and aluminium parts and provided no capacity to the whole section. However, the capacity of the combined section mainly relied on the bottom aluminium part as the material modulus of aluminium is much greater than the polyamide's and so is the geometry. The capacity of polyamide is therefore negligible. The total loading capacity of the section is the capacity of bottom aluminium part bending along its own centroidal axis. When aluminium hardened, the load carrying capacity gradually increased. This bending/failure mechanism is illustrated and plotted in the figures below to demonstrate the full process.

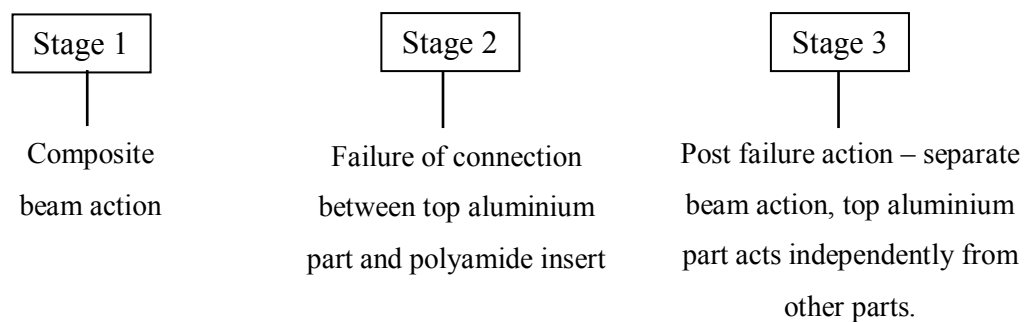


Figure 3.28 Failure mechanism

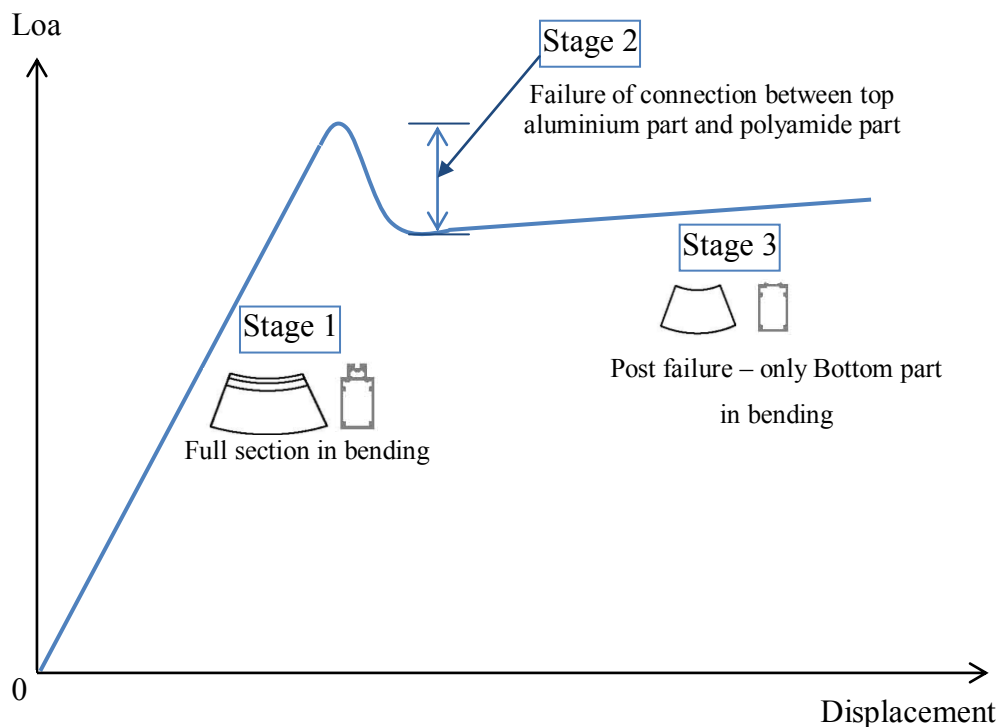


Figure 3.29 Illustration of failure mechanism of this façade beam

The three stages of beam failure process can also be observed from load vs mid-span displacement graphs plotted below for all types of beam specimens. All beam specimens showed these three stages of failure mechanism. As the span of beam increased, the load carrying capacity decreased and mid-span displacement increased. Due to the limitation of test instruments (LVDT), the full length of stage 3 cannot be plotted. The prolonged period of stage 3 of all types of beams showed a good ductile behaviour under bending which was the main loading condition under all lateral load cases.

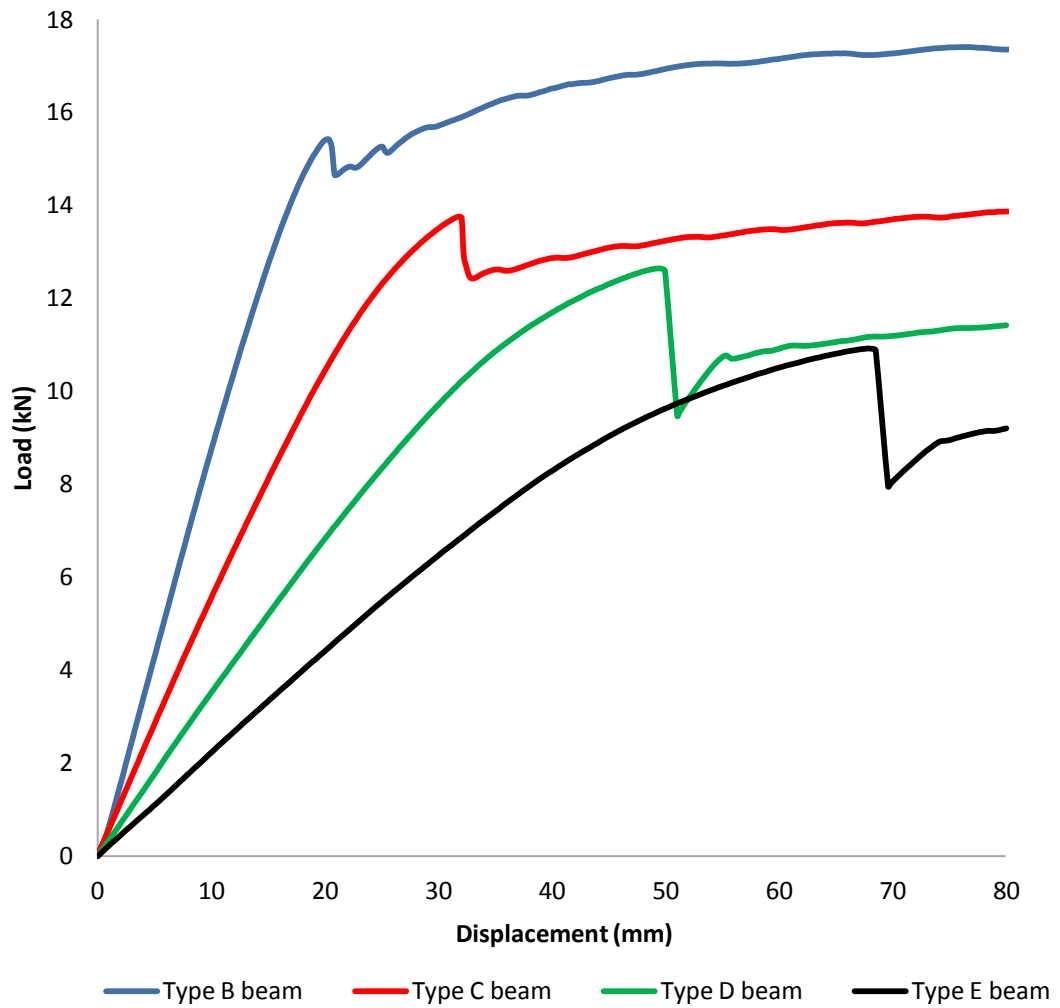


Figure 3.30 Typical load vs mid-span displacement for beam types

3.6 Summary and conclusions

In summary, section capacity of shear and transverse tensile tests under quasi-static loadings at various temperatures and under high strain rate loadings at room temperature were discussed in this chapter. Beam test results of four-point bending were also presented. All section capacity tests show similar failure modes under either quasi-static loadings or high strain rate loadings at various temperatures.

Shear failure of the polyamide due to it slipping away from connection was observed for all shear tests while polyamide was either pulled away from the connection or broken in all tensile tests. Test results show both shear and tensile section capacities, as well as elasticity constant are affected by temperature, i.e., the section capacities increase while the temperature decreases. Unfortunately, the high strain rate tests

displayed a mixed trend. The elasticity constant is clearly increased with the strain rate, however, the shear and tensile section capacities showed no clear correlation with the strain rate. Large quantities of further high strain rate tests are recommended for future study.

The four-point bending beam tests confirmed a good ductility of this type of façade mullion section. The failure mechanism was investigated and the failure mechanism at three stages was established. The bending capacity of the section after slippage is based on the capacity of bottom aluminium part which was bending along its own centroidal axis. The capacity drop is relatively small for short spanned beams (less than 10%) while it could reach a 30% drop in capacity for large spanned beams. As the material hardened, the total bending capacity of the section gradually increased.

Chapter 4

Numerical Investigation of the Typical Thermal Break Façade Section

4. Numerical investigation of the typical thermal break façade section

4.1 Introduction

Experimental investigation of this typical thermal break façade section presented in Chapter 3 revealed its connectivity behaviour when tested for its shear and tensile section capacities. Four batches of four-point bending tests also confirmed its beam bending behaviour. Based on the observation of these tests, this façade beam shows a complicated but typical composite action between the three components. To verify the experimental conclusion and provide comparable results, numerical investigations were carried out and presented in this chapter.

A series of commercial finite element softwares were surveyed and ABAQUS software was selected as it has powerful capacity to perform analysis of non-linear physical behaviour and a wide range of material modelling. Its capacities also include multi-physics analysis and dynamic analysis. In addition, its meshing technique is capable to supply various types of elements to suit any complicated profiles. Version 6.11 of ABAQUS /CAE, also called “Complete ABAQUS Environment”, was employed to carry out the analysis.

Material modelling of aluminium alloy and polyamide materials was performed. Stress-strain relationships of both materials were established and converted into true stress and true strain relationships which can be adapted by the software.

ABAQUS user manual and analysis manual were studied. Element types provided by the software were investigated and test models were built to identify the suitable element type for this section. Calibrated with the test results, quadratic reduced integration solid element (C3D20R) is assigned to both aluminium skins while linear element with incompatible mode (C3D8I) is adopted for polyamide insert.

As a composite section, interaction between the contact bodies plays an important role for the section capacity. Coulomb’s friction theory was adopted to model the interaction. Formulation of penalty frictional algorithm supplied by ABAQUS software was chosen to simulate the interaction. Two new models – “Proposed progressive failure model” and “Proposed partitioned multi-phase beam failure model” were initiated and applied to the models to reproduce similar failure modes of the experiments. Small sliding tracking formulation was used to model the relative motion between the contact surfaces.

Shear and tension models were built to simulate the shear and tensile tests under room temperature by ABAQUS software. Deformation and failure mode are presented in this chapter as well as typical results.

Four beam models were established by the software to replicate the laboratory experiments. Detailed setup of the FE model and deformation of beams as well as stress distributions are shown in this chapter.

These finite element models provide comprehensive details of connectivity between aluminium and polyamide interfaces. They also provide useful information for beam bending mechanism of this section. The two new models represent the shear and bending failure mechanism and can then be applied to future simulation of other façade sections having similar type of connection.

4.2 Material modelling

4.2.1 Aluminium material modelling

Material property of aluminium alloy 6063T6 listed in (Institution 2007) Table 3.2b is adopted. 0.2% proof strength $f_0 = 160\text{MPa}$ and ultimate strength $f_u = 195\text{MPa}$ for extruded profile, whose thickness is less than 25mm, are applied in the FE models.

Stress-strain relationship of aluminium alloy can be modelled as either piecewise linear model or continuous model. As the influence of alloy content lessens the sharpness of aluminium yield point in favour of a more non-linear response (Gardner & Ashraf 2006), it is therefore decided to adopt continuous model rather than piecewise model in this study. The material stress-strain law of a continuous model is based on the assumption that it can be described by means of a continuous relationship, representing the elastic, inelastic and plastic with hardening region. The characterization of the stress-strain relationship could be generally performed by either of the following.

- i) Continuous models in the form of $\sigma = \sigma(\varepsilon)$
- ii) Continuous models in the form of $\varepsilon = \varepsilon(\sigma)$

Ramberg-Osgood model (Osgood & Ramberg 1943) was recommended by (Institution 2007) in Annex E in order to apply the continuous material model for round-house type material, such as aluminium alloy. It describes the stress-strain relationship in the form of $\varepsilon = \varepsilon(\sigma)$. The general form of Ramberg-Osgood analytical expression is

$$\varepsilon = \frac{\sigma}{E} + \varepsilon_{0,e} \left(\frac{\sigma}{f_e}\right)^n \quad [4.1]$$

where:

f_e = conventional elastic limit

$\varepsilon_{0,e}$ = residual strain corresponding to the stress f_e

n = exponent characterizing the degree of hardening of the curve

A general accepted approach to define the conventional elastic limit (f_e) is to assume that it can be replaced by the equivalent yield point (f_0). This equivalent yield point is determined by means of 0.2% offset method (Gardner & Ashraf 2006; Institution 2007; Osgood & Ramberg 1943). The strain at this point is taken as

$$\varepsilon_{0,e} = 0.002$$

Therefore, Eqn. 4.1 can be re-written as

$$\varepsilon = \frac{\sigma}{E} + 0.002 \left(\frac{\sigma}{f_0}\right)^n \quad [4.2]$$

Eqn. 4.2 is plotted in Figure 4.1 with illustration of the 0.2% offset method.

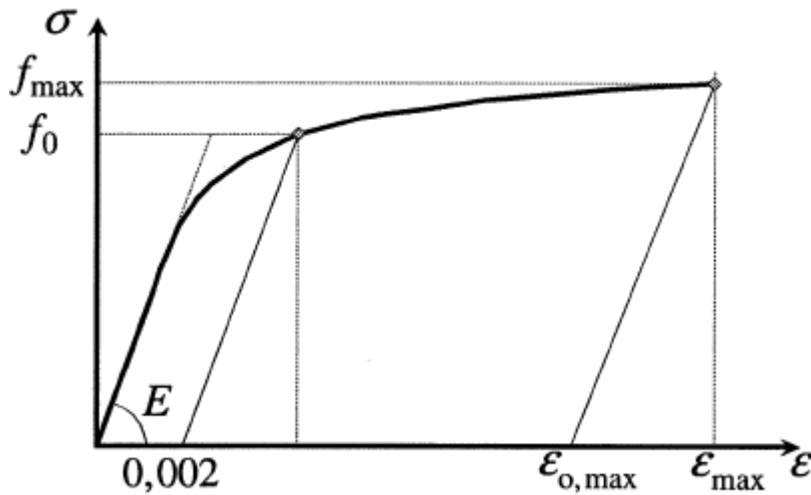


Figure 4.1 Stress-strain diagram of Ramberg-Osgood model in general form

To evaluate the exponent n , a second reference point on the stress-strain diagram with stress f_x and strain $\varepsilon_{0,x}$ is required. The choice of the second reference point depends on the strain range – elastic deformation or plastic deformation. It is therefore important to differentiate the n value of elastic range from plastic range. The n value can be generally expressed by:

$$n = \frac{\ln(0.002/\epsilon_{0,x})}{\ln(f_0/f_x)} \quad [4.3]$$

When considering the deformation in elastic range, the second reference point can be assumed by means of 0.1% offset method. In this instance, the stress f_x is taken as $f_{0,1}$ while the strain $\epsilon_{0,x}$ is taken as 0.001.

Therefore, Eqn. 4.3 can be re-written as

$$n_e = \frac{\ln 2}{\ln(f_0/f_{0,1})} \quad [4.4]$$

When considering the deformation in plastic range, the second reference point can be assumed at the maximum tensile stress location, which adopts f_{max} as f_x and $\epsilon_{0,max}$ as $\epsilon_{0,x}$. Hence, Eqn. 4.3 in the plastic range is revised as

$$n_p = \frac{\ln(0.002/\epsilon_{0,max})}{\ln(f_0/f_{max})} \quad [4.5]$$

The exponent n represented by Eqns. 4.4 and 4.5 can be approximated based on extensive experiments (Institution 2007) and specified as following by introducing a limit of proportionality f_p .

$$n_e = \frac{\ln(10^{-6}/0.002)}{\ln(f_p/f_0)} \quad \text{in elastic range } (f_x = f_p, \epsilon_p = 1 \times 10^{-6}) \quad [4.6]$$

As the limit of proportionality f_p depends on the value of 0.2% proof stress, f_p can be worked out as a portion of $f_{0,2}$ below.

$$f_p = f_{0,2} - 2\sqrt{10f_{0,2}} \quad \text{if } f_{0,2} > 160N/mm^2$$

$$f_p = f_{0,2}/2 \quad \text{if } f_{0,2} \leq 160N/mm^2$$

Or

$$n_p = \frac{\ln(0.002/\epsilon_u)}{\ln(f_0/f_u)} \quad \text{in plastic range } (f_x = f_u) \quad [4.7]$$

The value of n_e and n_p can be determined by applying the property of aluminium alloy 6063T6 listed above. Therefore, stress-strain relationship of aluminium alloy 6063T6 can be plotted by using Eqn. 4.2 as shown in the graph below.

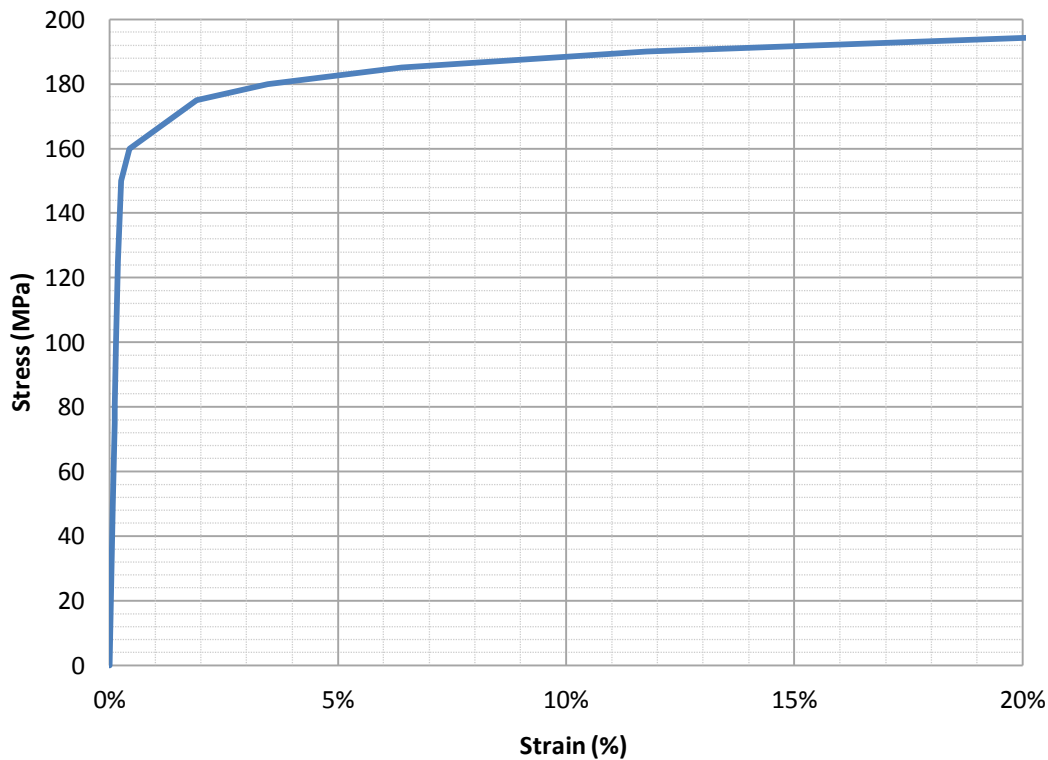


Figure 4.2 Stress-strain relationship of aluminium alloy 6063T6

The above stress-strain relationship diagram is based on engineering stress and engineering strain which are also called nominal stress and nominal strain. Nominal stress is defined as force per unit undeformed area in the metal while nominal strain is length change per unit undeformed length. However, when a metal is tested under tensile load, it experiences highly localized extension and thinning which is called necking in the plastic deformation range. The nominal stress ignores the necking phenomenon which produces much lower stress at failure than the actual ultimate strength. On the other hand, nominal stress obtained from compressive test on the same metal at failure is corresponding to the actual ultimate strength as it does not have necking problem. To account for the differences in the compressive and tensile behaviour independent of the metal specimen's geometry and applied loading types, true stress and true strain are introduced by a mathematical model. True stress and true strain are defined as the following.

1. True strain

When the deformation in length Δl and finite deformation dl both tend to zero, the strains in compression and tension are the same. Then,

$$d\varepsilon = \frac{dl}{l} \quad [4.8]$$

and

$$\varepsilon = \int_{l_0}^l \frac{dl}{l} = \ln\left(\frac{l}{l_0}\right) \quad [4.9]$$

where, l is the current deformed length and l_0 is the original length.

The strain ε defined by Eqn. 4.9 is called true strain or logarithmic strain.

2. True stress

True stress is the stress measurement conjugate to the true strain. It can be defined as

$$\sigma = \frac{F}{A} \quad [4.10]$$

where, F is the force acting on the material and A is the current area.

The true stress and true strain relationship of a ductile metal can represent loading conditions of both tension and compression in finite deformation. Therefore, these values shall be adopted in the finite element software to correctly define plasticity data. The values of true stress and true strain are strictly required by ABAQUS software to interpret the stress-strain relationship.

As the stress-strain relationship of aluminium alloy 6063T6 generated by Ramberg-Osgood model above is the relationship between nominal stress and nominal strain, formulas supplied by ABAQUS software (Systemes 2011b) are adopted to convert the nominal stress and nominal strain to true stress and true strain. These formulas are listed below.

1. Conversion between nominal strain and true strain

$$\varepsilon_{true} = \ln(1 + \varepsilon_{nom}) \quad [4.11]$$

2. Conversion between nominal stress and true stress

$$\sigma_{true} = \sigma_{nom}(1 + \varepsilon_{nom}) \quad [4.12]$$

Since the nominal strain indicates the total strain which includes the elastic strain and plastic strain, the true strain calculated by Eqn. 4.11 is the total true strain. As the ABAQUS software requires the true plastic strain only, the total true strain has to be separated into true elastic strain and true plastic strain. Formula provided by the software for the separation is given below.

$$\varepsilon^{pl} = \varepsilon^t - \frac{\sigma}{E} \quad [4.13]$$

where

ε^{pl} represents true plastic strain

ε^t represents true total strain

σ represents true stress

E represents Young's modulus

Table 4.1, comparing nominal stress with true stress and nominal strain with true total strain and true plastic strain, is given below. The true stress and true strain relationship diagram is given in Figure 4.3.

Table 4.1 Stress and strain conversion

Nominal stress (MPa)	Nominal strain	True stress (MPa)	True strain	Plastic strain
80	1.143E-03	80.1	1.143E-03	-9.602E-07
100	1.429E-03	100.1	1.428E-03	-3.028E-06
125	1.792E-03	125.2	1.790E-03	1.139E-06
150	2.580E-03	150.4	2.576E-03	4.280E-04
160	4.286E-03	160.7	4.277E-03	1.981E-03
175	1.904E-02	178.3	1.886E-02	1.631E-02
180	3.470E-02	186.1	3.411E-02	3.145E-02
185	6.393E-02	196.5	6.197E-02	5.916E-02
190	1.176E-01	211.1	1.112E-01	1.082E-01
195	2.148E-01	232.9	1.946E-01	1.912E-01

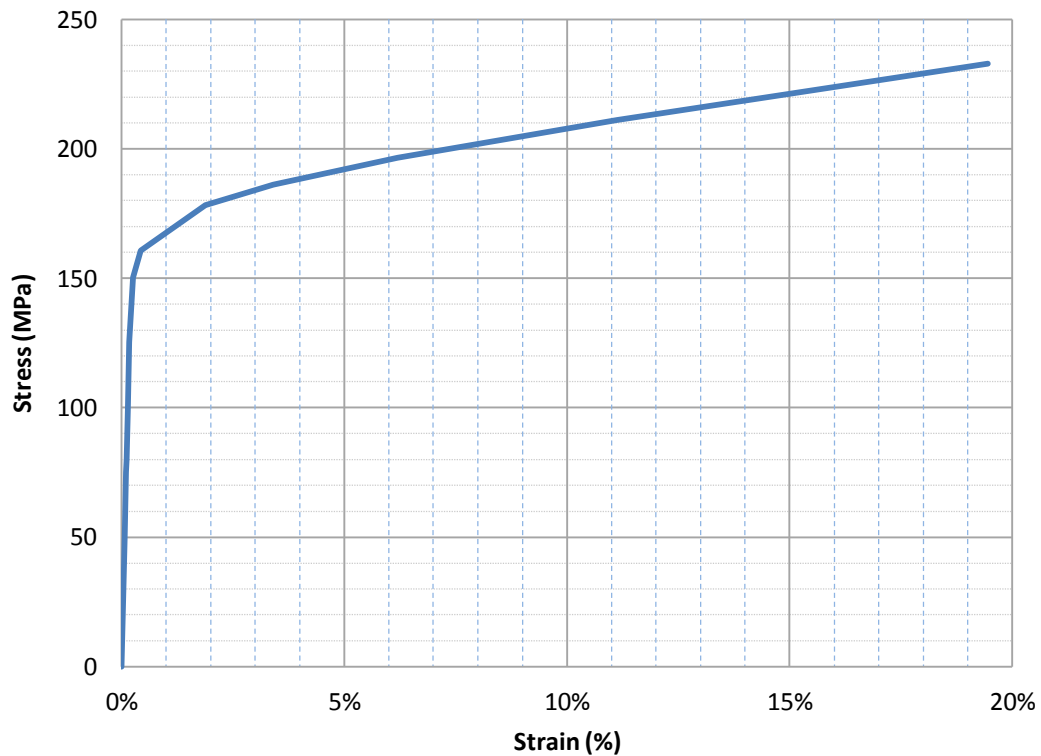


Figure 4.3 True stress – true strain relationship of aluminium alloy 6063T6

4.2.2 Polyamide material property

The thermal break joining the two aluminium profiles is a 25% glass-fibre reinforced polyamide PA66. The tensile property in longitudinal direction (along glass fibre direction) was obtained by laboratory testing. Standard specimens were supplied by sponsor, Permasteelisa Group. Specimen geometry complied to the requirements of ISO 527-2 (Standardization 1993b). Five specimens were tested for tensile strength under the guidance of ISO 527-1 (Standardization 1993a). Tests were carried out on Shimadzu Hydraulic Universal Testing Machine, model REH 50/50 tonne. Loading rate was set at 2.5mm/min. An extensometer was attached to the specimen to measure the change of gauge length during tests. To protect the extensometer, the extensometer was removed from the specimen when the elongation reached 3mm before failure. Test data were recorded by a data taker and transferred into a spread sheet format.

Engineering stress and strain were evaluated by the methodology specified by (Standardization 1993a). Stress-strain graph is shown in Figure 4.4. The Young's modulus in longitudinal direction is 4,477 MPa.

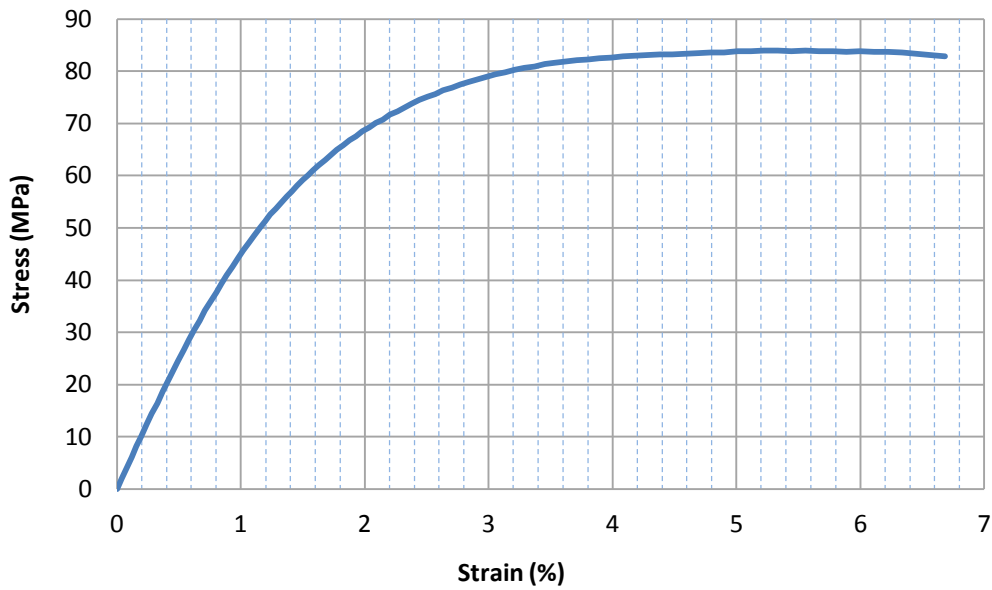


Figure 4.4 Stress-Strain relationship of PA66 in longitudinal direction

As the glass-fibre reinforced polyamide is an anisotropic material whose material property varies according to the glass fibre direction, in transverse direction (normal to the glass fibre direction), the material properties of PA 66 are weaker. As it is not possible to carry out laboratory tests for the transverse direction, the stress-strain relationship was adopted by the data supplied by Permasteelisa Group. The detailed data sheet is attached as an appendix. The stress-strain diagram is shown below and the Young's modulus is 2,681 MPa.

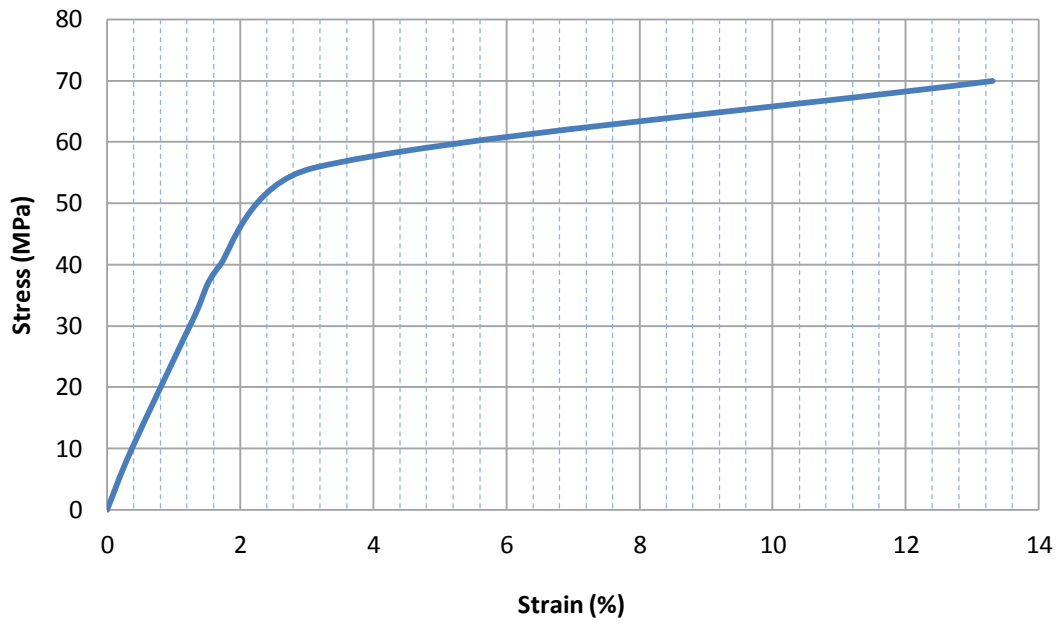


Figure 4.5 Stress-Strain relationship of PA66 in transverse direction

As explained in section 4.2.1, engineering stress and strain need to be converted into true stress and true strain representing finite deformation and accepted by ABAQUS software. Therefore, the above engineering stress-strain relationships of PA66 in the longitudinal direction as well as the transverse direction was translated to true stress-true strain relationships below.

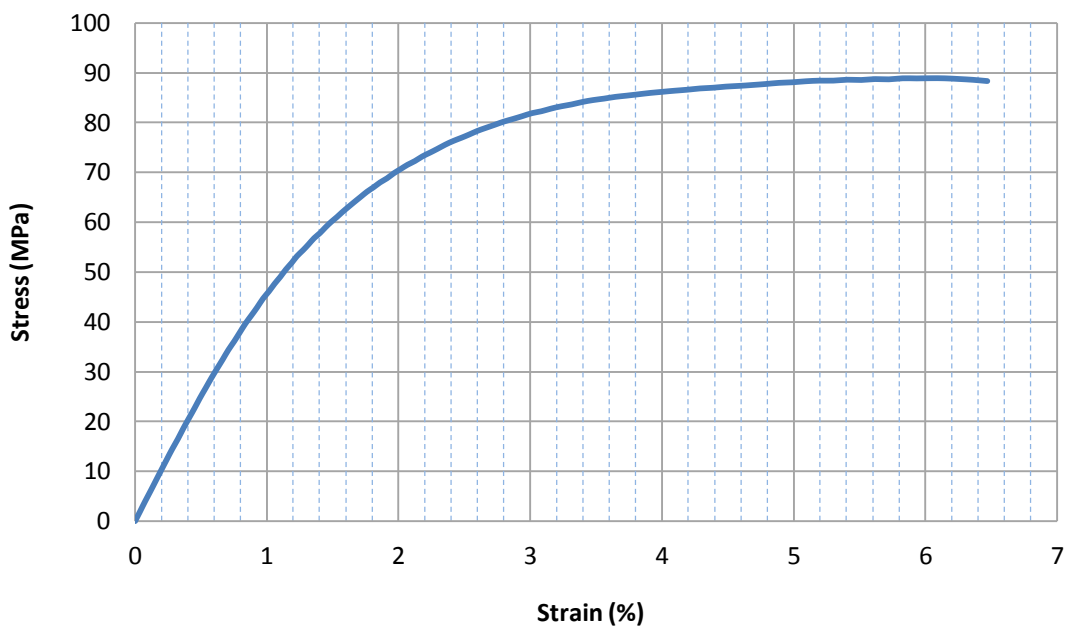


Figure 4.6 True stress - true strain relationship of PA66 in longitudinal direction

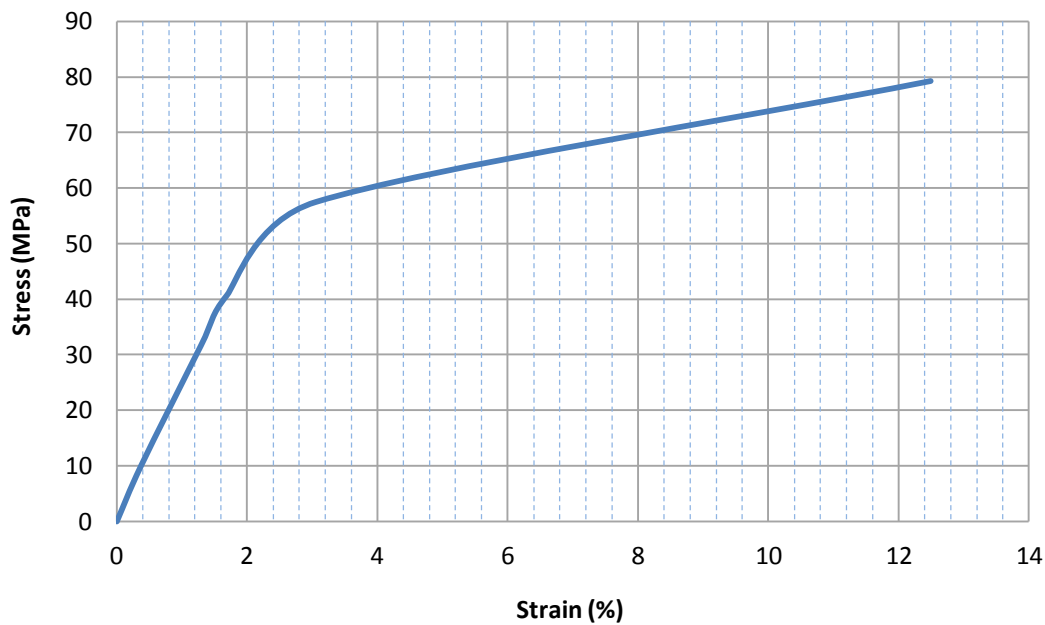


Figure 4.7 True stress - true strain relationship of PA66 in transverse direction

4.3 Investigation of the influence of element types

The composite façade mullion section has a complicated profile shape (Figure 3.1). The complexity is not only reflected in its profile shape but also in the composite action between aluminium and polyamide parts. To model it accurately and efficiently, three dimensional solid elements were adopted in the numerical analysis.

As this façade section is a semi-continuous section, it behaves differently from continuous or forged section. When it goes through shear, tensile or bending deformation, the interfaces will go through complicated deformation and interaction. The characteristic behaviours between different element types will largely affect the deformation and stress distribution of the whole section and the interfaces in the connections. It is therefore important to choose suitable element types to model both aluminium and polyamide portions under each loading condition.

As ABAQUS software was chosen to do the analysis, the type of solid element was selected from the software library. In the library (Systemes 2011b), first-order (linear) interpolation elements and second-order (quadratic) interpolation elements in three dimensions using either full or reduced integration, such as tetrahedral, triangular wedges and hexahedra, are available. In addition, hybrid and incompatible mode elements are provided by the software.

Full integration is to provide exact integration of all stiffness coefficients of an undistorted element by using enough sampling points (Cook, Malkus & Plesha 1989). In other words, full integration means that the stiffness matrix of an element with uniform material behaviour will be integrated by the Gaussian scheme chosen only if the Jacobian of the mapping from the isoparametric coordinates to the physical coordinates is constant throughout the element. The limitation of full integration is that opposing sides or faces in three dimensional elements must be parallel and the mid-side nodes must be at the middle of the element sides for the second-order elements. If the element does not satisfy these conditions, it will lead to inaccuracy in the integration and forming of stiffness matrix.

Reduced integration adopts fewer sampling points. It usually implies that an integration scheme one order less than the full scheme is used to integrate the element's forces and stiffness. This method provides several advantages. First, reduced sampling points means less integration and therefore less cost. By using reduced integration method, the computational cost is lowered when forming an element. For instance, a fully integrated quadratic 20-node three dimensional element requires 27 points for full integration while the same element only needs eight points in the reduced integration version.

Second, this low-order rule tends to soften an element. Reduced integration decreases the number of constraints introduced by an element when internal constraints are modelled in the continuum theory. This is because certain high-order polynomial terms happen to vanish at Gauss-points of a low-order rule. Therefore, these terms make no contribution to strain energy, which means these complicated displacement modes offer less resistance to deformation. It is particularly beneficial to apply reduced integration to a second-order solid element subjected to bending. With full integration, this type of element will become too stiff and "lock" itself. The results provided by them are not usable. This will be further discussed in the examples (trial models) later. In general, for a second-order element whose isoparametric coordinate lines remain orthogonal in the physical space, reduced integration method provides high accuracy of the nodal displacements (Barlow 1976) and therefore higher accuracy of strains.

However, there is some deficiency in reduced integration method. The rank of stiffness matrix is less than the number of element degree of freedom minus the number of rigid body modes. This leads to the appearance of singular modes (hourglass modes) in

response, typically in first-order elements. Singular modes existing in second-order three dimensional elements can only propagate in a single stack of elements while the only mode existing in second order two dimensional reduced integration elements cannot propagate more than one element. As these modes rarely cause any trouble in second order elements (Systemes 2011b), no special control techniques are required. The second order one dimensional elements will not generate a rank deficient stiffness matrix.

To overcome shear locking in linear fully integrated elements, the incompatible deformation modes are added internally to the elements. The main effect of the additional degrees of freedom is to eliminate the parasitic shear stress in regular displacement elements in bending. These degrees of freedom also eliminate the artificial stiffening due to Poisson's effect in bending and therefore prevent overestimation of the stiffness. Lower order elements with incompatible modes can produce results in bending problems which are comparable to second order elements but at significantly lower computational cost.

To be able to choose a suitable element type for this composite façade section, parametric study of a simplified section similar to the bottom aluminium portion was carried out. Based on the test results, bending behaviour was observed not only in four-point bent beam tests but also in section tensile capacity tests as discussed in Chapter 3. The purpose of the exercise is to determine the element type appropriate for bending with low computational cost.

The geometry of the trial section is taken as similar to half of bottom aluminium portion plus the polyamide insert. The connection between polyamide and aluminium was deleted to remove unnecessary complexity. The material property of the whole section was defined as aluminium alloy 6063T6. This section was tested in ABAQUS software by using solid hexahedra element for full integration, reduced integration and incompatible mode under same loading and boundary conditions. Loading and boundary conditions similar to the tensile tests were applied to the model. Aluminium material property of 6063T6 was modelled by Ramberg-Osgood expression. True stress – true strain relationship shown in Figure 4.3 was used to define the plasticity of the material. Details of the model setup are shown in Figure 4.8 and Figure 4.9 below. Theoretical bending moment diagram of this structure is plotted in Figure 4.9.

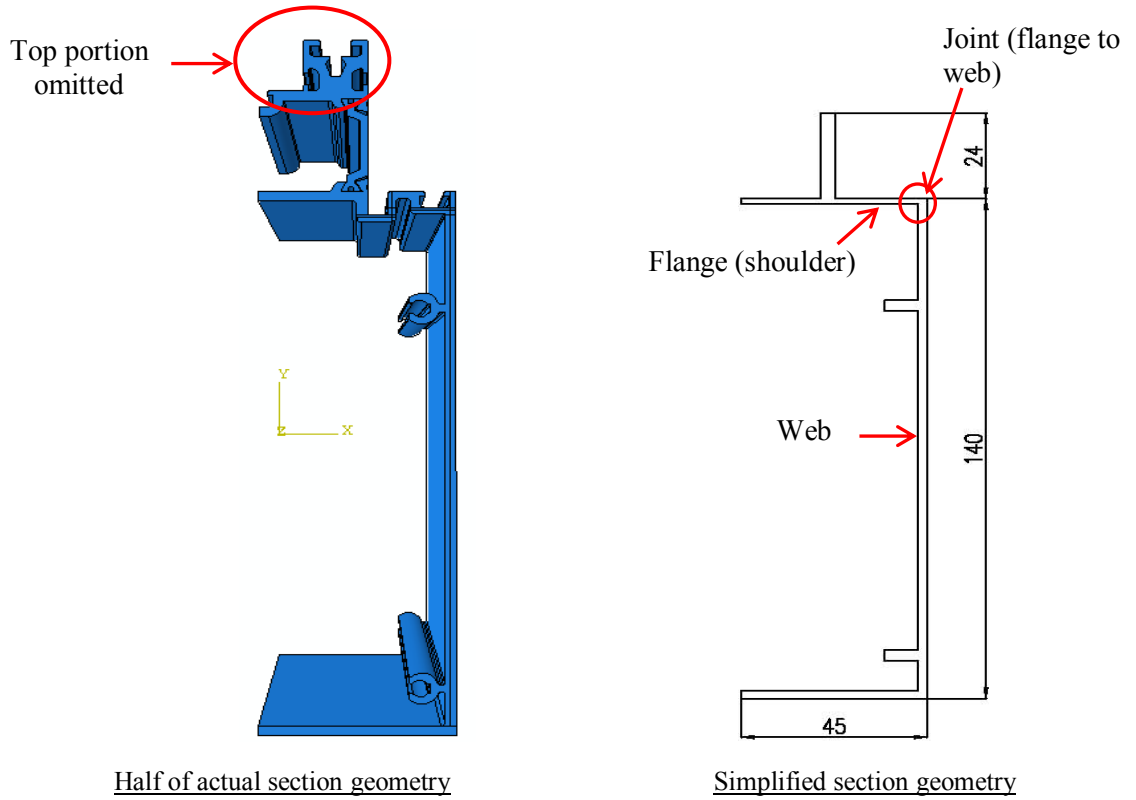


Figure 4.8 Trial model geometrical details

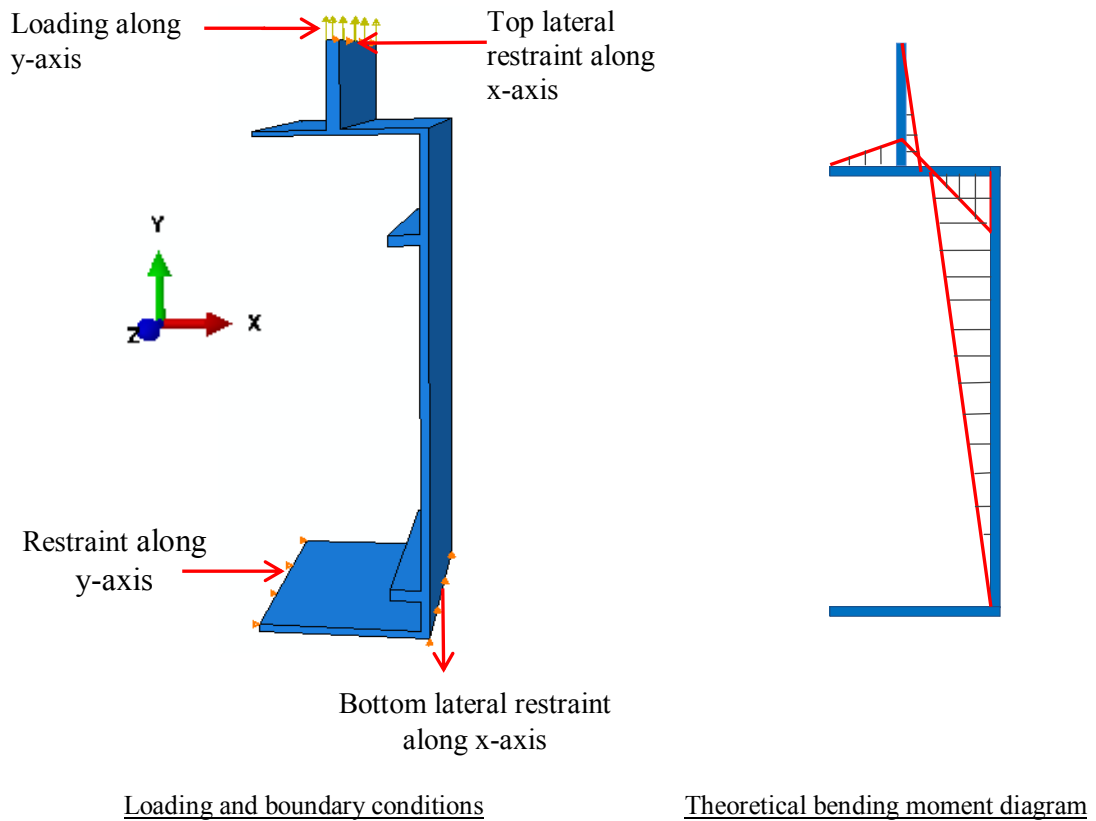


Figure 4.9 Boundary condition and theoretical reaction force diagram

Five types of three dimensional stress elements were tested. The element types are

- a) An eight node linear brick element with full integration (C3D8);
- b) An eight node linear brick element with reduced integration and hourglass control (C3D8R);
- c) An eight node linear brick element with incompatible modes (C3D8I);
- d) A twenty node quadratic brick element with full integration (C3D20);
- e) A twenty node quadratic brick element with reduced integration (C3D20R)

Comparisons of deformed shapes and bending stresses for the above element types are listed below.

Table 4.2 Comparison of deformed shapes

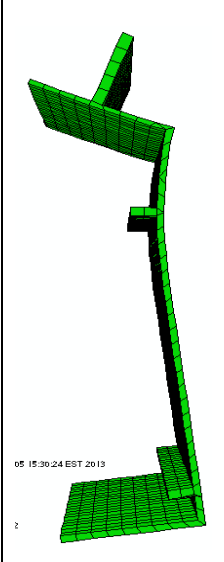
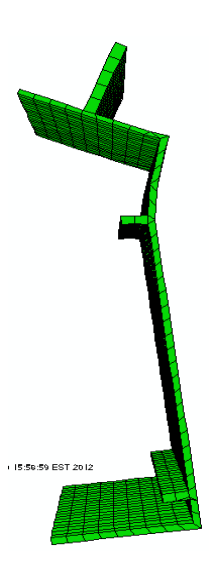
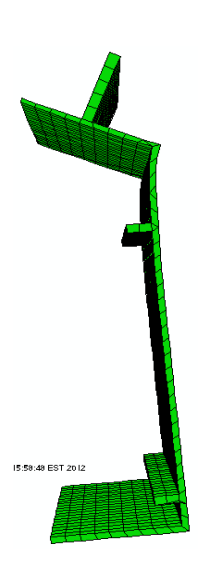
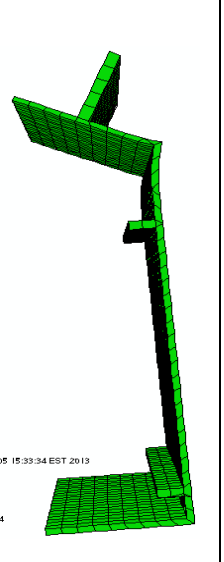
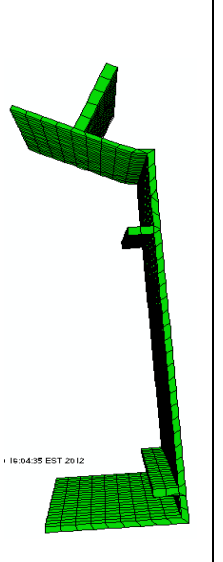
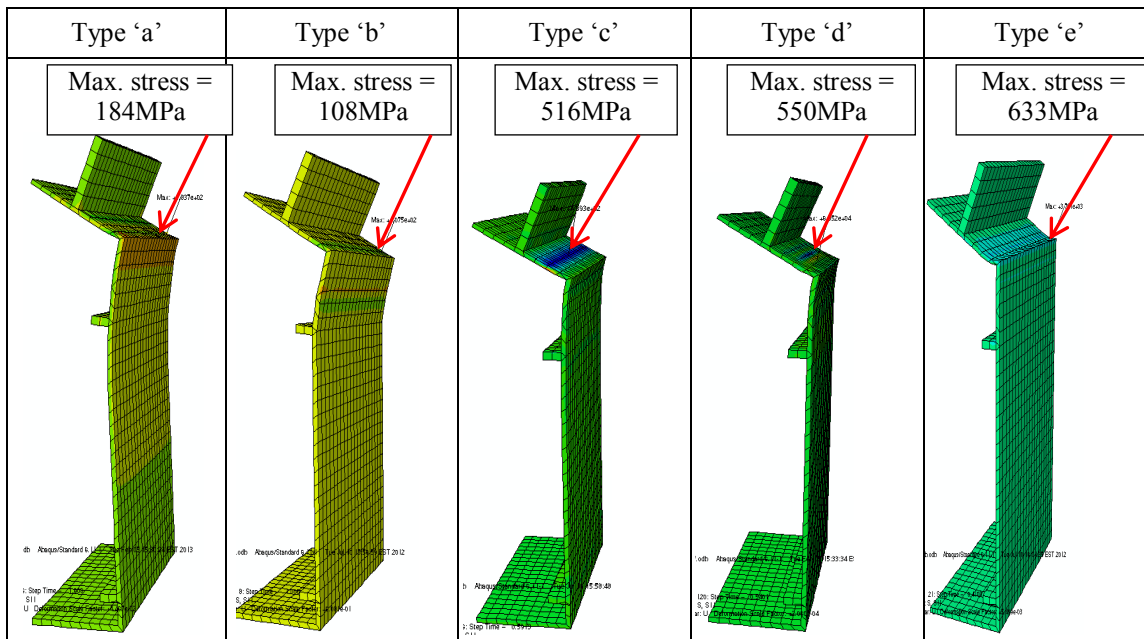
Type 'a'	Type 'b'	Type 'c'	Type 'd'	Type 'e'
				

Table 4.2 shows displacement modes between quadratic elements and linear elements under common loading and boundary conditions as well as material property. Types 'a' and 'b' show similar deformed shapes. The section bends at web. The joint between flange and web remains orthogonal (rigid). Type 'c' shows similar displacement mode as Type 'd'. The incompatible mode reduced the “shear lock” effect slightly, but did not remove it completely. The angle at the joint between flange and web still remains orthogonal. However, the web doesn't bend as much as types 'a' and 'b'. This proves that the performance of linear element with incompatible mode is comparable to quadratic fully integrated element in this case. The quadratic element with reduced integration (type 'e') exhibits completely different displacement mode – the joint

between flange and web is fully flexible and rotates against each other which indicates the rigid joint becomes plastic hinged. There is no bending deformation observed on the web as with the other four types. This deformed shape is close to the actual deformed shape of the bottom aluminium portion from laboratory tensile tests (Figure 3.13).

The bending stresses of these five types of elements are shown in Table 4.3. The maximum bending stress of Type 'a' and 'b' is located on the flange near the joint to the web. For Type 'c', the maximum stress is located in the middle of the flange while it is located between the middle of the flange and the joint to the web for Type 'd' element. As the bending moment diagram shows the bending moment at the flange is much smaller than that at the joint with web, and hence, the maximum stress location shown on Type 'c' and 'd' structures are obviously not correct. With the maximum bending stress shown at the joint to the web, the bending stress distribution of Type 'e' structure is consistent to the bending moment distribution. Although the bending stress distribution of Type 'a' and 'b' structures is close to the bending moment distribution, the deformation of these two structures indicates the maximum bending is occurring at the web while the joint remained unaffected. This shows the "shear lock" effect prevented the model to generate consistent results therefore linear elements with full or reduced integration are not suitable for simulating bending behaviour. On the contrary, quadratic element with reduced integration gives consistent bending stress distribution and deformation shape. Hence, it shall be adopted in FE model for the top and bottom aluminium portion.

Table 4.3 Comparison of bending stresses



In addition, the advantage of adopting quadratic reduced integration elements is to prevent “volumetric locking”. As the top and bottom portions are made of aluminium alloy, its incompressible nature of plastic deformation in metals places limitations on the types of elements that can be used for an elastic-plastic simulation (Systemes 2011a). “Volumetric locking” is caused by element over-constraint. When modelling, incompressible material behaviour adds kinematic constraints to an element, and the limitations constrain the volume at the element’s integration points to remain constant. If these elements cannot resolve all of these constraints, they suffer from “volumetric locking”. This is typically for the fully integrated quadratic solid elements. However, reduced integration solid elements have fewer integration points at which the incompressibility constraints must be satisfied. Hence, they are not over-constrained and can be used for most elastic-plastic modelling. However, quadratic reduced integration recommended to take caution if the strains exceed 20%-40% (Systemes 2011a). When strains reach this magnitude, this type of element can still suffer from “volumetric locking”. To reduce this effect, fine meshing is recommended (Systemes 2011a).

From the laboratory tensile tests, plastic hinge is clearly visible (Figure 3.13). As the quadratic reduced integration solid element is proved to be the most suitable element for modelling top and bottom aluminium portions, fine mesh of seed 5 (in tensile and shear

test simulations) and seed 9 (in beam test simulation) was adopted to reduce the “volumetric locking” and provide reasonable results.

Quadratic reduced integration solid element is also assigned to the middle polyamide core for shear and tension models as this type of element will tolerate bending behaviour which is certain in tensile tests. However, the polyamide core is expecting only shear deformation during bending as to the sandwich theory; linear element with incompatible mode was adopted in the beam models to save computational costs. Fine meshes of seed 3 (in tensile and shear test simulations) and seed 7 (in beam test simulation) were also adopted to work together with the aluminium skins (top and bottom portions).

In summary, intensive research was carried out to determine the most suitable element type for this typical façade section. As a sandwich type composite section, the skins take bending while the core takes shear only. Also, the top and bottom skins will go through large deformation during simulation. The quadratic reduced integration solid element (C3D20R) is adopted in the model to avoid “shear lock” and “volumetric locking”. However, linear element with incompatible mode (C3D8I) is used in the simulation to take only shear deformation and save on computational cost. Mesh sizes are also refined to produce reasonable results.

4.4 Interaction between aluminium profile and polyamide insert

A typical façade section comprises three portions which are top and bottom aluminium and middle polyamide insert. The polyamide provides thermal isolation for energy efficiency. The connection between polyamide and aluminium is not forged together but by rolling polyamide into the joint with high pressure. It deforms the aluminium extrusions and transfers the pressure to the polyamide inserts. This contributes to the friction between aluminium and polyamide. Hence, it is a semi-continuous section. The section capacity mainly relies on the connectivity of the joints. The connectivity of the joints depends on the pressure created during manufacturing process and the geometry of the contact surfaces. As mentioned in the previous chapters, the pressure depends on several factors, such as the knurled shape of the aluminium profile, the sharpness and newness of the knurled wheels, etc.

To be able to model this section correctly, it is important to understand the frictional interaction between aluminium and polyamide. Early studies of this type of thermal break section suggested adopting sandwich theory to analyse the composite action at connections. A typical sandwich structure consists of top and bottom thin stiff sheet of dense material joined by a thick layer of low density material which is much less stiff. The sandwich theory (Allen 1969) assumes the core makes no contribution to the flexural rigidity of the sandwich, EI , and the shear stress is constant through the depth of the core. For a thick faced sandwich structure, the faces have significant local bending stiffness and no longer behave as flexible membranes. The faces may undergo local bending when it bends about its own centroidal axis rather than about the centroidal axis of the complete sandwich section. The faces may also undergo purely extensional deformation when it is subjected to a uniform tensile or compressive stress. This section behaves close to the assumption of the thick faced sandwich structure and therefore shall be considered as a thick faced sandwich structure when sandwich theory is adopted in the study.

Previous studies (Franz Feldmeier 1988) and (Heinrich, Schmid & Stiell 1980) considered shear deformation in the core (middle polyamide insert) and assumed the top and bottom aluminium portion/skin bent in same curvature as other typical sandwich structures, such as honey comb panels (Bitzer 1997) or plied structures. Other types of sandwich structures such as (Corigliano, Rizzi & Papa 2000) studied a syntactic-foam/glass-fibre composite sandwich. It applied bonding between skins and core. Maximum shear stress limit was adopted to assign debonding interface condition. Johnson, Pickett and Rozycki (Johnson, Pickett & Rozycki 2001) described the technique used in material modelling and numerical simulation of fibre reinforced composite shell structure. It modelled the interface between pliers as “sliding interface” which were tied together. This technique was later improved by Johnson and Holzapfel in (Johnson & Holzapfel 2006).

In terms of this typical façade section, the interaction between aluminium skin and polyamide core is mainly achieved during manufacturing process. As the glass fibre reinforced polyamide is rolled into pre-knurled aluminium profile during manufacturing process, normal pressure and friction are created between the interface of polyamide and aluminium. To determine the normal pressure created during knurling and rolling process is complicated as this involves many uncertainties, such as aluminium material

grade, sharpness of thumbwheel, settings of knurling machine and geometry of the aluminium profile, etc. The uncertainty introduced in the manufacturing process is too complex to study. However, the change of internal force distribution at each loading step is presented by studying the interface detail.

Figure 4.10 below is the enlarged interface geometry. The applied shear force introduces shear stresses on the vertical contact surfaces. Normal stresses as well as shear stresses are also generated on the inclined contact surfaces. As the aluminium penetrates into the polyamide in the overlapped zone, the connection tends to rotate around this zone under applied shear force. Whether the rotation will occur or not depends on the area of overlapped zone and the rigidity of this zone. This possible rotation will introduce normal stresses along the vertical contact surfaces. If we assign case 1 as the normal stresses introduced by shear force to the three interfaces, then, case 2 is assigned to the normal stresses by rotation.

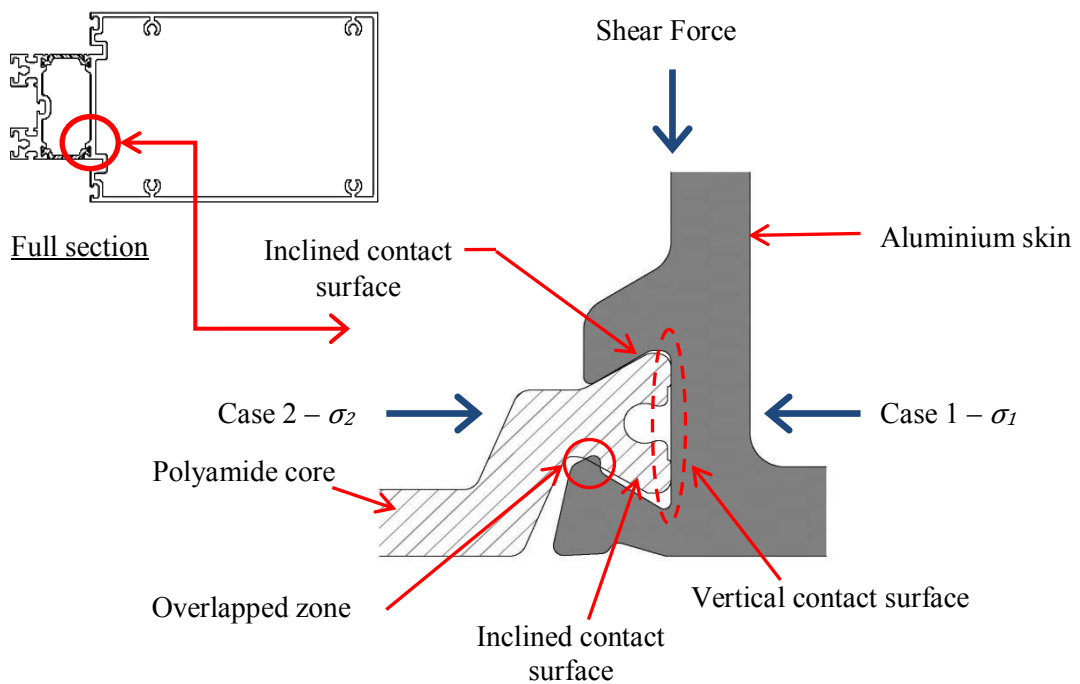


Figure 4.10 Enlarged contact surface detail

In case 1, normal stress tends to push polyamide surface away and open up the connection, therefore, causing localized bending in the inclined contact surfaces. In case 2, normal stress is helping to stick the two surfaces together. Also, when shear force increases, both surfaces go through deformation and internal stress redistribution. Therefore, normal and shear stresses in both case 1 and 2 vary under every loading increment. Internal forces at the end of an early loading increment contribute to the

deformation and stress distribution at next increment. Hence, it is not practical to include all these uncertainties into the FE model. However, it is obvious that frictional stress is the main contribution to the connectivity. Friction is therefore adopted to simulate the interface contact actions.

To model the frictional interaction between aluminium and polyamide contact surfaces, classical Coulomb's friction theory was adopted. According to this theory, the friction can be divided into static friction and kinetic friction. Static friction coefficient (μ_s) represents the friction force opposing the onset of relative motion between two bodies while kinetic friction coefficient (μ_k) is representing the force opposing the continuance of relative motion once that motion has started. These two frictions can be defined below (Blau 2001).

$$\mu_s = F_s/P \quad [4.14]$$

$$\mu_k = F_k/P \quad [4.15]$$

where,

F_s represents the force just sufficient to prevent the relative motion

F_k represents the force needed to maintain relative motion between two bodies

P represents the force normal to the interface between the two sliding bodies

Static and kinetic friction coefficients are largely related to the material property and system (Blau 2001; Kogut & Etsion 2004). The system refers to geometry of the interfaces (surface roughness and asperity interlocking), fluid dynamics approaches, and considerations of electrostatic forces between surface atoms. In this study, friction coefficients depend on the material properties of aluminium alloy and polyamide, the geometry of the interfaces, manufacturing process and internal force redistribution in each loading increment. In addition, temperature environment also affects the value of friction coefficient which was proven in the tests discussed in Chapter 3.

Proposed progressive failure model

Due to the complexity surrounding the friction coefficient, test results are adopted to provide guidelines for the coefficient value. From the load vs slip graph (Figure 3.9), load increased linearly with the increase of slip until it reached the peak value. It then dropped with slip continuously increasing. From observation, the polyamide slipped

away from the connection right after reaching the peak load. Unlike the loading stage, the unloading (failure) stage of the test doesn't show linear rather a quadratic reduced loading capacity with increased displacements. The mechanism of failure is a progressive failure process.

The quadratic shape of progressive failure process doesn't comply with the classic rule set in Eqn.4.14 and Eqn. 4.15 above. It is probably caused by a combination of reduced friction coefficient and micro-structural damage in the materials. As the reduced friction coefficient plays a major role in the progressive failure process, a proposed multi-phase simulation of this process was initiated. This proposed multi-phase progressive failure model assumes the loading phase before slippage occurs as the first phase (Phase I). After slip occurs, the static friction co-efficient drops to the first kinetic friction co-efficient in Phase II. It then keeps dropping in Phase III and IV until it equals to zero in Phase V. The proposed model is illustrated in Figure 4.11 below. In the graph, τ_{crit} represents critical frictional shear stress while γ_{crit} represents slip between the two bodies.

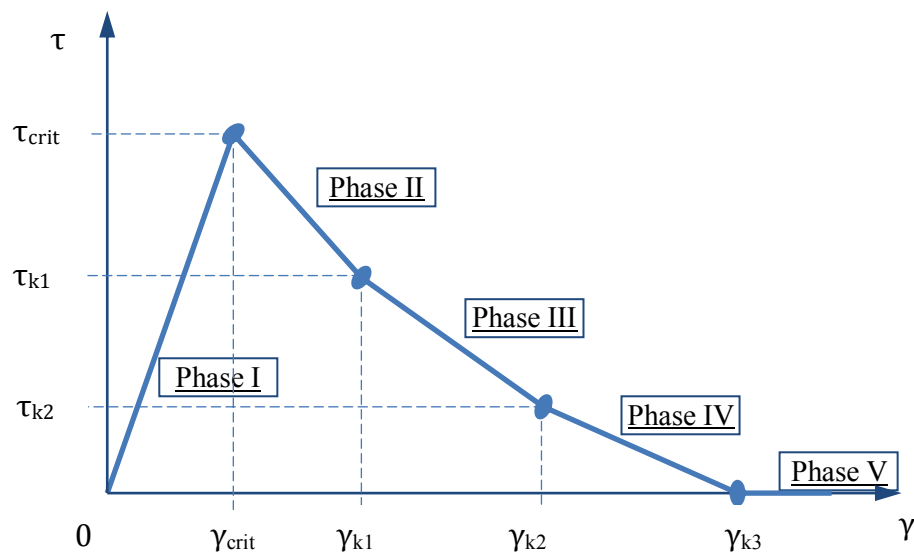


Figure 4.11 Proposed model of progressive failure mechanism at aluminium and polyamide contact surfaces

The proposed progressive failure model presents a practical approach to simulate the failure mechanism of the connection. The basis of this approach is to identify the suitable friction co-efficient at each phase.

As it was explained before, the friction co-efficient is related to the material properties of contact bodies and system. The complicated connection geometry and uncertainty introduced by manufacturing process add more difficulties in determining the co-efficient. It is, therefore, necessary to utilize experimental results as guide to define the values of friction co-efficient and update the model. Updating the FE model to match the experimental results involves model optimization with multi-objectives. This is a very complicated topic which is beyond the scope of this study. However, it is worth to carry out as part of future research work.

In this study, the model updating process was done manually. After intensive calculation, friction co-efficient at each phase was determined. The outcome of the FE model matches the experimental results. The initial frictional coefficient μ of 0.3 for both connections was adopted and then reduced to two-thirds of initial coefficient at the beginning of failure. After the coefficient was reduced a further three-quarter and a two-third drop based on the previous value was assumed and finally was set to zero to represent complete failure of the connection. The friction co-efficient applied in each phase is listed in the table below. This approach will be applied in the FE model.

Table 4.4 Frictional coefficient assignment for the proposed progressive failure model

Phase	Shear stress and strain range	Frictional coefficient
I	0 to τ_{crit} , 0 to γ_{crit}	0.3
II	τ_{crit} to τ_{k1} , γ_{crit} to γ_{k1}	0.2
III	τ_{k1} to τ_{k2} , γ_{k1} to γ_{k2}	0.15
IV	τ_{k2} to 0 , γ_{k2} to γ_{k3}	0.1
V	Contact bodies separated	0

Application of the proposed progressive failure model for FE modelling

As ABAQUS software supplies several frictional formulations, it is important to select a suitable one for the modelling.

A classical Coulomb theory assumes there is no relative motion between two contact surfaces if the equivalent frictional stress is less than the critical stress τ_{crit} . From Eqn. 4.14 and Eqn. 4.15, the critical stress is proportional to the contact pressure (normal pressure) p and frictional coefficient μ (Systemes 2010), which can be presented as a formula below.

$$\tau_{crit} = \mu p \quad [4.16]$$

This formula indicates that no relative motion occurs when the frictional shear stress (τ) is less than the critical stress (τ_{crit}). On the other hand, when the frictional shear stress is larger than or equal to the critical stress, relative motion called slip between the two contact surfaces starts. This can be demonstrated in the graph below. γ_{crit} represents slip between the two bodies.

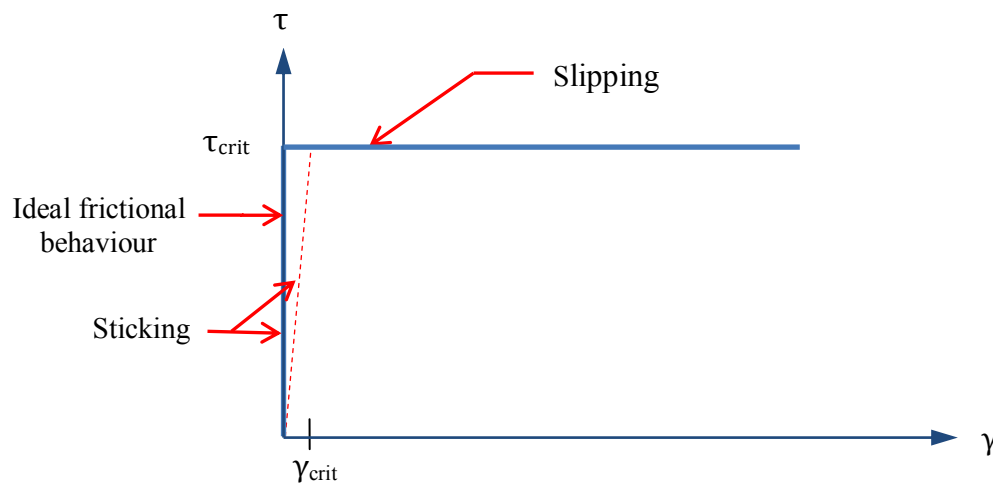


Figure 4.12 Frictional behaviour between two contact bodies

The thicker line representing the ideal frictional behaviour based on Coulomb theory shows there is no slippage occurring before the frictional shear stress reaches the critical stress. This phenomenon can be modelled by applying Lagrange multiplier formulation (Systemes 2010) in ABAQUS software. However, the Lagrange frictional algorithm has two disadvantages. The additional Lagrange multipliers increase the time of analysis by adding more degrees of freedom to the model. As it increases the number of iterations, the presence of rigid constraints tends to slow or prevent convergence during solving process sometimes, especially, if there is a strong local interaction between slipping and sticking conditions. Apart from these disadvantages, the load vs slip graph from the tests is not exactly the same as the ideal one. It showed a small slip occurring before reaching the critical frictional shear force.

To overcome the shortcomings of Lagrange multiplier formulation, penalty frictional interface traction-displacement law (Inc 2001) was introduced to define surface to surface interaction. Penalty contact algorithm provided by ABAQUS software approximates ‘no relative motion’ by stiff elastic behaviour. The stiffness is chosen such that relative motion from the position of zero shear stress is bounded by the

allowable maximum elastic slip γ_{crit} . This critical slip value γ_{crit} adopted here is set to default value of 0.5% of the average length of all contact elements in the model. Once the relative motion between the contact surfaces exceeds the γ_{crit} , slip occurs. This behaviour is illustrated by a dashed line in Figure 4.12. This concept is consistent with the test results. When slippage occurs in the contact surfaces, the coefficient of static friction is not applicable. Kinetic friction coefficient, which is smaller than the static one (Meriam & Kraige 2008; Sheri D. Sheppard 2004), shall apply. The smaller kinetic friction coefficient is used in the progressive failure modelling.

Defining the interaction between two contact bodies not only relies on the mechanical contact property but also depends on contact formulation. ABAQUS software offers several contact formulations. Each formulation is based on a variety of a contact discretization, a tracking approach and assignment of “master” and “slave” roles to the contact surfaces.

There are two contact discretization options available in ABAQUS software (Systemes 2011a):

1. Node to surface discretization
2. Surface to surface discretization

To establish the traditional “node to surface” discretization contact condition, “slave” node on one side of a contact surface effectively interacts with a point of projection on the “master” surface on the opposite side of the contact interface. In this case, each “slave” node interacts with a group of nearby “master” nodes. The values from the “master” nodes are then interpolated to the projection point. The “slave” nodes are constrained not to penetrate into the “master” surface, but, the nodes of the “master” surface can penetrate into the “slave” surface. The constraints provided to prevent the “slave” nodes penetrating into the “master” surface will attract forces concentrated at these “slave” nodes. The force concentration leads to an uneven distribution of pressure across the surface.

In terms of “surface to surface” discretization, it considers the shape of both “slave” and “master” surfaces in the region of contact constraints. The formulation of “surface to surface” discretization enforces contact conditions in an average sense over regions of nearby “slave” nodes rather than only at individual “slave” node. As the average regions are approximately centred on the “slave” nodes, each contact constraint will not only

consider one “slave” node but also the adjacent “slave” nodes. Although some penetration might be observed at some individual nodes, large undetected penetrations of “master” nodes into “slave” surface do not occur with this discretization. Comparing to “node to surface” discretization, “surface to surface” discretization generally provides more accurate stress and pressure results. It also provides smoothing effect for resisting penetrations in an average sense over finite regions of the “slave” surface. Mesh refinement will lead to less discrepancies between the discretization and improve accuracy in stress. The other advantage of adopting “surface to surface” discretization is that this discretization formulation is less sensitive to “master” and “slave” surface designation than “node to surface” discretization. Working example shown in (Systemes 2011a) indicated a 30% error improvement comparing to using “node to surface” discretization. However, “surface to surface” discretization requires higher computational cost as it involves more nodes per constraint. As the contact area of this façade section takes a small fraction of the whole section which has only one layer of interface, the “surface to surface” discretization formulation will provide accurate results with reasonable computational cost. The assignment of larger “master” mesh size than the “slave” one will also reduce the cost. Thus, the “surface to surface” discretization is chosen in the modelling.

To model the relative motion of two contact surfaces, ABAQUS software provides two tracking approaches (Systemes 2011a). They are finite sliding tracking approach and small sliding tracking approach. Finite sliding contact is the most general tracking approach which allows for arbitrary relative separation, sliding and rotating of the contact surfaces. For a surface to surface contact pair, there are two tracking algorithms available for the finite sliding contact. One is path based tracking algorithm and the other one is state based algorithm. The path based algorithm considers carefully the relative paths of points on the slave surface with respect to the master surface within each increment. However, the state based algorithm is available only for three dimensional finite sliding surface to surface contact pairs with either deformable or discrete rigid surfaces. This algorithm updates the tracking state based on the tracking state related to the onset of the increment together with geometric information associated with the expected configuration. Both algorithms require the software constantly to determine the portion of master surface which is in contact with each slave

node. This calculation is very complicated especially when involving both deformable contact surfaces, like the façade section studied here.

Small sliding contact assumes a relatively little sliding of one surface along the other and is based on linearized approximations of the master surface per constraint. This tracking formulation is a limited case of finite sliding formulation as it is deemed unnecessary to use finite sliding tracking approach for a large number of contact problems, including geometry nonlinearity. When using small sliding tracking formulation, ABAQUS software establishes the relationship between the slave nodes and the master surface at the beginning of the analysis. During analysis, the software determines the interactive pair of master and slave surface segments and maintains these relationships throughout the analysis. To handle the geometric nonlinearity, the small sliding formulation accounts for any rotation and deformation of the master surface and updates the load path through which the contact forces are transmitted. Using small sliding formulation, the software does not need to monitor slave nodes for possible contact along the entire master surface as the interactive pair has been set and maintained through. This approach reduces the computational cost dramatically especially for three dimensional contact problems.

Based on the results from the laboratory tests, the polyamide slips only at a fraction of the total contact length. This confirms that the section under study is suitable for applying small sliding tracking approach. The nonlinear geometry of the section and contact interfaces can be well measured by this formulation with reasonable computational cost. The small sliding formulation is also recommended by Johnson and Holzapfel (Johnson & Holzapfel 2006), Allix, Ladeveze and Corigliano (Allix, Ladevéze & Corigliano 1995) and Cheng, Lee and Lu (Cheng, Lee & Lu 2006) for calculating the relative sliding of the interfaces.

As aluminium is much stiffer than polyamide, it is obvious that aluminium surfaces were assigned as master surfaces while polyamide as slave surfaces.

To assign the “master” and “slave” surfaces, rules stated in (Systemes 2011a) shall be followed. Generally, when a smaller surface contacts a larger surface, the smaller surface is to be defined as “slave” surface. The stiffness of the material and structure shall be considered as well. It is usually acceptable to assign a surface as “master” surface if its material property is much stiffer than the other surface. However, the

structure system also affects the selection. For instance, if a piece of thin steel sheet contacting with a larger block of rubber, the surface of the larger block of rubber shall be assigned as “master” surface regardless of the fact that steel modulus is much larger than the rubber’s. Other rules such as

- Analytical rigid surfaces and rigid element based surfaces must always be the “master” surface.
- A node based surface can only be assigned as “slave” surface and always uses node to surface discretization.
- “Slave” surfaces must always be attached to deformable bodies or deformable bodies defined as rigid.
- Both surfaces in a contact pair cannot be rigid surfaces with the exception of deformable surfaces defined as rigid.

The material property and structural system of this façade section mainly determined the “master” and “slave” assignment. As the Young’s modulus of aluminium alloy 6063T6 is much larger than the glass fibre reinforced polyamide PA66 and the size of the top and bottom aluminium profiles is much greater than the thin polyamide inserts, the aluminium surfaces therefore can be defined as “master” surfaces while the polyamide surfaces as “slave” surfaces. The interface of aluminium profile is larger than the interface of the polyamide. Both aluminium profiles and polyamide inserts are defined as deformable solid in the model.

In conclusion, mechanical contact property of penalty friction model is adopted to simulate the frictional behaviour between aluminium and polyamide interfaces. Based on the observation of the laboratory tests, a proposed progressive failure model is created to describe the failure mode of the connection. Small sliding tracking approach with surface to surface discretization is used to model the sliding behaviour of the interfaces. Aluminium contact surfaces are assigned to “master” surfaces while polyamide surfaces are assigned as “slave” surfaces.

4.5 Numerical investigation of the section shear capacity

4.5.1 Model setup

To simulate the quasi-static shear tests, a three dimensional finite element model was set up by using ABAQUS software. Since this section is symmetrical with respect to the y-axis, the section was cut along the line of symmetry and then modelled in the software (refer to Figure 4.13). Utilizing the section symmetry can save half of the computational cost while producing the same results.

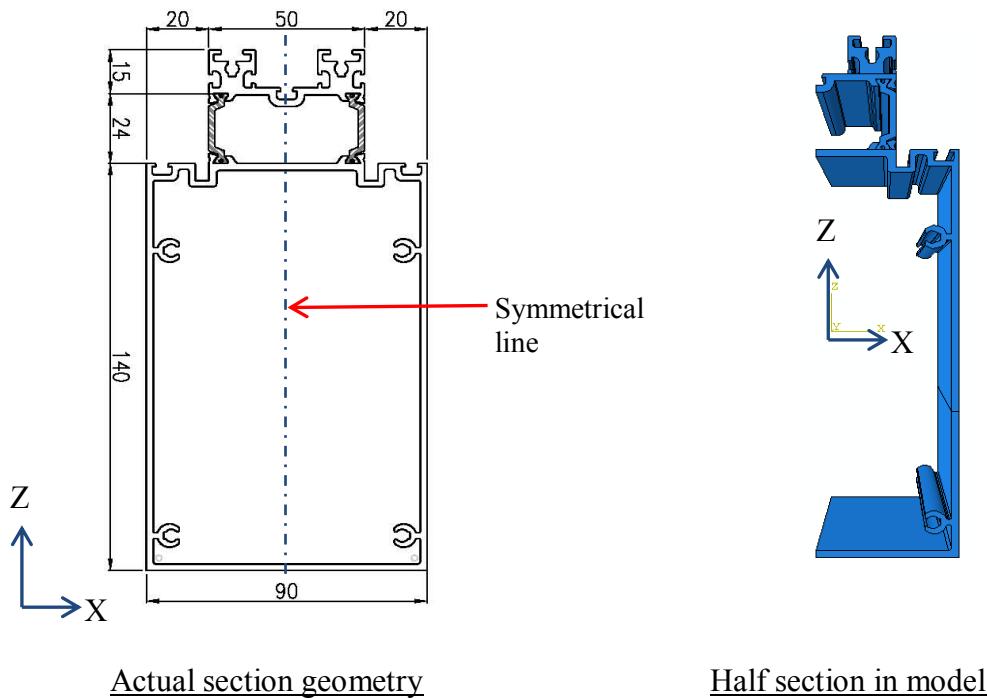


Figure 4.13 Section geometry details

The geometry of this half section was converted from an Autocad drawing file supplied by the manufacturer to a standard ACIS text file (SAT) and then imported into ABAQUS software. This section was imported as three separate parts and assembled together by position constraint tools.

Each part is 100mm long in length to match the test specimen and was imported as a deformable solid. The top small aluminium part (AL1) in Figure 4.14 was partitioned into several portions to allow boundary condition and load area assignment. Similarly, the bottom large aluminium part (AL2) in Figure 4.14 was partitioned into two portions for assigning the boundary condition. However, polyamide part (PA) was kept as one piece. Edge, face and cell partition toolsets were used to subdivide the parts. When

creating a partitioned cell, edge partition toolset was used to define the location of the cell. Details of the partition assignment are shown in Figure 4.14 below.

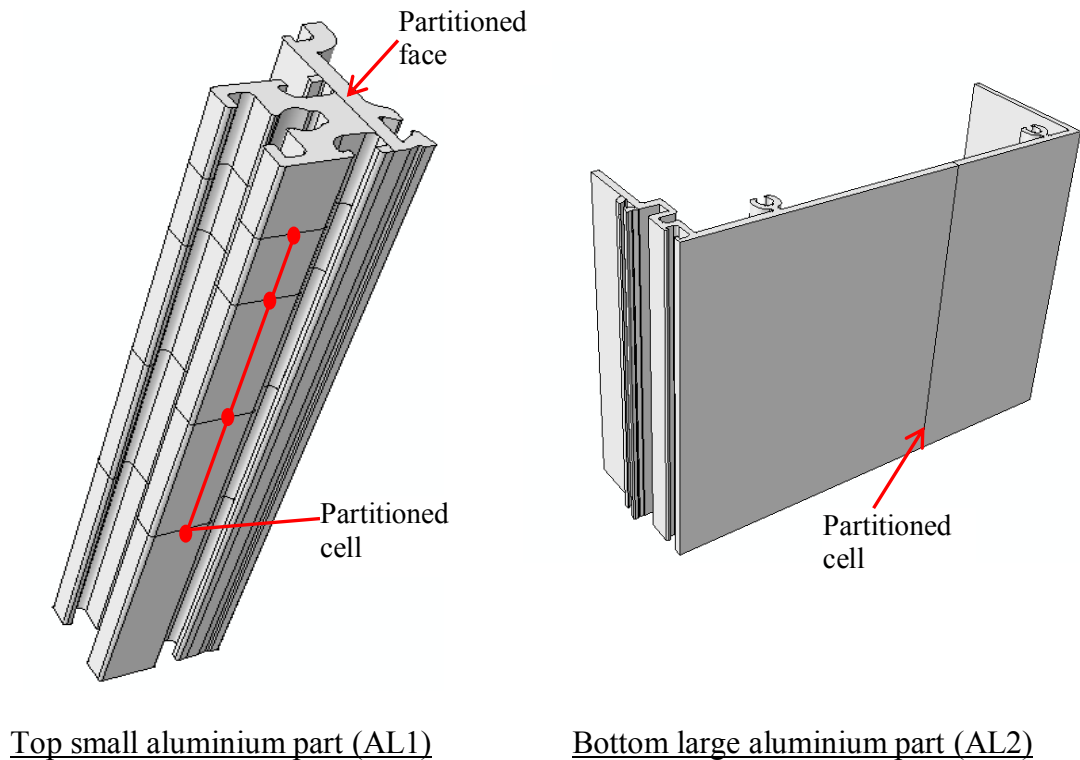


Figure 4.14 Partition assignment

Material property of aluminium alloy 6063T6 was assigned to top and bottom parts while 25% glass fibre reinforced polyamide PA66 was assigned to the middle part. Both elastic and plastic material properties of these two materials were defined in the model. For aluminium alloy, the Young's modulus, yield strength and ultimate strength was defined according to Section 4.2.1. As a ductile metal, the aluminium alloy is an isotropic material. Its stress-strain relationship was discussed in Section 4.2.1 and Ramberg-Osgood continuous model was adopted to define the plastic hardening stage. True stress and true plastic strain listed in Table 4.1 were input into ABAQUS model to define the material plasticity.

Since glass fibre reinforced polyamide PA66 is an orthotropic material, its property at longitudinal direction is different from the one at transverse direction. Meanwhile the simulation of shear test is to evaluate the connectivity between the interfaces of aluminium and polyamide, and hence material property of polyamide at transverse direction is assumed to be governing. To simplify the modelling, polyamide material is defined as an isotropic material with transverse material properties which was discussed

in Section 4.2.2. Stress-strain relationship shown in Figure 4.7 was input into the model to define the elasticity and plasticity of the material. Validity of the assumption will be discussed in next section when discussing results.

As discussed in Section 4.4, the mechanical contact property shall be assigned to tangential behaviour. Penalty friction formulation was chosen to apply to the interface in an isotropic direction. According to the proposed progressive failure model illustrated in Section 4.4, Figure 4.11 and Table 4.4, frictional coefficient was set at 0.3 at step1 and then gradually dropped to zero. Each loading step reflects each phase of progressive failure process shown in Figure 4.11.

“Surface to surface” discretization was assigned to the interaction between aluminium surface and polyamide surface. “Small sliding” tracking formulation was assigned for the tracking approach between the two contact bodies. Aluminium contact surface was assigned to “master” surface while polyamide surface was assigned to “slave” surface. The master and slave contact pairs are shown in Figure 4.15 below. Interference fit option was chosen to remove minor degree of overclosures between master and slave contact pairs when defining interactions.

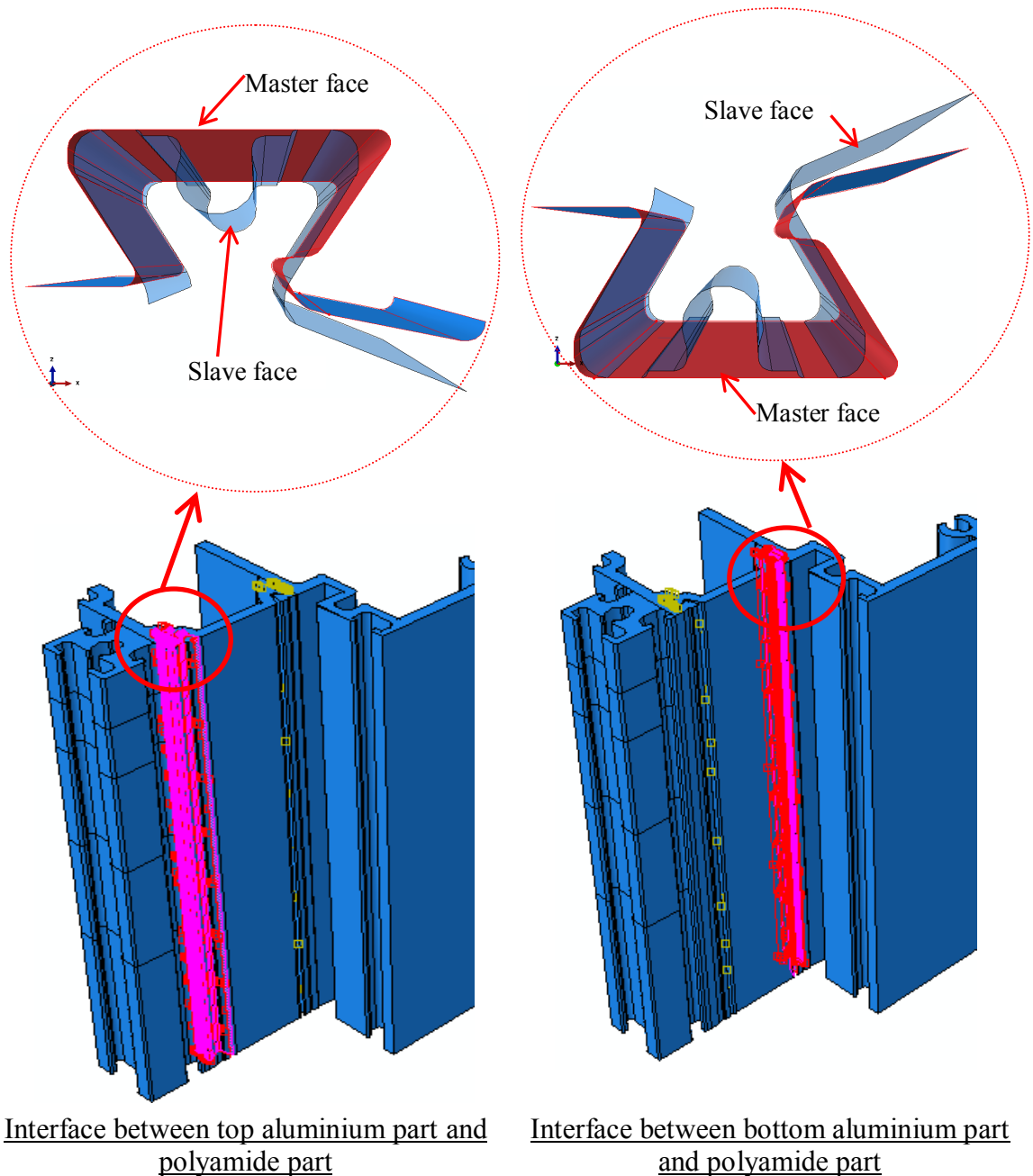


Figure 4.15 Master-slave assignment

Loading and boundary conditions were simulated to match test setup. As the tests were done to displacement control, displacement was applied instead of loading in the model. Loading was applied as a linear ramp up function in the step. During testing, the specimen was sitting on the supporting frame which was moved upwards with the test machine platform. To simulate this loading condition, displacement was applied to bottom 90mm length of the large aluminium portion (AL2) which was divided by cell partition.

Boundary conditions of fixed supports were applied at the top of the small aluminium portion (AL1) to simulate the load cell which was acting as a fixed support during

testing. Lateral restraint was provided 10.5mm below the top of AL1 in the length of 10.5mm. Since this façade section was cut along the symmetrical axis (Z-axis) in XZ plane, boundary condition of “XSYMM” shall be assigned to the regions which were cut along Z-axis (Systemes 2011a). Lateral restraints were also assigned to AL2 along the specimen height to prevent the movement in x-axis direction. Detailed loading and boundary conditions are shown below in Figure 4.16.

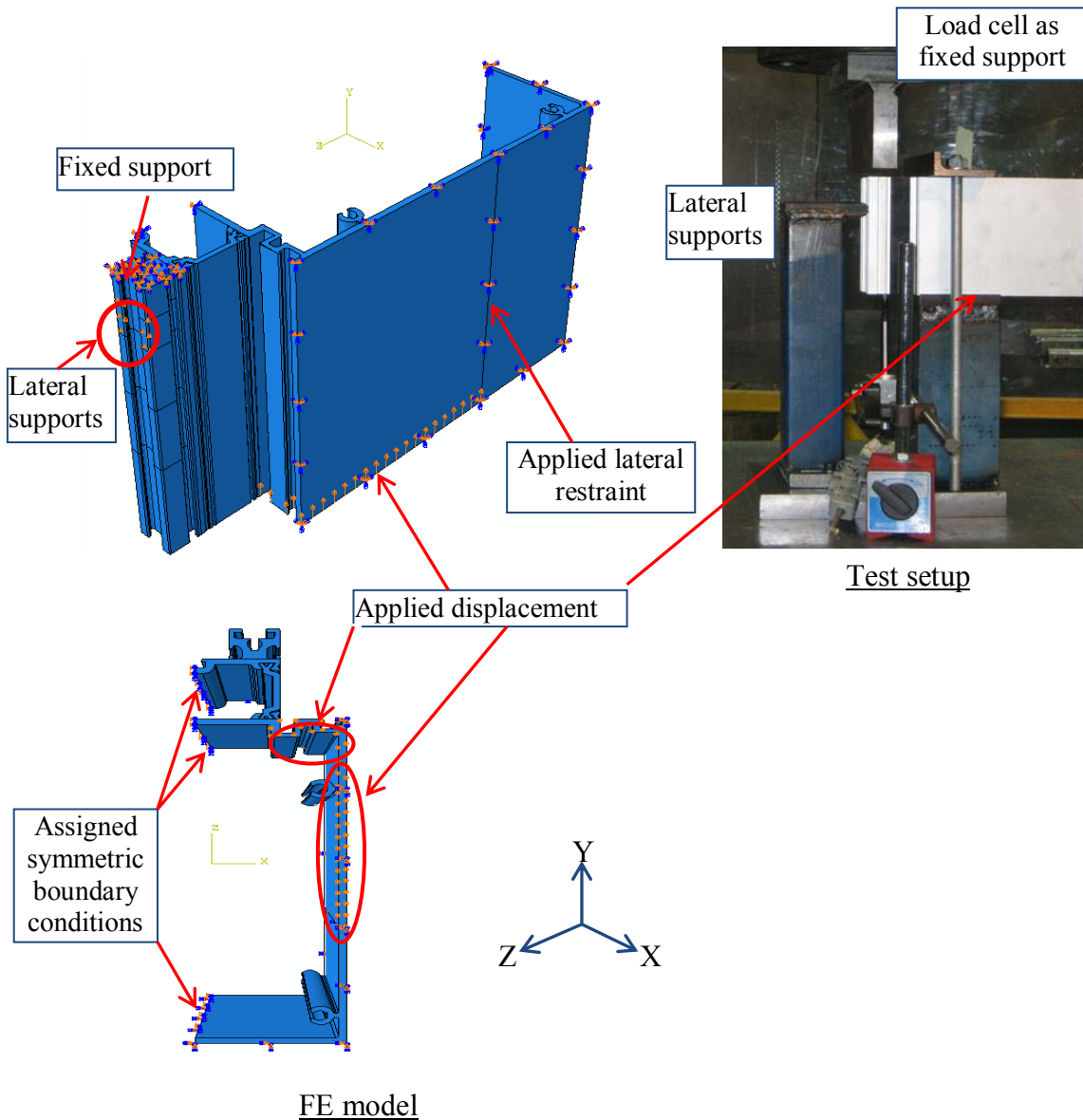


Figure 4.16 FE model details and comparison with test setup

The assignment of displacements was simulating the test process. The initial step represents the setup of the test. In step 1, displacement was assigned as 1.35mm. It was increased to 1.8mm in step 2 as slip was observed in the test and therefore friction coefficient was reduced to the value shown on Table 4.4. In step 3, a further increase of

the displacement to 2mm was assumed. Then, the displacement set in step 3 was propagated through step 4 and step 5.

This half section was then meshed by applying quadratic reduced integration solid element (C3D20R) to both aluminium parts and polyamide part as discussed in Section 4.3. Detailed mesh of all three parts is shown in figures below. This model was calculated by eight computer processors for two hours due to the complexity of its geometry and contact interactions.

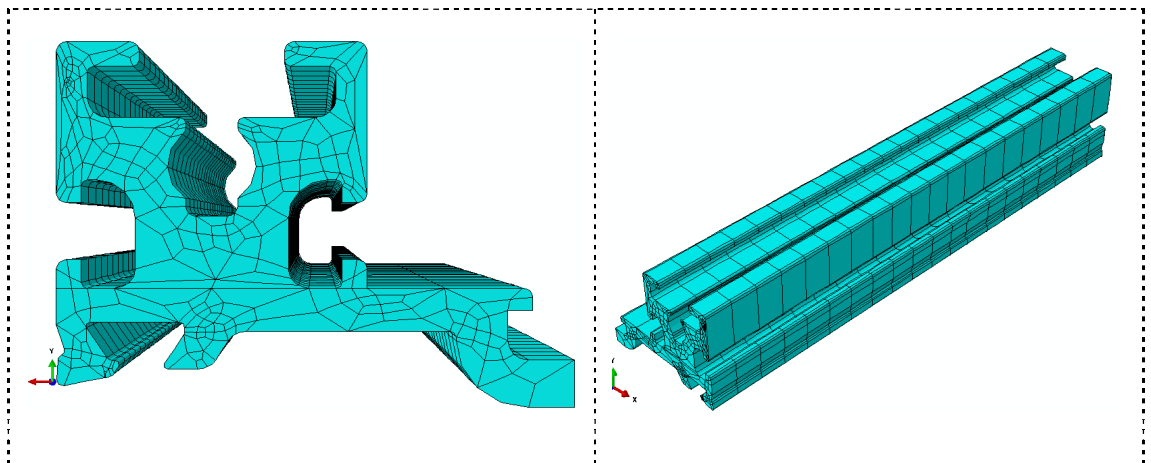


Figure 4.17 Mesh assignment of part 1 (AL1) from different view angles

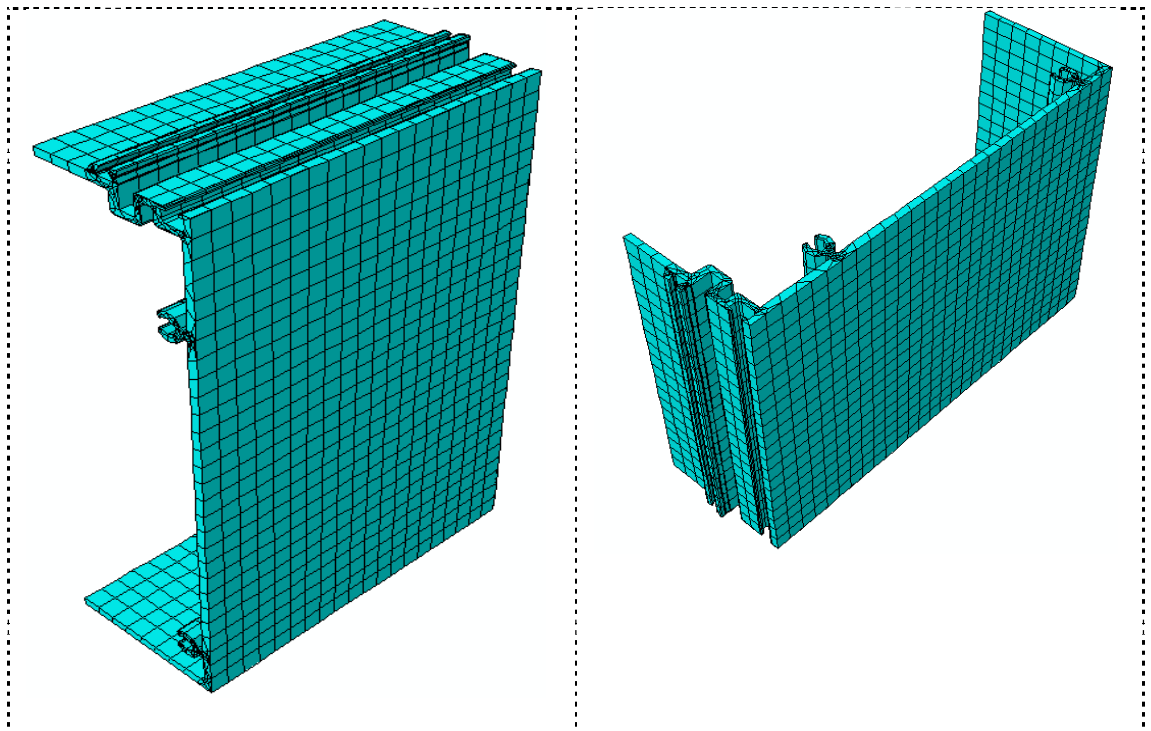


Figure 4.18 Mesh assignment of part 2 (AL2) from different view angles

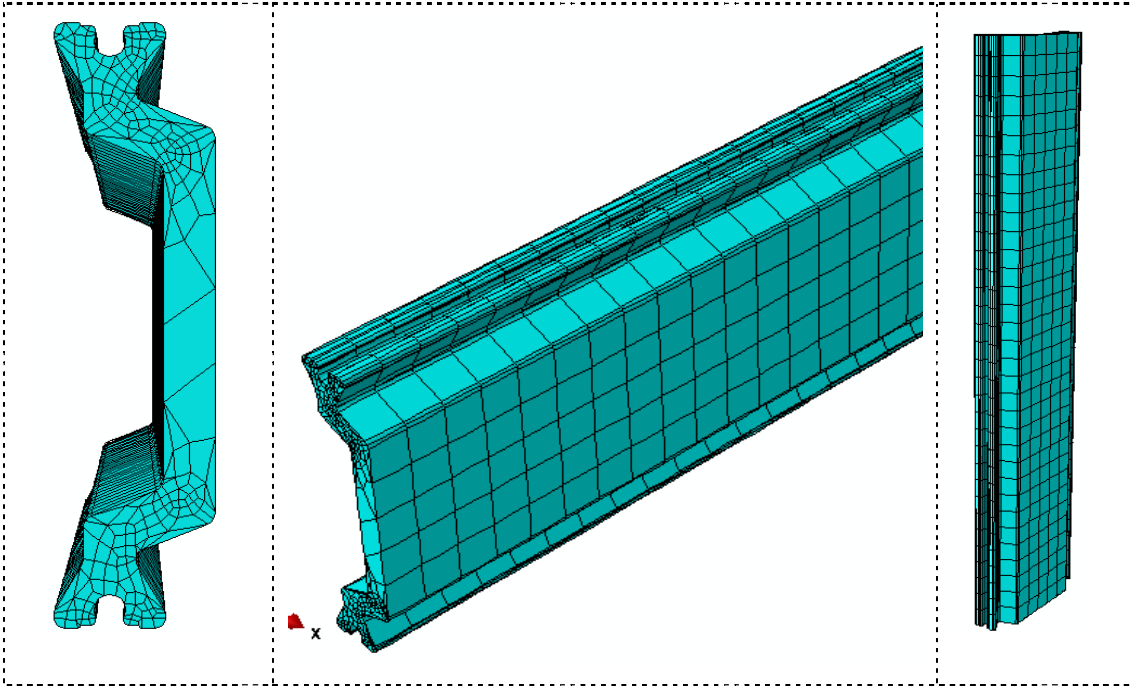


Figure 4.19 Mesh assignment of part 3 (PA) from different view angles

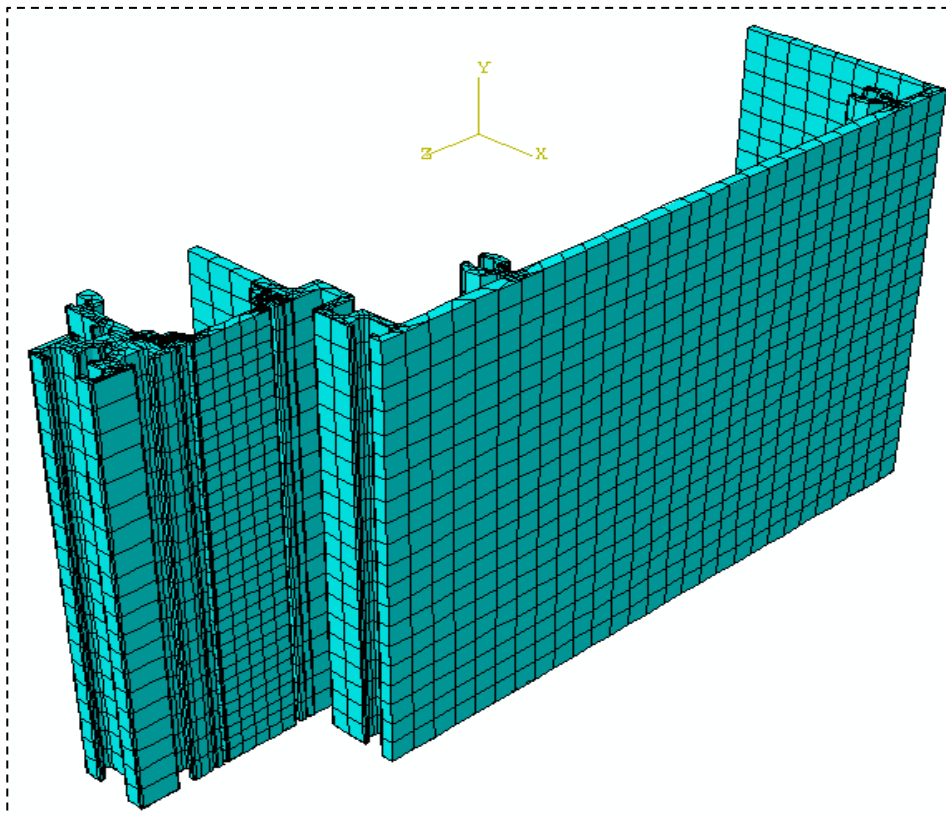


Figure 4.20 Mesh assignment of the assembled whole section

4.5.2 Typical results

The FE model shows the connection between aluminium and polyamide fails. The polyamide insert slipped away. The deformed shape of FE model is shown in Figure 4.21 below.

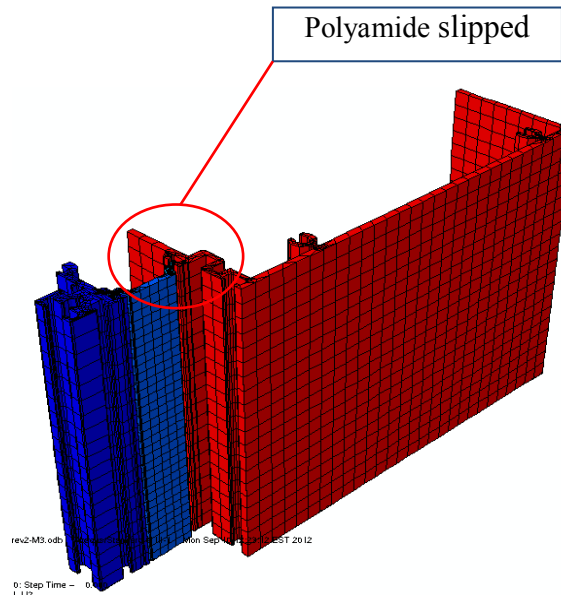


Figure 4.21 Deformed shape

The contact shear stresses along the direction of applied displacement at selected analysis steps are shown in Table 4.5 and Table 4.6. The maximum shear stresses occur at the overlapped zone at both aluminium and polyamide contact surfaces at top and bottom connections. The contact stresses at top connection started at 9.2MPa at aluminium interface and 5.5MPa at polyamide in the beginning of loading. Similarly, the contact stresses at bottom connection started at 7.4MPa at aluminium interface and 5.3MPa at polyamide interface. They then increased to 55.3MPa and 37.1MPa at the end of step 1 for AL and PA interface at top connection, respectively, while they were at 53.1MPa at bottom aluminium interface and 19.9MPa at bottom polyamide interface. Displacement was at 1.35mm. As slip occurred, the contact shear stresses started to drop. They were recorded at 48.7MPa and 32.5MPa for AL and PA at top connection in the middle of step 2 and corresponding displacement was increased to 1.95mm. At the same time, the contact stresses at bottom aluminium interface was 39.9MPa and 25.5MPa at bottom polyamide interface. The contact stresses continued to drop to 42.6MPa at top aluminium interface and 28.0MPa at top polyamide interface at the end of step 2 until zero while the slip increases. In terms of the bottom connection, contact

stresses at AL interface were 32.7MPa and 19.9MPa at PA interface at the end of step 2. It also continued to decrease to zero at the end of calculation.

Table 4.5 Contact shear stresses at top connection

Analysis steps	Contact shear in aluminium (MPa)	Contact shear in polyamide (MPa)
Step 1 – increment 1 T=0.1s		
Step 1 – increment 8 T=1s		
Step 2 – increment 4 T=0.575s		
Step 2 – increment 6 T=1s		

Table 4.6 Contact shear stresses at bottom connection

Analysis steps	Contact shear in aluminium (MPa)	Contact shear in polyamide (MPa)
Step 1 – increment 1 T=0.1s	<p>CSHEAR2</p> <ul style="list-style-type: none"> +7.409e+00 +6.505e+00 +5.602e+00 +4.698e+00 +3.794e+00 +2.890e+00 +1.987e+00 +1.083e+00 +1.791e-01 -7.247e-01 -1.628e+00 -2.532e+00 -3.436e+00 	<p>CSHEAR2</p> <ul style="list-style-type: none"> +5.301e+00 +4.117e+00 +2.932e+00 +1.748e+00 +5.637e-01 -6.205e-01 -1.805e+00 -2.989e+00 -4.173e+00 -5.358e+00 -6.542e+00 -7.726e+00 -8.910e+00
Step 1 – increment 8 T=1s	<p>CSHEAR2</p> <ul style="list-style-type: none"> +5.313e+01 +4.598e+01 +3.883e+01 +3.168e+01 +2.453e+01 +1.738e+01 +1.023e+01 +3.085e+00 -4.063e+00 -1.121e+01 -1.836e+01 -2.551e+01 -3.266e+01 	<p>CSHEAR2</p> <ul style="list-style-type: none"> +1.994e+01 +1.672e+01 +1.349e+01 +1.027e+01 +7.053e+00 +3.832e+00 +6.105e-01 -2.611e+00 -5.832e+00 -9.053e+00 -1.227e+01 -1.549e+01 -1.872e+01
Step 2 – increment 4 T=0.575s	<p>CSHEAR2</p> <ul style="list-style-type: none"> +3.996e+01 +3.488e+01 +2.981e+01 +2.473e+01 +1.966e+01 +1.459e+01 +9.511e+00 +4.437e+00 -6.376e-01 -5.712e+00 -1.079e+01 -1.586e+01 -2.094e+01 	<p>CSHEAR2</p> <ul style="list-style-type: none"> +2.553e+01 +2.088e+01 +1.623e+01 +1.158e+01 +6.934e+00 +2.284e+00 -2.365e+00 -7.014e+00 -1.166e+01 -1.631e+01 -2.096e+01 -2.561e+01 -3.026e+01
Step 2 – increment 6 T=1s	<p>CSHEAR2</p> <ul style="list-style-type: none"> +3.265e+01 +2.873e+01 +2.482e+01 +2.091e+01 +1.699e+01 +1.308e+01 +9.164e+00 +5.250e+00 +1.337e+00 -2.577e+00 -6.491e+00 -1.040e+01 -1.432e+01 	<p>CSHEAR2</p> <ul style="list-style-type: none"> +1.994e+01 +1.672e+01 +1.349e+01 +1.027e+01 +7.053e+00 +3.832e+00 +6.105e-01 -2.611e+00 -5.832e+00 -9.053e+00 -1.227e+01 -1.549e+01 -1.872e+01

Load versus slippage of connection is plotted in Figure 4.22.

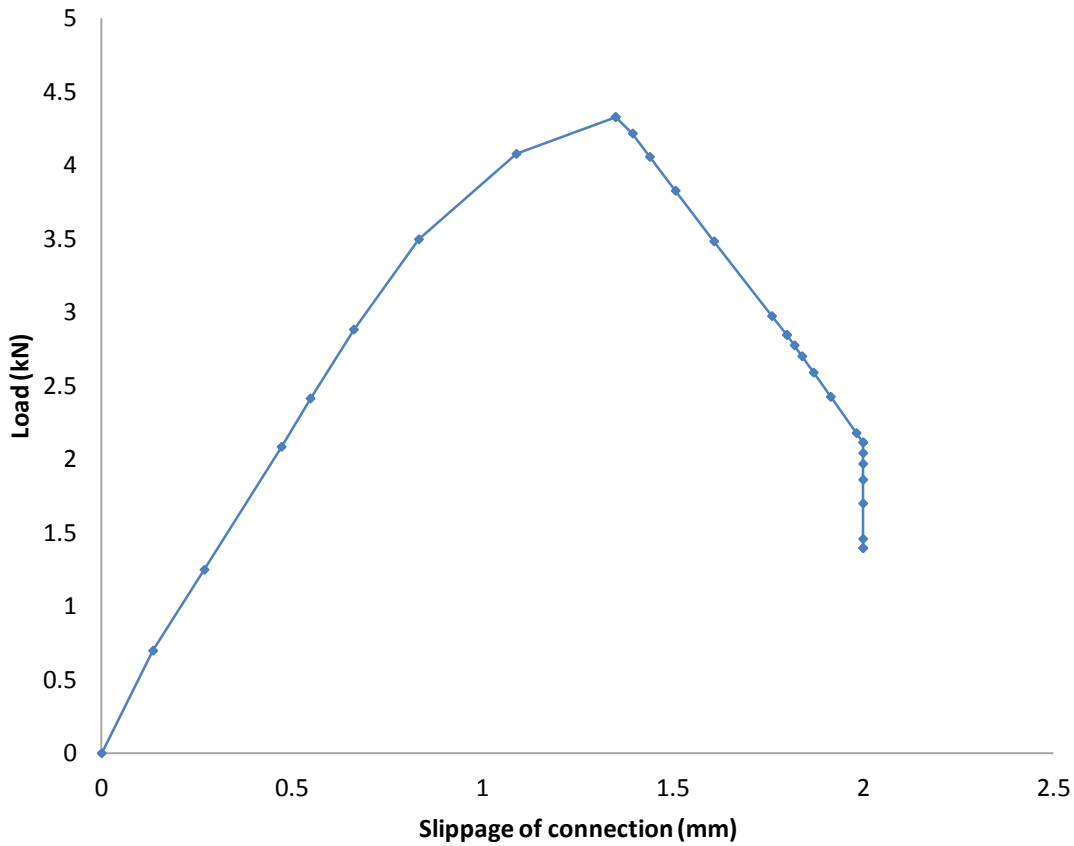


Figure 4.22 Load vs slippage of connection from FE model

Normal stresses are also studied to understand the stress distribution at the sections cut along the length of the model. Normal stress distributions at longitudinal direction of polyamide material (2-axis) and transverse direction of polyamide part (3-axis) at the end of Phase I (step 1) show stresses at both directions are almost evenly distributed along the length. From the stress distribution diagrams, it can be seen that the stresses at transverse direction of polyamide (66.6MPa) is about 10 times larger than the stresses at longitudinal direction of polyamide (6.6MPa).

This confirmed the assumption of material properties of polyamide at transverse direction dominating the behaviour of the section under shear. Therefore, the simplification of applying material properties at transverse direction in isotropic case is justified. The comparison of stresses at longitudinal and transverse directions at maximum loading is given in the figure below.

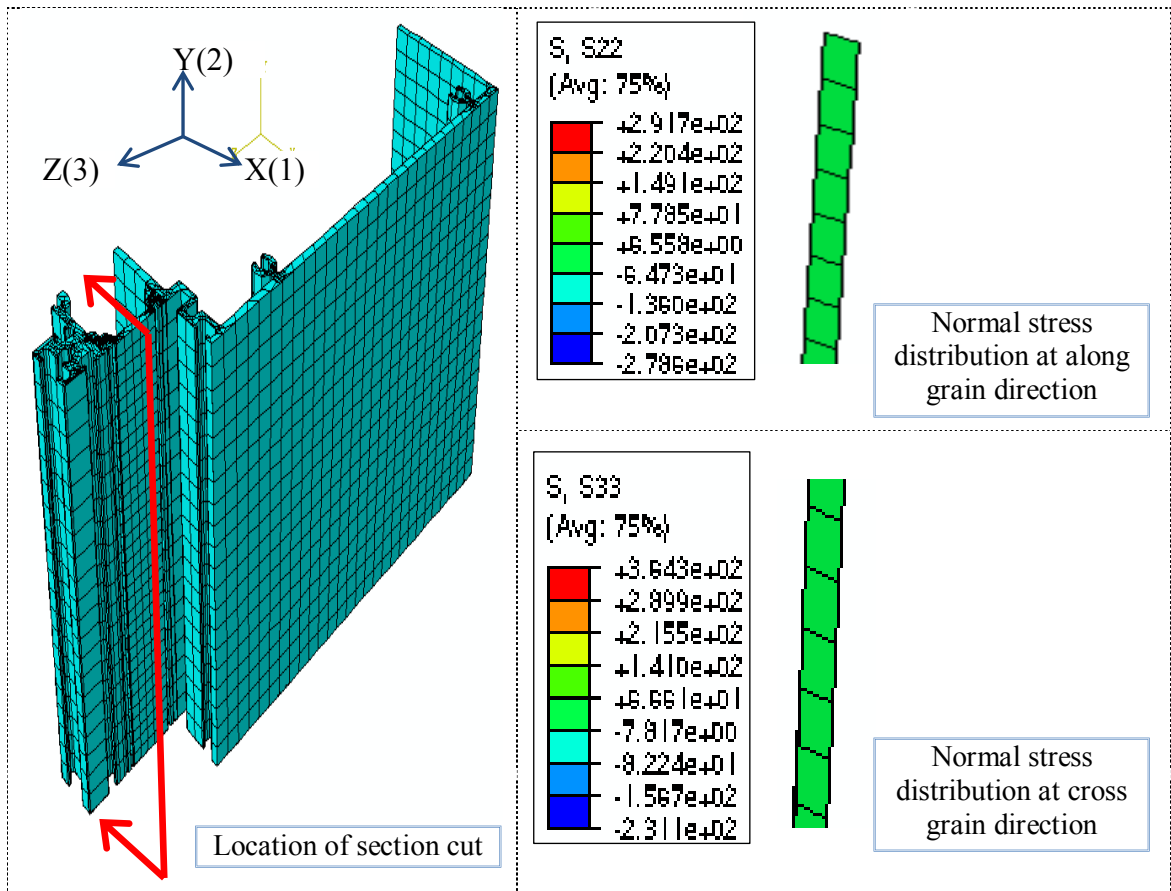


Figure 4.23 Comparison of Stresses at along and cross direction at maximum loading

In summary, the deformed shape generated by FE model shows the failure of connection – polyamide slipped. The contact stresses in both aluminium and polyamide increase with the loading. Once slippage occurred, the stresses started to drop gradually and finally reached zero when connection failed. This reflects the assumption of the proposed progressive failure model. Stress distributions shown on the cut section at polyamide confirmed that the material properties at transverse direction of polyamide dominate the behaviour and the simplified material model of polyamide is valid.

4.6 Numerical investigation of section transverse tensile capacity

4.6.1 Model setup

To simulate the tensile tests at room temperature, a 3D FE model was established by using ABAQUS software. Section symmetry was utilized similar to shear model. Section was cut along the symmetrical axis into half according to Figure 4.13. Geometry of half section with 100mm in length was adopted in the model.

Same ACIS file of the half section used in shear model was imported into ABAQUS software. This section was imported as three separate parts as well. Each part was defined as deformable solid. The section was then assembled by applying position constraint to join the three parts together. The top small aluminium part is named AL1 while the bottom large aluminium part is called AL2. The polyamide part is named PA. To be able to model the bending deformation at the shoulder of the bottom aluminium part, the meshes at this area need to be refined. To refine the mesh at AL2, this aluminium part was partitioned by edge and cell partition toolsets. Details of the partition assignment are shown in Figure 4.24 below. However, AL1 and PA parts were kept as one single region.

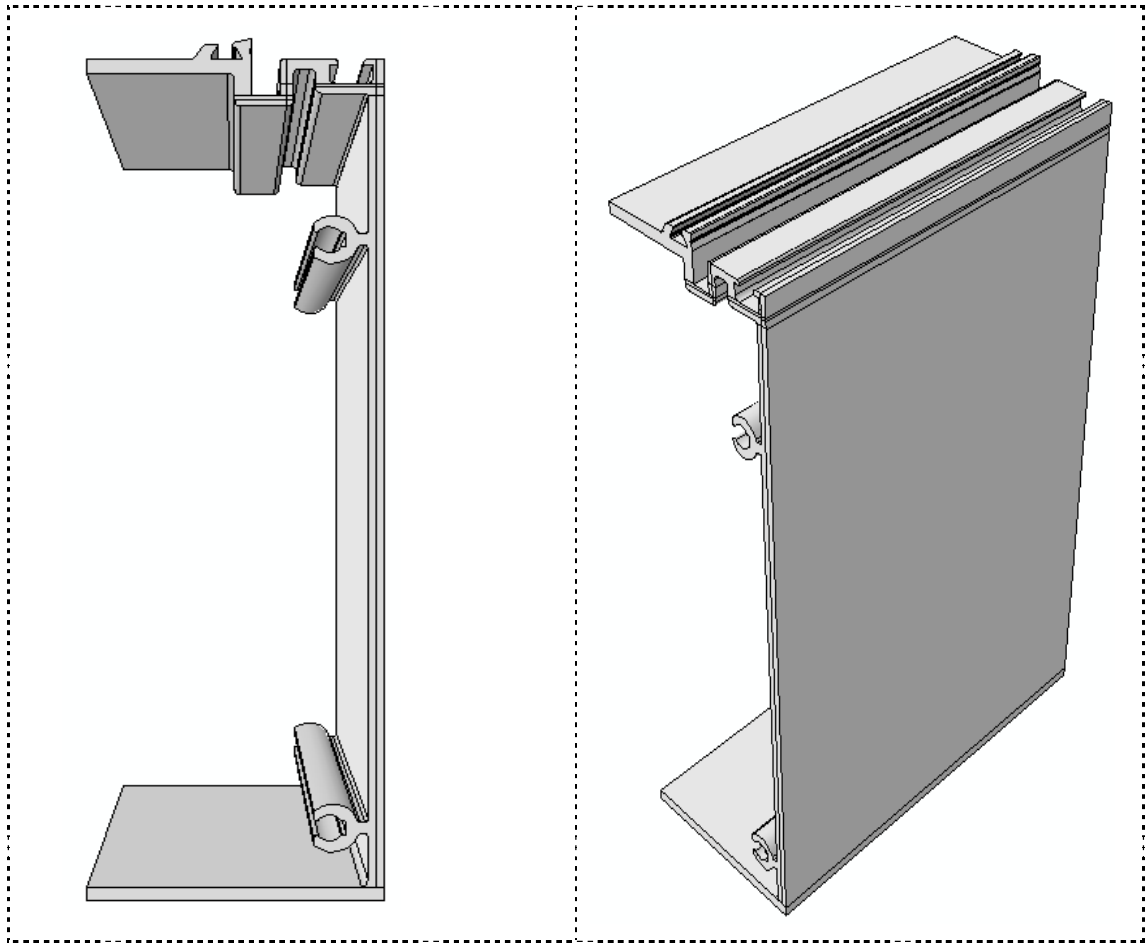


Figure 4.24 Partition assignments of AL2 in front and side views

Material properties of aluminium discussed in Section 4.2.1 was adopted in the model for both elastic and plastic stages. Ramberg-Osgood continuous model was assigned to represent the aluminium plastic hardening stage. True stress and true plastic strain listed in Table 4.1 were input into the software to define the material plasticity. Aluminium was defined as an isotropic material.

For defining the material property of glass-fibre reinforced polyamide PA66, similar approach was adopted as mentioned in Section 4.5.1. Material properties at longitudinal direction were ignored as it is perpendicular to the loading direction which is assumed to have minimum influence on the overall behaviour. The polyamide material properties at transverse direction are governing the tensile capacity. To simplify the model, polyamide is defined as an isotropic material with material properties at transverse direction. This assumption will be verified by the results from the model. True stress and true strain relationship discussed in Section 4.2.2 Figure 4.7 was input into ABAQUS model to define the elastic and plastic material properties.

Similar to the shear test model, the interaction between the aluminium and polyamide was assigned as tangential behaviour. Penalty friction formulation was chosen to apply to the interface in an isotropic direction. The failure modes of the laboratory tests show the polyamide was either pulled away from the connection or torn apart. There was no slippage of the polyamide from the connection observed in all tensile tests. Progressive failure mechanism, therefore, is not suitable in this situation. Since the tensile tests exhibited different behaviour from shear tests, values of friction co-efficient used in the shear model are not relevant. After manual model updating, friction co-efficient μ of 0.9 was adopted in the tension model.

However, “surface to surface” discretization was assigned to the interfaces of aluminium and polyamide. “Small sliding” tracking formulation was again assigned for the tracking approach between the two contact bodies as the shear model. As discussed in Section 4.4, aluminium contact surface was assigned to “master” surface and polyamide contact surface was assigned to “slave” surface. Same master-slave surfaces shown in Figure 4.15 were assigned in this tensile model. The façade section was assembled in different orientation as shown in figure below with contact surfaces highlighted.

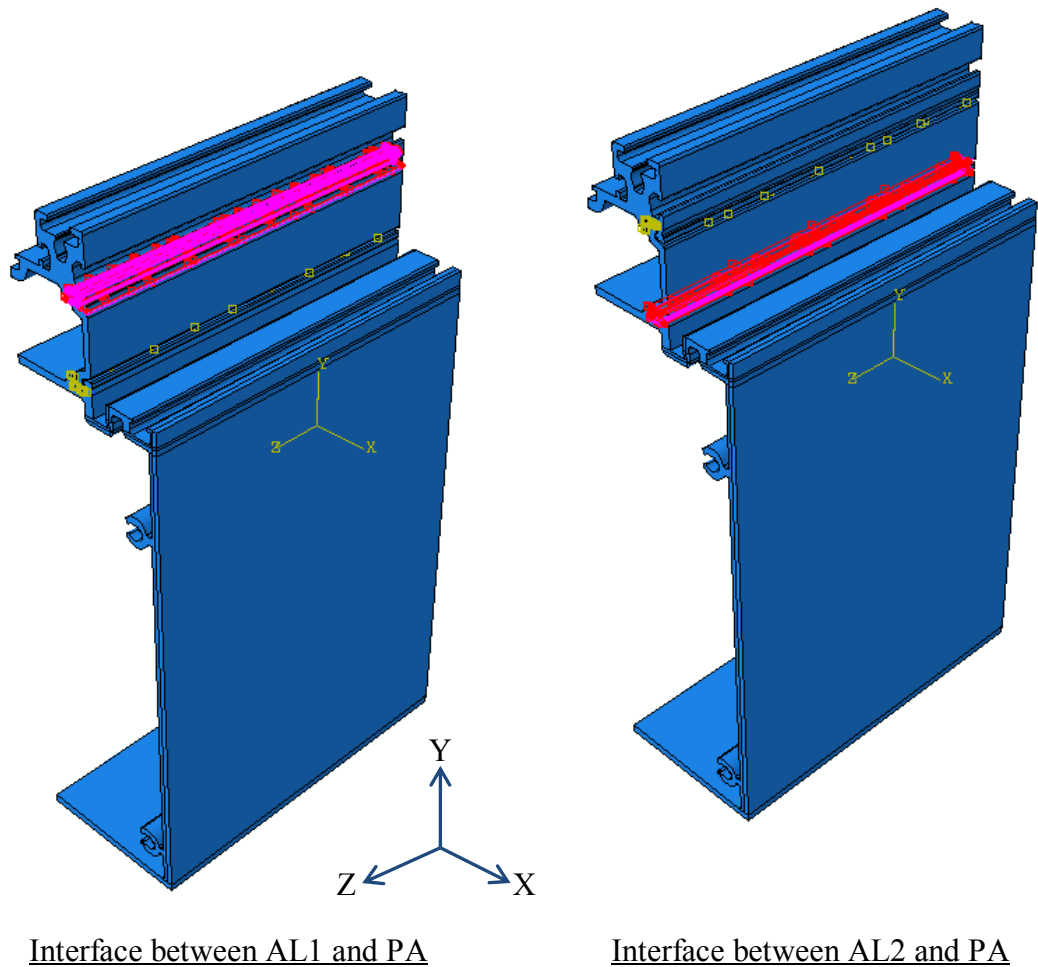
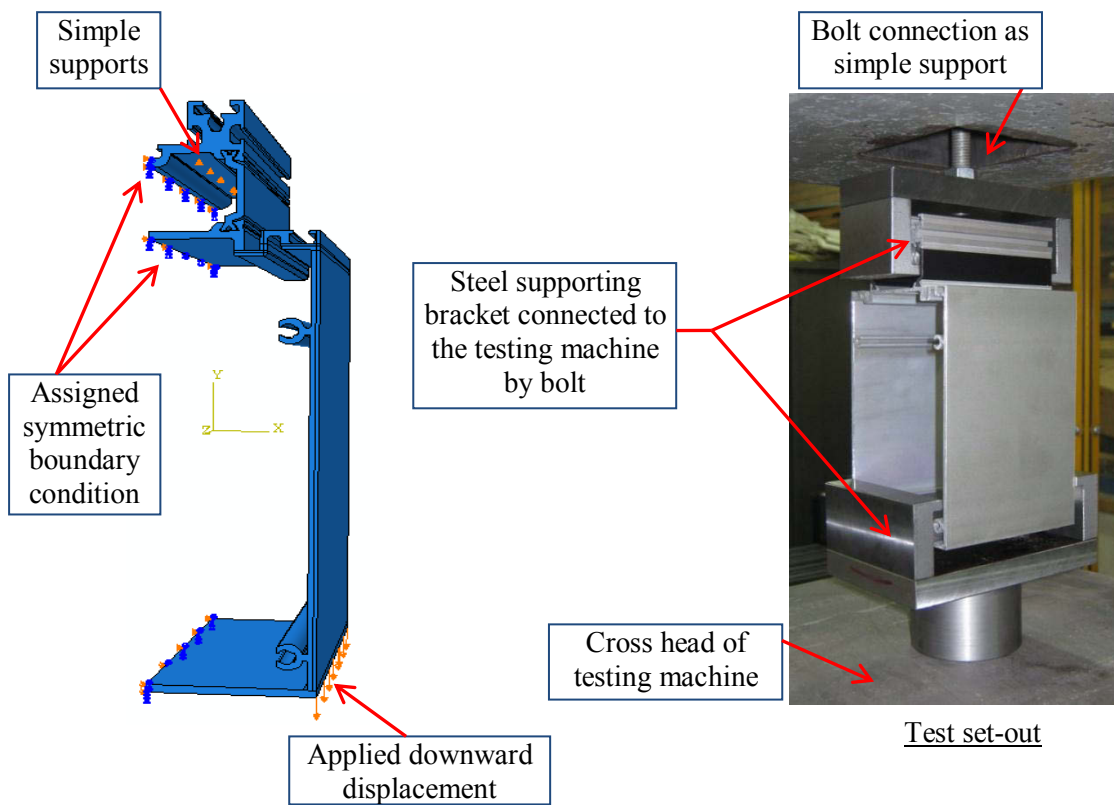


Figure 4.25 Interaction assignment

To simulate the displacement control of loading method during test, displacement was applied instead of applying load onto the section. Since the specimen was supported by the testing machine through steel brackets and bolt connections which were tied in y-axis, simple support was assumed to restrain the specimen at the top aluminium portion only along y-axis at the centre of AL1. Displacement along y-axis was applied at the bottom of the aluminium portion to pull the section down to allow consistency with the test machine movement. Based on the test results, the displacement was assigned to be 32mm in the loading step. Symmetric boundary condition was assigned to this half section to simulate the full section behaviour. “XSYMM” was assigned to the regions along the symmetrical axis. Detailed model setup comparing with the test setup is shown in Figure 4.26 below.



FE model set-out

Figure 4.26 FE model setup details and comparison with test setup

Fine meshes of seed 5 were used to mesh the aluminium portions in the model while finer meshes of seed 3 were adopted to mesh the polyamide portion as determined in Section 4.3. The deformation presented in the tensile tests is not the pure tensile deformation, it includes bending deformation as well. Hex dominated quadratic reduced integration elements (C3D20R) were assigned to model all three parts. Details of the mesh are shown in figures below. Similar to the shear model, the tensile model also required eight computer processors and the calculation lasted more than two hours.

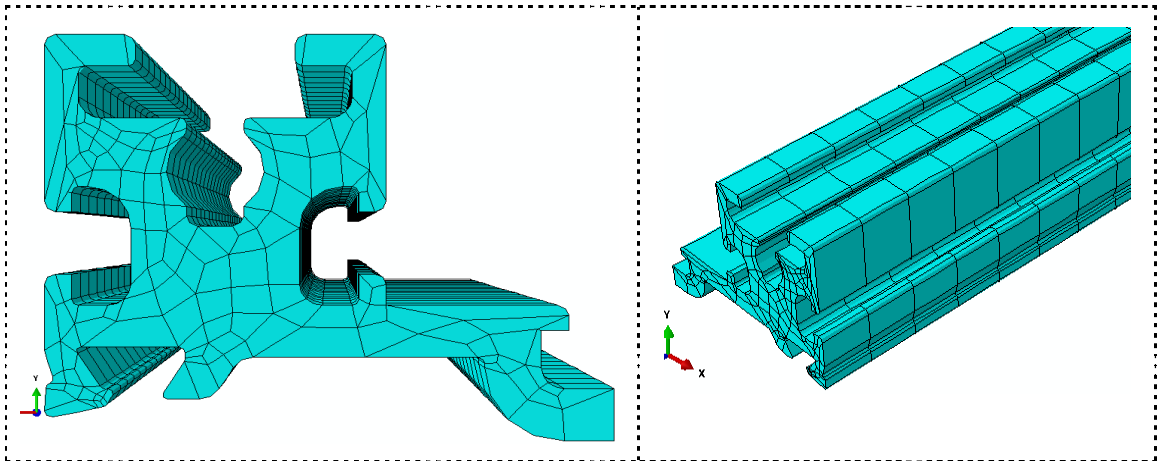


Figure 4.27 Mesh assignment of part 1 (AL1) from different view angles

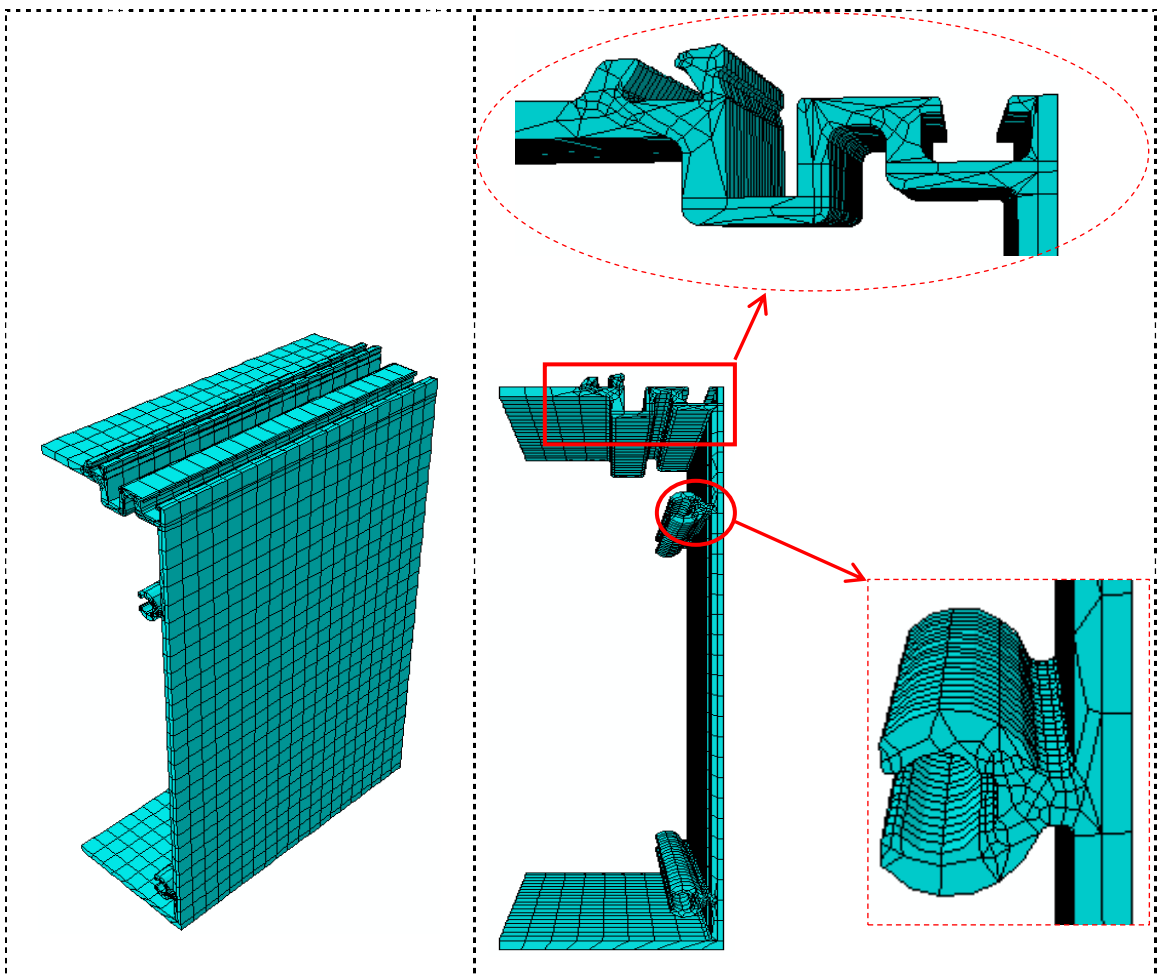


Figure 4.28 Mesh assignment of part 2 (AL2) from different view angles

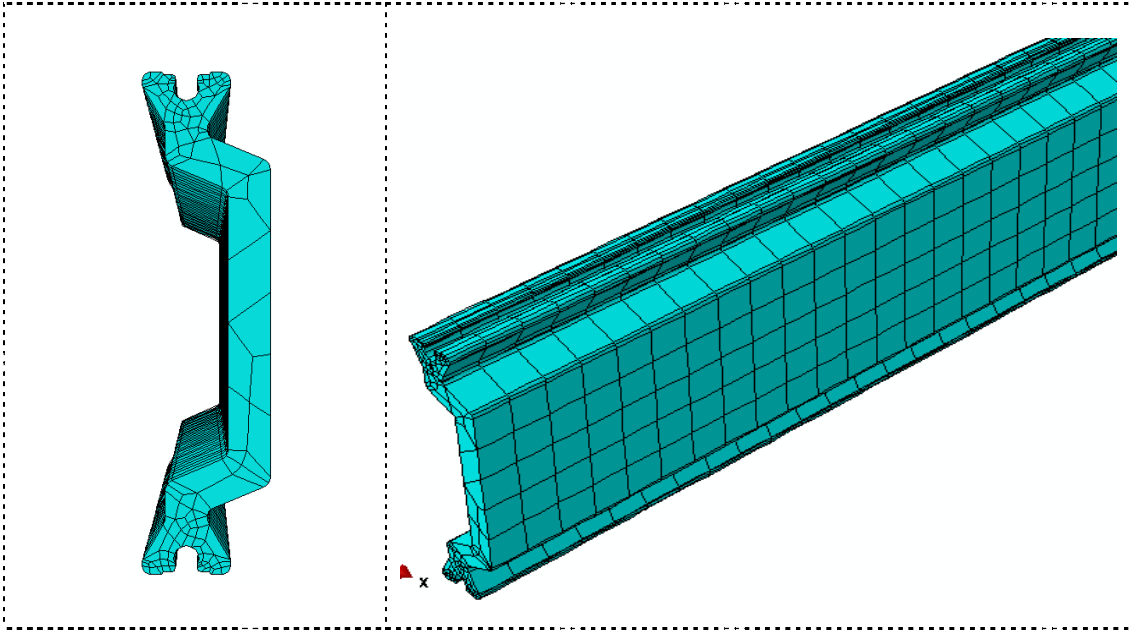


Figure 4.29 Mesh assignment of part 3 (PA) from different view angles

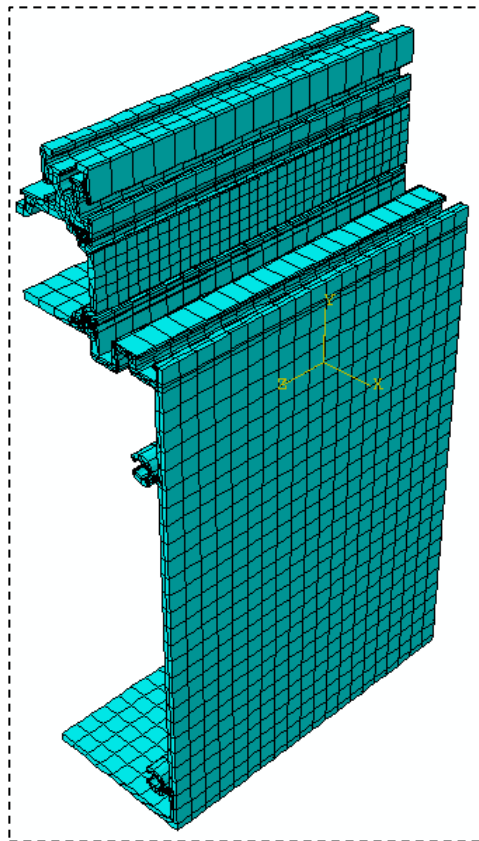


Figure 4.30 Mesh assignment of the assembled whole section

4.6.2 Typical results

The deformed shape of FE model shows the shoulder of AL2 went through not only tensile deformation but also bending deformation. The shoulder of the section went through mainly bending deformation and rotated 60° approximately to almost vertical. The profile of the shoulder portion was either pulled open or pressed closed. The stress distribution at this portion is complicated and worth investigation. The top aluminium AL1 was rotated upwards around the top connection. The polyamide was deformed as well. The deformed shape is shown in Figure 4.31 below and load vs displacement graph is plotted in Figure 4.32.

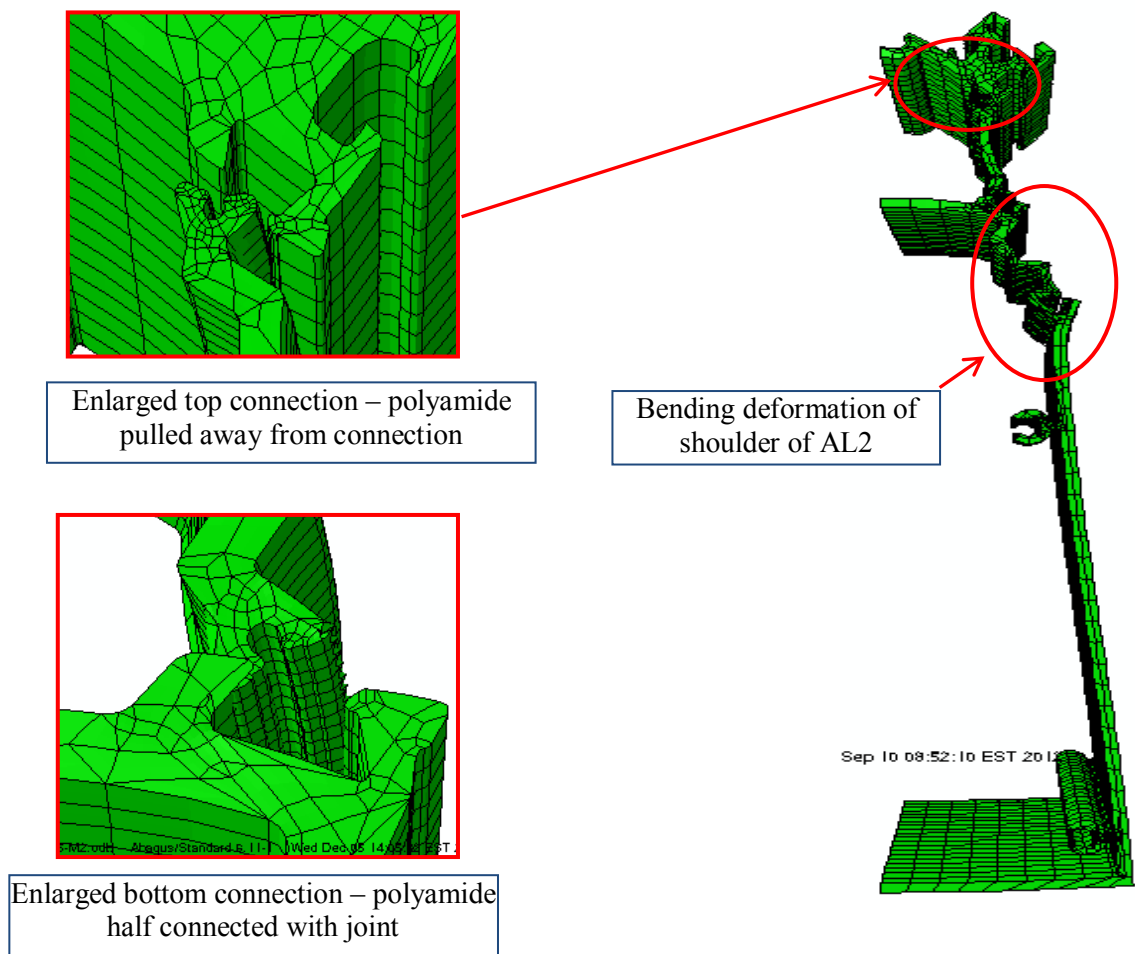


Figure 4.31 Deformed shape

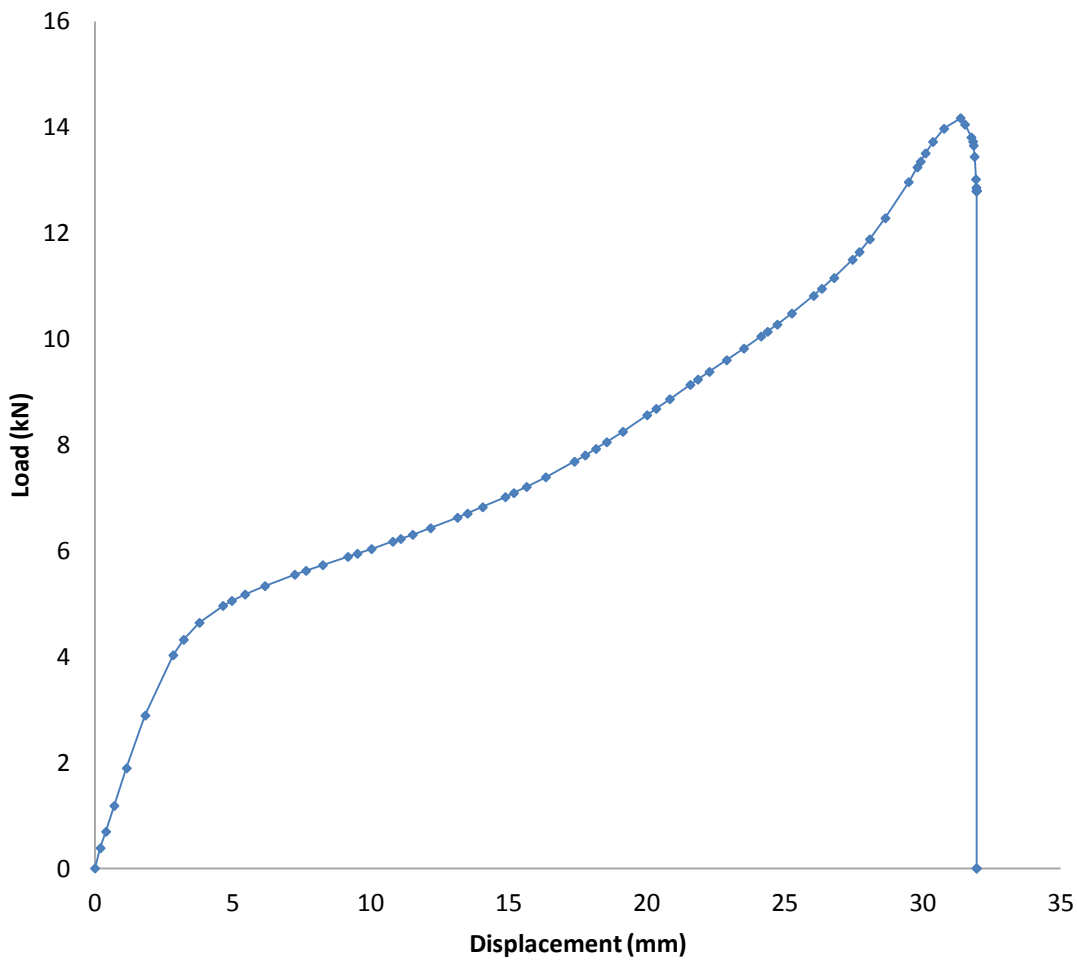


Figure 4.32 Load vs displacement from FE model

Normal stress along Y-axis (loading direction) at the whole half section is plotted at the end of loading step in Figure 4.33 below. To understand stress distribution along the cross section, stress plot at each section cut is presented next to the stress plot of whole section. Section 1 is cutting through the top aluminium part. Section 2 is cutting through the connection between top aluminium part and polyamide insert. Section 3 is cutting at middle of polyamide insert. Section 4 is cutting through the connection between bottom aluminium part and polyamide. Sections 5 to 8 are cutting through the shoulder portion of bottom aluminium which went through bending deformation as well as tensile deformation. The last cut – section 9 is cutting through the web of bottom aluminium part. To be able to find out the dominant stress direction, normal stresses at X and Z axes are also shown in the stress plot for each section defined in Figure 4.34.

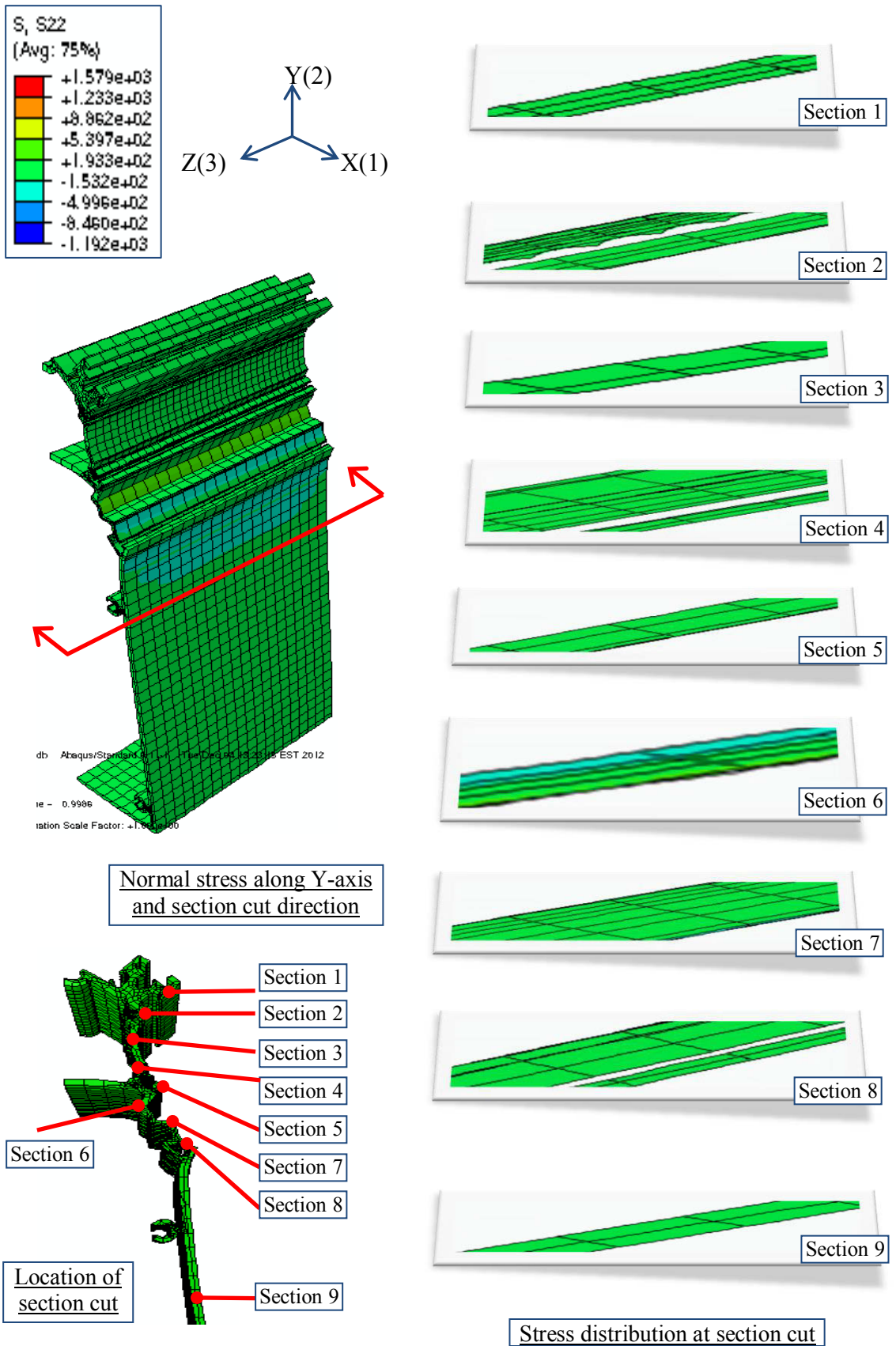


Figure 4.33 Normal stress plot along Y-axis



Figure 4.34 Normal stress plot along X and Z axis

The above stress plots have confirmed uniform stress distribution across the length of model at each section cut in all three directions. Along Y-axis direction (loading direction), the stress varies from 540 MPa in tension to 153 MPa in compression between all section cuts. Along Z-axis direction, the stress varies from 450 MPa in tension to 251 MPa in compression between all section cuts. Along X-axis direction, the stress varies from 431 MPa in tension to 317 MPa in compression between all section cuts. The larger stress along loading direction than other directions indicates the façade section is mainly deformed under axial loads. However, stresses at X-axis reflect the bending behaviour which is significant enough not to be ignored. The bending deformation associated with bending stresses was observed during laboratory testing. This confirms the quadratic element with reduced integration (C3D20R) selected for aluminium parts is appropriate.

The stresses at section 3 which lies in the middle of polyamide part vary at all three directions. The stress along X-axis direction is 57 MPa approximately. The stress along Y-axis direction (at transverse direction of polyamide) is 193 MPa approximately while the stress along Z-axis (longitudinal direction of polyamide) is only 99 MPa approximately. The stress at transverse direction of polyamide is almost double the stress at longitudinal direction. It, therefore, confirms the assumption made to simplify the polyamide material properties is valid.

In conclusion, the deformed shape shows not only tensile deformation but also bending deformation especially at the shoulder of the section. At failure, the polyamide insert was completely pulled out of the top connection while remaining semi-connected to the aluminium at bottom connection. Normal stresses at all three directions were plotted at sections cutting along the height of whole cross-section. Stresses at polyamide transverse direction, which is along the loading direction, dominate the other two directions. However, bending stresses across the thickness of the cross-section are also significant. They indicated the whole section exhibited bending behaviour as well as the governing tensile behaviour. For polyamide insert, the stresses at transverse direction are much larger than the stresses at longitudinal direction. This confirmed the assumption made to simplify the material properties of polyamide as applying transverse material properties to the whole part is relevant.

4.7 Numerical investigation of façade beam in four point bending

4.7.1 FE Model setup – model geometry, boundary conditions and mesh assignment

Façade mullion is a major load bearing element running vertically supporting glass panels. It works as a simply supported beam resisting wind, earthquake and thermal loads, etc. These loads are generally acting as uniformly distributed loads. They generate bending and shear forces on the façade beam.

In this study, the façade beam is investigated considering four-point bending behaviour. Since four-point bending provides not only bending/shear combined behaviour but also pure bending behaviour at middle of the span, this loading pattern explores different loading situations for a beam model. However, a simply supported beam under uniformly distributed loads can only offer bending/shear combined behaviour. Therefore, the four-point bending was chosen for the experimental works as mentioned before.

As this façade mullion section is a composite section, the interactions between the contact bodies are complicated. The connectivity created during manufacturing process adds uncertainty onto the complexity.

To understand the behaviour of the façade beam further, FE models were setup to simulate the laboratory four-point bending tests. Four FE models were created by using ABAQUS software to represent the different length specimens tested.

As mentioned in the previous sections regarding simulating shear and tensile tests, the 100mm long solid model required more than two hours to analyse. The extensive calculation time required is mainly due to the complex profile details of the section. When the length of the model increases by 25 to 40 times, the computation time will increase accordingly. In addition, unlike the section capacities, the aluminium profile details contribute little to the global bending behaviour of the façade beam. It is therefore necessary to simplify the section geometry and reduce computational cost. Since the four point bending behaviour largely relates to the geometry of cross section and neutral axis of the beam as well as the contact interactions, the profile details make minimum contribution. The top and bottom aluminium parts were modified slightly to have minimum change of neutral axis location. As the interaction is based on the contact surface, therefore, the geometry of the contact interface shall be maintained as

the actual shape to reflect the true interface behaviour. To eliminate unnecessary calculations, section symmetry was utilized. Simplified section was cut in half along the symmetrical axis and analysed. The simplified section is shown in the figure below.

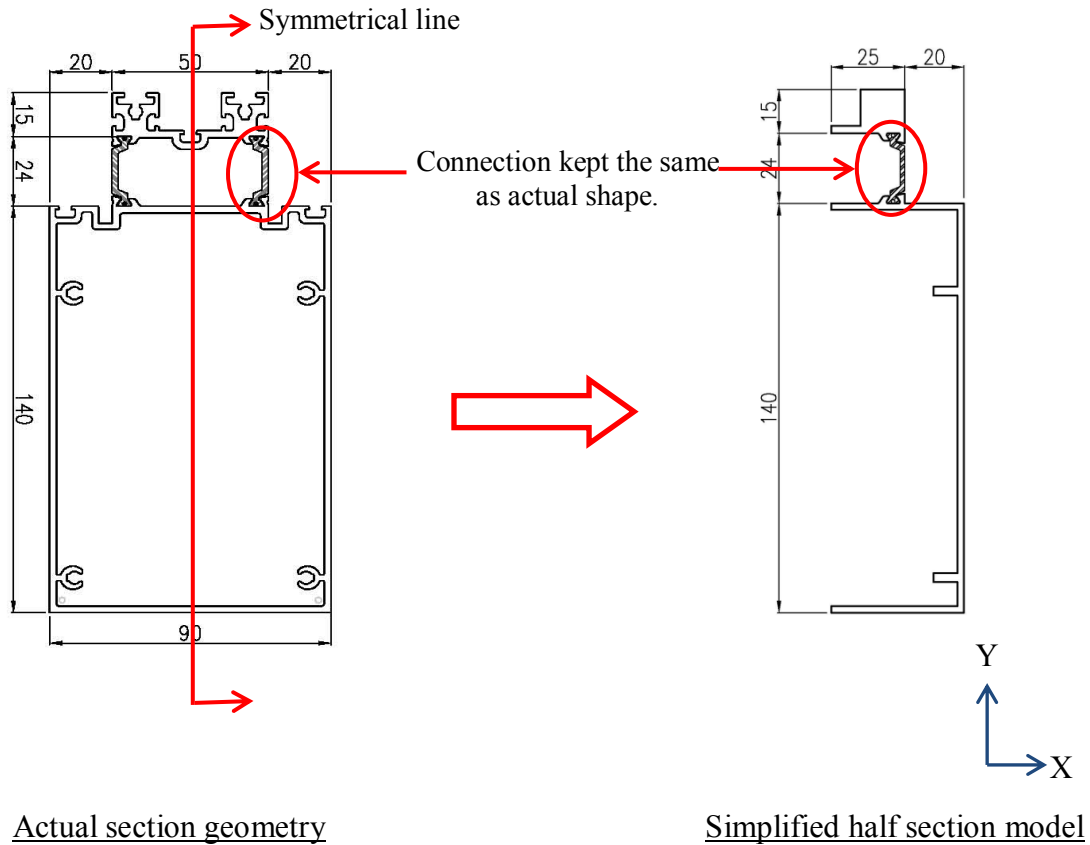


Figure 4.35 Details of simplified section

The geometry of the simplified section was drawn in Autocad drawing format and then converted to a standard ACIS text (SAT) file. The beam was imported as three separate parts as other FE models. All three parts were assigned as deformable solids and then joined together by position constraint tools.

Material properties of aluminium alloy 6063T6 were assigned to top and bottom aluminium parts. Middle polyamide part was assigned by the property of 25% reinforced polyamide PA66. Similar to shear and tension models, material model of aluminium discussed in Section 4.2.1 was applied. Aluminium young's modulus, yield stress and ultimate stress defined in Section 4.2.1 were input into the models and aluminium was defined as an isotropic material. To determine the stress and strain relationship in the plastic range, Ramberg-Osgood continuous model was adopted. True stress and true plastic strain from

Table 4.1 were used to define the plasticity.

As the façade beam is mainly deformed under bending, polyamide inserts add bending capacity to the whole section. Therefore, the material properties of the polyamide at longitudinal direction shall be considered rather than the ones at transverse direction. This is different from shear and tension models when loading direction is consistent with polyamide material properties at transverse direction (tension) and connectivity of the interfaces is to be evaluated. As the bending contribution from polyamide insert dominates the deformation behaviour, material properties at transverse direction are therefore insignificant in the beam models. To simplify modelling, polyamide was treated as an isotropic material with material properties along longitudinal direction taken into consideration. Young's modulus of polyamide in longitudinal direction discussed in Section 4.2.2 was adopted to define the elasticity of the material. True stress - true strain relationship of polyamide in longitudinal direction shown Figure 4.6 was input into the models to define plasticity.

To match the test set-out, FE model geometry and locations of loading and support points were defined according to the tests. Since the tests were conducted according to displacement control, displacements were applied instead of loading. During testing, the platform, where the roller supports are placed, moved upwards while loading pads were kept still. To match this loading situation, boundary conditions were applied to restraint the beam vertically along y-axis at one-third and two-thirds of the span at beam shoulder to simulate the loading pads while displacements were applied at both ends of the beam to simulate the upward movement of the machine platform. To simplify the calculations, interaction between rollers and beam was ignored as well as the interaction between loading pads and beam. In addition, boundary condition of "XSYMM" was assigned to the regions which were cut along Z-axis similar to shear and tension models. Details of the model setup are shown in Figure 4.36, Figure 4.37 and Table 4.7 below.

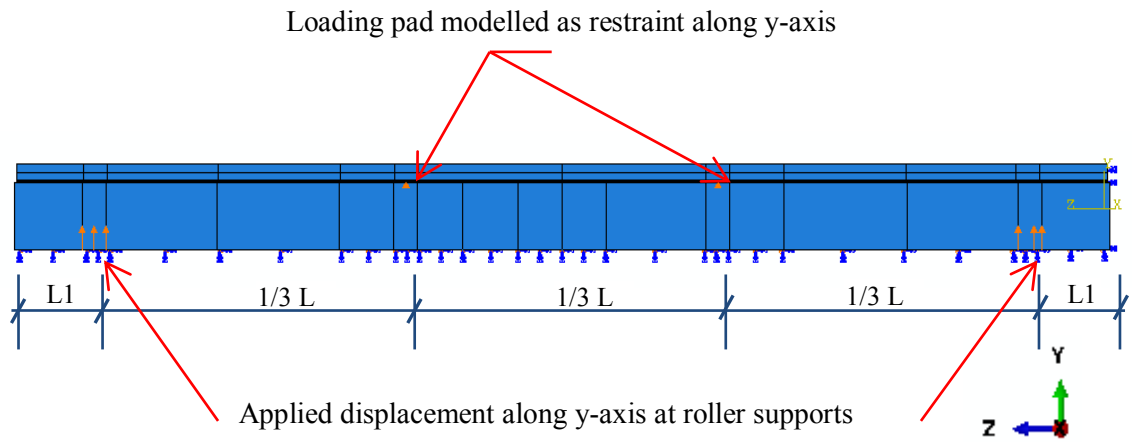


Figure 4.36 Model setup diagram

Table 4.7 FE model type and span details

Beam Model Type	L1 (mm)	L (mm)
B	180	2120
C	180	2620
D	180	3120
E	180	3640

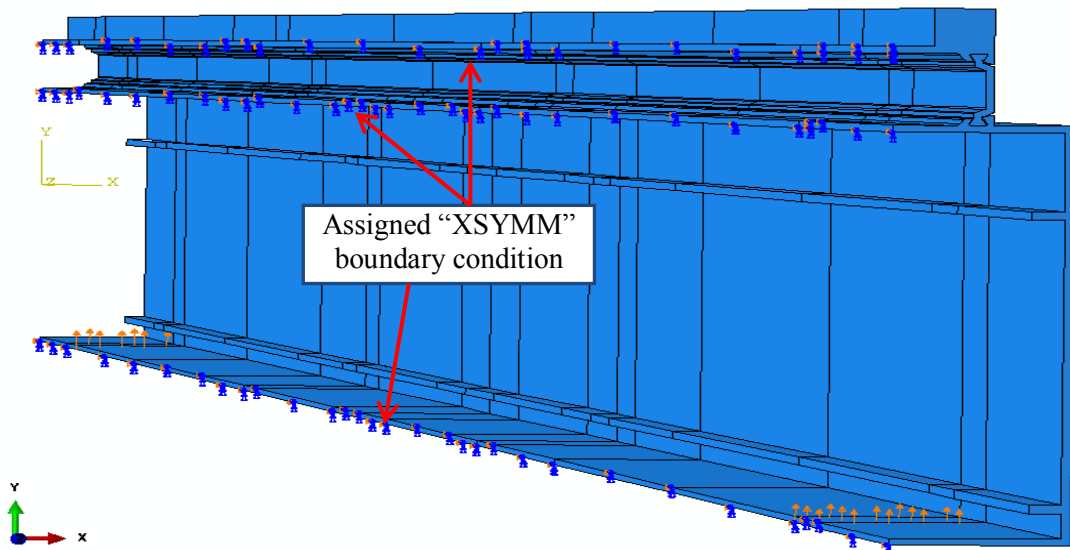


Figure 4.37 Symmetrical boundary assignments

The beam models are meshed by fine meshes. Top and bottom aluminium parts (AL1 & AL2) were assigned to hex dominated quadratic reduced integration solid element (C3D20R). The mesh size is seed 9. Finer mesh of seed 7 was assigned to polyamide part (PA). Similar to shear model, hex dominated linear elements with incompatible mode (C3D8I) were assigned to polyamide part. Detailed mesh assignments are shown in figures below.

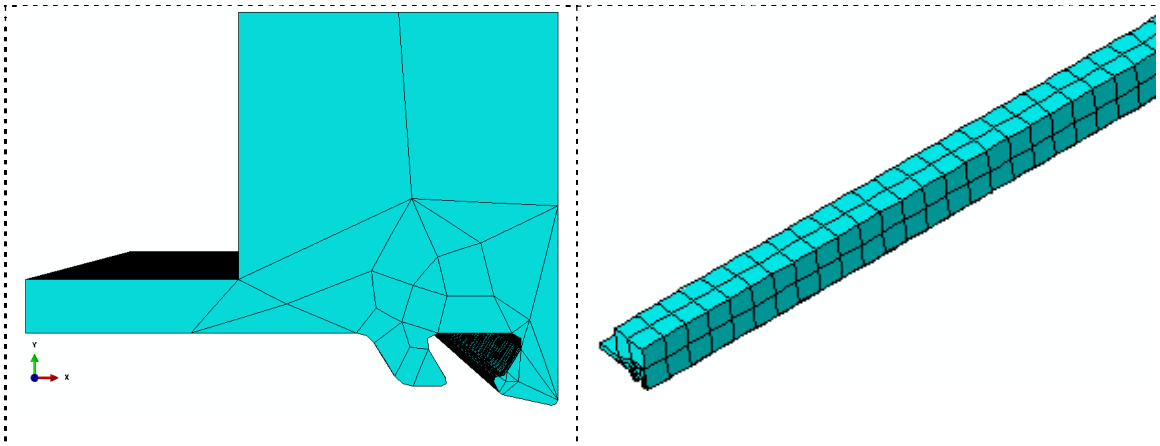


Figure 4.38 Mesh assignment of part 1 (AL1) from different view angles

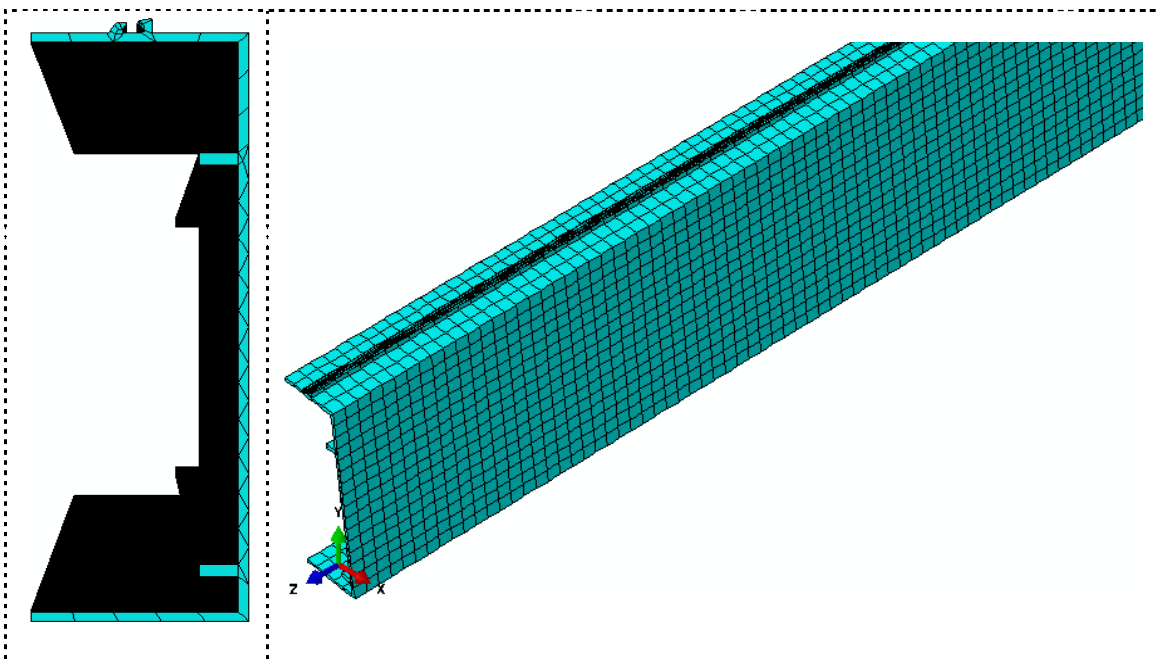


Figure 4.39 Mesh assignment of part 2 (AL2) from different view angles

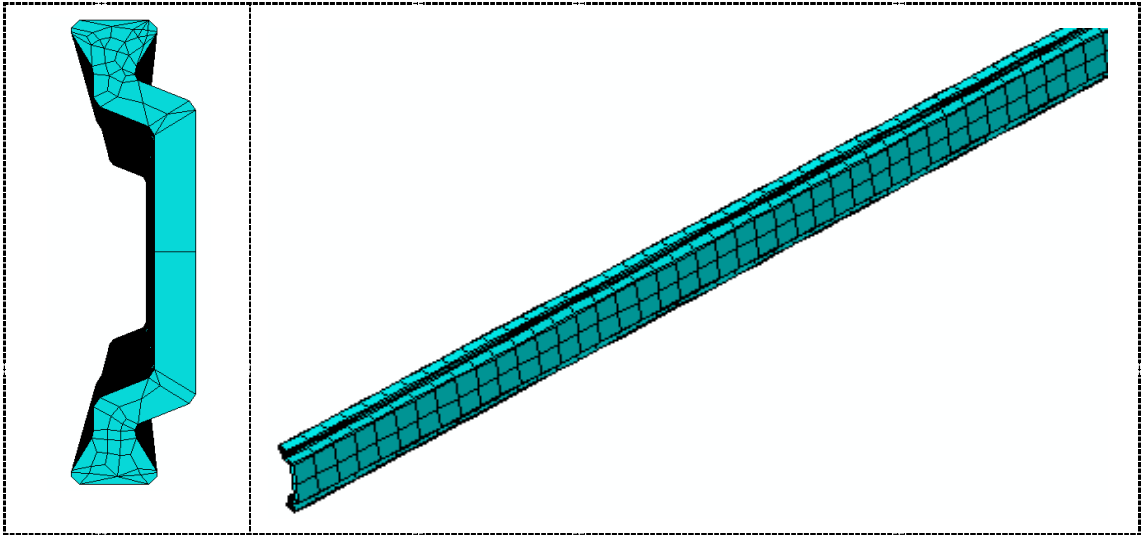


Figure 4.40 Mesh assignment of part 3 (PA) from different view angles

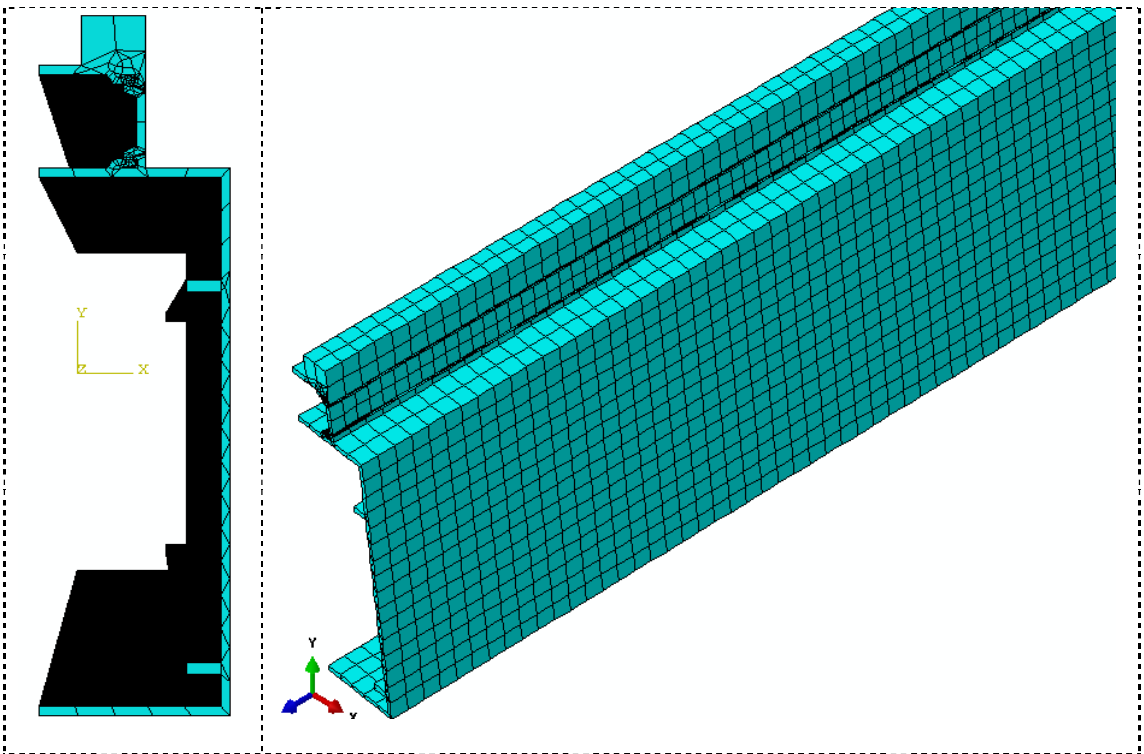


Figure 4.41 Mesh assignment of assembled whole section

4.7.2 Proposed partitioned multi-phase beam failure model

Partition setup

The façade beams were divided into several regions during modelling as shown in Figure 4.36. The partition toolsets were utilized to locate the regions for assigning loading and boundary conditions as well as contact interaction. In addition, locations of Linear Variable Differential Transformer (LVDT) and strain gauges were assigned by partition toolset. The bottom aluminium part (AL2) was partitioned differently from top aluminium part and polyamide part as AL2 needed to be partitioned to locate the LVDTs. The partition details of all three parts are shown in Figure 4.42 and Figure 4.43. The dimension details for all four models are listed in Table 4.8 below.

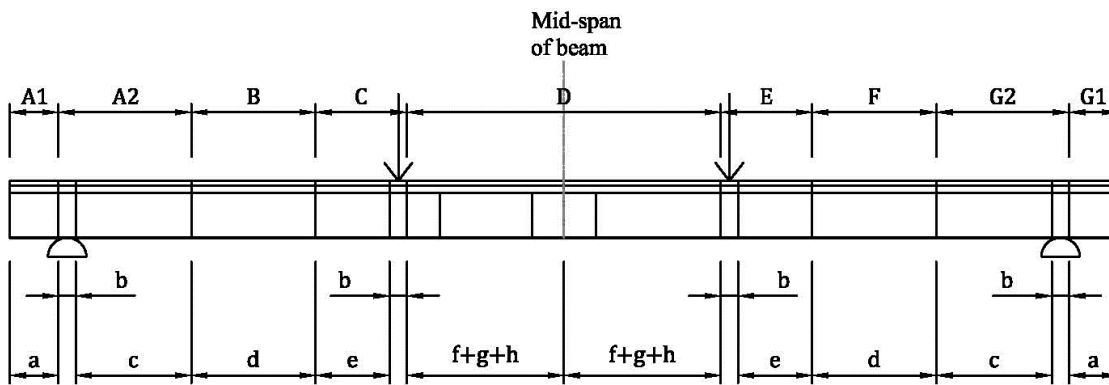


Figure 4.42 Partition assignment of top aluminium part (AL1) and polyamide (PA)

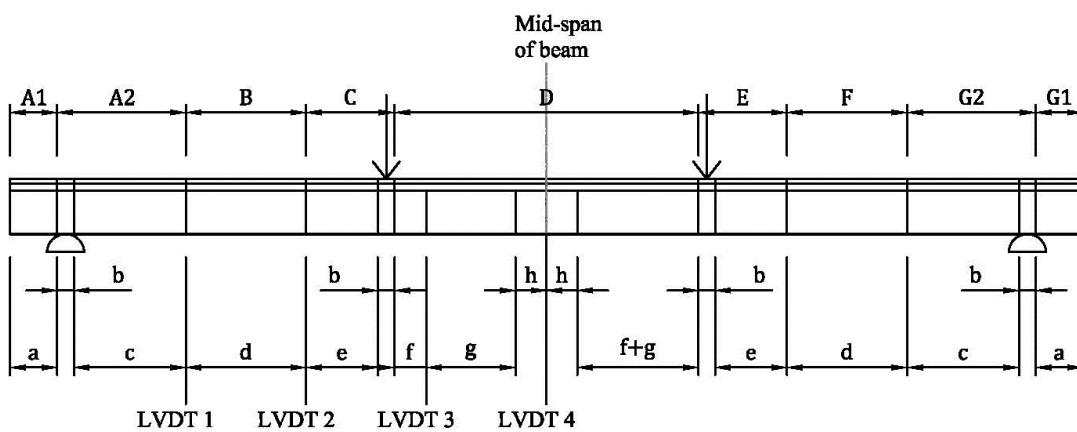


Figure 4.43 Partition assignment of bottom aluminium part (AL2)

Table 4.8 Detailed dimension of partition

Beam model type	a (mm)	b (mm)	c (mm)	d (mm)	e (mm)	f (mm)	g (mm)	h (mm)
B	153	54	251	278	124	100	126	100
C	153	54	303	330	186	90	220	100
D	153	54	363	390	233	103	290	100
E	153	54	428	455	276	125	355	100

Table 4.8 shows the clear overhang dimension ‘a’ is fixed for all the models. This assumption is purely based on the laboratory tests. Adding half width of the support, the length of overhang to the centre of support is matching the dimension shown in Figure 3.23. The width of roller support and loading pad were modelled as 54 mm which approximated the actual sizes. Locations of LVDTs according to the test setup are indicated in Figure 4.43. Regions of A1-G2 were divided for assigning the contact interaction.

Multi-phase beam failure model

Similar approach to the proposed progressive failure model discussed in Section 4.4 was adopted. A proposed multi-phase progressive beam failure model was introduced to simulate the connection degradation after slippage occurs. Friction co-efficient of both connections at the regions of A2, B, C, E, F and G2 (μ_1) were reduced to one-seventh of the initial value (μ_0) after slip. The remaining one-third of the span between two loading points at middle of the beam (region D) is under pure bending without any shear stresses involved. There is no relative motion between the contact surfaces in this region. The friction co-efficient is therefore kept as the initial value. The overhung regions A1 and G1 were allowed to copy down the test setup which were not subjected to any loading and, therefore, had no contribution to the beam bending. Hence, the friction co-efficient was also kept as the initial value. When loading increases, the friction co-efficient of both connections at regions of A2, B, C, E, F and G2 will decrease until zero when connections totally fail. This process is illustrated in the graph below. As the simulation is not aiming for the strength of the composite beam, complete failure of the

connection is not modelled. The FE models are to only simulate Phase I and Phase II of the failure model.

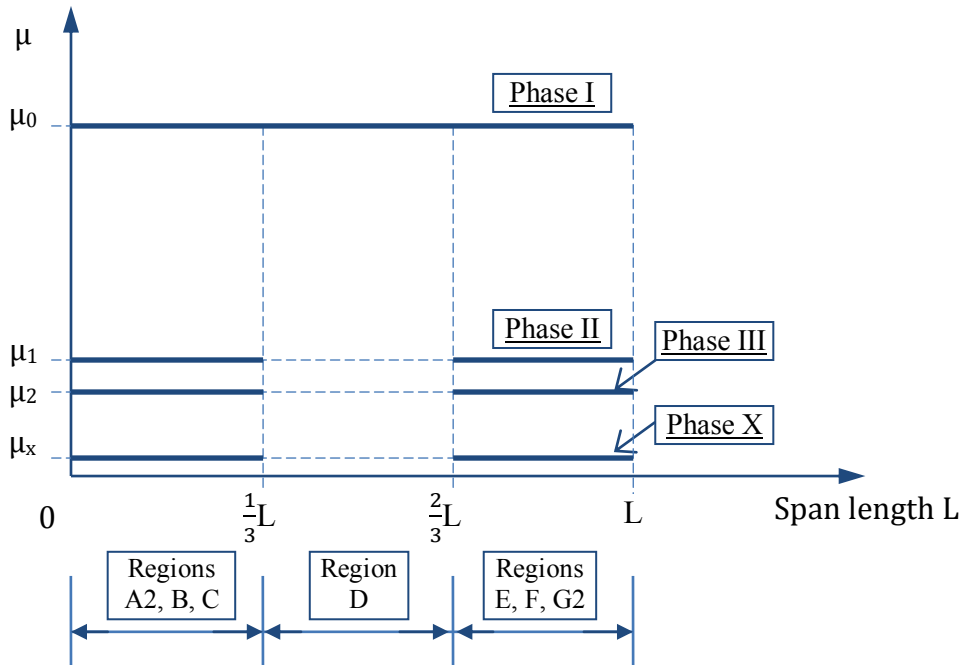


Figure 4.44 Proposed progressive beam failure model

The mechanical contact property was assigned to tangential behaviour as discussed in Section 4.4 which is similar to shear and tension models. Penalty friction formulation was adopted for the contact bodies in the isotropic direction. As the four-point bending specimens were subjected to beam bending only, the friction co-efficient could not be assigned the same as pure shear or tension specimens. Therefore, the initial friction co-efficient is assigned as 0.7 for both top and bottom connections by updating model manually to match the experimental results.

“Surface to surface” discretization was again assigned to the interaction between aluminium and polyamide contact surfaces. The aluminium interface was assigned as “master” surface while polyamide interface was assigned as “slave” surface. The details of master-slave surfaces are similar to shear model which is shown in Figure 4.15. “Small sliding” tracking formulation was assigned for the tracking approach between master and slave surfaces. The assignment of top and bottom interactions is visualized in Figure 4.45. Similar to shear model, interference fit option was chosen to remove minor degree of overclosures between the contact pairs.

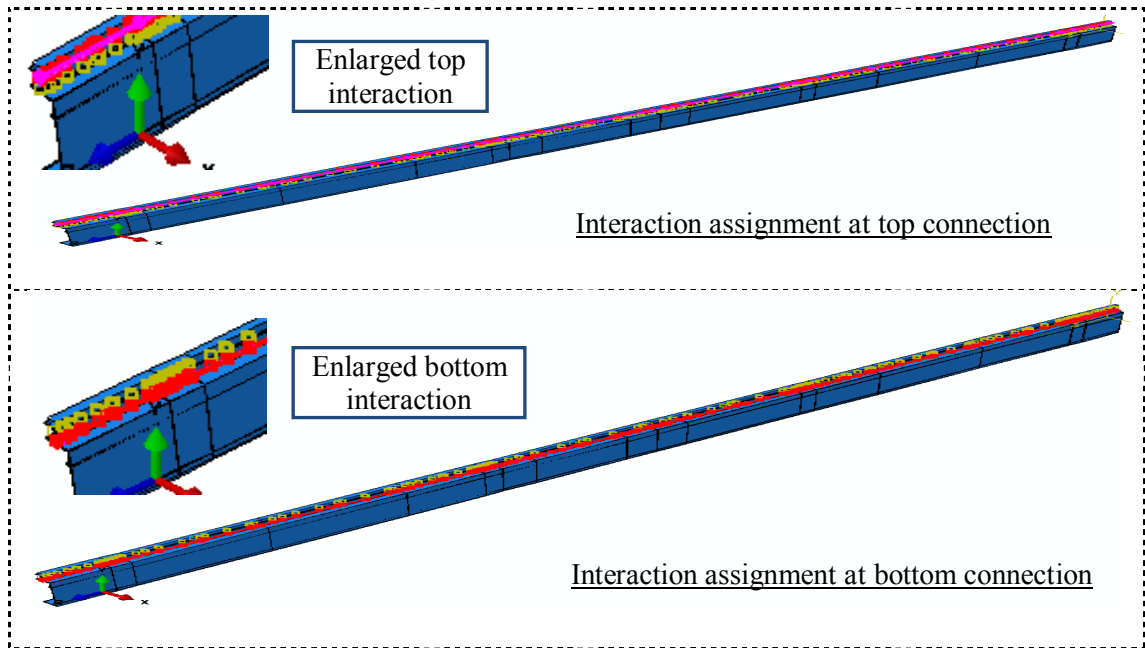


Figure 4.45 Interaction assignment

The value of the applied displacement was based on the observation of laboratory tests and applied in three loading steps. The displacement was applied linearly from zero to the displacement before slip occurred in first loading step. In second loading step, the displacement was kept the same as the first step while the friction co-efficient reduced. This indicated the first slippage and the reduction of friction effect which is referred to as Phase II in Figure 4.44. In the third step, the displacement keeps increasing while the frictional co-efficient is maintained. The simulation was only done up to Phase II as beam failure was not within the scope of this study. The other phases relate to the degradation of connection at increased loading and lead to the complete failure of connection. The failure of façade beam is also related to the material failure of profile parts as well as connection failure. Detailed displacement assignment for each model at each loading step is listed in Table 4.9.

Table 4.9 Assignment of displacement and friction co-efficient

Beam model type	Step 1 - Phase I		Step 2 - Phase II		Step 3 - Phase II	
	Assigned displacement (mm)	Friction co-efficient	Assigned displacement (mm)	Friction co-efficient	Assigned displacement (mm)	Friction co-efficient
B	19	0.7 for all regions	Propagated from Step 1	0.7 for A1,D, G1; 0.1 for other regions	40	As step 2
C	30	0.7 for all regions	Propagated from Step 1	0.7 for A1,D, G1; 0.1 for other regions	50	As step 2
D	50	0.7 for all regions	Propagated from Step 1	0.7 for A1,D, G1; 0.1 for other regions	80	As step 2
E	60	0.7 for all regions	Propagated from Step 1	0.7 for A1,D, G1; 0.1 for other regions	90	As step 2

4.7.3 Typical results

All four models show comparable results. Beams bent under the two applied loading (displacement). Typical deformed shape at the end of step 3 is shown in Figure 4.46 below from model D.

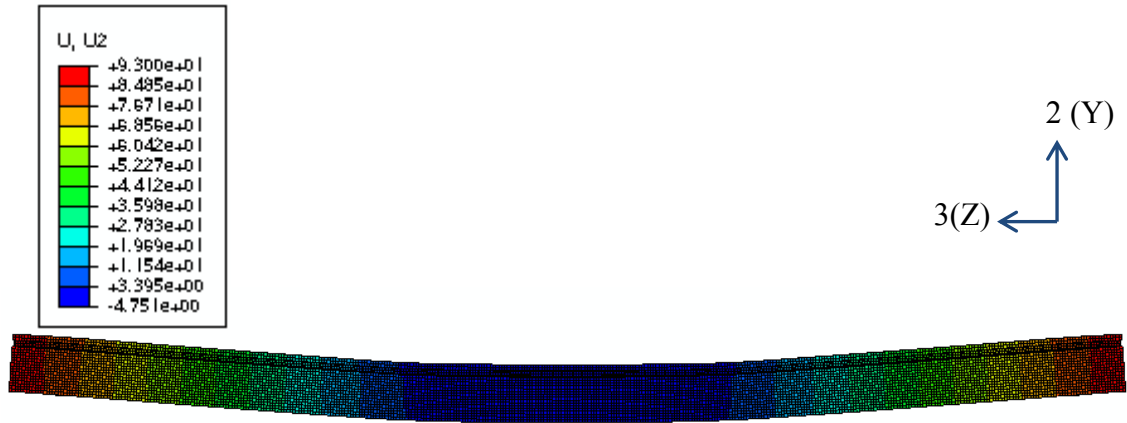


Figure 4.46 Deformed shape and displacement contour along 2-axis (vertical displacement)
 The horizontal displacement (along 3-axis) is plotted below to show the differential movement between each part of the section. The region at mid-span of the beam shows no differential displacement at the connections which means no slippage occurred. This confirmed the assumption made when assigning proposed progressive beam failure model. Connections at both ends of the beam show clear differential displacements.

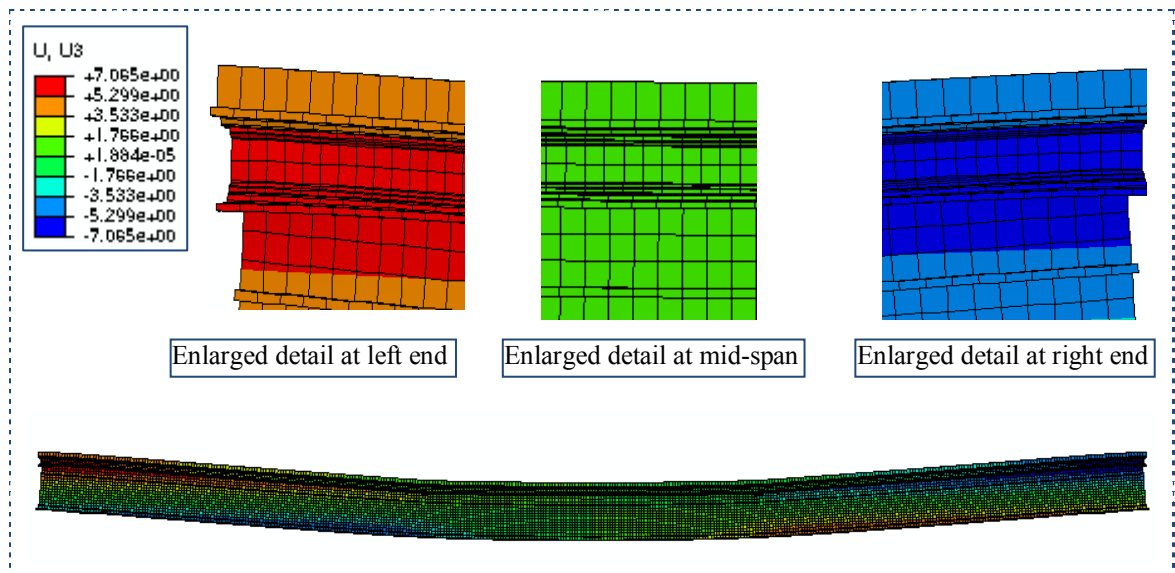


Figure 4.47 Displacement contour along 3-axis (horizontal displacement)

Load vs mid-span displacement graph was plotted for each model. The combined graph presenting comparison of the models is shown in Figure 4.48. This graph confirmed the loading capacity of the beam decreased with increased span length while displacement increased together with span length increasing.

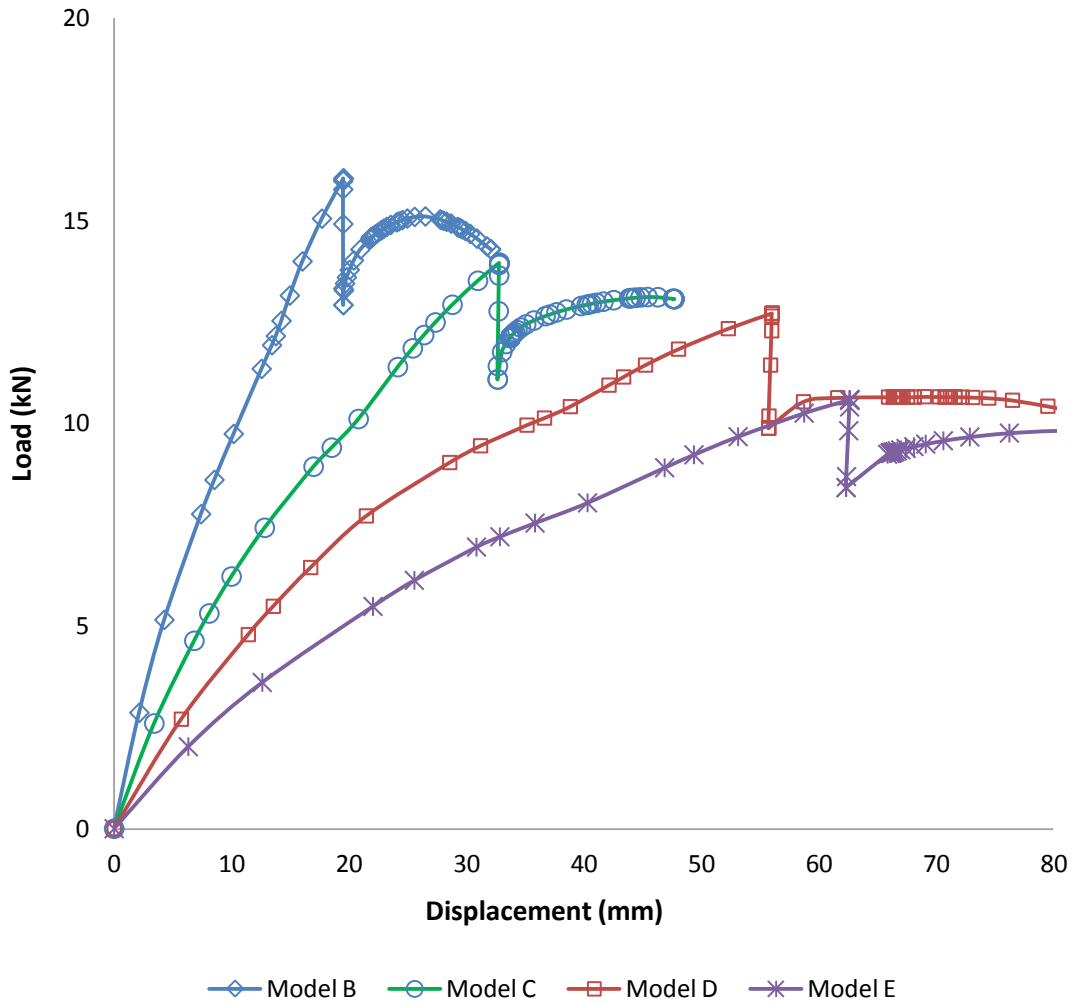


Figure 4.48 Load vs mid-span displacement for all models

Typical contact stresses in top and bottom contact pairs at the end of step 3 are plotted from model D in tables below. Since the beam performed symmetrically according to the mid-span, stresses plotted for regions A2, B and C can reflect the stresses in regions G2, F and E. Region D is area at mid-span.

Table 4.10 Contact stress along Z-axis at top connection

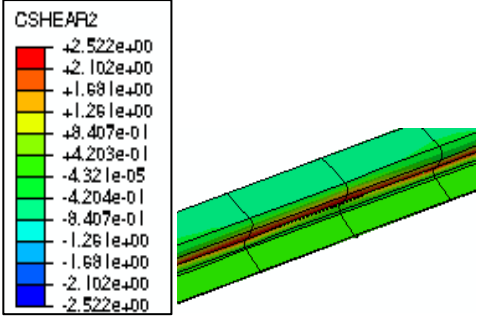
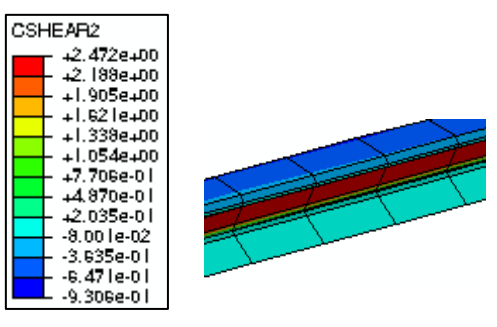
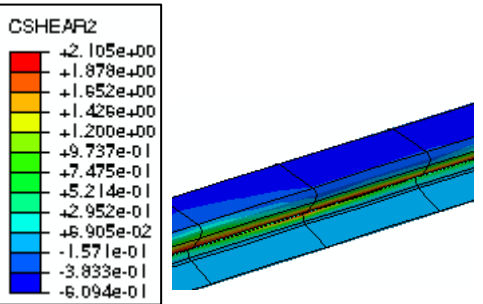
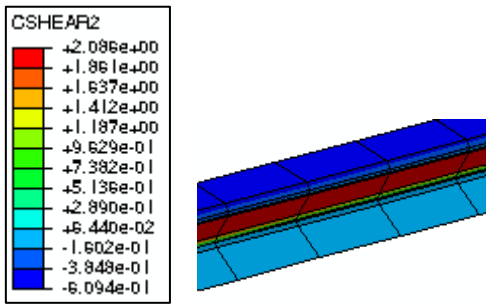
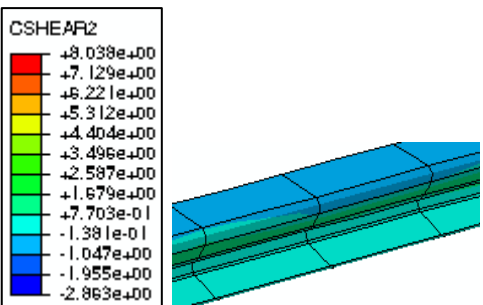
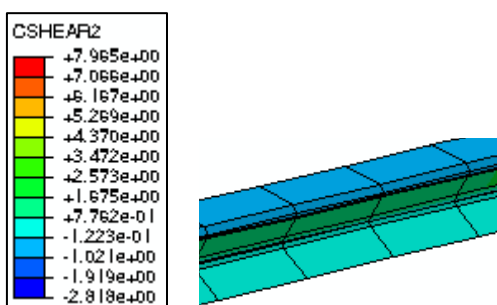
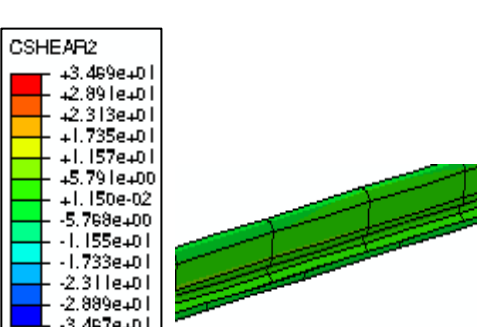
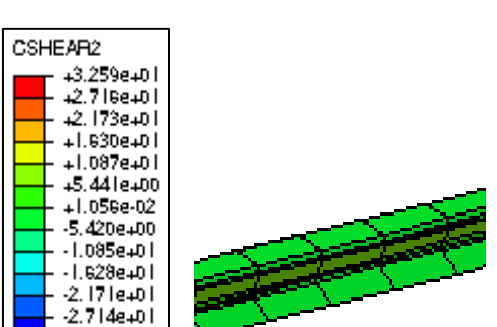
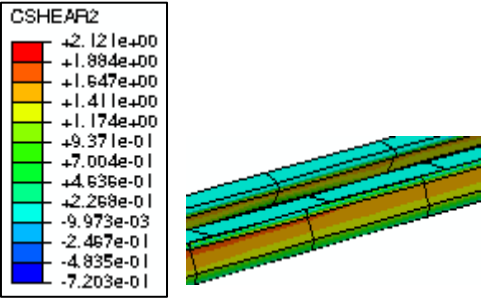
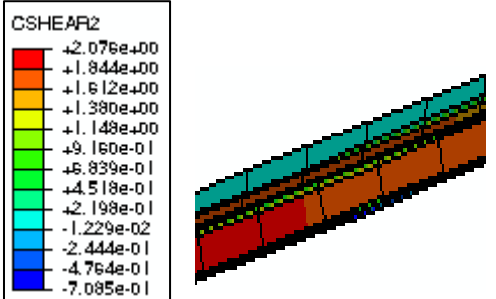
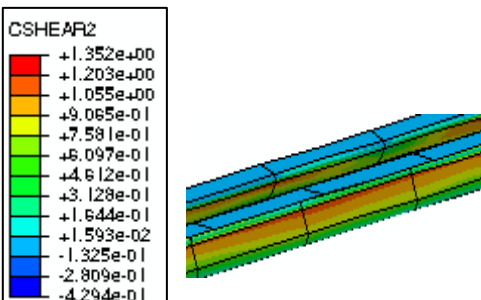
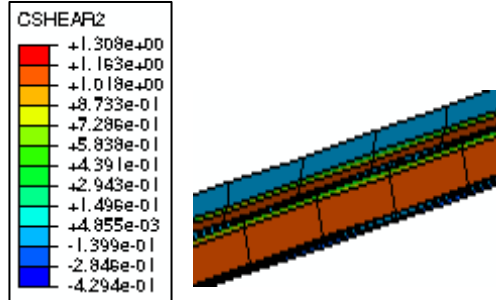
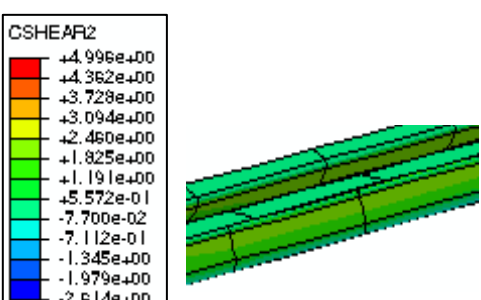
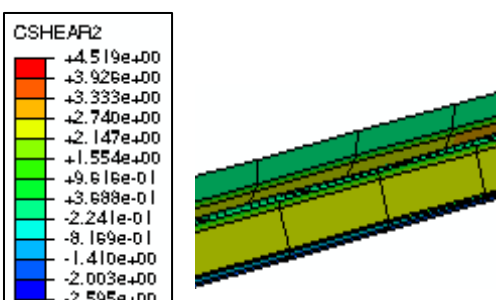
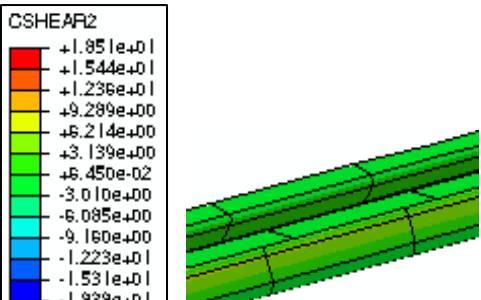
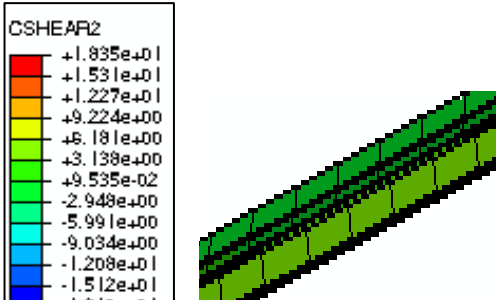
Region	AL1 (MPa)	PA1 (polyamide connected to part AL1) (MPa)
A2		
B		
C		
D		

Table 4.11 Contact stress along Z-axis at bottom connection

Region	AL2 (MPa)	PA2 (polyamide connected to part AL2) (MPa)
A2		
B		
C		
D		

The above tables show the longitudinal contact stresses (along Z-axis) in the top connection are greater than in the bottom connection. In region D of both top and bottom connections, the longitudinal contact stresses are close to zero as these regions

are under pure bending. The vertical shear stresses equal to zero at these regions. This is confirmed in Figure 4.49 below. Bending stress along 3-axis is also plotted in Figure 4.50.

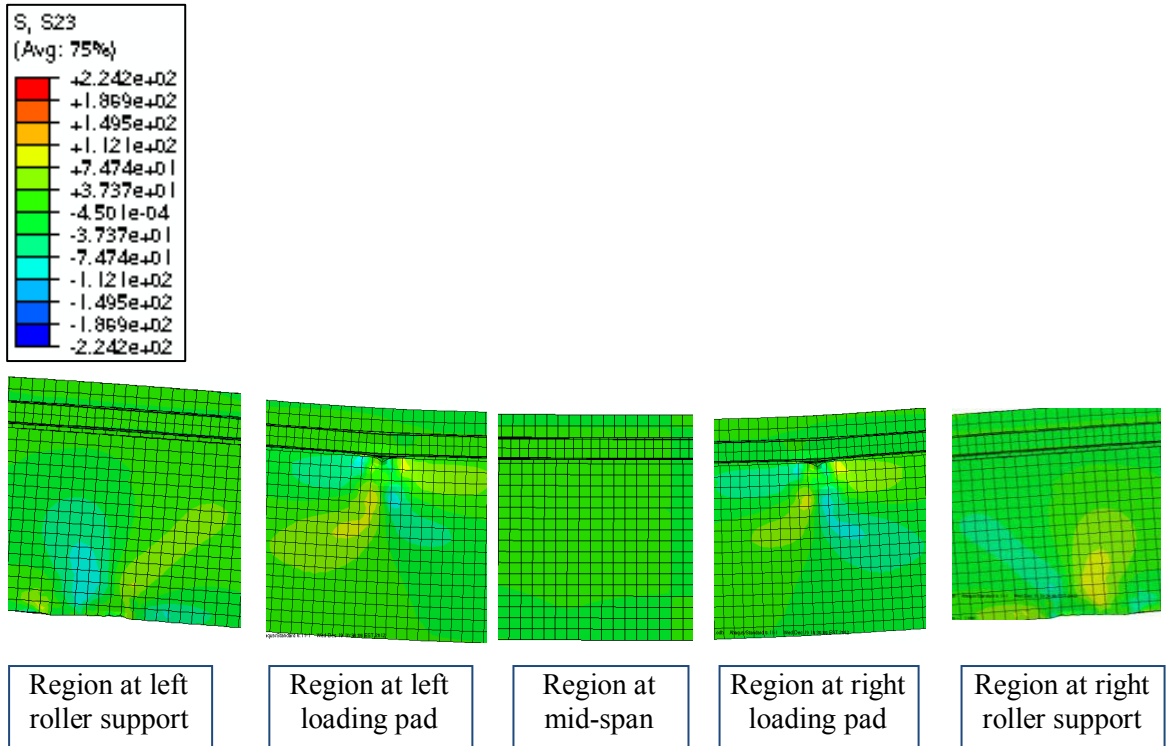


Figure 4.49 Shear stress contour from model D

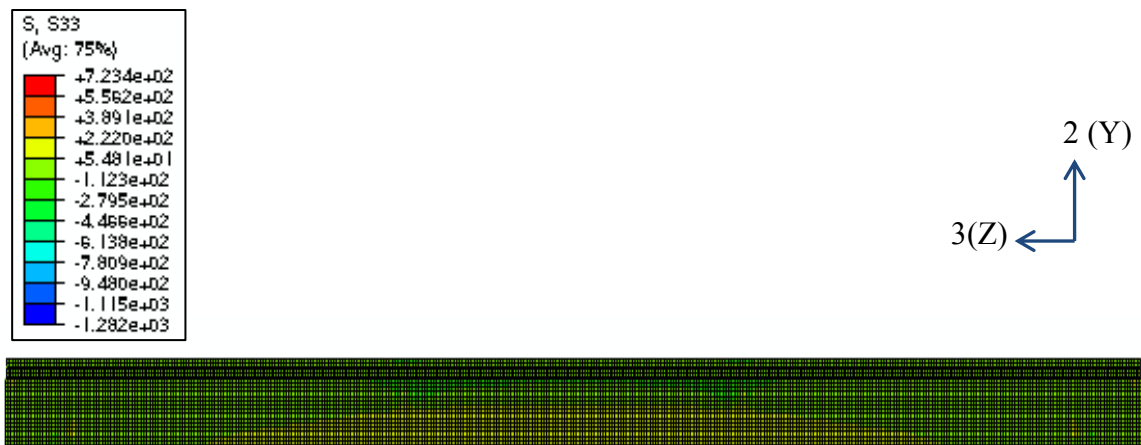


Figure 4.50 Bending stress contour from model D

In conclusion, the proposed partitioned multi-phase beam failure model was applied to all four beam models. Deformed shapes of all models are similar which is bending under the loading as other classical beams. Horizontal differential displacement plot and

longitudinal contact stress plot confirmed there was no slippage occurring at mid-span region. It, therefore, confirmed the assumption made in the proposed partitioned multi-phase beam failure model. However, there is clear differential displacement observed at top connection at both ends of the beam which indicates the failure of top connection in the regions which experience shear/bending combined action.

4.8 Summary and conclusions

In summary, details of FE models simulating shear and tension tests as well as four beam models loaded under four-point bending were presented in this chapter. All models were built and analyzed by ABAQUS/CAE software.

Detailed discussions of mesh assignment, material modelling and contact interactions were carried out. Simplified assumption was made by applying isotropic material properties of polyamide at transverse direction to the whole part in shear and tensile models. However, polyamide material properties at longitudinal direction were applied as in isotropic case for the beam models. Isotropic material of aluminium alloy was applied and Ramberg-Osgood continuous material model was adopted.

As the interaction between polyamide and aluminium is complicated and uncertain, the failure mechanism of the connections under different loading conditions was proposed based on the experimental investigations. Two new modelling techniques were invented and applied to the models to simulate the progressive failure process under pure shear force and under bending/shear combined action. These two new models are

- Proposed progressive failure model – under pure shear force
- Proposed partitioned multi-phase beam failure model – under bending/shear combined action

Failure modes of shear and tension models were discussed. For shear model, the polyamide slipped away from the connection. In terms of tension model, the polyamide was pulled away completely from the top connection while it rotated half out of the bottom connection but remained connected by the other half of interface. The beam models showed the slippage of polyamide and the three-stage progressive failure mode.

The deformed shapes of all FE models were presented and discussed. Stress distributions were plotted to provide further understanding of this façade section at all

three loading conditions. Load-displacement relationship for both tension and beam models were plotted as well as load-slip relationship for shear model.

In conclusion, FE models were built to simulate the experimental works on shear, tension and beam bending. Two new models, namely, proposed progressive failure model and proposed multi-phase beam failure model were successfully applied to the models.

For shear model, the failure mode confirmed the connection failure. The gradually decreased contact stresses in both aluminium and polyamide after slip confirmed the progressive failure mechanism. Stress distributions along longitudinal and transverse directions of polyamide part confirmed the assumption of simplifying polyamide material properties as isotropic with material properties in transverse direction.

For tension model, deformed shape confirmed the tensile deformation as dominant; however, bending deformation, particularly at the shoulder of the section cannot be ignored. The normal stresses along loading direction dominated the other two directions. Normal stresses in the direction across the thickness of the whole cross-section were reasonably large to be taken into consideration. This reflects the bending behaviour exhibited in the model deformation although tensile deformation was governing. Stress distribution at polyamide confirmed the stress in transverse direction is governing. Therefore, the assumption of applying material properties of polyamide along transverse direction to the whole polyamide part is appropriate.

For the beam models, all models showed similar deformed shapes. The beams bent under the loading. Load vs displacement relationship of all models was plotted together. It shows that the beam loading capacity reduces with the span increasing and the mid-span displacement increased with the increased span. This phenomenon is consistent with beam bending of isotropic sections. Longitudinal contact shear stresses showed close to zero value at the region between two point loads which is under pure bending. In addition, there was no horizontal differential displacement in this region of the beam. These confirmed the assumption made in proposed partitioned multi-phase beam failure model of no slippage occurring in this region. The differential displacement at top connection at both ends of the model confirmed the failure of top connection. Bending and shear stress distribution along the beam span were plotted to confirm the classical beam bending behaviour.

The finite element models provided more insight and details of failure mechanism and stress distribution including contact stresses which cannot be determined by experimental work. Comparison of FE model results and test results will be carried out in the next chapter.

Chapter 5

Comparison of Experimental and Numerical Investigation

5. Comparison of experimental and numerical investigations

5.1 Introduction

Laboratory experiments and FE models have been presented in Chapter 3 and Chapter 4, respectively. Detailed setup of experiments and typical results were illustrated in Chapter 3. In Chapter 4, two proposed failure models were created to simulate the failure modes of experiments for shear capacity and beam bending. The proposed progressive failure model was adopted when setting up FE shear model. To set up the FE beam models, the proposed partitioned multi-phase failure model was initiated and adopted. The setup of FE models were based on the setup of experiments. Detailed description of FE model setup and comparison with test setup was made in Chapter 4. Typical results and failure modes obtained from FE models were displayed in Chapter 4 as well.

As the purpose of building FE models is to provide inclusive and cost effective results, it is essential to verify the results generated by FE models by experimental results. In this chapter, a comprehensive discussion of the experimental results compared with FE model results will be presented. Comparisons will only be performed between the experiments at room temperature and FE models for this study.

Comparison will involve shear and tensile capacity tests and those obtained from the FE models, as well as four-point bending beam tests and relevant FE model results. In comparing shear test results with those of FE model, failure mode and deformed shape will be compared. Load-slippage of connection graphs obtained from both experiments and FE model are plotted together for discussion. Conclusions are drawn based on the comparisons and discussions.

For comparison of tensile capacity tests with FE model, failure modes and deformed shapes between experimental and FE modelling results will be discussed. In addition, load-displacement (elongation of the specimen) graphs obtained from experiments and FE model will be plotted and studied.

In terms of the four-point beam bending, result comparisons between experiments and FE models will be carried out for all types of beams. Although laboratory tests were carried out much further into the plastic range than FE models, all beam specimens were not tested to their ultimate capacities. Both experiments and FE models performed in

the serviceability limit state of this type of façade beam. Therefore, comparisons will be made only for the deformed shapes and slippage of connection rather than the failure modes. Load vs mid-span displacement relationships for all beam types will be compared with the FE model results as well as strain distribution at mid-span along the cross-section and moment-curvature relationships.

5.2 Comparison of shear test results and FE modelling

As FE model was built to simulate the experimental work, it is necessary to compare the results of FE model to those from experiments. Comparison of the results between experiments and FE modelling has been made on deformation and load-slippage relationship. The comparison is limited to experiments at room temperature only as the temperature effect is too complicated to be included in the FE modelling at this stage.

Comparison of deformed shapes between FE model and experiment are shown in Figure 5.1 below. The photo taken from the test (Figure 5.1) shows consistent deformation shape as the FE model which is the failure of connection between polyamide to bottom aluminium part.

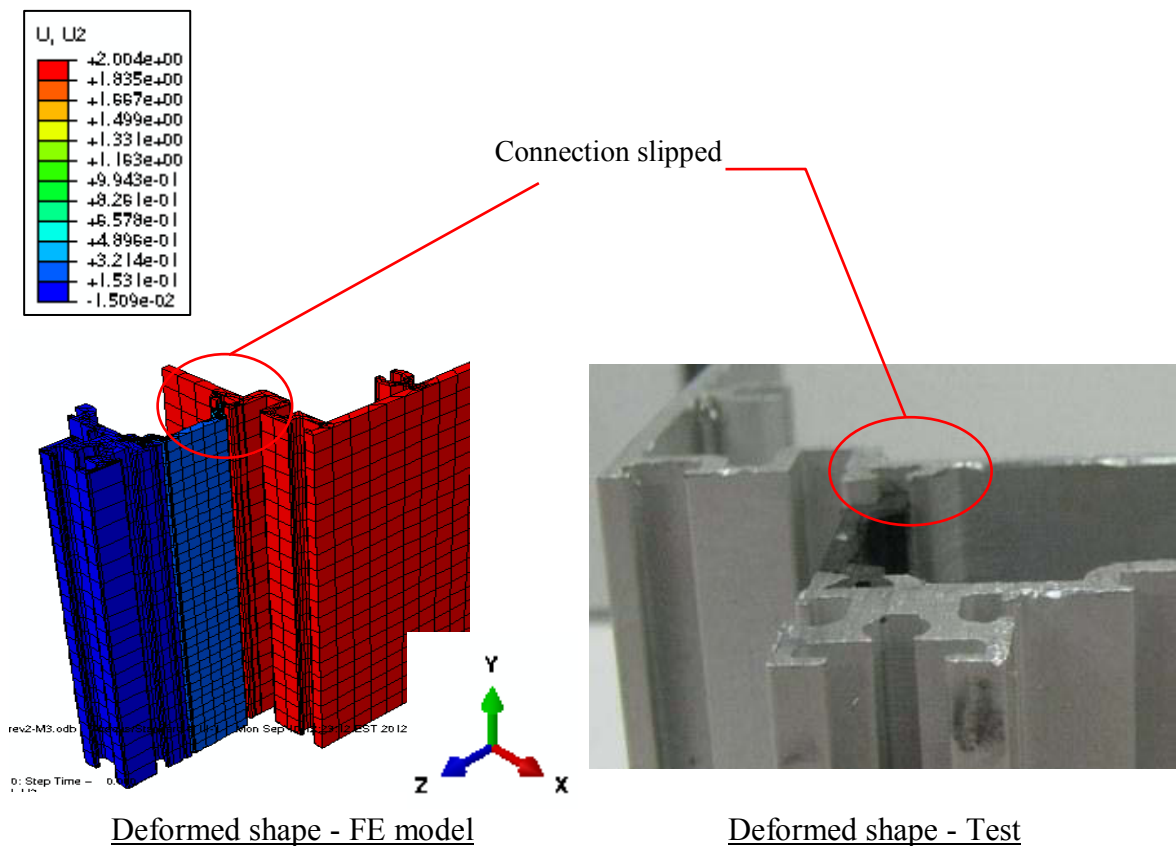
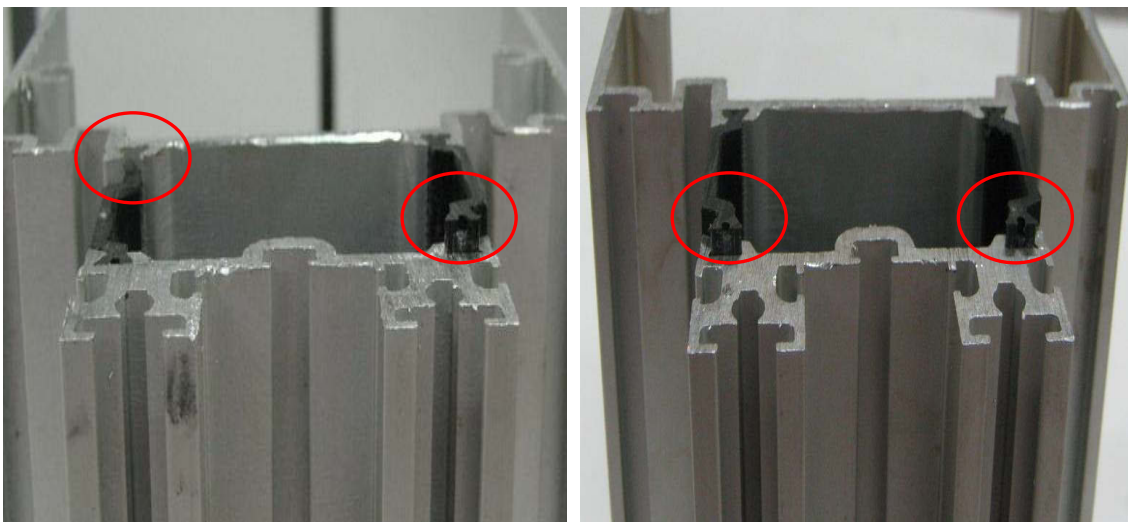


Figure 5.1 Comparison of deformed shapes

As the connectivity relies on the manufacturing process, it is impossible to maintain every connection identical for all specimens. Therefore, the slippage happened randomly at not only the bottom connection but also the top connection for some specimens during testing. In some cases, one connection at the top and the other one at the bottom slipped. These special deformation cases are shown in Figure 5.2 below. Since the FE model assigned identical connection properties to all connections, it reported idealised deformation shapes. This idealised deformation shape was confirmed by some tests whose specimens had relatively identical connectivity.



One connection at both sides slipped

Top connection failed

Figure 5.2 Random slippage at connections

As mentioned in Chapter 3, displacement measured by the Linear Variable Displacement Transformer (LVDT) at cross head was adopted instead of direct measurement under the specimen. This displacement was plotted against loading for all test specimens at room temperature on one graph and compared with the results from the FE model. The combined test and FE model load-displacement relationship graphs are presented in Figure 5.3.

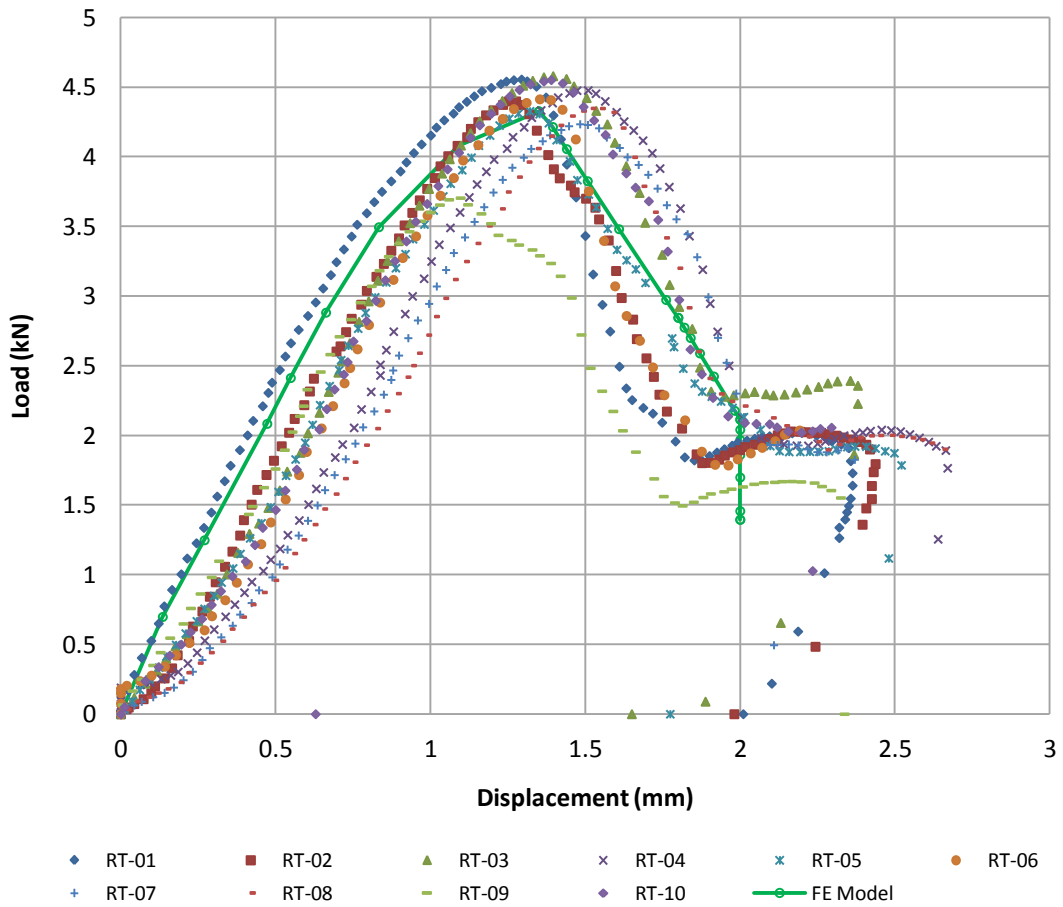


Figure 5.3 Relationship of load – slippage of connection comparison

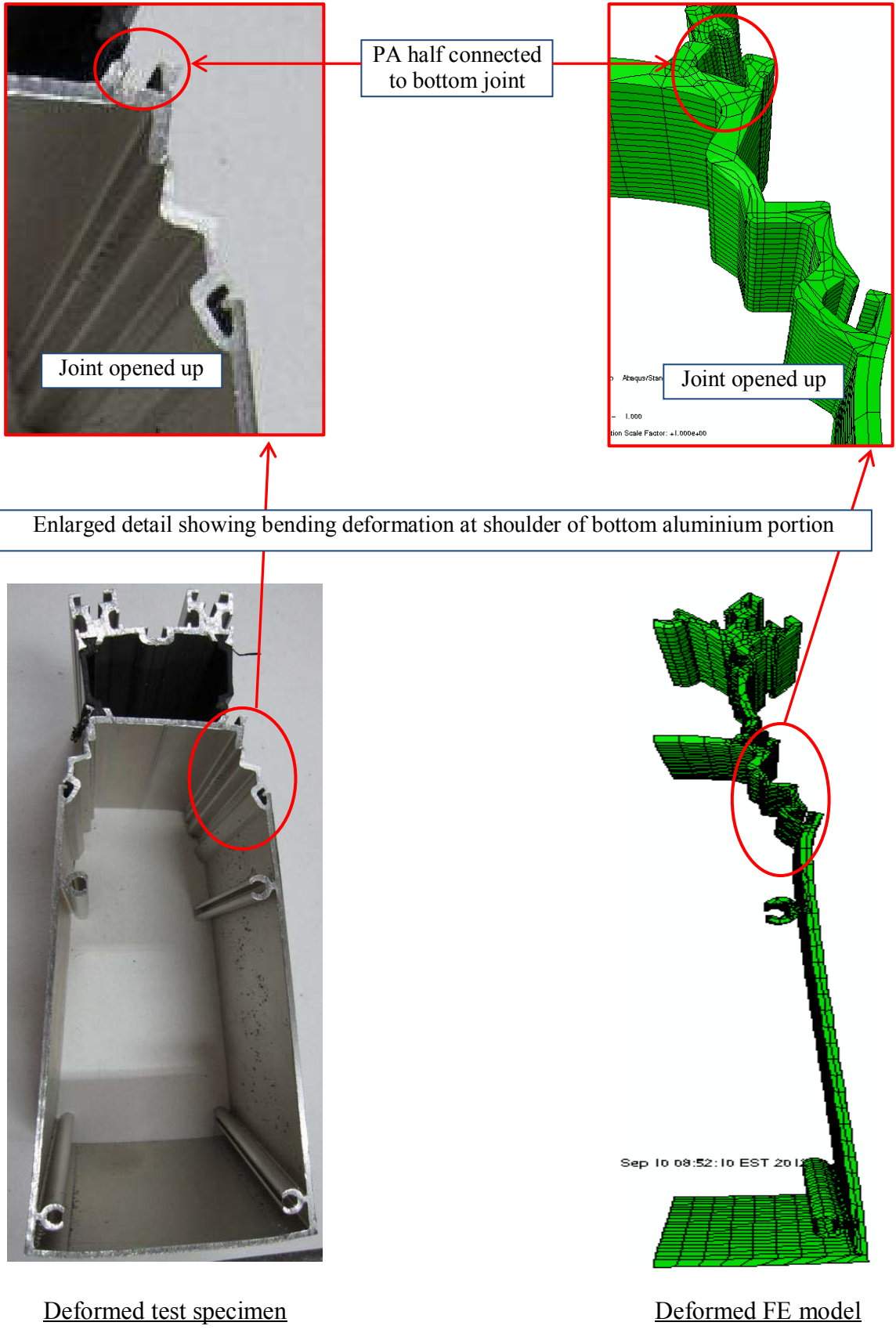
Load-slippage curves from experimental work exhibit large variations between the specimens. This phenomenon confirms the variation of connectivity between specimens as discussed before. The load-slippage curve obtained from the FE model falls within the range of test curves. The maximum loading capacity from the FE model is 4.3kN which is slightly lower than the highest value obtained from the experiments of 4.6kN. Slippage of the connection at the maximum load of FE model reaches 1.35mm. There are two test specimens (RT-01 and RT-10) which achieved a similar maximum loading value whose slippages are 1.27mm and 1.40mm at this point. The FE model result again fell in between the test results. Before slipping occurred, the load-slippage curve from the FE model stays at the top range of test curves. After the connection failed, this curve lies in the middle range of test curves. It also shows the loading capacity drops to 2.2kN almost linearly with increasing slippage. However, the load-slippage curves from the experiments demonstrate a non-linear rather than a linear behaviour after connection slipped. It can be seen that the curve from the FE model displays a similar load

decreasing rate as the test curves with increased slippage. Therefore, the load-slippage curve from the FE model provides a good simulation and simplification of test curves.

In summary, the FE model provides good correlation with experimental work. Based on uniform connectivity for all connections, the FE model demonstrates the idealised slippage location which is at bottom connections. This has been confirmed by some test specimens. However, other specimens showed random slippage of connections which were mainly due to the unevenness of connectivity, largely due to manufacturing process. Load-slippage curve obtained from the FE model gives good prediction of the actual testing curves. The proposed progressive failure model is now confirmed to be successfully simulating the degradation of connection after slip occurs. Hence, the simulation methodology can be applied to other similar façade composite profiles to predict the sectional shear capacity and connectivity.

5.3 Comparison of tensile test results and FE modelling

To verify the FE tension model, comparison of deformation and load-displacement relationship obtained from laboratory tests and model is discussed here. Deformation and failure modes recorded from both the experiments and the FE model were listed in Chapter 3 and Chapter 4. To make comparison between the deformations, deformed shapes are plotted side by side in Figure 5.4 below.



Deformed test specimen

Deformed FE model

Figure 5.4 Comparison of deformed shape

Figure 5.4 shows similar deformed shapes between the test specimen and the FE model. Bending deformation at the shoulder of bottom aluminium part was clearly observed in both cases. The profile on the shoulder of the FE model exhibits similar deformation as the test specimen. The shoulder of the FE model rotated almost the same 60° angle as the specimens from the experiments. The web in both cases is dominated by tensile deformation. The rigid joint between shoulder and web was transformed to hinged joint for both test specimen and FE model. The enlarged detail of the specimen also demonstrates that polyamide at bottom connection was half joined with the connection similar to the model. The reason for a small discrepancy in deformation between test specimen and the model is that the rotation of top aluminium part in the model is much greater than that from the test specimen. However, this has little influence of overall deformation of the section.

Load-displacement relationship obtained from test shows a good correlation between each specimen. The variation between test specimens is minor, unlike the shear tests. Again, unlike the shear test, which mainly tested the connectivity of section, tension tests relied more on the material properties and cross sectional area, especially the bottom aluminium part. As the aluminium material has stable properties and the area of the bottom part is uniform for all specimens, therefore, the load-displacement curves of all test specimens displayed a uniform pattern. All test data are plotted in Figure 5.5 below.

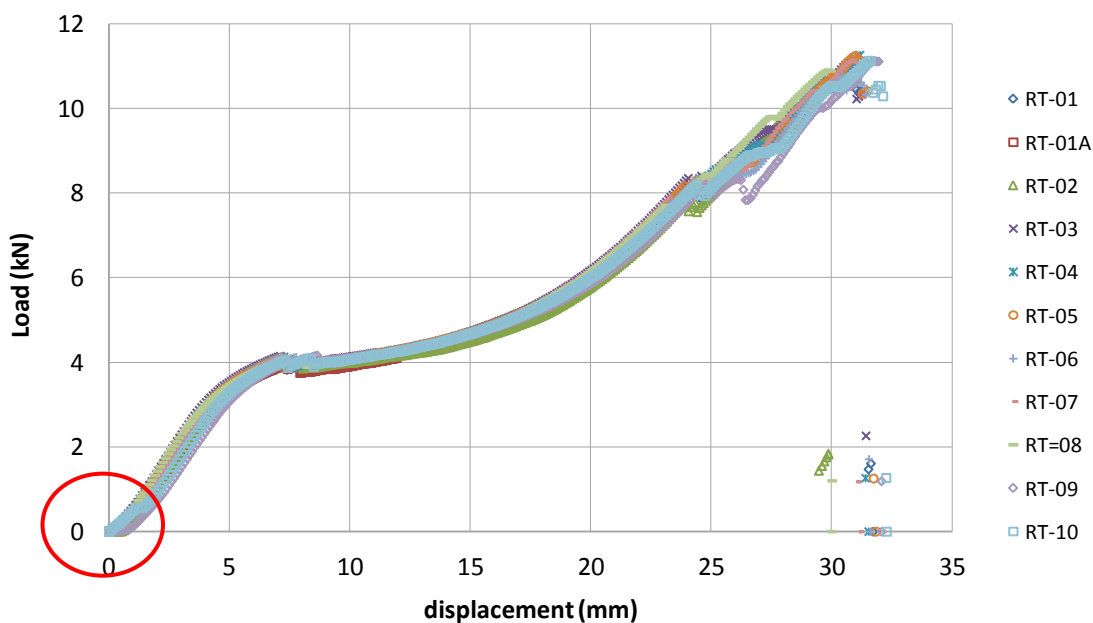


Figure 5.5 Load-displacement relationships from test data

The load-displacement relationship curves show an initial settlement of specimen/test jigs at the beginning of test which is circled in red. As the FE model represents the ideal loading condition, no external noise is included. It is, therefore, important to remove the initial settlement from the test curves when making comparison with the FE model. To eliminate the initial settlement of the test, all test data were modified to make displacement equal to zero at 0.5kN. The revised load-displacement curves from all tests are plotted in Figure 5.6 below.

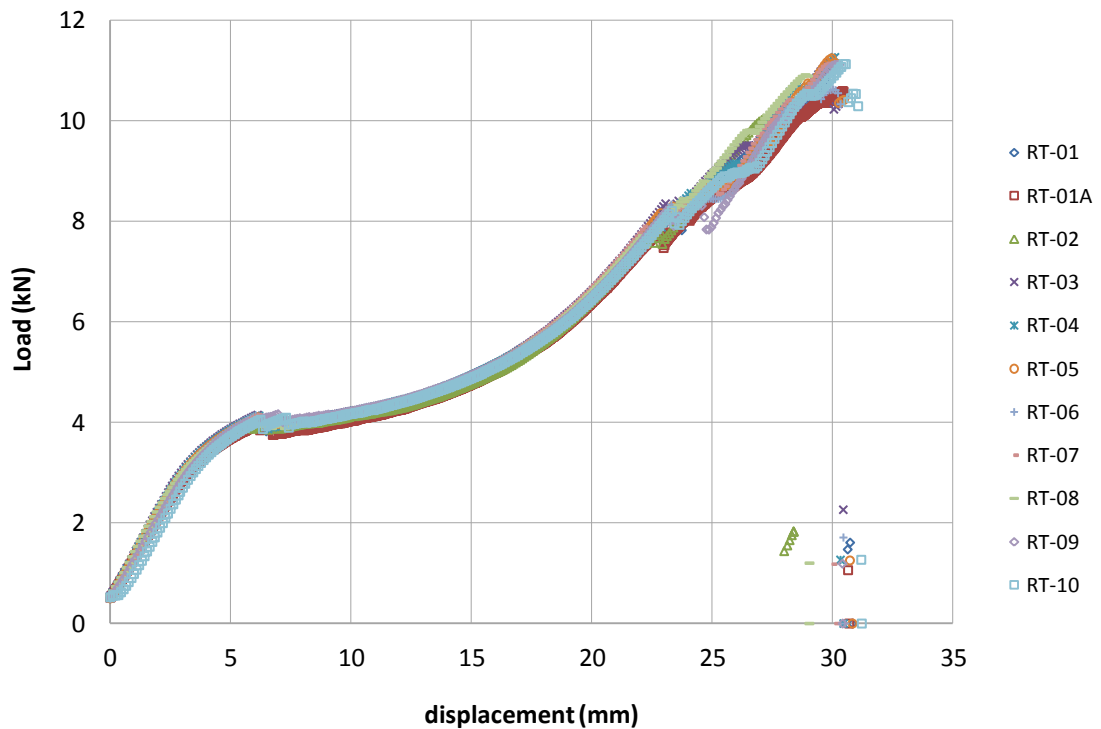


Figure 5.6 Revised load-displacement relationships from test data

For easy comparison, the load-displacement curve generated by the FE model was plotted together with all revised test curves in Figure 5.7 below. The results from FE model were also modified to match the modification of test data shown in Figure 5.6.

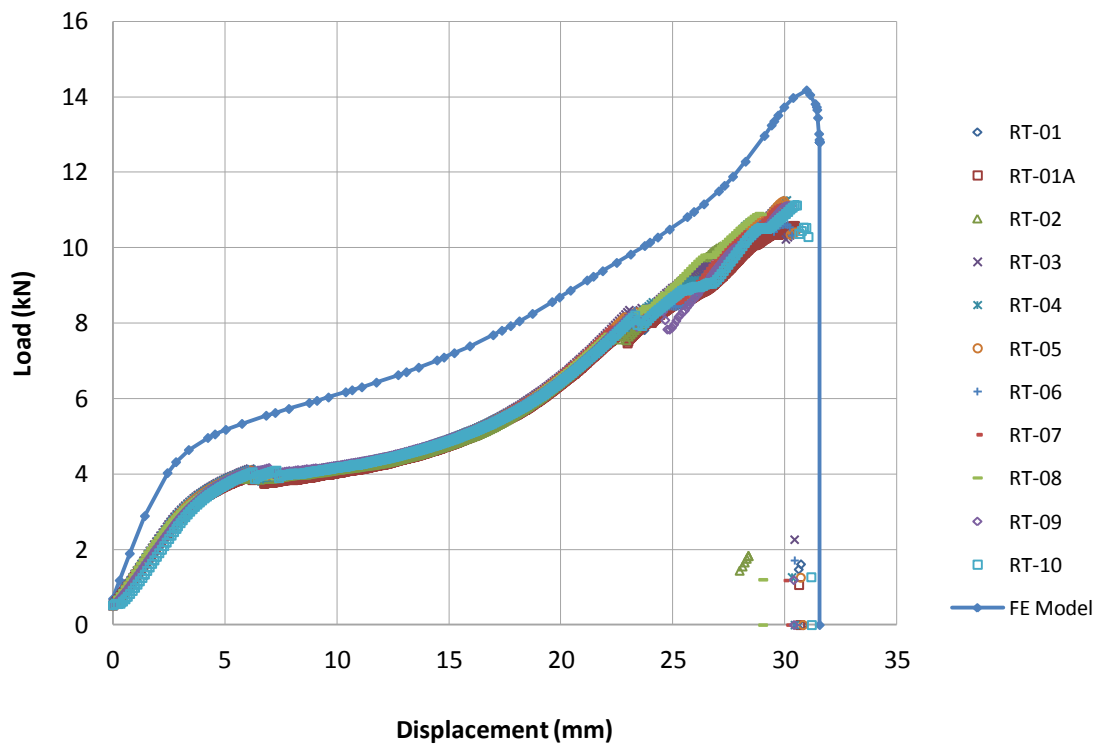
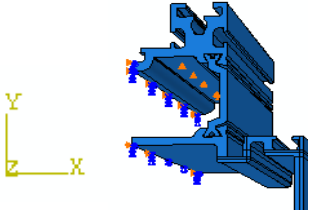
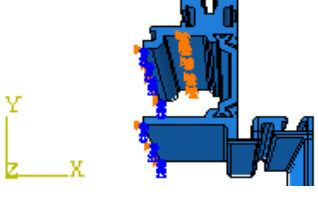
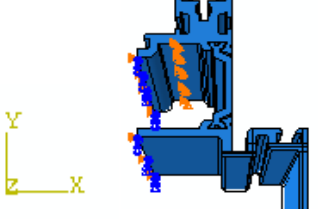
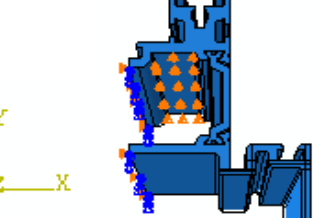
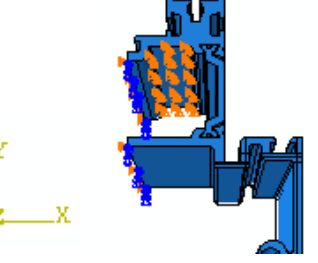
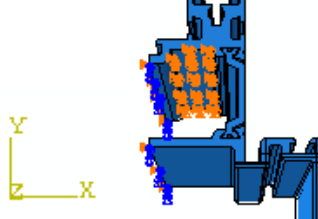


Figure 5.7 Load-displacement relationships – comparison of test and FE model

Figure 5.7 shows that the FE model is much stiffer in the elastic range as well as in the plastic range. The tensile capacity of the FE model is also approximately 30% higher than the test data. Generally speaking, FE modelling simulates ideal situations which have the tendency to give high bound values. However, boundary conditions assigned in the model might affect the results. To find out whether the higher bound results generated from FE models were caused by the boundary conditions, several models with different boundary conditions were generated. As symmetrical section geometry was adopted, symmetrical boundary conditions should be applied for all models so that the applied displacements match the experimental conditions.

Therefore, testing the relevance between boundary conditions and section tensile capacity are only related to changing the top support conditions. The results shown in Figure 5.7 was based on the boundary conditions shown in Figure 4.26 where a simple support (restraint in Y- axis only) was applied at the centre line of the top aluminium part. This model is named as model-1, which is tabulated in the table below together with the other five models with different boundary conditions.

Table 5.1 Boundary conditions

Model Name	Boundary conditions	
Model-1	Line restraint applied at centre line of the top aluminium part. Restrained along Y-axis only.	
Model-2	Line restraint applied at centre line of the top aluminium part. Restrained along all three axes.	
Model-3	Line restraint applied at centre line of the top aluminium part. Restrained along X and Y axes only.	
Model-4	Area restraint applied at the top aluminium part. Restrained along Y-axis only.	
Model-5	Area restraint applied at the top aluminium part. Restraint at X and Y axes only.	
Model-6	Area restraint applied at the top aluminium part. Restrained along all three axes.	

The load vs displacement relationship diagrams of the above models are plotted together in Figure 5.8 below.

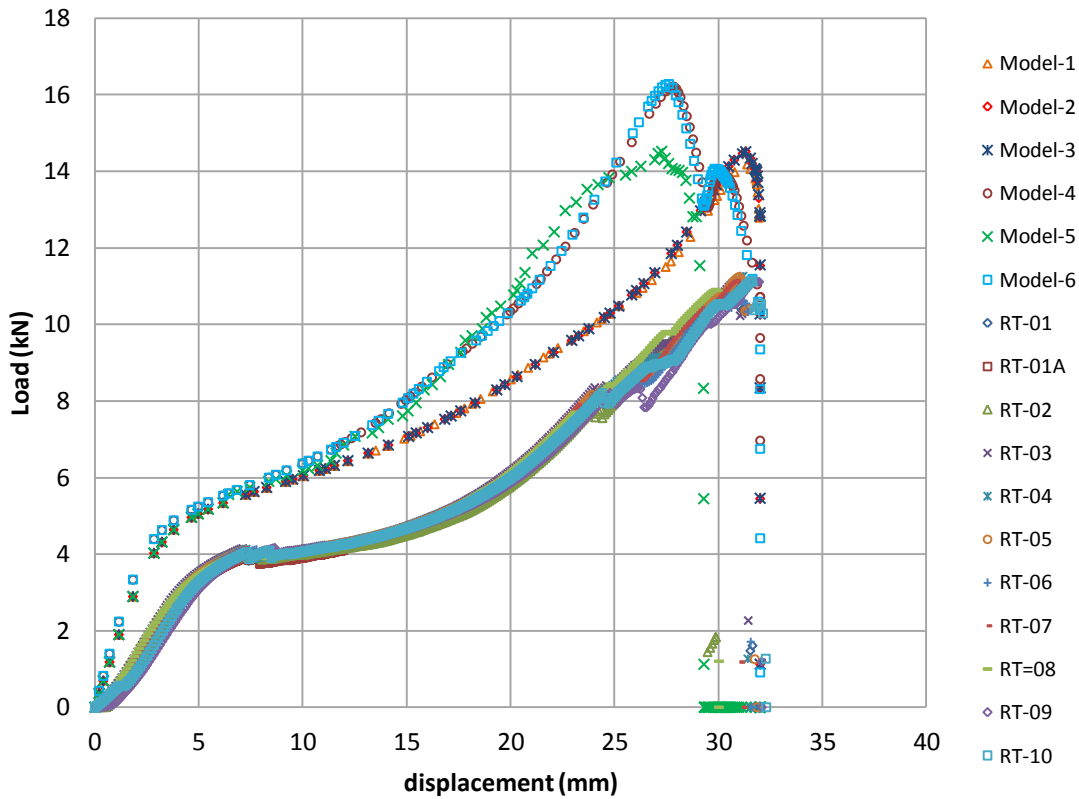


Figure 5.8 Comparison of load-displacement relationship under different boundary conditions

Figure 5.8 shows the results from model-1 to model-6 are all well above the results obtained from experiments. Results from Model-1 to Model-3 are merged into one line which indicates the numbers and directions of restraints applied to the models have no influence on the section tensile capacity. However, results from Model-4 to Model -6 show that section capacity increases as restraint areas increases. Results from Model-1 to Model-3 are closer to the actual test results than the ones from Model-4 to Model-6. Hence, the boundary conditions assigned in the model as Model-1 are suitable.

Calibration of FE model results

Unlike the section shear capacity, the tensile section capacity relies on both material tensile capacity, especially the aluminium alloy, and the connectivity of the connection between aluminium and polyamide. Top and bottom aluminium were distorted before the connection failed. This phenomenon is completely different from shear tests in which the aluminium profiles remained undeformed after the connection failed. This

indicated that material properties play an important role in tensile tests. Therefore, adjusting the material properties of aluminium may be a useful method for calibration of results.

In order to calibrate the FE model to reflect the real situation in experimental testing, equivalent material properties were considered in FE modelling, e.g. Young's modulus, 0.2% proof strength and ultimate tensile strength (E , f_0 and f_u) of aluminium material mentioned in section 4.2.1 were reduced by 30% to match the elastic range of the FE model to the test results. According to section 4.2.1, Ramberg-Osgood continuous material model was adopted to work out reduced nominal stress–nominal strain relationship at plastic and hardening regions. The reduced engineering stress and strain were translated into true stress and true strain. The relationship between them is plotted in Figure 5.9 below.

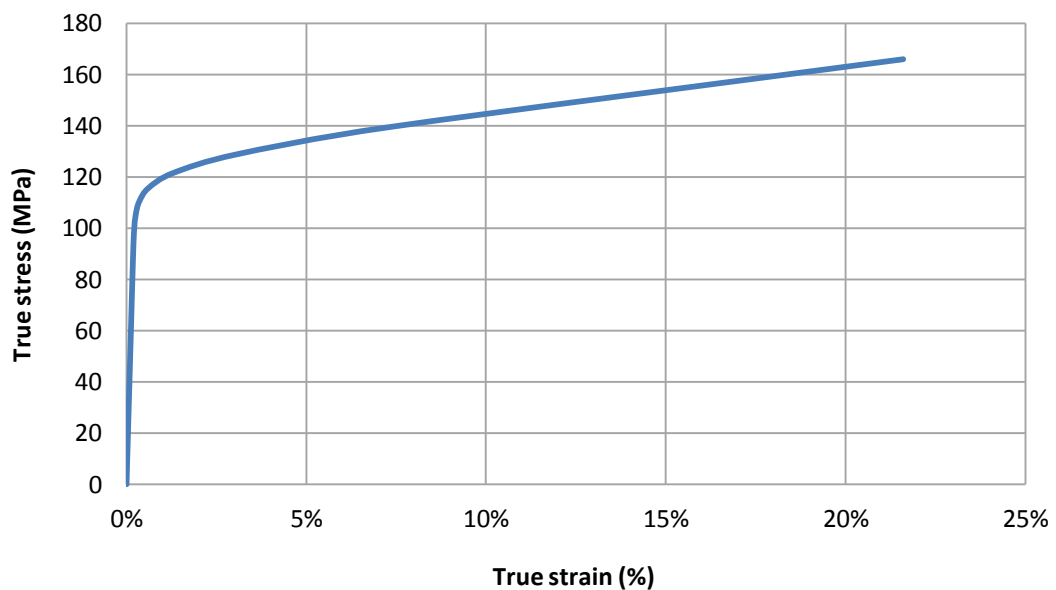


Figure 5.9 True stress – true strain relationship of aluminium alloy 6063 T6 with equivalent Young's modulus and strength

To eliminate the initial settlement of the test, the revised FE model was also modified to make displacement equal to zero at 0.5kN, the same as the revised test data. Comparison of the revised FE model results with test results is shown in Figure 5.10.

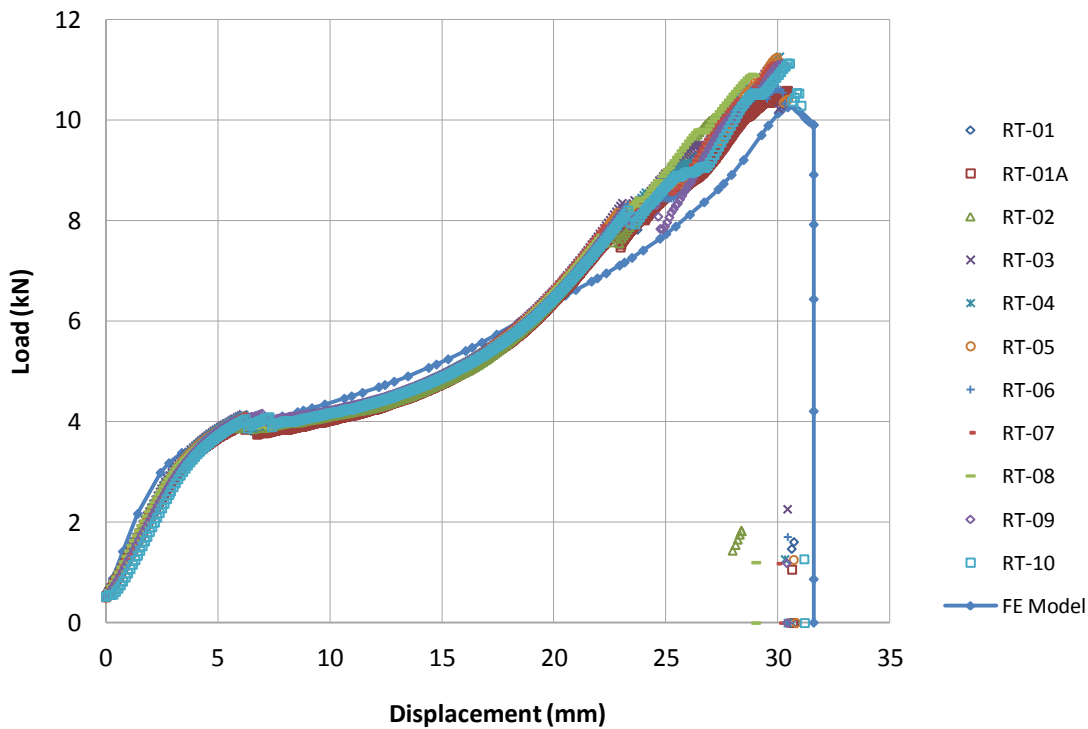


Figure 5.10 Load-displacement relationships – comparison of test and modified FE model

The modified FE model shows good correlation with test data. The elastic portion of the FE model matches the test data although it lies in the top range of the data set. The peak load is in the lower bound of the data which provides a conservative result. The middle plastic portion shows a good approximation with the curves obtained from test data as well. Therefore, the modification method provides an effective and conservative approach to model this type of façade composite profiles in tension.

In conclusion, comparison of deformation and load-displacement relationships between the experiments and the FE modelling was discussed in the section. Deformed shape generated by the FE model provides good match to test specimens. Tensile elongation, as well as bending deformation, dominated the distorted shape. The FE model also provided good simulation of connection failure, i.e., polyamide slipped away from connection.

The load-displacement relationship generated from the FE model results showed stiffer behaviour than the one obtained from experiments. However, the calibration method of using equivalent material properties of aluminium brought the two graphs together. The modified load-displacement curve exhibited good correlation to the experimental curves with a slight conservatism.

5.4 Comparison of beam test results and FE modelling

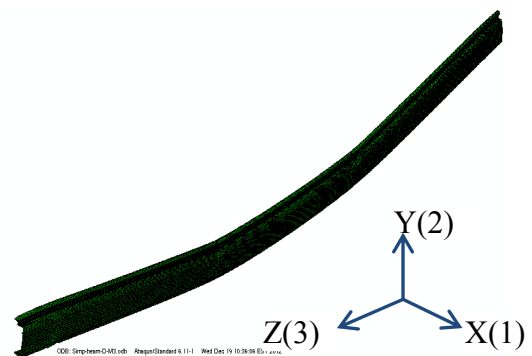
As mentioned in previous chapters, façade mullions are the major load bearing elements in a curtain wall system. The applied lateral loads make them behave as beams in bending. The FE simulation of the façade mullion provides tools to explore the bending behaviour of this type of mullions. A proposed partitioned multi-phase beam failure model was introduced in Chapter 4 to simulate the failure mechanism of this façade mullion. To verify the effectiveness and validity of the FE models, results obtained from experiments and FE modelling are compared and discussed in this section. The comparisons are carried out in relation to deformed shape, load-displacement relationship as well as moment-curvature relationship and strain distribution. The validity of the FE model will be confirmed here.

5.4.1 Comparison of deformed shapes

The deformed shapes generated by the FE models for all types of beams at the end of simulation shows similar behaviour. The beams bent with respect to Y-axis as typical classical beams but the connections failed. This behaviour is comparable to the experimental results. As mentioned in section 3.5, the deformation of all specimens is mainly due to bending but also due to slippage of top connection. This phenomenon is also observed in the FE models. Typical deformed shapes from the FE models are plotted together with test results in Figure 5.11 and Figure 5.12 below for discussion.



Bending deformation of test specimen



Bending deformation of FE model

Figure 5.11 Comparison of bending deformation

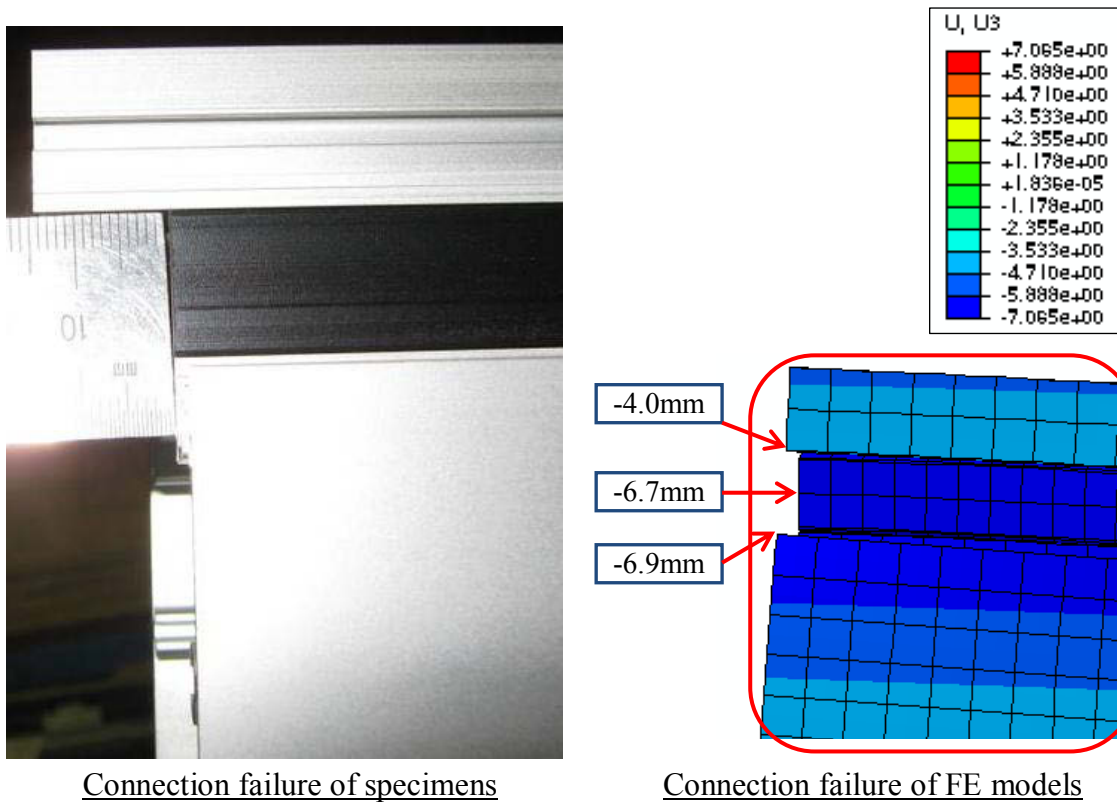


Figure 5.12 Comparison of connection failure

The above displacement diagrams shown in Figure 5.11 indicate that the beam specimens deflect mainly along the Y-axis (local axis of 2-2) which is in the direction of loading. This is consistent with the deformed shape shown on the right of Figure 5.11 for the FE model. In addition, Figure 5.12 displays the comparison of horizontal deformation of the beam between experimental and FE modelling results. As the top of the beam is under compression, the differential displacements shown on the FE model are negative. The differential displacement between polyamide and bottom aluminium part, recorded from both experiments and FE models, are negligible. However, the differential displacement between polyamide and top aluminium part is 2.7mm from the FE models and 14mm, approximately, from the test specimens at the end of the experiments. The differential displacement observed at the end of the experiments is much larger than that recorded from the FE models as the applied displacement on the test specimens was much larger than the applied displacement on the FE models. In order to avoid convergence problems, the applied displacements to the FE models had been limited. The specimens went further into plastic deformation than the FE model. Nevertheless, the FE model was able to capture the phenomenon of top connection failure which was confirmed by the experiments.

5.4.2 Comparison of load vs mid-span displacement

Vertical displacements at mid-span versus loading, for both experimental tests and FE models, were plotted together for easy comparison. Graphs are shown below in Figure 5.13 to Figure 5.16 for each type of beam.

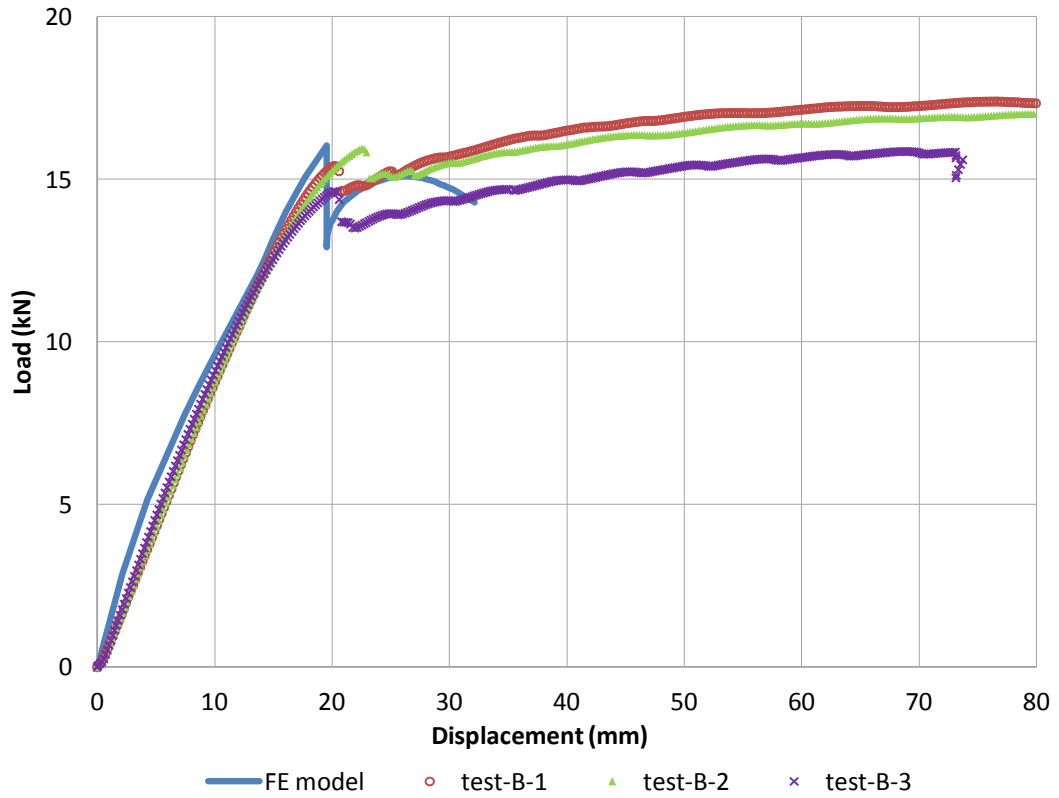


Figure 5.13 Load vs mid-span displacement graph – Type B beam

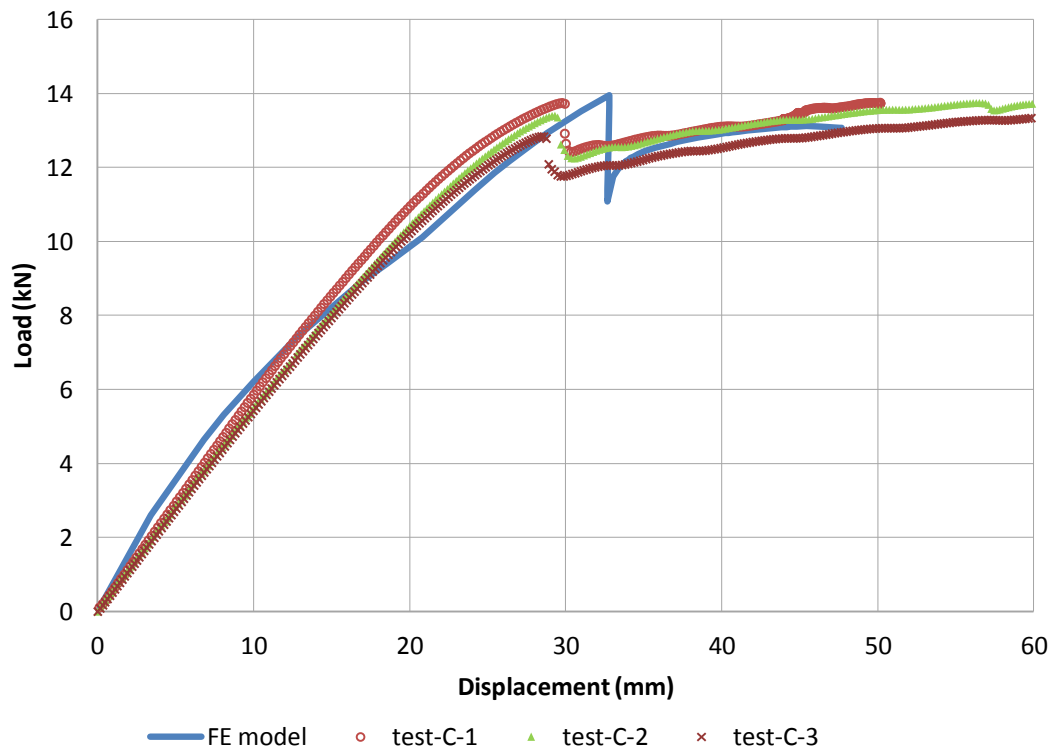


Figure 5.14 Load vs mid-span displacement graph – Type C beam

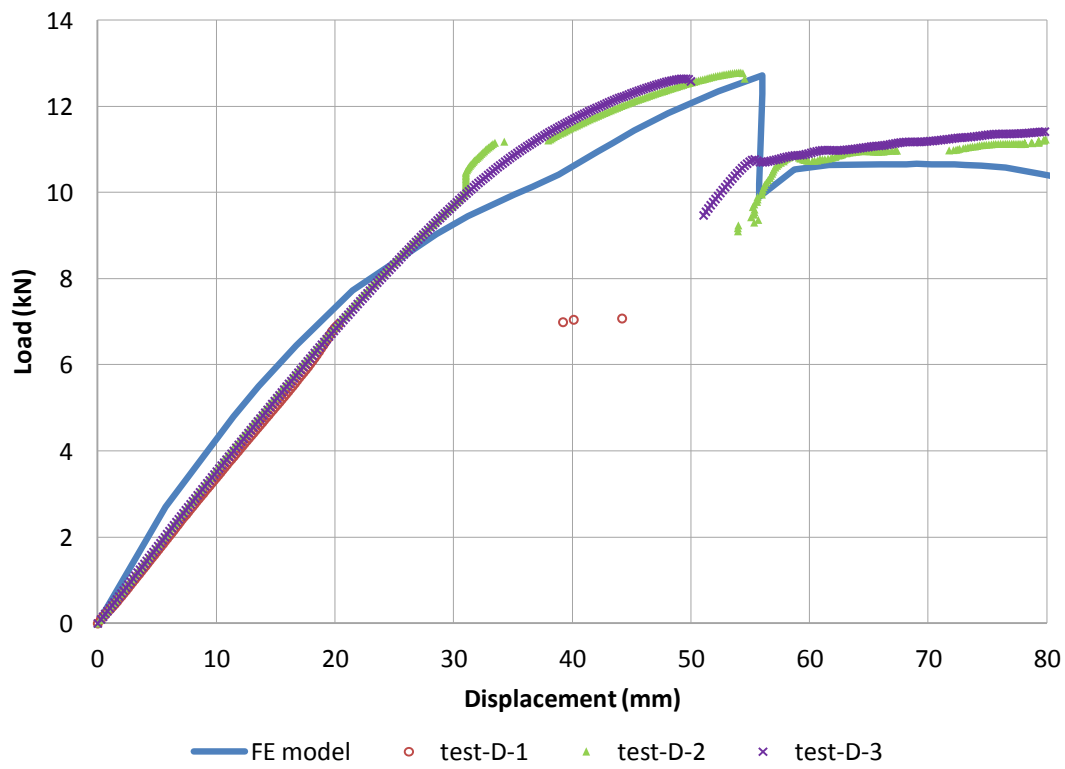


Figure 5.15 Load vs mid-span displacement graph – Type D beam

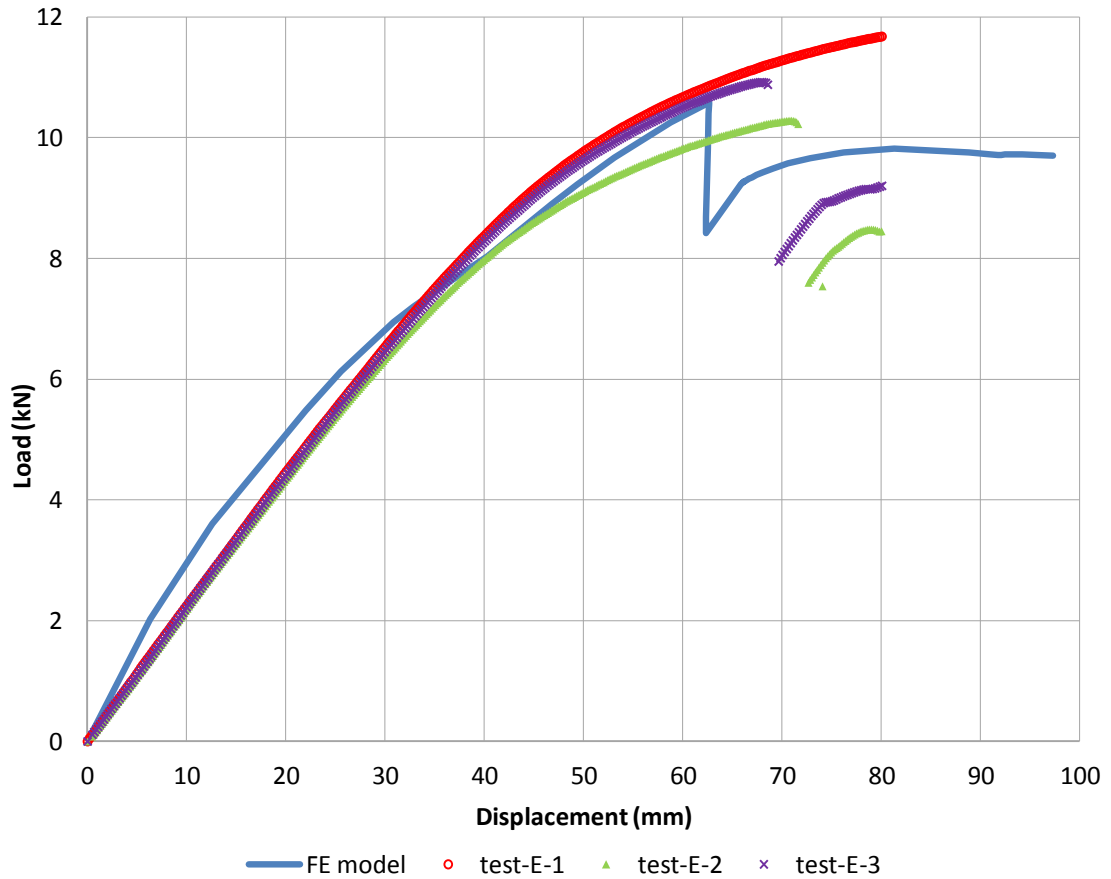


Figure 5.16 Load vs mid-span displacement graph – Type E beam

The above comparison graphs show good correlation between experimental and FE modelling results. The loading capacity of all types of beams reached a peak value, and then dropped down after the polyamide encountered a major slip at the top connection. However, the loading capacity soon picked up after reaching the lowest value at dip. It then went back to the value between peak and dip loads and continuously increased in a slow rate while displacement increased. This three stage failure mechanism was reflected by the FE models although the peak loads reached in the FE models were not at the exact displacements with experiments. However, the specimens within each beam type also showed a small discrepancy regarding displacement when reaching the peak load. This is due to the uncertainty introduced by the manufacturing process to the connections in the specimens. It is, therefore, acceptable. Meanwhile, the values of peak load and dip load obtained by the FE models are comparable to the experimental results.

5.4.3 Comparison of strain distribution diagrams

Since seven strain gauges were placed along the cross section during tests (Figure 3.24), the strain distributions of all specimens can therefore be plotted along the cross-section against the FE model results. Comparison of mid-span strain distributions at critical loading stage – elastic, peak and dip loads are plotted in Figure 5.17 to Figure 5.20 for all four types of beams.

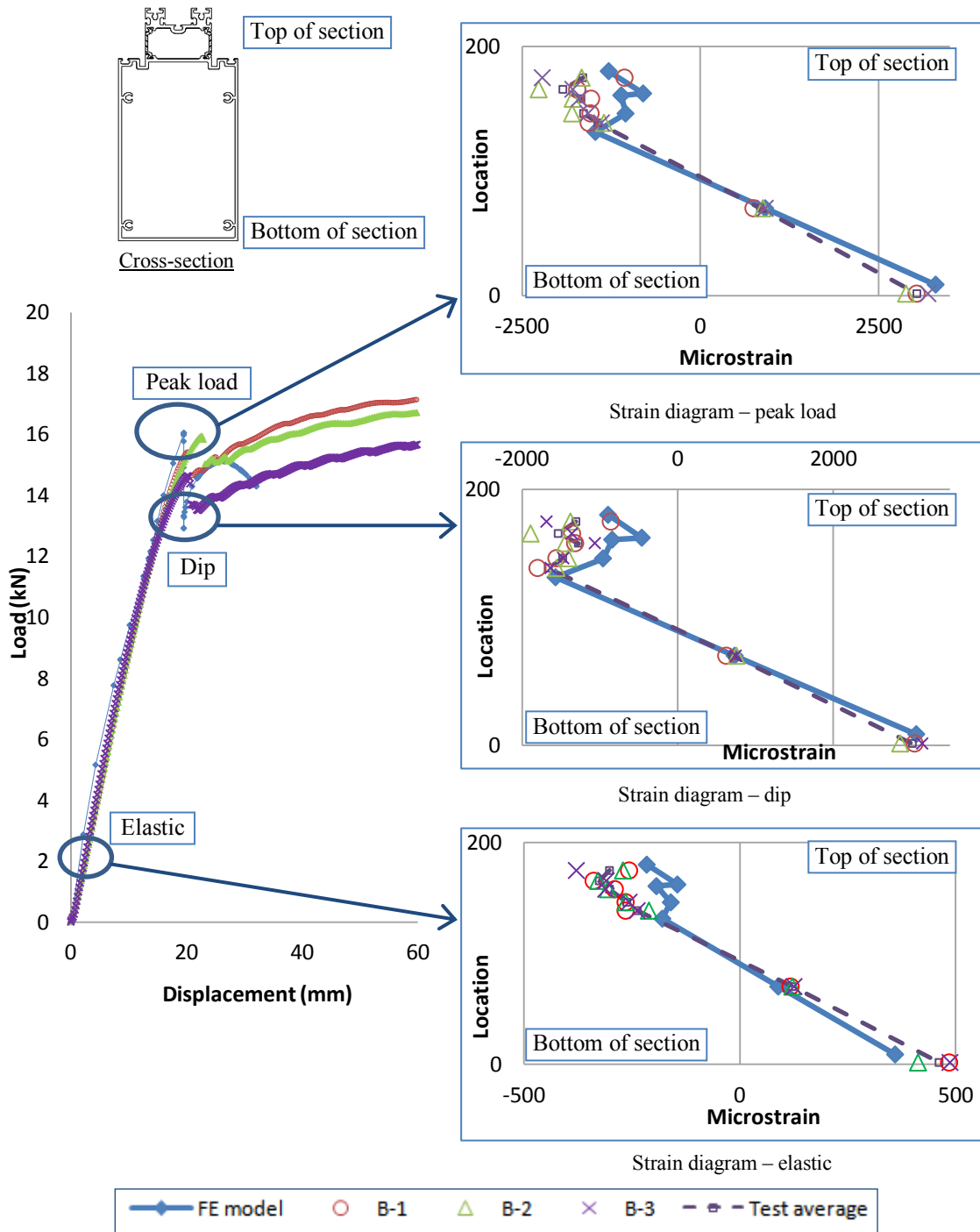


Figure 5.17 Mid-span strain distribution diagrams at critical loading stages – Type B beam

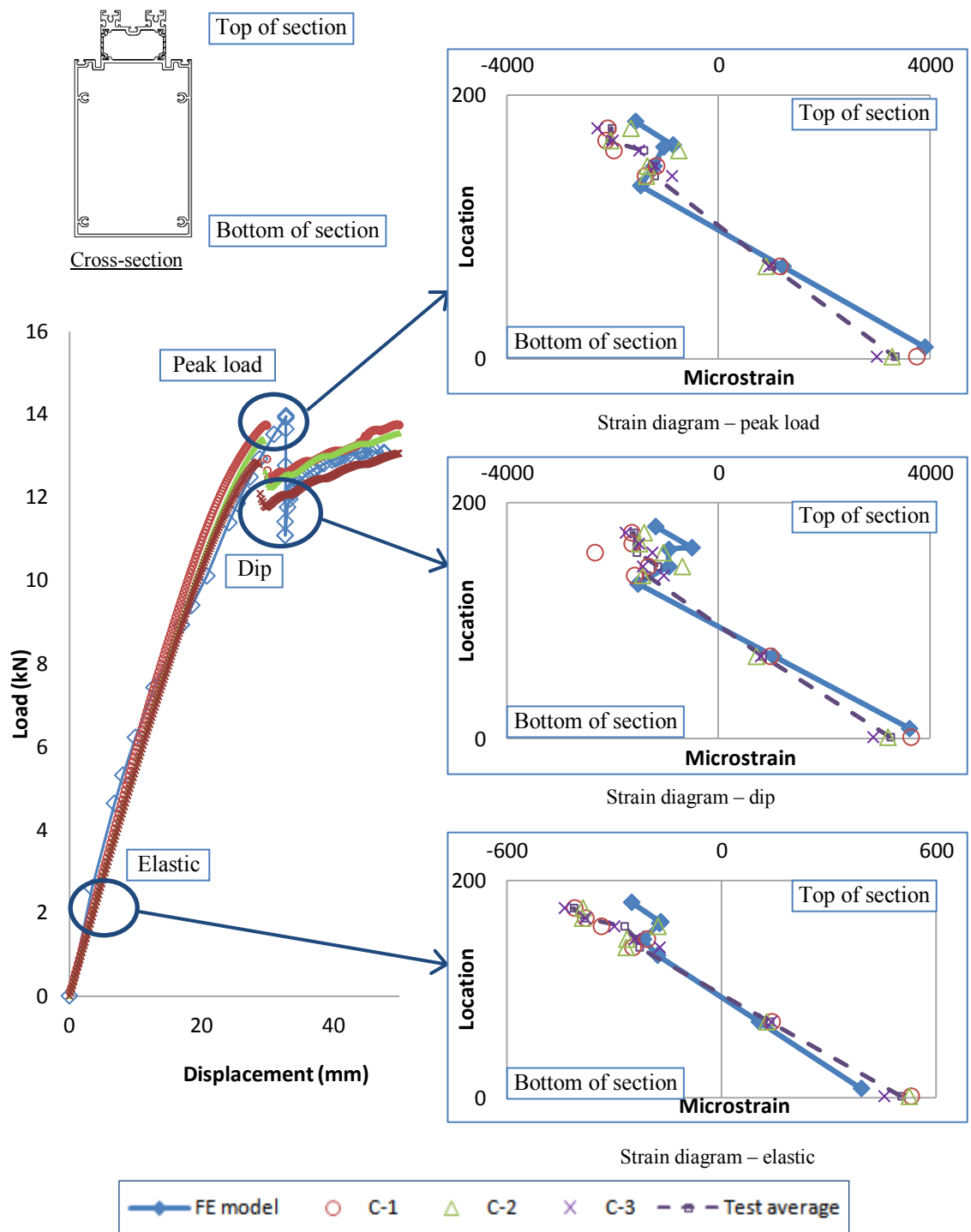


Figure 5.18 Mid-span strain distribution diagrams at critical loading stages – Type C beam

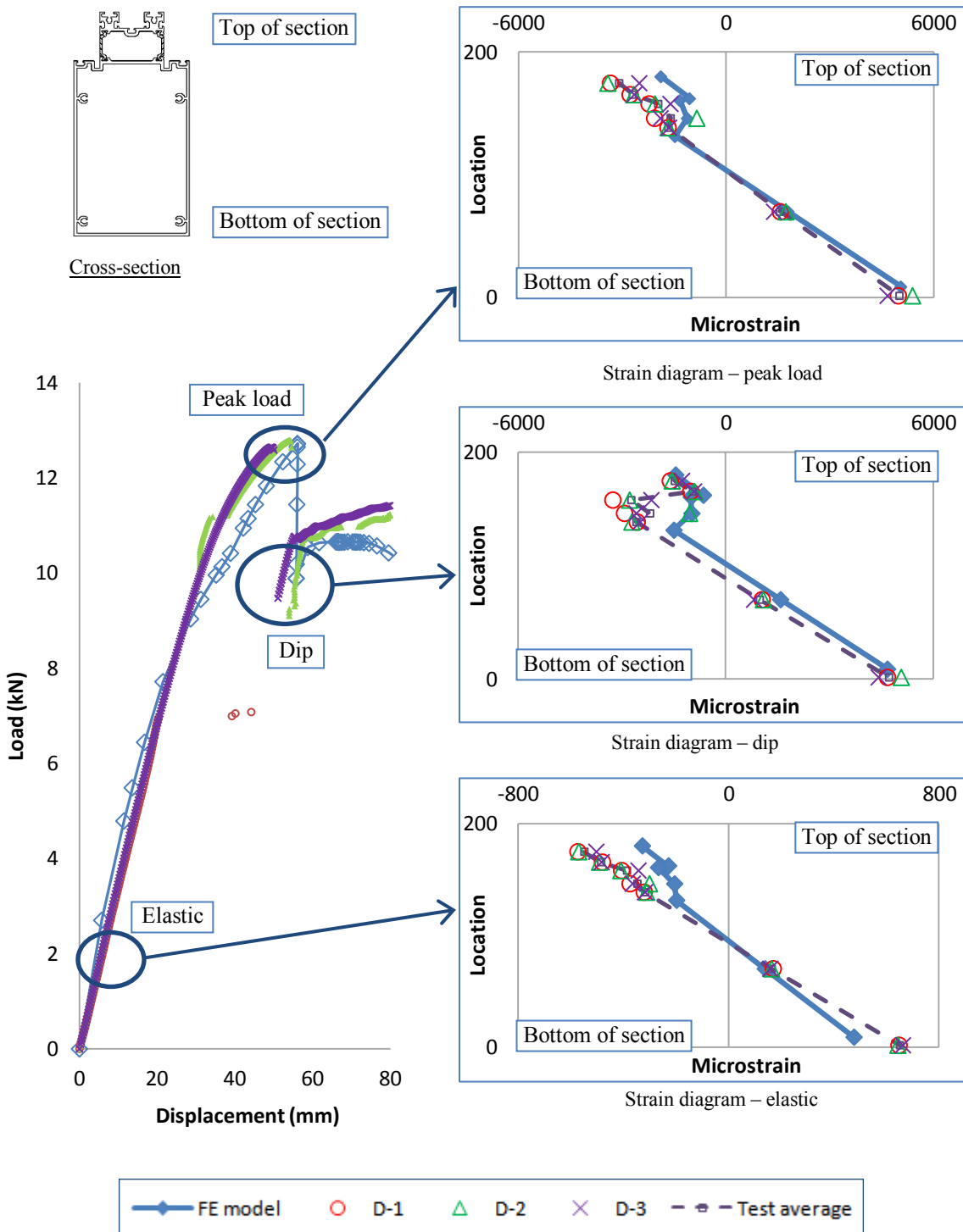


Figure 5.19 Mid-span strain distribution diagrams at critical loading stages – Type D beam

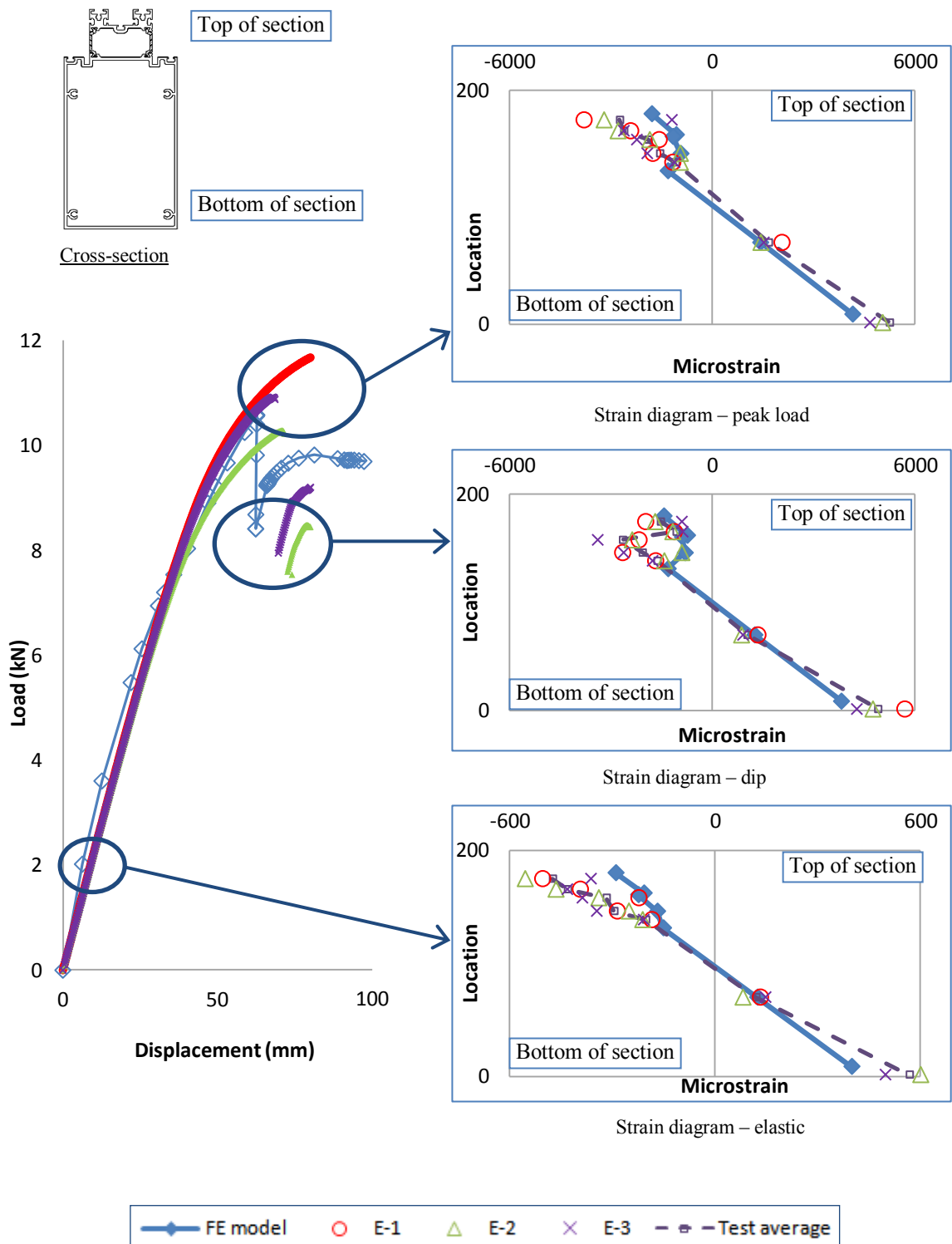


Figure 5.20 Mid-span strain distribution diagrams at critical loading stages – Type E beam

The above mid-span strain distribution diagrams at different loading stages show reasonable correlation between experimental and FE modelling results. The neutral axis location obtained from the FE models is generally consistent with the experimental results. In the elastic range, FE models behaved slightly stiffer than the test specimens as the strain at bottom of AL2 part was smaller than the experimental results. With the

span length increased, the strain distribution of larger span beams were closer to linear than the smaller span beams in the elastic range. This phenomenon was reflected in both experimental and FE modelling results. This is because the effect of elastic connection between aluminium and polyamide increases with the span length increasing (Standard 2004). However, larger strains were observed from FE models than the experimental results in the plastic range. This phenomenon is consistent with the load vs mid-span displacement graphs. It can be observed that the strain distribution obtained from both experiments and FE models is non-linear at peak and dip loads when major slip started and continued. The top aluminium part was under compression. Since the failure process of beam bending was a partitioned multi-phased one, the interfacial actions between the top aluminium part and polyamide at mid-span under pure bending was observed to display only minor changes. However, as the other parts which were under combined bending and shear forces lost composite action, the bending part which did not go through major slippage of connection can no longer act as a compressive top portion of the whole section. It just rested on the top of polyamide and bottom aluminium combined section working independently and was subjected to compression only. However, the compressive strain was small. The strain at this top part of the cross-section shows small discrepancies between FE modelling and experimental results. As the connectivity of the connections is not uniform across the specimens, the experimental results between specimens were also showing discrepancies as well. However, improvements might be able to be made in future refinement of the FE models in further studies of this type of composite façade mullions.

5.4.4 Comparison of moment-curvature relationship

In a composite section, it was assumed in the sandwich theory that thick faces of a sandwich structure may undergo local bending deformation (Allen 1969). When the sandwich bends as a whole, the faces take part in bending about its own centroidal axis plus bending about the whole sectional centroidal axis. Due to the different geometry of top and bottom aluminium parts (faces), the curvature of top and bottom faces might not be the same. It is therefore necessary to investigate the curvatures at top and bottom extreme fibres and obtain further understanding of the bending deformation.

Classic beam theory with full composite action

Like other homogeneous flexural members, when the connections are intact, this composite façade mullion section is assumed to remain plane after bending; the neutral axis of the cross-section is constant along the beam length. Curvatures on the cross-section can be calculated by strain and neutral axis location. To calculate curvature, the methodology presented by (Hibbeler 2008) was adopted to study a segment from a beam in bending.

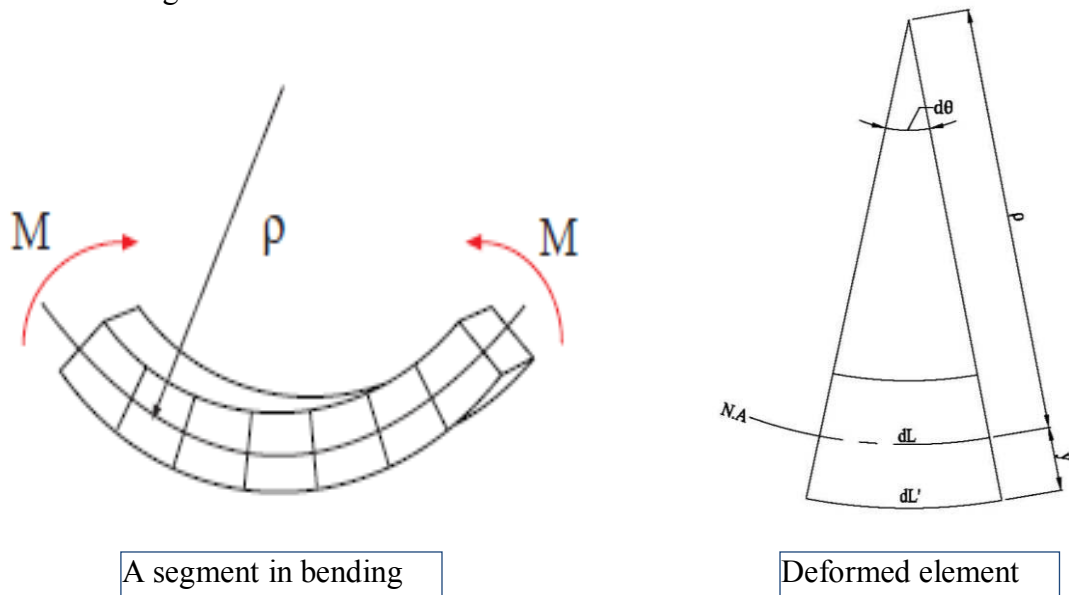


Figure 5.21 Illustration of a bent segment

In Figure 5.21 above,

ρ indicates the radius of curvature

$N.A$ indicates the neutral axis of the section

M indicates the applied bending moment

For the small element shown in Figure 5.21, the following relationships can be obtained

$$dL' = (\rho + y)d\theta$$

$$dL = \rho d\theta$$

$$dL' - dL = y d\theta$$

$$\text{Therefore, strain } \epsilon = (dL' - dL) / dL = y d\theta / dL = y / \rho \tag{5.1}$$

$$\text{Since curvature } K = 1 / \rho \tag{5.2}$$

Combining Eq.5.1 and Eq.5.2, we get

$$K = \epsilon / y \quad (\text{strain and curvature relationship}) \quad [5.3]$$

From elastic beam bending theory, we know the extreme fibre stress is

$$\sigma = My/I \quad (\text{bending stress due to } M) \quad [5.4]$$

$$\epsilon = \sigma/E \quad (\text{Hook's Law}) \quad [5.5]$$

Combining Eqns. 5.4 and 5.5, we obtain

$$\epsilon = My/EI \quad [5.6]$$

Substituting for ϵ from Eq. 5.6 into Eq. 5.3, we can find moment-curvature relationship as

$$K = M/EI \quad [5.7]$$

where, EI is the flexural stiffness of the beam

The strain-curvature relationship stated in Eq. 5.3 and the moment-curvature relationship stated in Eq. 5.7 are general forms for composite beams only where the strain distribution is linear along the cross-section (Ferdinand P. Beer and E. Russell Johnston 1992). Unfortunately, it is only in the elastic range before slip when the strain distribution can be treated as approximately linear. With increasing loading, minor slippage might take place. After major slippage occurred, the strain at top of the section had no correlation to the bottom part at mid-span location as shown in Figure 5.17 to Figure 5.20 for both experimental and FE modelling results. However, it still kept a linear relationship between the polyamide and bottom aluminium parts. Therefore, the curvature at bottom of the section can be calculated by Eq. 5.3. As the top aluminium part was under pure compression without bending at mid-span, it is meaningless to discuss curvature at this section. Hence, the moment-curvature relationship was studied against bottom extreme fibre curvature only for the full loading process.

As seven strain gauges were installed onto every specimen during testing, the strains at these points can be used to calculate the neutral axis location and curvatures at bottom extreme fibre of the cross-section at each loading increment by Eq. 5.3. For FE models, seven corresponding points were chosen along the cross-section at mid-span to obtain strains at these points and work out neutral axis location and, therefore, calculate curvatures at each loading increment.

Moment-curvature graphs of bottom extreme fibre at mid-span location for each type of beam were plotted together with experimental results below for comparison (Figure 5.22 - Figure 5.25).

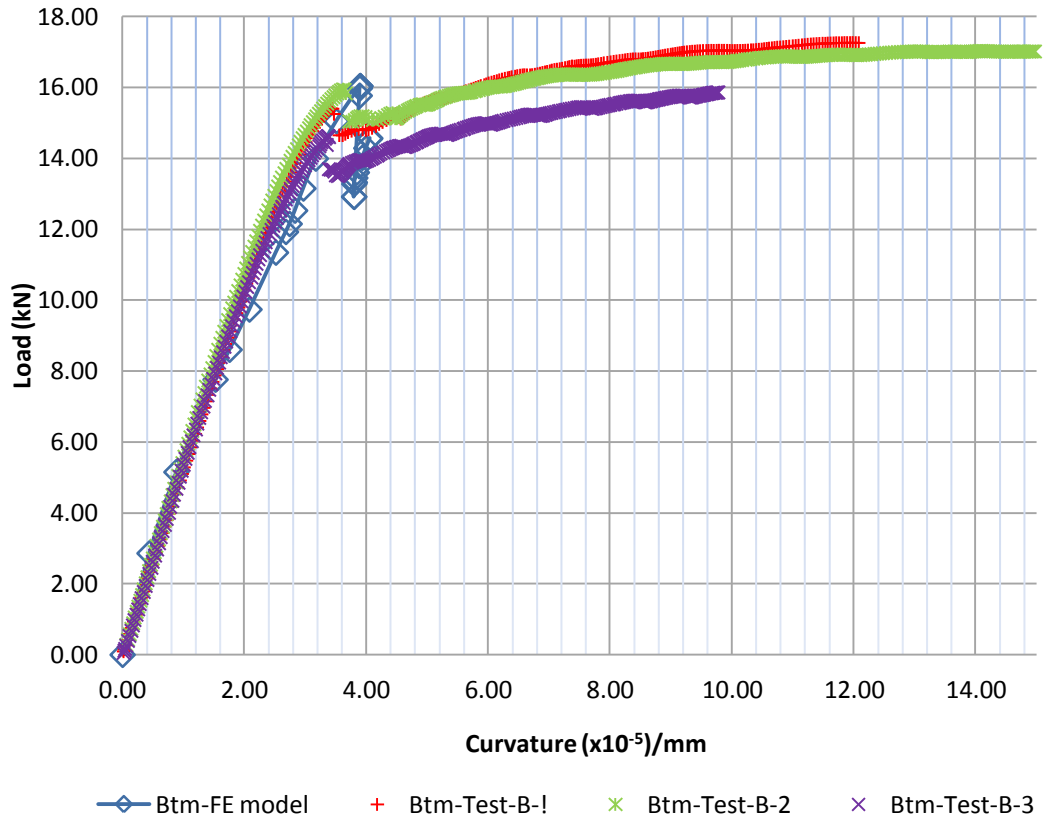


Figure 5.22 Load vs bottom curvature at mid-span location – Type B beam

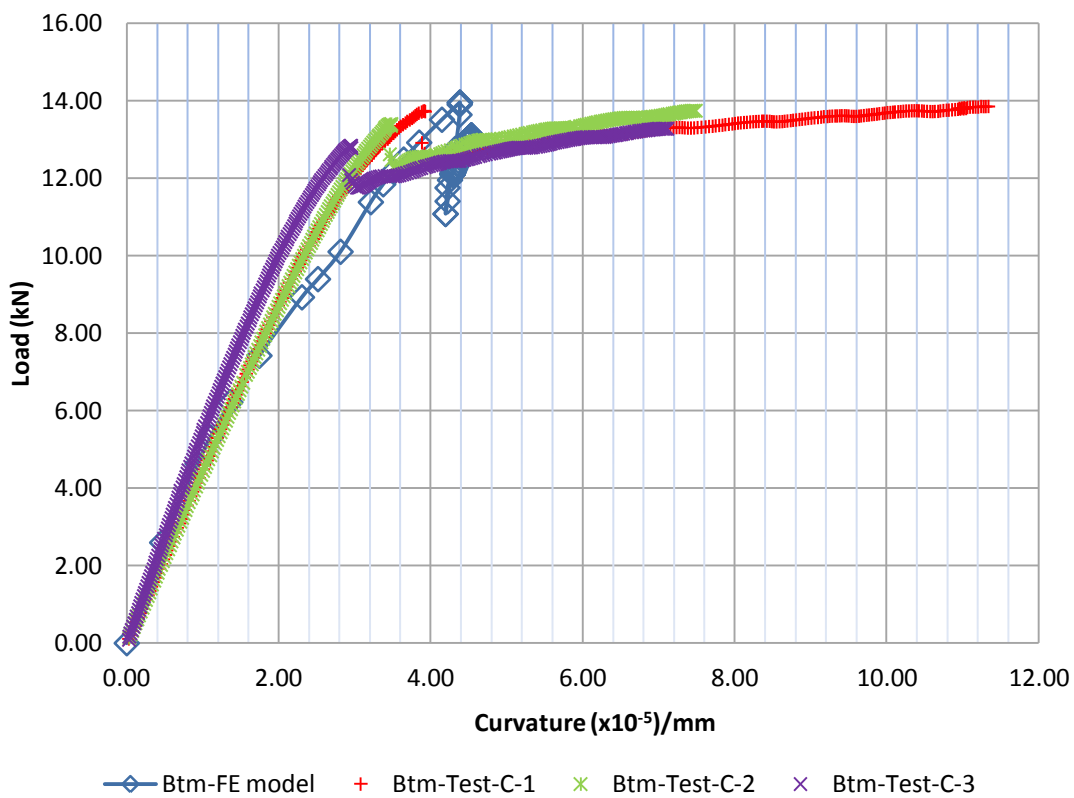


Figure 5.23 Load vs bottom curvature at mid-span location – Type C beam

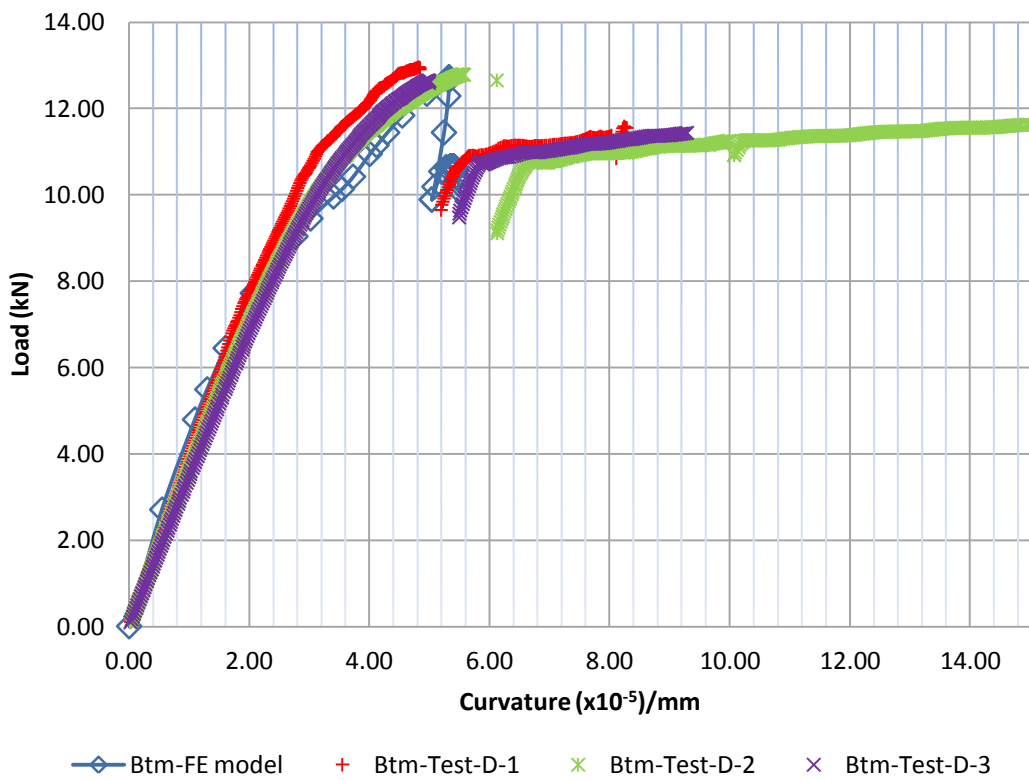


Figure 5.24 Load vs bottom curvature at mid-span location – Type D beam

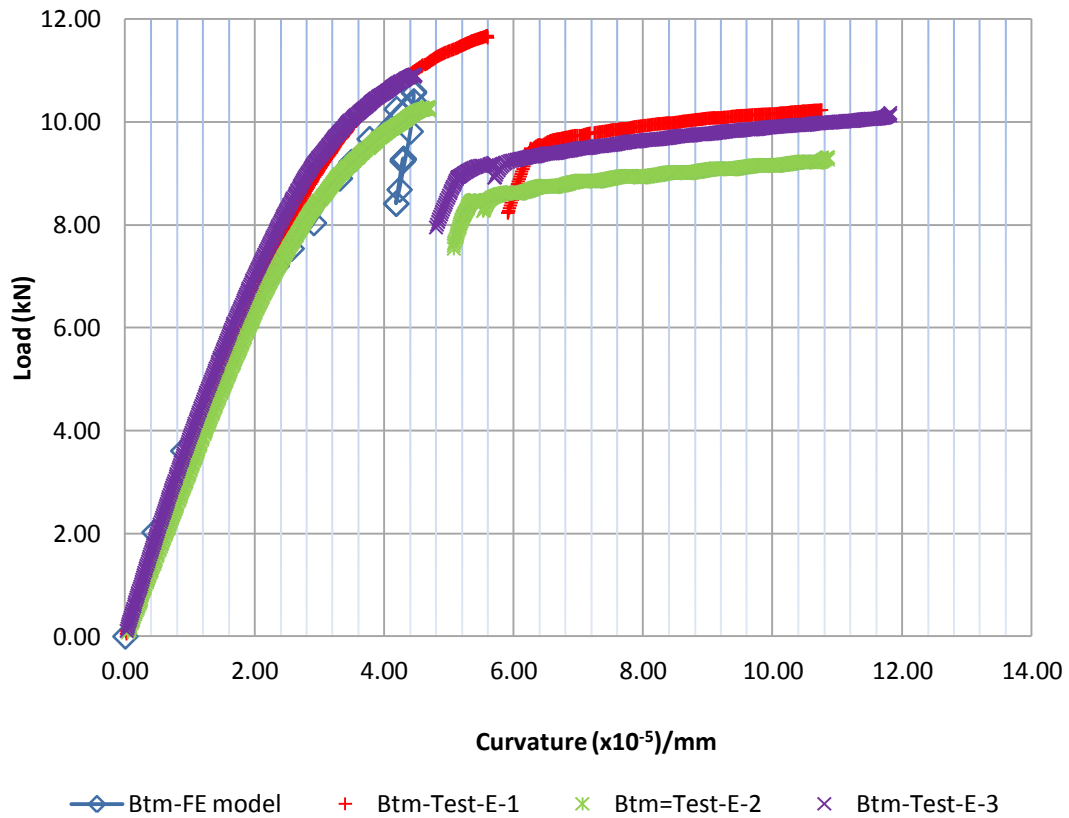


Figure 5.25 Load vs bottom curvature at mid-span location – Type E beam

The graphs above show comparable results between experiments and FE models. The moment-curvature curves generated by FE models fell in the range of experimental results. Based on the comparisons of deformation, strain distribution and moment-curvature relationship at mid-span, it can be concluded that the FE models were able to provide good correlation to the experiments and, therefore, are useful for further investigation of the façade beam.

Further investigation of bending behaviour in plastic range

Further investigation into the strain distribution in the combined bending and shear loaded portion of the beam is based on the results from FE models. The strain distribution diagrams are plotted for each type of beam in Figure 5.26 below at the location of region C (refer to Figure 4.42) near one-third of span to investigate the behaviour of top aluminium part after slip. It was found that the top aluminium was bent at its own centroidal axis. The top extreme fibre was under compression while the bottom one was under tension. In the meantime, the bottom aluminium part was also bent at its own centroidal axis as well. This phenomenon confirmed the curvature at top and bottom extreme fibre of the composite section was different after slippage occurred

in the plastic range. In addition, comparison of strain distribution diagram at mid-span location with the above one (at near one-third of span) at dip load, shown in Figure 5.26, clearly reported the different behaviour between regions along the beam span. At the pure bending region, although only minor slippage might occur, the failure of interfacial section on the other regions stopped this region of the top aluminium part bending together with the bottom part. With the failure of connection in combined bending and shear force loaded regions, the top and bottom aluminium parts acted separately. This finding confirmed the validity of the proposed partitioned multi-phase failure model and will help to develop the analytical model to calculate this type of composite sections.

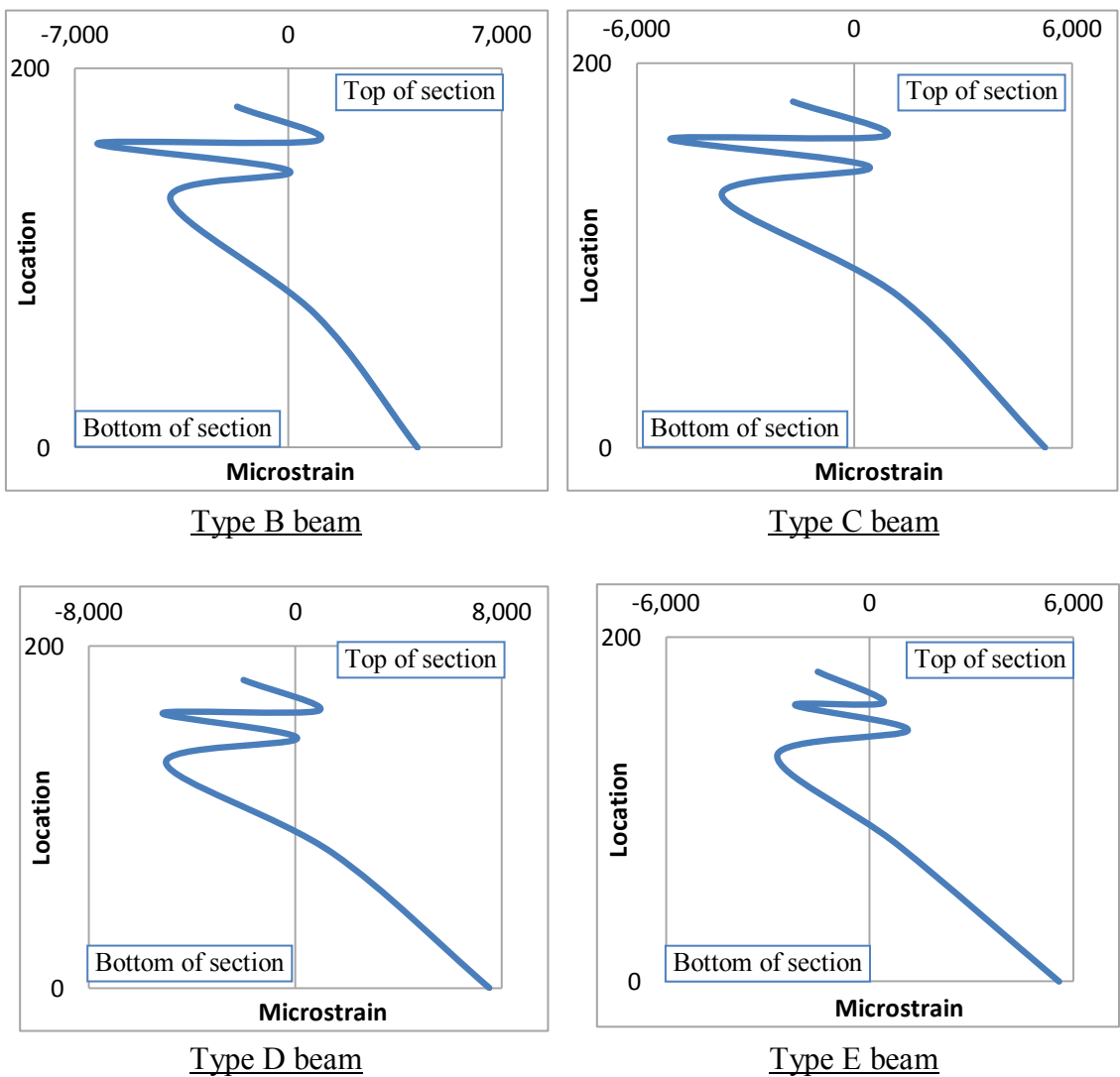


Figure 5.26 Strain distribution diagrams in the location of combined bending and shear forces – all beam types

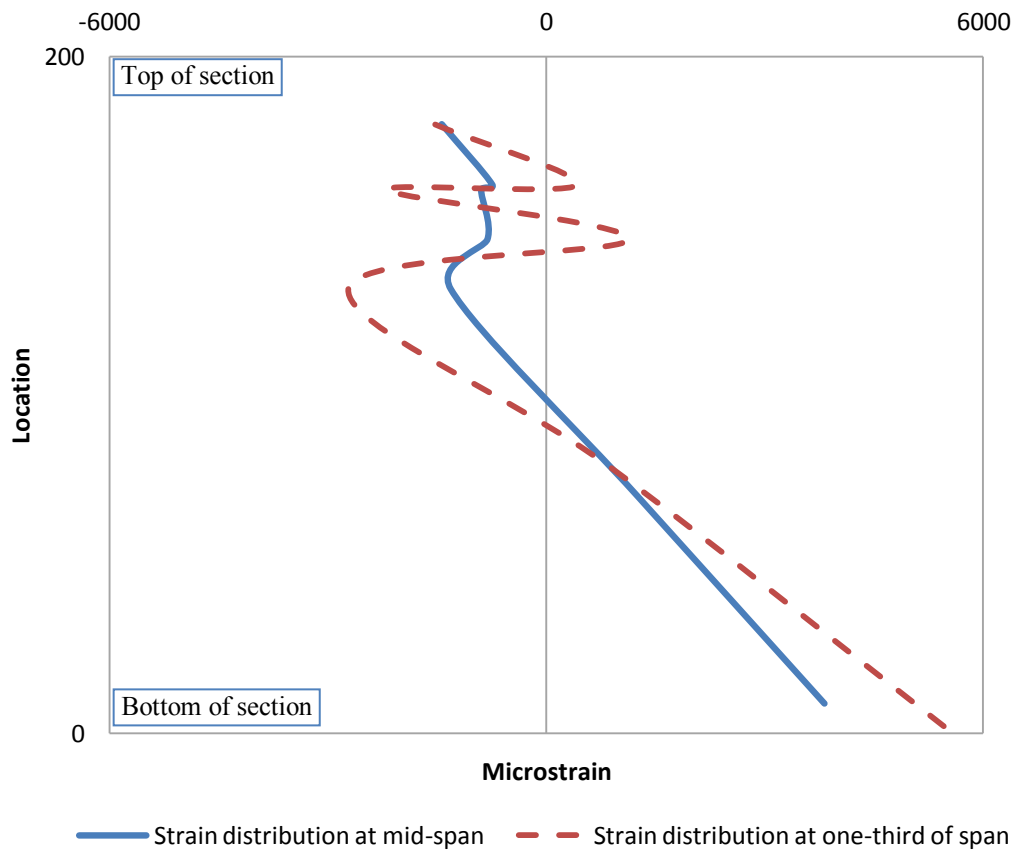


Figure 5.27 Comparison of typical strain distribution diagrams at dip load between regions under pure bending and under combined bending and shear forces

In conclusion, the FE models provided good correlation to the experiments. Deformed shapes generated by FE models well matched the experimental ones. Failure of top connection between aluminium and polyamide was observed in both experiments and FE models while the bottom connection was kept intact in FE models and experiments. Strain distribution at mid-span was studied and comparison was made. The results from FE models have relatively good consistency with experimental ones although improvement can be made in future studies. Comparison was also made to load vs mid-span displacement relationship graphs. Again, the FE models provided good correlation with experimental works. When the beam reached the peak load, slippage occurred at the top connection. The load carrying capacity dropped down quickly to the dip load then rose to the capacity between peak and dip load and then gradually went up with increasing displacement. Mid-span moment vs curvature relationships at bottom extreme fibre of all beam types, obtained from FE models and experiments, were consistent. Further investigation at the location under combined bending and shear forces at plastic range were carried out based on the FE models. The strain diagrams

showed the top and bottom aluminium parts bent along their own centroidal axis after major slip. It, therefore, confirms that the top and bottom curvatures have no relationship after slippage occurs in the plastic range.

5.5 Summary and conclusion

In this chapter, comparisons of results between experiments and FE models were made and discussed. For shear capacity test and FE model, failure mode and deformed shape were compared as well as relationships of load-slippage of connection. Similar comparisons were made to the tensile capacity tests and FE model. To eliminate the initial settlement generated in the tensile experiments, both test data and FE model results were modified to make displacement equal to zero at the loading of 0.5kN. To calibrate the FE modelling results to match the test ones, a rectification method by applying equivalent aluminium material properties was adopted. This method helped to match the load-displacement graph generated from the FE model to the ones from experiments.

To verify the FE models of four-point bending beams, deformed shapes and slippage of connections were compared between experiments and FE models for all types of beams. Comparisons were also made to the relationship of load vs mid-span displacement, strain distribution at mid-span along the cross-section and relationships of moment to bottom curvature as well.

In conclusion, the FE models had generally good correlation with the experiments. The deformed shape generated from the FE model for shear capacity test, provided idealised slippage location which was confirmed by the experimental work. The load-slippage curve obtained from the FE model matched the experimental results very well. The consistency between the FE model and experiments strongly proved that the proposed progressive failure model created to simulate the shear tests was appropriate.

The comparison of deformed shapes between the FE model and tensile tests showed a reasonable correlation. Both deformed shapes showed not only tensile deformation but also bending deformation, especially at the shoulder of specimens. The failure mode produced by the FE model matched the experimental ones which was the polyamide slipping away from the connection. Although load-displacement graphs between the FE model and experimental works had discrepancies, an effective rectification method was able to reduce the gap between them. As the tensile strength of the section is affected by

tensile strength of the aluminium alloy and the connectivity of the joint, adjusting material properties of aluminium alloy is an effective approach. By applying the equivalent material properties of aluminium, the relationship of load-displacement obtained from the FE model showed good agreement to the results from the experimental ones.

In terms of beam bending models, results generated by the FE models and experimental works indicated a good correlation between them as well. After successfully applying the proposed partitioned multi-phase failure model, the FE models generated consistent deformations with the experiments. At the end of loading, the top aluminium part slipped away and lost load carrying capacity while the bottom connection was intact for both tests and the FE models. Consistency was observed when studying the relationship of load vs mid-span displacement between FE models and experimental results. Both reached the peak loads before major slippage occurred. After slip, the load carrying capacity dropped down quickly to the dip load, and then gradually picked up in a flat rate with increasing displacement.

The mid-span strain distribution diagrams in the elastic range showed linear relationship across the section and consistent between experiments and the FE models. After major slippage occurred, the top aluminium part lost connection to the bottom part at the regions under combined bending and shear forces. It was observed under pure compression at mid-span but with a relatively small compressive strain, although negligible, slippage was detected in this region from the FE models (Figure 4.46). The results obtained between experiments and FE models were relatively consistent; however, further improvements can be made in future studies. Further investigation was carried out to study the behaviour of the section after major slip. Strain distribution diagrams generated by the FE models were plotted at the location for all types of beams involving combined bending and shear forces. The comparison of strain distribution between these regions was also plotted. These strain distribution diagrams showed the top and bottom aluminium bent at their own centroidal axis after slip.

The relationship between moment and curvature at bottom extreme fibre obtained from the FE models and experiments at mid-span matched relatively well. In general, the FE models of all types of beams provided consistent results with the experimental works.

This finding confirmed the effectiveness of the proposed partitioned multi-phase failure model in numerical simulation.

Chapter 6

Numerical Investigation of Other Profiles with Similar Connection Details

6. Numerical investigation of other profiles with similar connection details

6.1 Introduction

Aluminium has been used widely as the major building material for modern curtain wall façades since twentieth century. Its material property of being able to be extruded into any shape brings architect's imagination into reality. Now, the aluminium extrusions are designed with unlimited shapes and complexity. To improve thermal isolation, glass fibre reinforced polyamide was introduced as a thermal break to join the external and internal aluminium extrusions together. The various external and internal combinations of extrusions add countless variety of façade curtain walls. As a major load bearing element in the curtain wall system, thermal break façade mullions are shaped to suit architectural requirements.

Although the thermal break mullions can be built in many desired shapes, the connection between aluminium extrusions to polyamide thermal break is almost identical. The glass fibre reinforced polyamide is machine rolled into pre-knurled aluminium extrusion.

In this research, a typical thermal break façade mullion section was investigated. Methodology of carrying out numerical analysis was detailed in Chapter 4. The developed methodology will be used in this chapter for numerical investigation of another profile – a special asymmetrical mullion profile. Finite element models will be built to test the shear and tensile capacity of this asymmetrical mullion profile. A four-point bending beam will be built as well. ABAQUS/ CAE version 6.11 is adopted for all FE modellings. The numerical investigation will provide comprehensive details of connectivity between aluminium and polyamide and section shear and tensile capacity as well as bending capacity.

6.2 Numerical investigation of the section shear capacity

6.2.1 Section geometry

An asymmetrical mullion section comprising external and internal aluminium profiles made of aluminium alloy 6063T6 and joined by 25% glass fibre reinforced polyamide is studied. The geometrical details of the section are presented in the graph below.

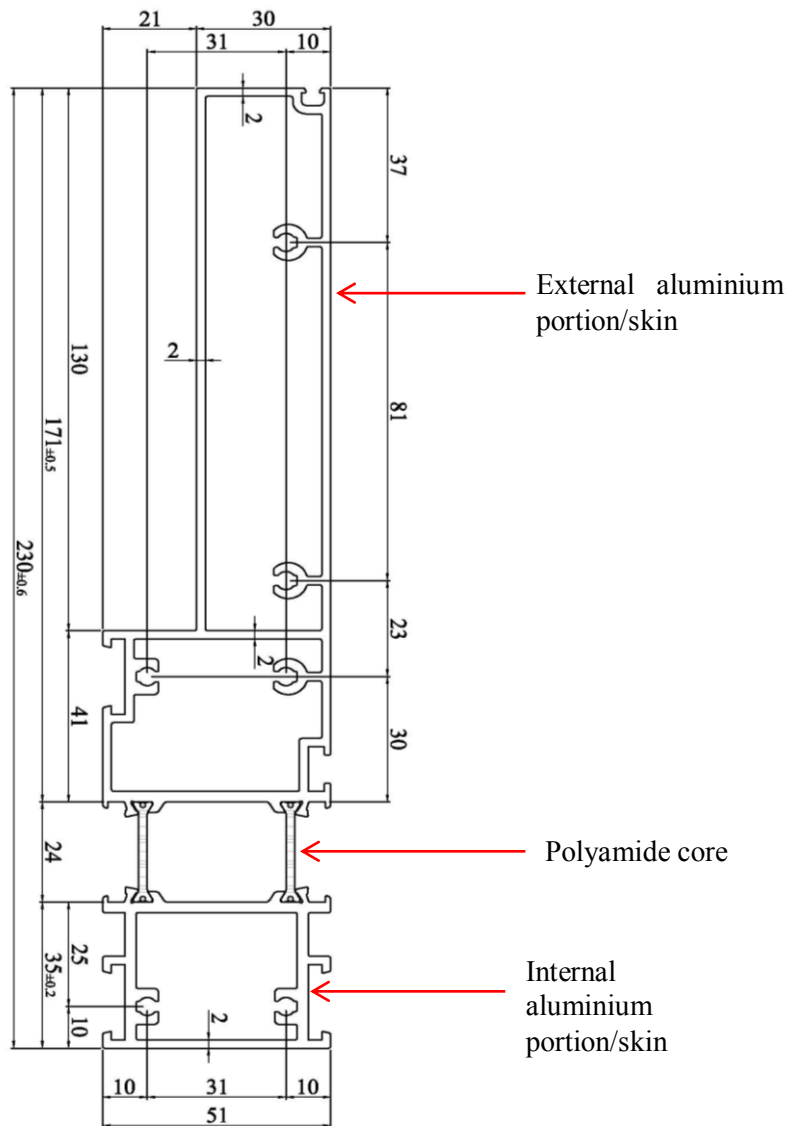


Figure 6.1 Geometry of the asymmetrical mullion section under study

6.2.2 Model setup

To investigate the shear capacity of this asymmetrical thermal break section, a three dimensional finite element model was set up by using ABAQUS software. The geometry of this section was converted from an Autocad drawing file supplied by the manufacturer to a standard ACIS text file (SAT) and then imported into ABAQUS software. This section was imported as three separate parts and assembled together by position constraint tools.

Each part is 100mm long, according to the requirement of EN14024:2004 (Standard 2004), and imported as a deformable solid. The internal aluminium part (AL1) was partitioned into several portions to allow boundary condition and load assignments. The external aluminium part (AL2) was also partitioned into two portions for the assignment of boundary conditions. The polyamide core was kept as one piece. The partition assignment is shown in Figure 6.2 below. When partitioning the aluminium parts, same principles mentioned in Chapter 4 were adopted. Edge, face and cell partition toolsets were used to define the location of cells.

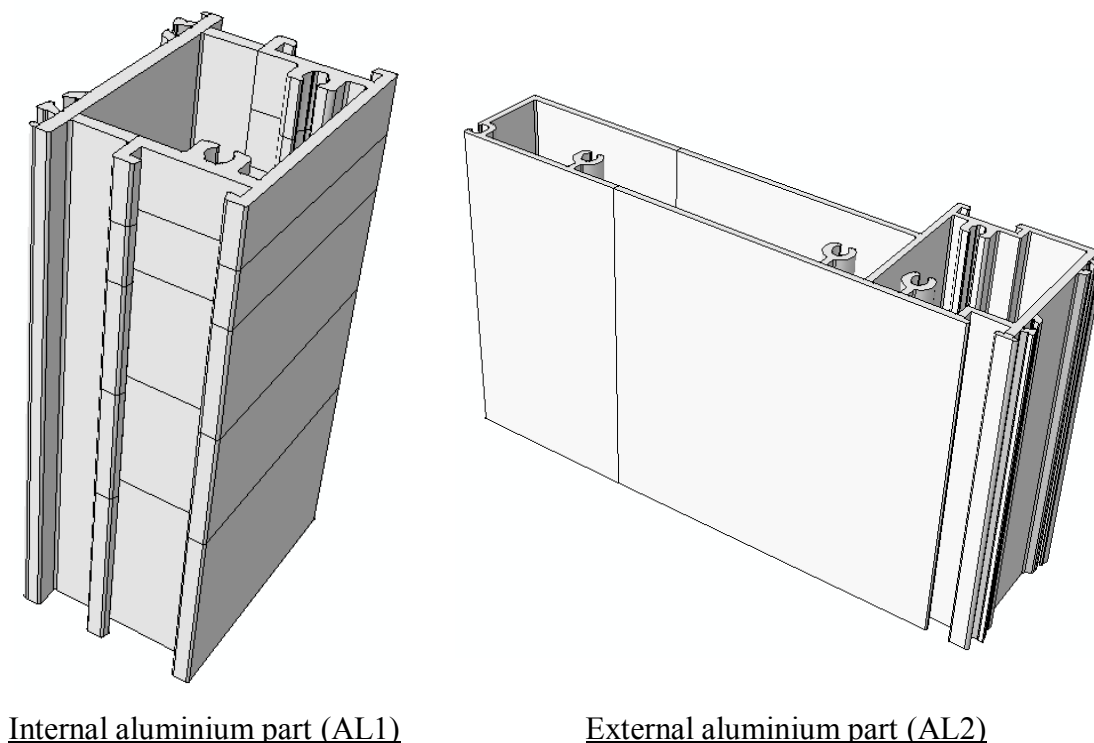


Figure 6.2 Partition assignment

Material property of aluminium alloy 6063T6 was assigned to the aluminium parts while 25% glass fibre reinforced polyamide PA66 was assigned to the core. Both elastic and plastic material properties of these two materials were defined in the model. For aluminium alloy, the Young's modulus, yield strength and ultimate strength was defined according to Chapter 4 as well as the material model. Stress-strain relationship specified in Chapter 4 was adopted here. True stress and true plastic strain listed in Table 4.1 were input into ABAQUS model to define the material plasticity. Similarly, material properties of glass fibre reinforced polyamide defined in Chapter 4 was adopted in the model as well. Polyamide material was simplified as an isotropic material with transverse material properties as this simplification was confirmed valid in Chapter 4. Stress-strain relationship shown in Figure 4.7 was input into the model to define the elasticity and plasticity of the material.

As a composite section, the interface action between aluminium and polyamide was defined as tangential behaviour as specified in Section 4.5.1. Penalty friction formulation was also applied to the interface in the isotropic direction. The proposed progressive failure model initiated in Chapter 4 was used here to model the failure mechanism. Since the connection of this asymmetrical section is identical to the typical section, same friction co-efficient specified in Section 4.5.1 was adopted in the FE model. Similar to the shear FE model of typical section, discretization of surface to surface was assigned to the interaction between aluminium surface and polyamide surface. "Small sliding" tracking formulation was assigned for the tracking approach between the two contact bodies. Aluminium contact surface was assigned to "master" surface while polyamide surface was assigned to "slave" surface. The master and slave contact pairs are shown in Figure 6.3 below.

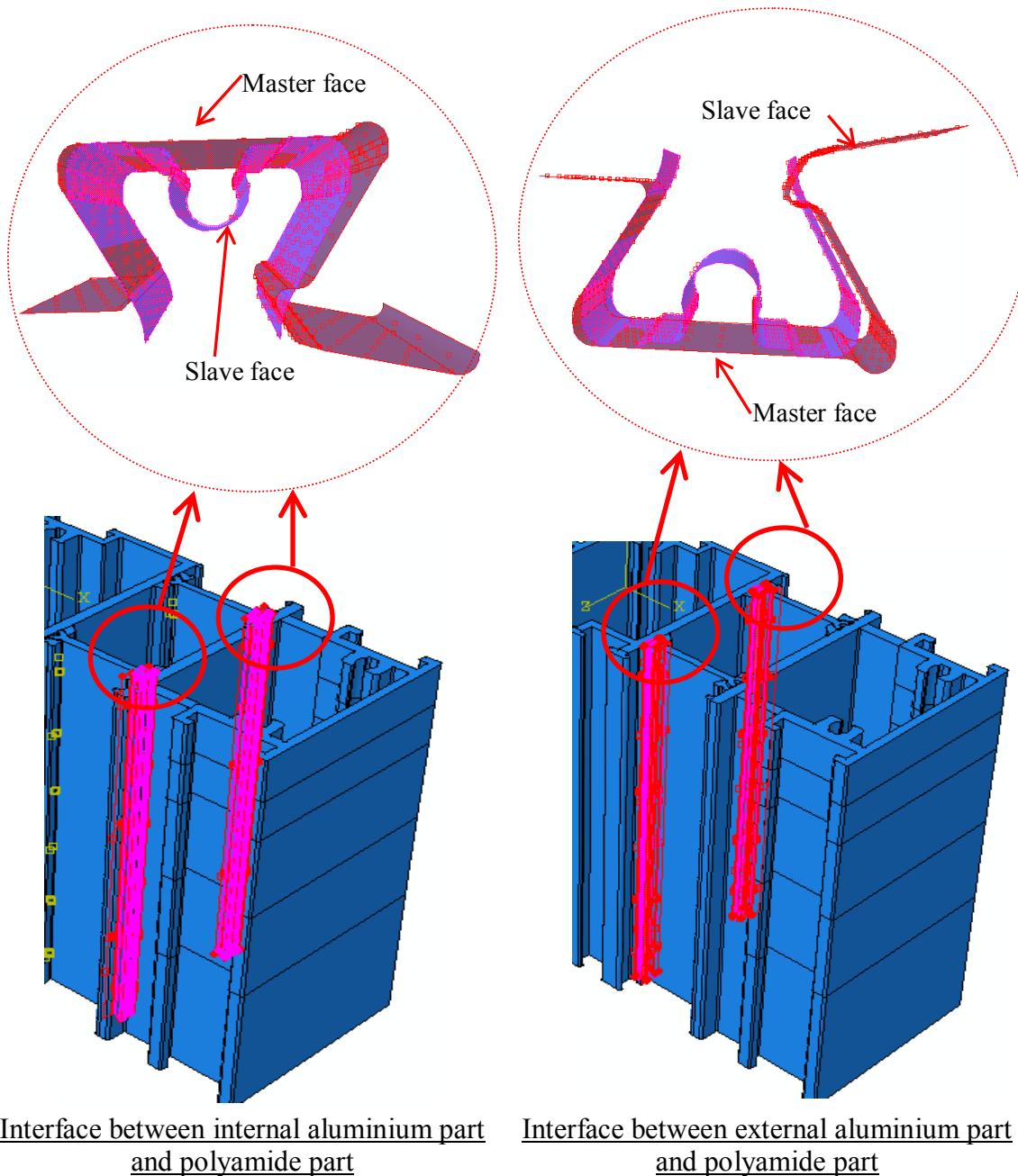


Figure 6.3 Master-slave assignment

Loading and boundary conditions were assigned to match the shear FE model of the typical section illustrated in Chapter 4. Displacement was applied in the model as loading. Linear ramp up function was applied in the step for the assigned displacement. According to Section 4.5.1, displacement was applied to two-thirds of bottom of the large external aluminium part (AL2). Boundary conditions of fixed supports were applied at the top of the small aluminium portion (AL1) and lateral restraint was also provided at 10.5mm below the top of AL1 in the length of 10.5mm. Lateral restraints were also assigned to AL2 along the specimen height to prevent the movement in z-axis

direction. Details of loading and boundary condition assignments are shown in Figure 6.4 below.

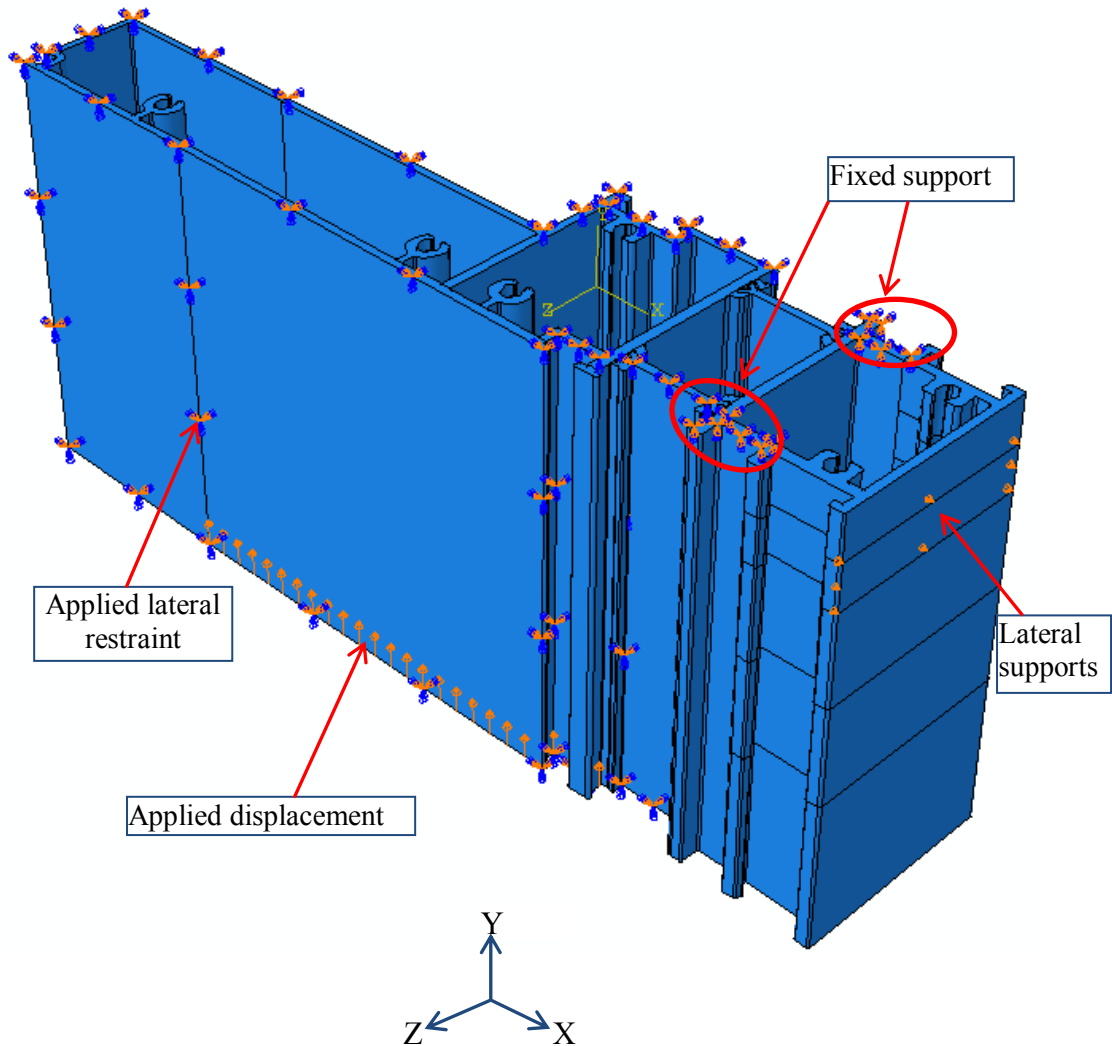


Figure 6.4 Boundary conditions and applied displacement

As the connection between aluminium and polyamide of this asymmetrical section is identical to the typical section, the displacements at each loading step were assigned to match the FE model of the typical section. The initial step represents the setup of the typical section. In step 1, displacement was assigned as 1.35mm. It was increased to 1.8mm in step 2 and the friction co-efficient was reduced to the value shown in Table 4.4. In step 3, a further increase of the displacement to 2mm was assumed. Then, the displacement set in step 3 was extended through step 4 and step 5. As the setup of the typical section was based on the experimental results, the FE model results of this asymmetrical section needs to be verified by experimental investigation in future studies.

The same quadratic reduced integration solid elements (C3D20R) used in the FE model of typical section were applied to both aluminium and polyamide parts. Fine meshes of seed 5 were applied to the aluminium parts and finer meshes of seed 3 were applied to the polyamide part. Detailed mesh of all three parts is shown in Figure 6.5 to Figure 6.8 below.

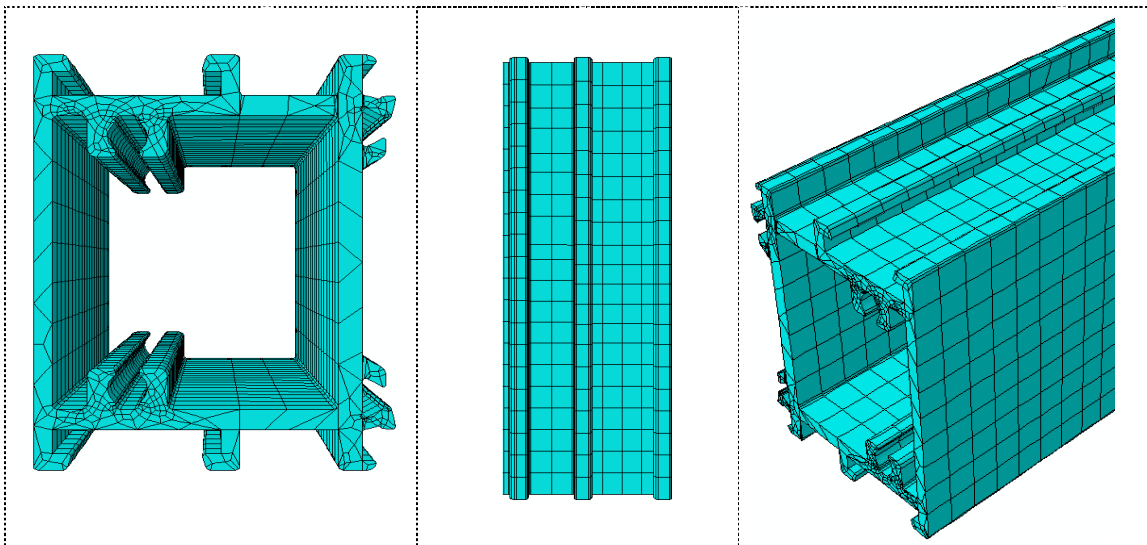


Figure 6.5 Mesh assignment of part AL1 from different view angles

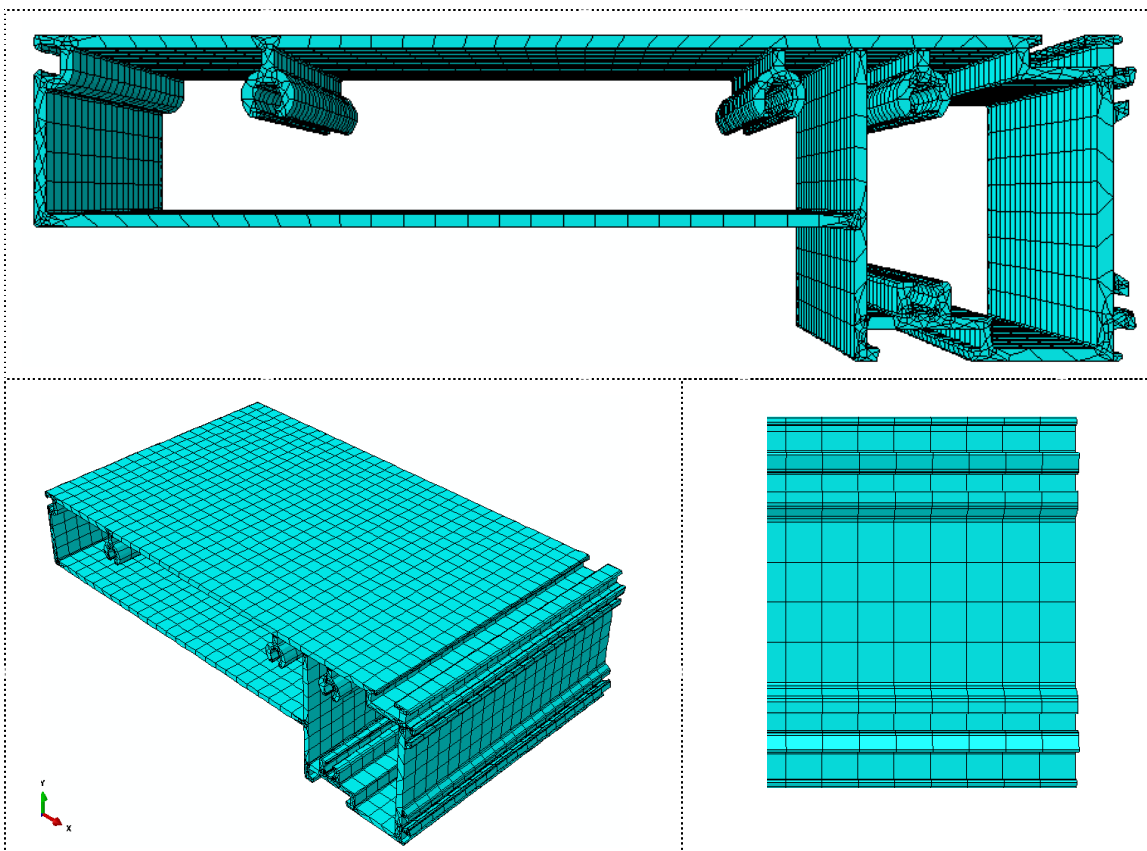


Figure 6.6 Mesh assignment of part AL2 from different view angles

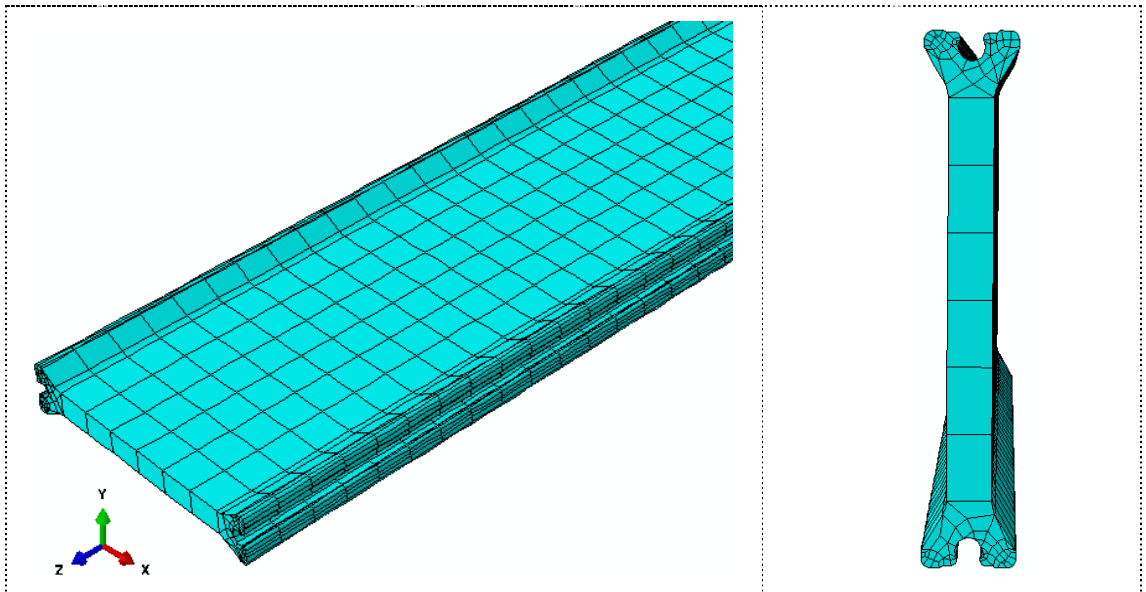


Figure 6.7 Mesh assignment of polyamide part PA from different view angles

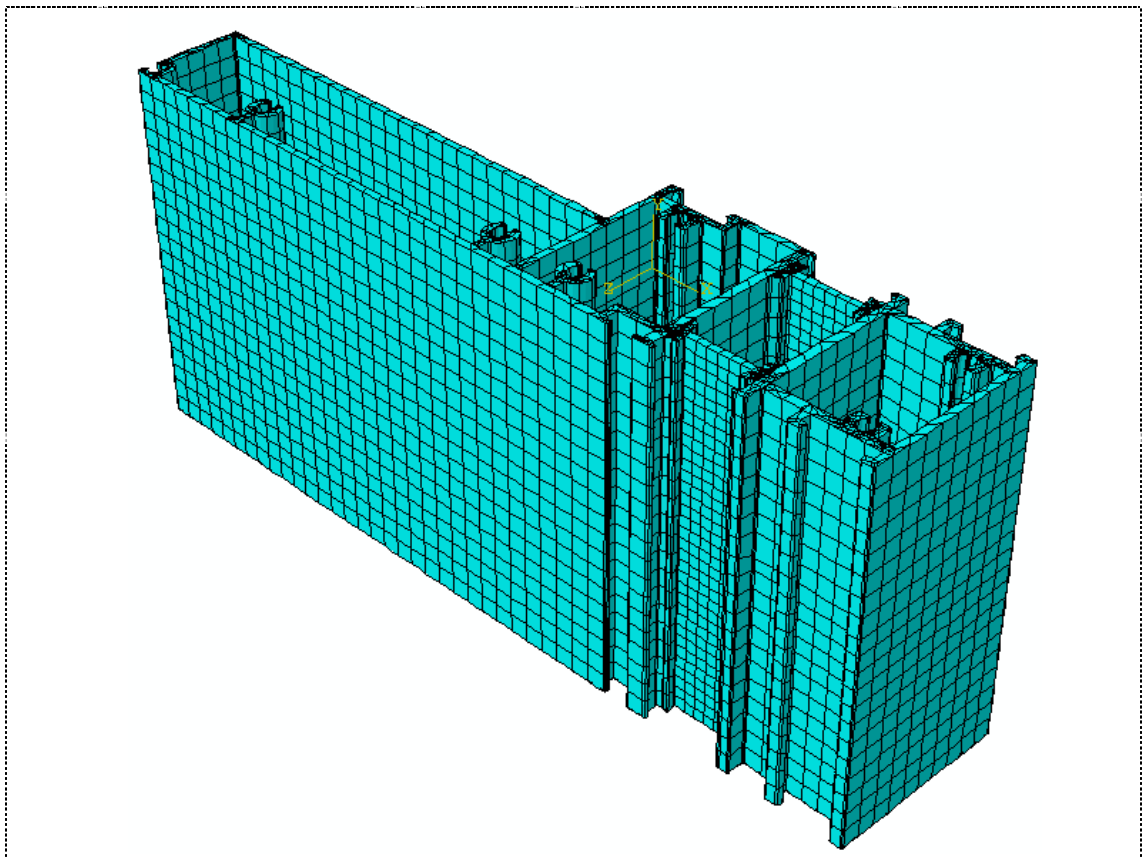


Figure 6.8 Mesh assignment of the assembled whole section

6.2.3 Typical results

The FE model showed similar failure mode as the typical section. The polyamide insert slipped away from the connection. The failure mode and deformed shape obtained from the FE model is shown in Figure 6.9 below. The bottom connection failed and slipped away by about 2mm.

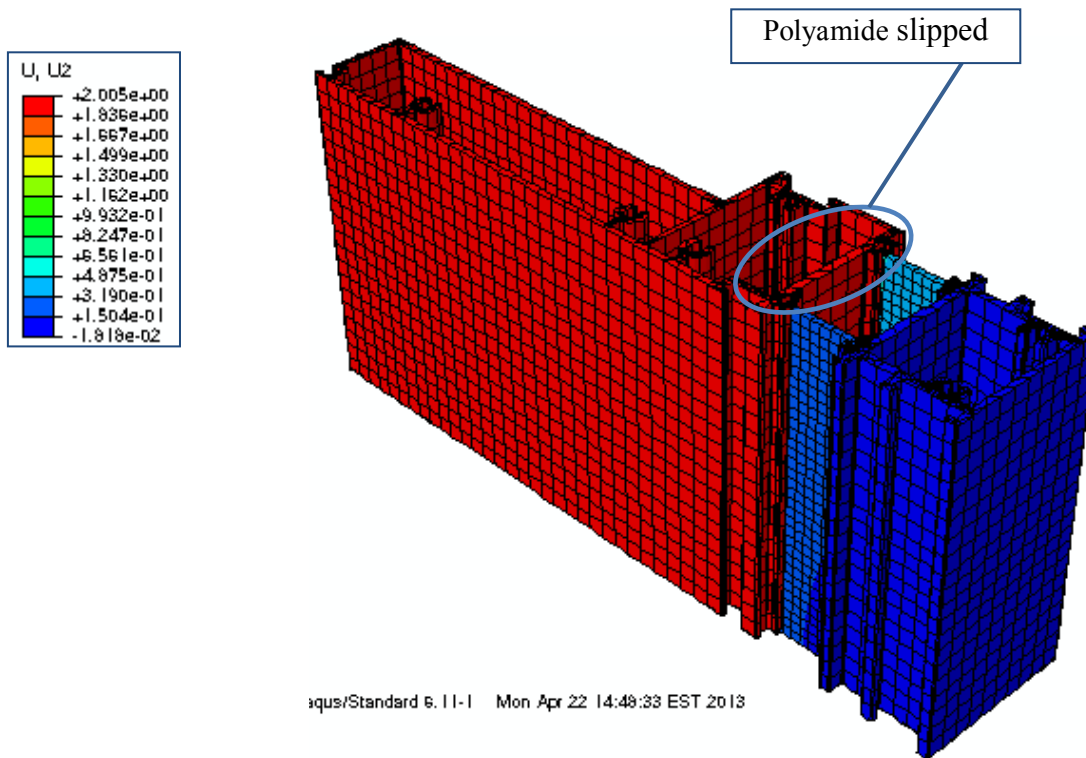


Figure 6.9 Deformed shape

The contact stresses along the direction of applied displacement of both left and right interfaces are plotted in Table 6.1 and Table 6.2 below. The contact stresses were selected at the beginning of step 1, middle of step 2 and end of steps 1 and 2 to display the change of connectivity of the interfaces. Similar to the typical section, the contact stresses at aluminium and polyamide at top and bottom connections increased from the beginning of loading and reached peak values. They, then, started decreasing when slip occurred. At the end of calculation (step 5), the contact stresses decreased to zero which indicated the failure of connection. As the section is not symmetrical, the contact stress distribution of the left interface differs from the one on the right side.

Table 6.1 Contact shear stresses at the connection between internal aluminium part and polyamide

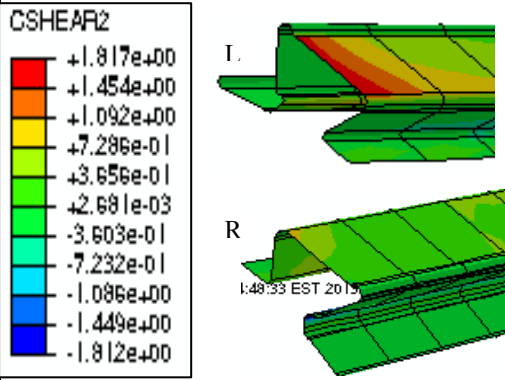
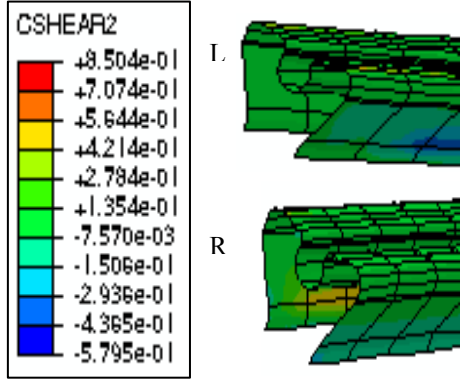
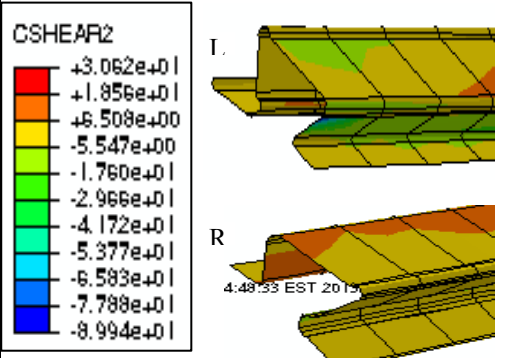
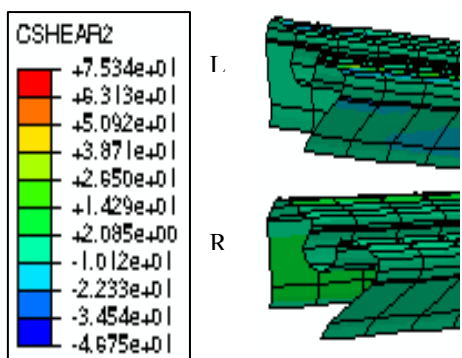
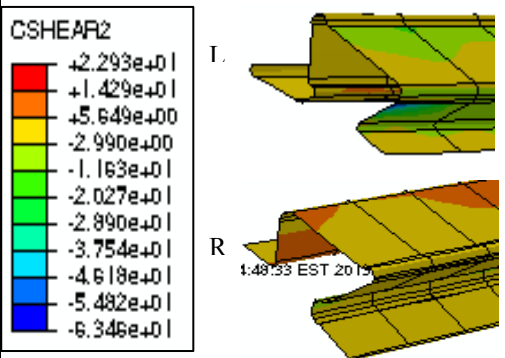
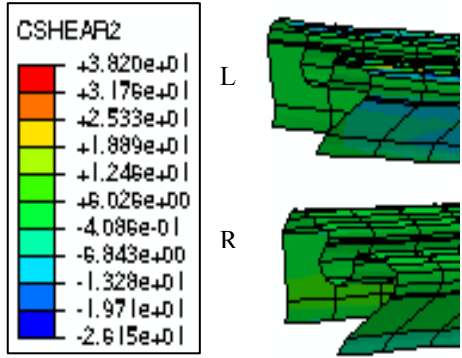
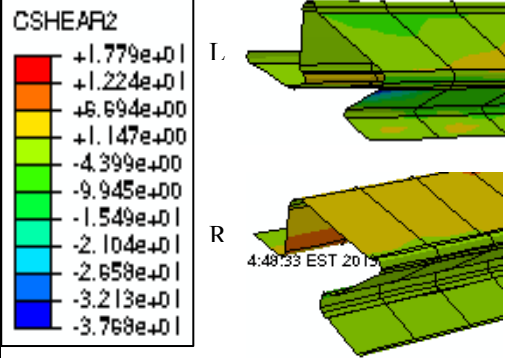
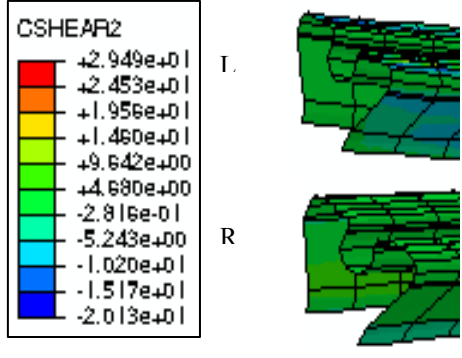
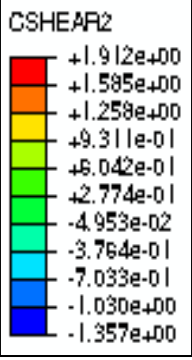
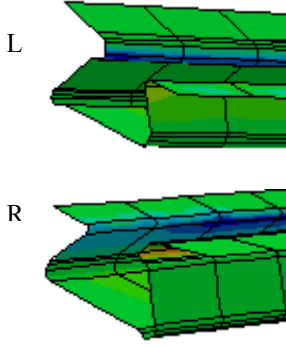
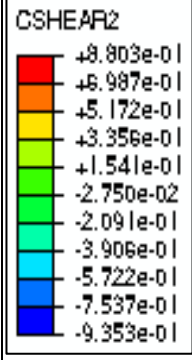
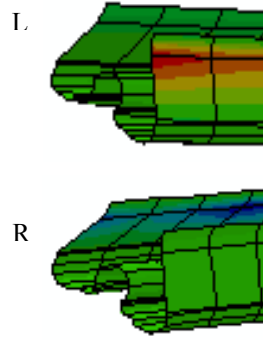
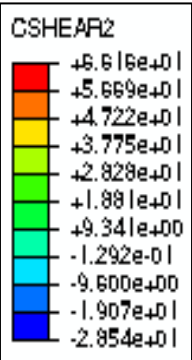
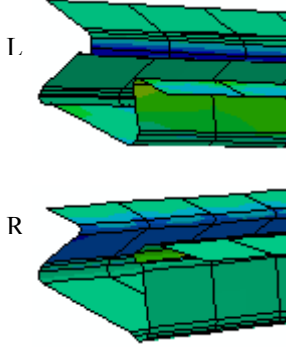
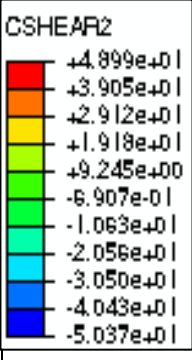
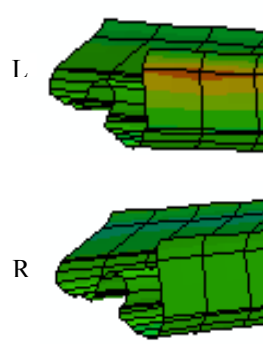
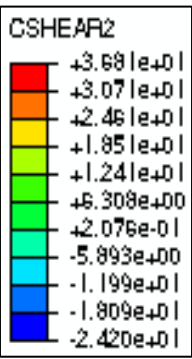
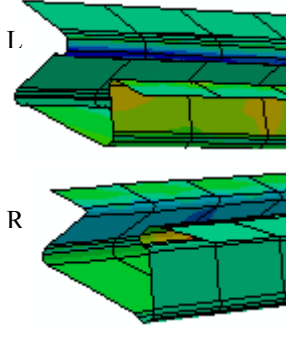
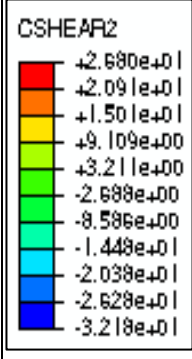
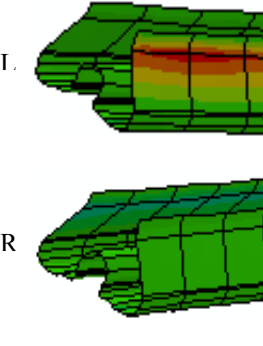
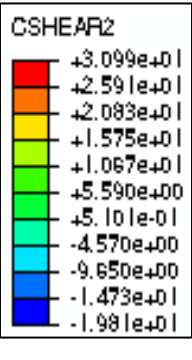
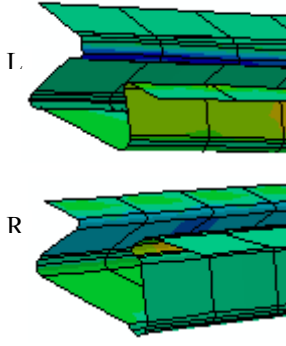
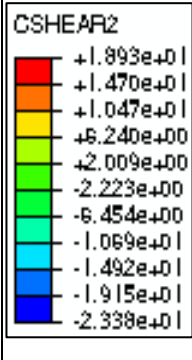
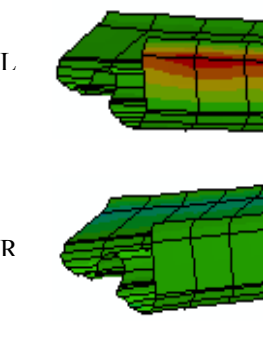
Analysis steps	Contact shear in aluminium (MPa)	Contact shear in polyamide (MPa)
Step 1 – increment 1 T=0.0025s		
Step 1 – increment 8 T=1s		
Step 2 – increment 4 T=0.575s		
Step 2 – increment 6 T=1s		

Table 6.2 Contact stresses at the connection between external aluminium part and polyamide

Analysis steps	Contact shear in aluminium (MPa)	Contact shear in polyamide (MPa)
Step 1 – increment 1 T=0.0025 s	 	 
Step 1 – increment 8 T=1s	 	 
Step 2 – increment 4 T=0.575s	 	 
Step 2 – increment 6 T=1s	 	 

The load versus slippage of the connection was studied. The relationships between the load and the slippage are plotted in the graph below (Figure 6.10).

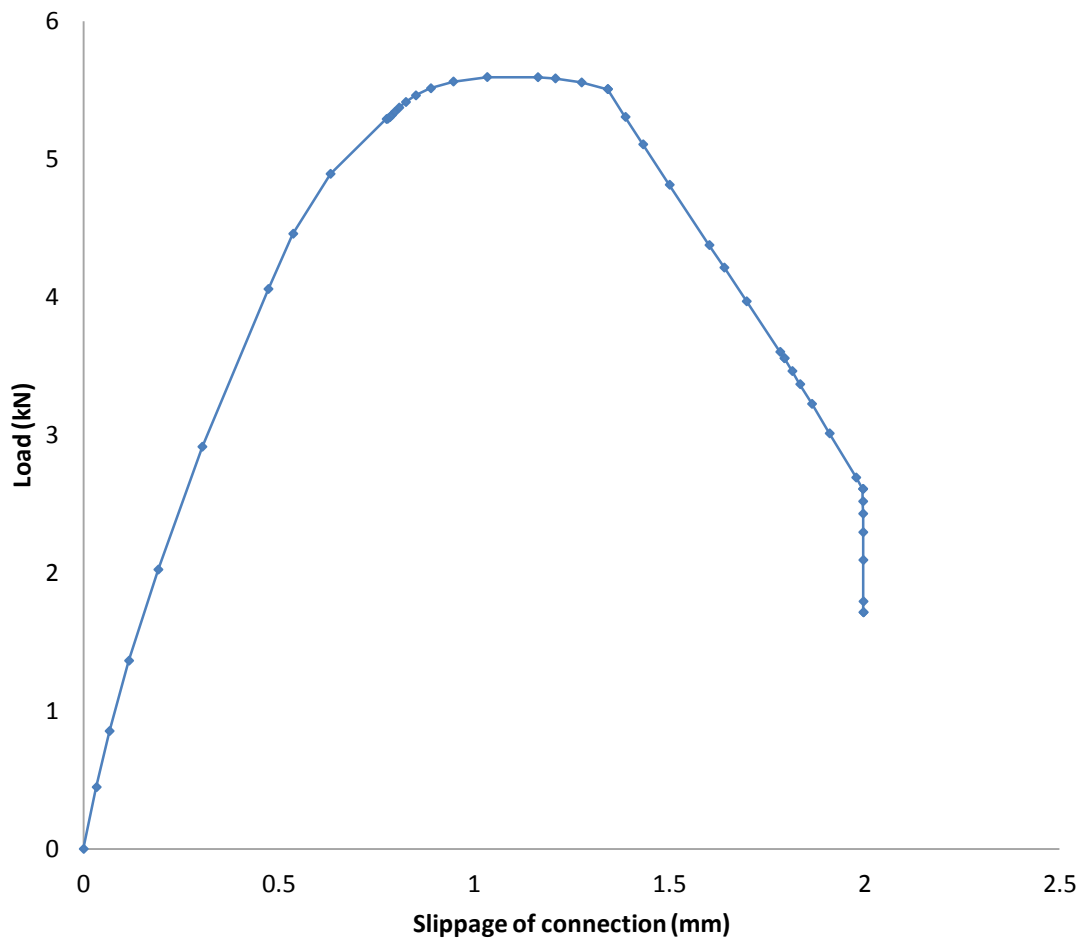


Figure 6.10 Load vs slippage of connection

In summary, the deformed shape generated by the FE model shows the failure of connection – polyamide slipped. This failure mode is consistent with the typical section. The contact stresses in both aluminium and polyamide increase with the loading. Once slippage occurred, the stresses started to drop gradually and finally reached zero when connection failed. This confirms that the proposed progressive failure model is applicable to simulate this irregular thermal break section as well.

6.3 Numerical investigation of the section transverse tensile capacity

6.3.1 Model setup

To investigate the tensile capacity of this asymmetrical thermal break façade mullion section, a three-dimensional finite element model was built by using ABAQUS software. The standard length of 100mm was adopted in the modelling. The FE model geometry was imported into ABAQUS software from an ACIS file which was generated from Autocad drawing file provided by the manufacturer.

Similar to the shear model, the section was imported into the software as three separate parts. Each part was imported as a deformable solid. The section was then assembled by applying position constraint to join the three parts together. To be able to apply loading and boundary conditions, both external and internal aluminium portions were partitioned by edge and cell partition toolsets. Details of the partition assignments are shown in Figure 6.11 below. However, the polyamide core was kept as a single region.

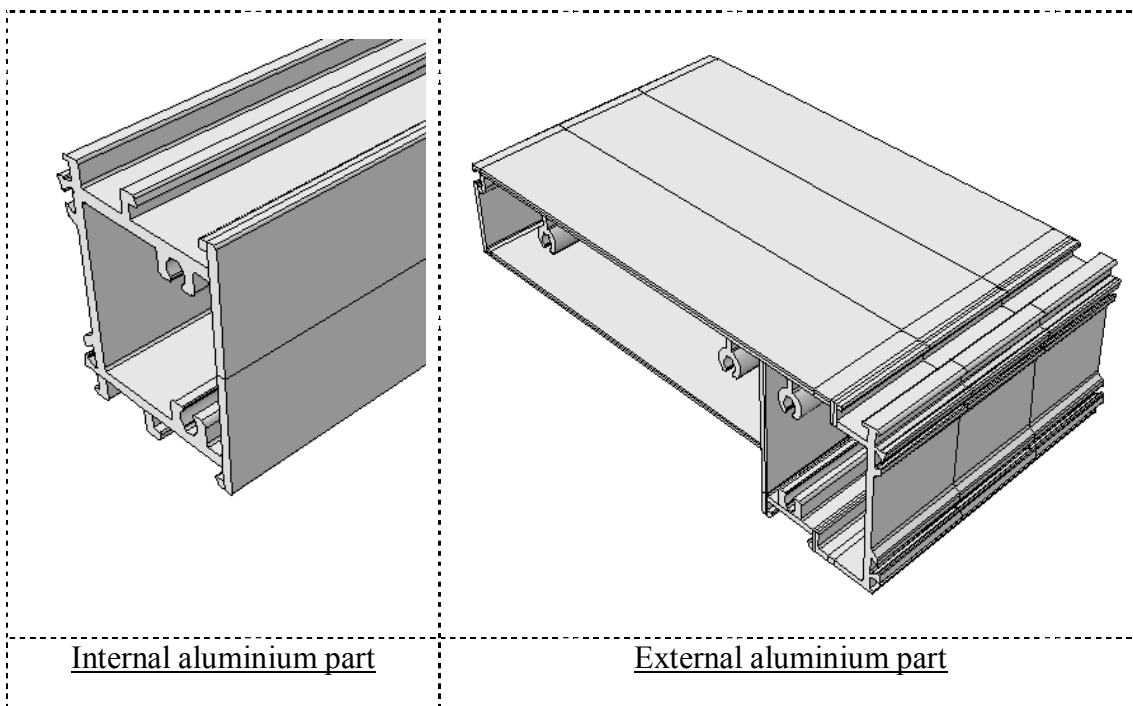


Figure 6.11 Partition assignment of internal and external aluminium parts

Material properties of aluminium discussed in Section 4.2.1 was adopted in the model for both elastic and plastic stages. Ramberg-Osgood continuous model was also assigned to represent the aluminium plastic hardening stage as the shear model. Based on the conclusion of Chapter 5, Section 5.3, the equivalent Young's modulus and strength of aluminium alloy shall be applied into the model to achieve comparable results with the experimental ones. Revised stress and strain relationships of this

aluminium alloy, shown in Figure 5.9, were adopted and input into the software to define the material plasticity. Aluminium was defined as an isotropic material, the same as the typical section model.

For defining the material property of glass-fibre reinforced polyamide PA66, a similar approach as mentioned in Section 4.5.1 was adopted. The simplified material model was adopted as the shear model. The polyamide material was defined as an isotropic material with material properties in transverse direction. True stress and true strain relationship, discussed in Section 4.2.2 Figure 4.7, was input into ABAQUS model to define the elastic and plastic material properties.

Similar to the shear test model, the interaction between the aluminium and polyamide was assigned as tangential behaviour. Penalty friction formulation was chosen to apply to the interface in isotropic direction. As the connections are identical to those of the typical section, frictional co-efficient μ of 0.9 used in the tension model of the typical section was adopted in this model.

“Surface to surface” discretization was assigned to the interfaces of aluminium and polyamide. “Small sliding” tracking formulation was again assigned for the tracking approach between the two contact bodies as the shear model as well as the tension model of the typical section. As discussed in Section 4.4, aluminium contact surface was assigned to “master” surface and polyamide contact surface was assigned to “slave” surface. The same master-slave surfaces shown in Figure 6.3 were assigned in this tensile model. The section was assembled as shown in Figure 6.12 below with contact surfaces highlighted.

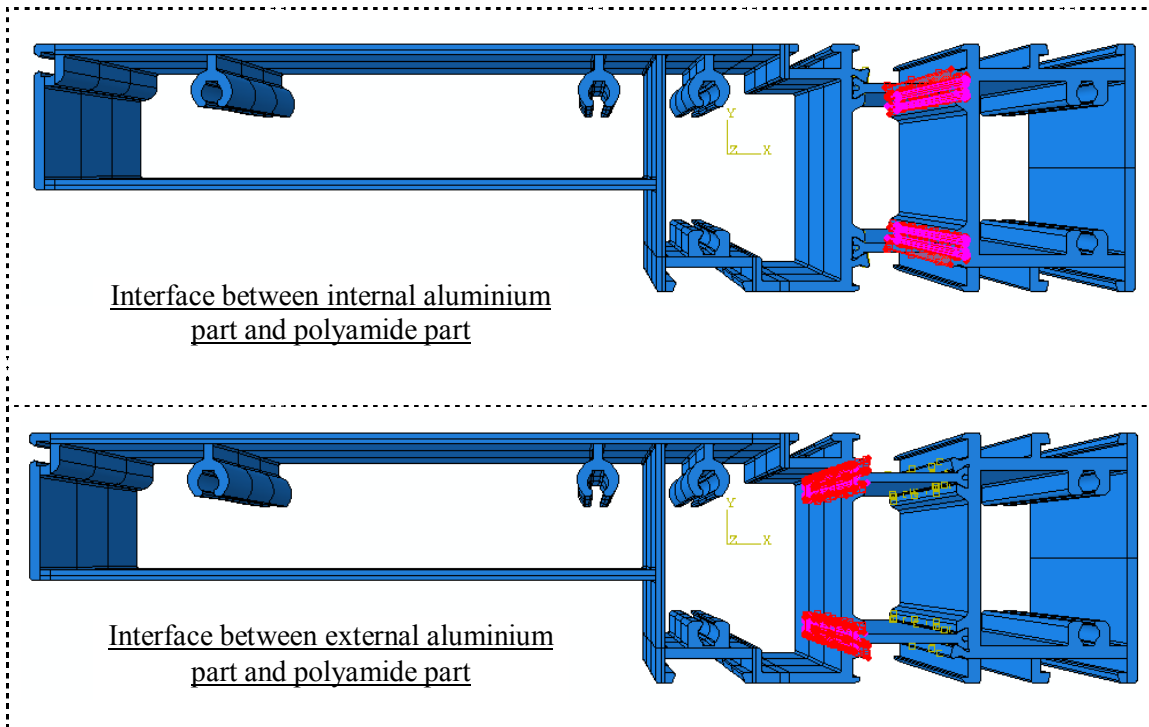


Figure 6.12 Interaction assignment

Similar to the FE model of the typical section, displacement was assigned instead of loading. Displacement along x-axis was applied at the external aluminium part while simple support was assigned to restrain the section at the internal aluminium part. Detailed model setup is show in Figure 6.13 below.

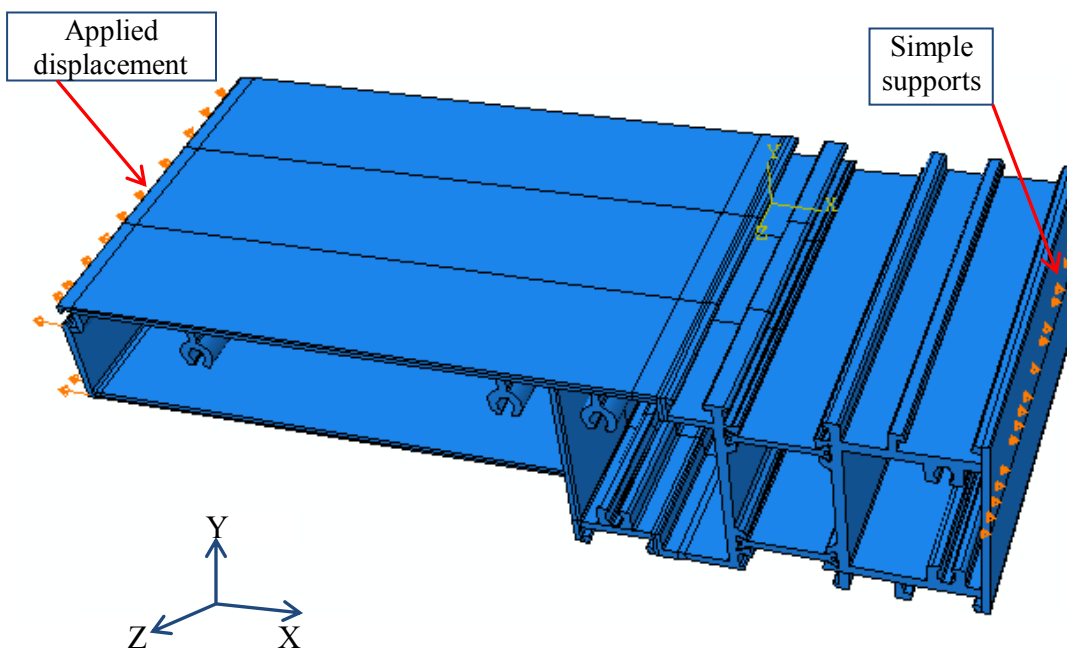


Figure 6.13 Displacement and boundary conditions

Fine meshes of seed 5 were used to mesh the aluminium portions in the model while finer meshes of seed 3 were adopted to mesh the polyamide portion as determined in Section 4.3 for the typical section. As the deformation presented in the tensile experiments showed combined tensile and bending deformation for the typical section, hex dominated quadratic reduced integration elements (C3D20R) were assigned to model all three parts to prevent shear locking. Details of the mesh are shown in Figure 6.14 to Figure 6.17 below.

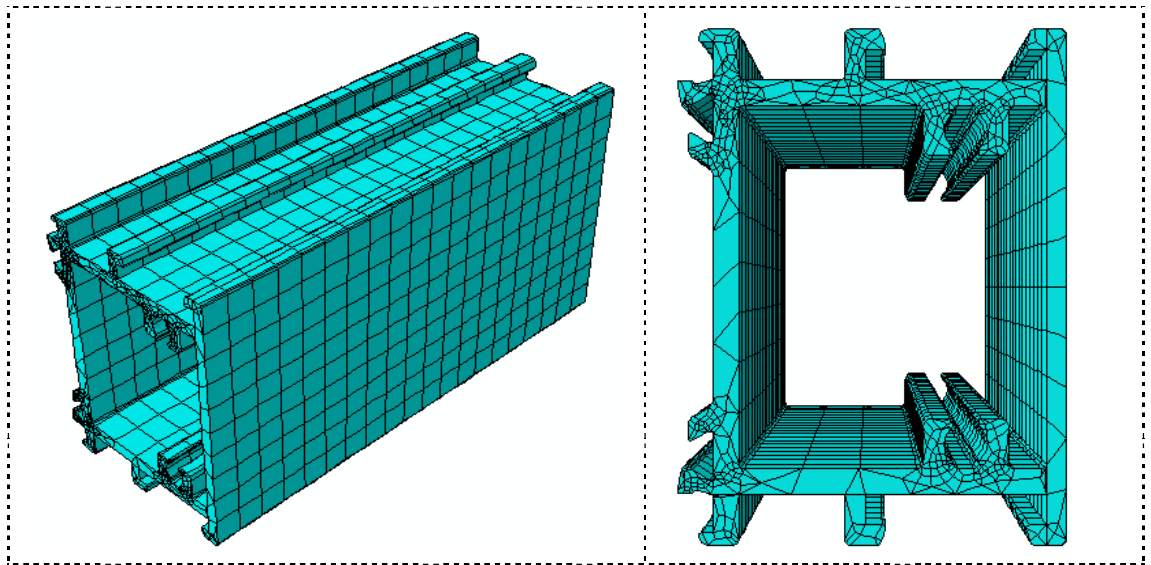


Figure 6.14 Mesh assignment of the internal aluminium part from different view angles

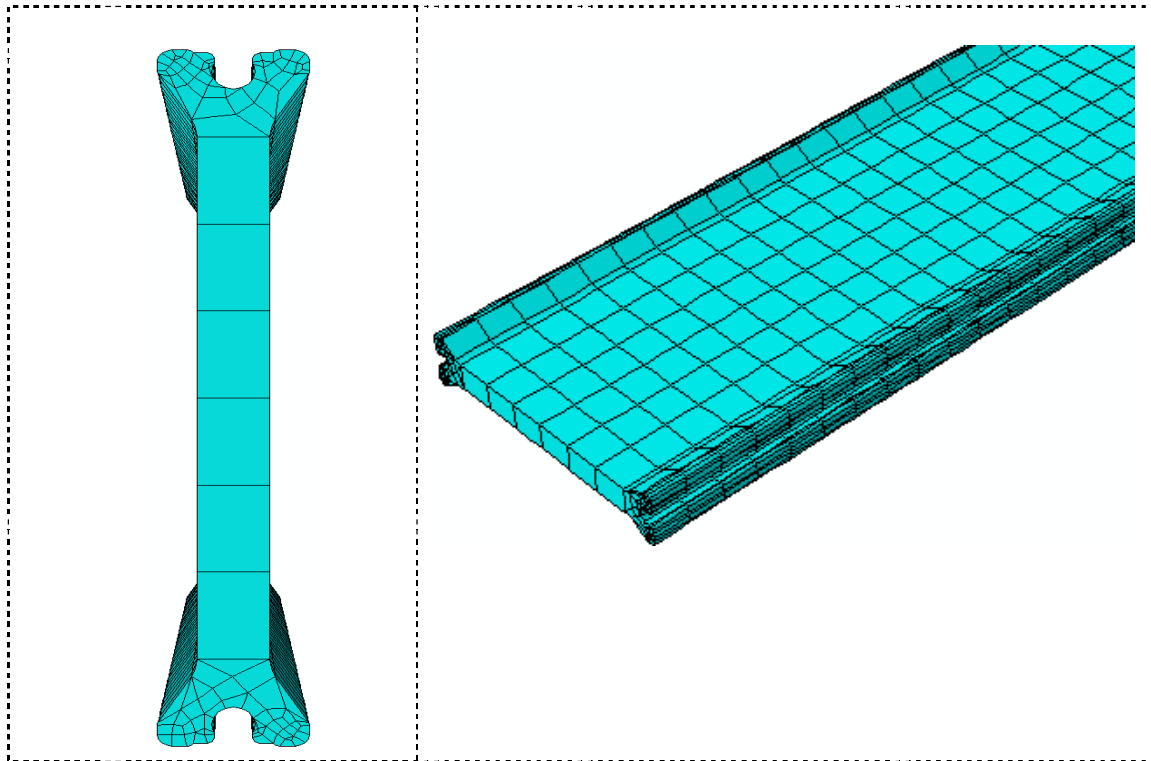


Figure 6.15 Mesh assignment of polyamide part from different view angles

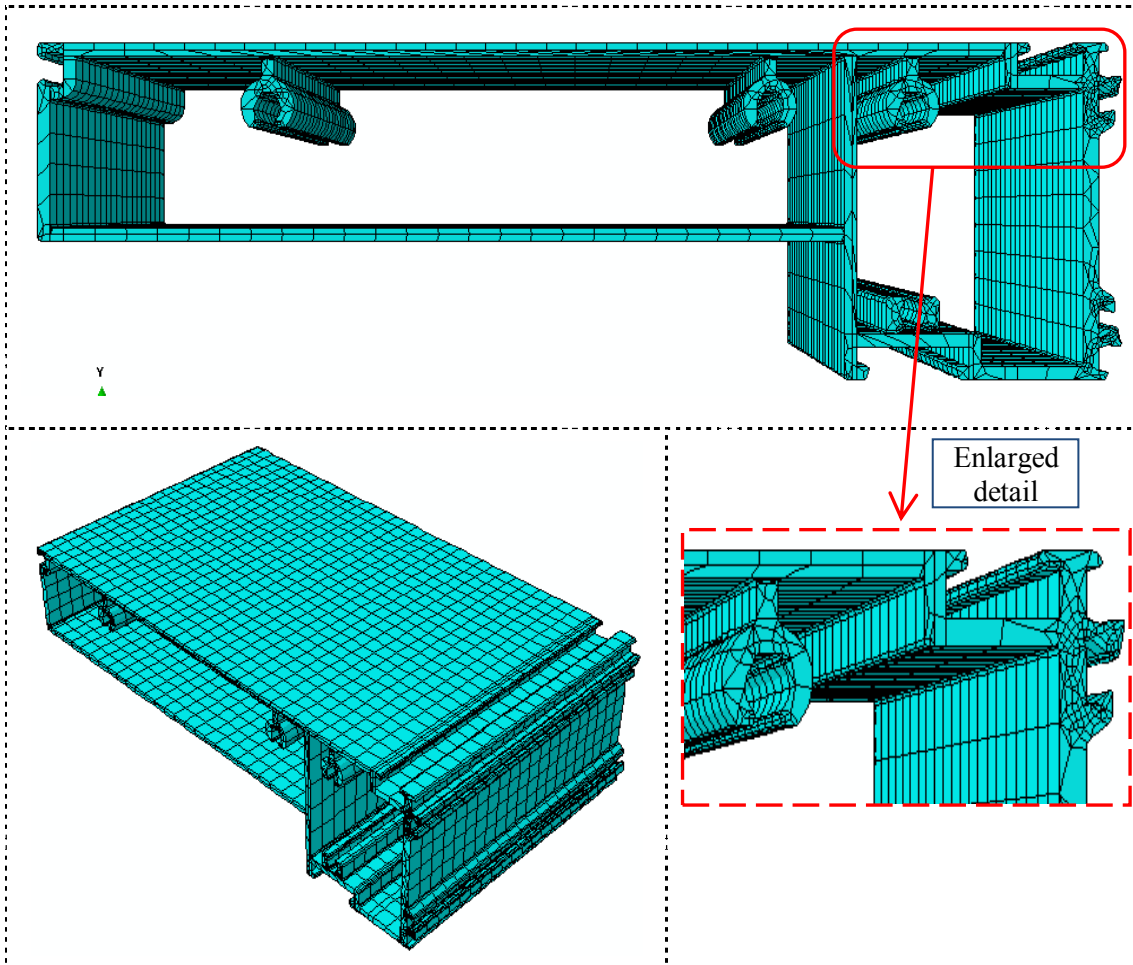


Figure 6.16 Mesh assignment of the external aluminium part from different view angles

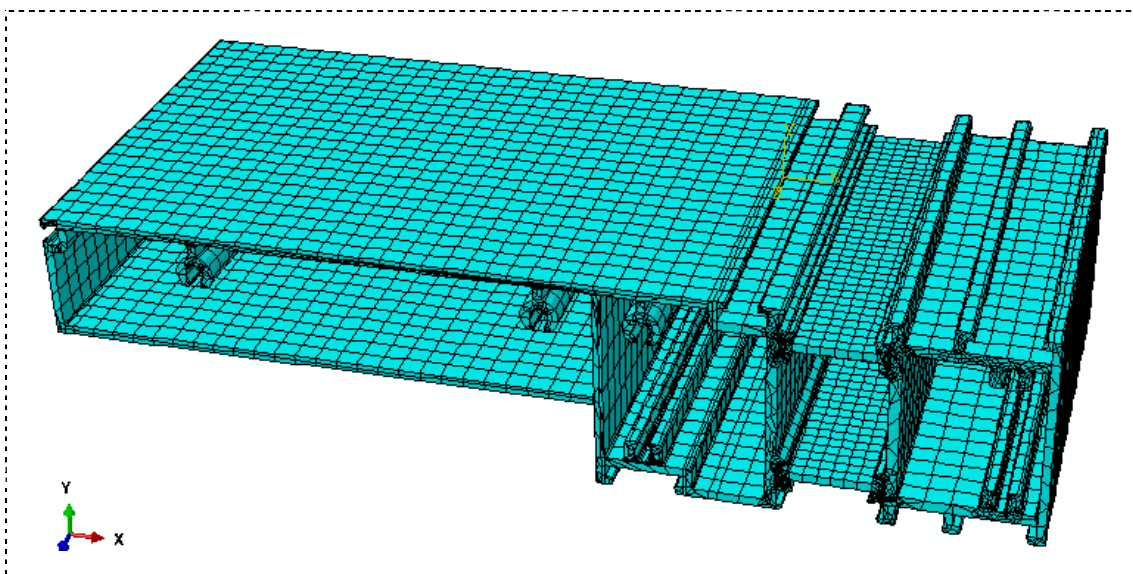


Figure 6.17 Mesh assignment of the assembled whole section

6.3.2 Typical results

The deformed shape shows combined tensile and bending deformations similar to the typical section. However, the deformed shape is quite different from the one generated from the typical section as the geometry of the two sections is completely different. The bending deformation exists on both external and internal aluminium parts of this asymmetrical section. The deformed shape is shown in Figure 6.18 below.

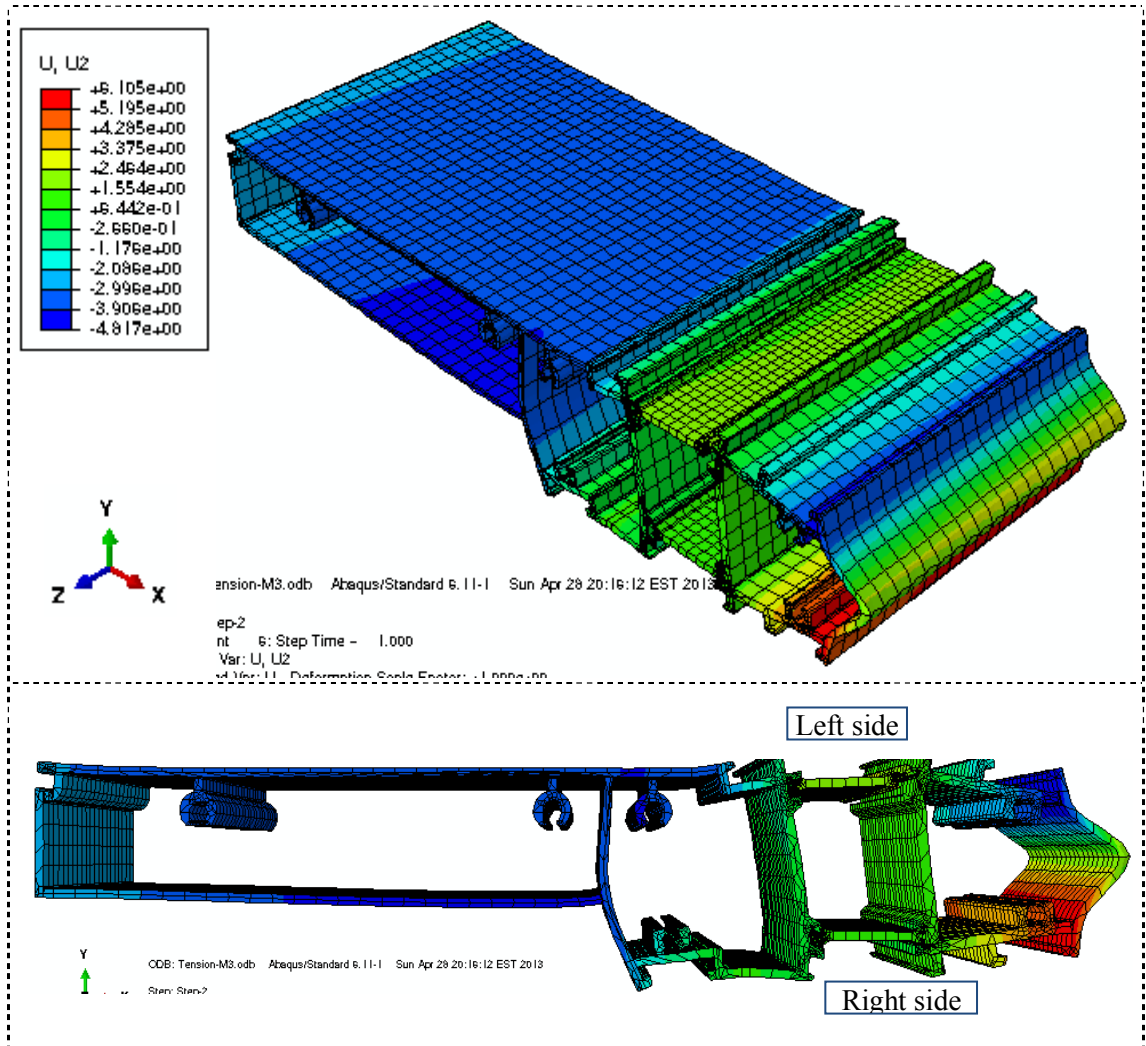


Figure 6.18 Deformed shape from different view angles

The failure mode is the polyamide being pulled out from the connections which is similar to the typical section as well. The enlarged details of failure mode are shown in Figure 6.19 below.

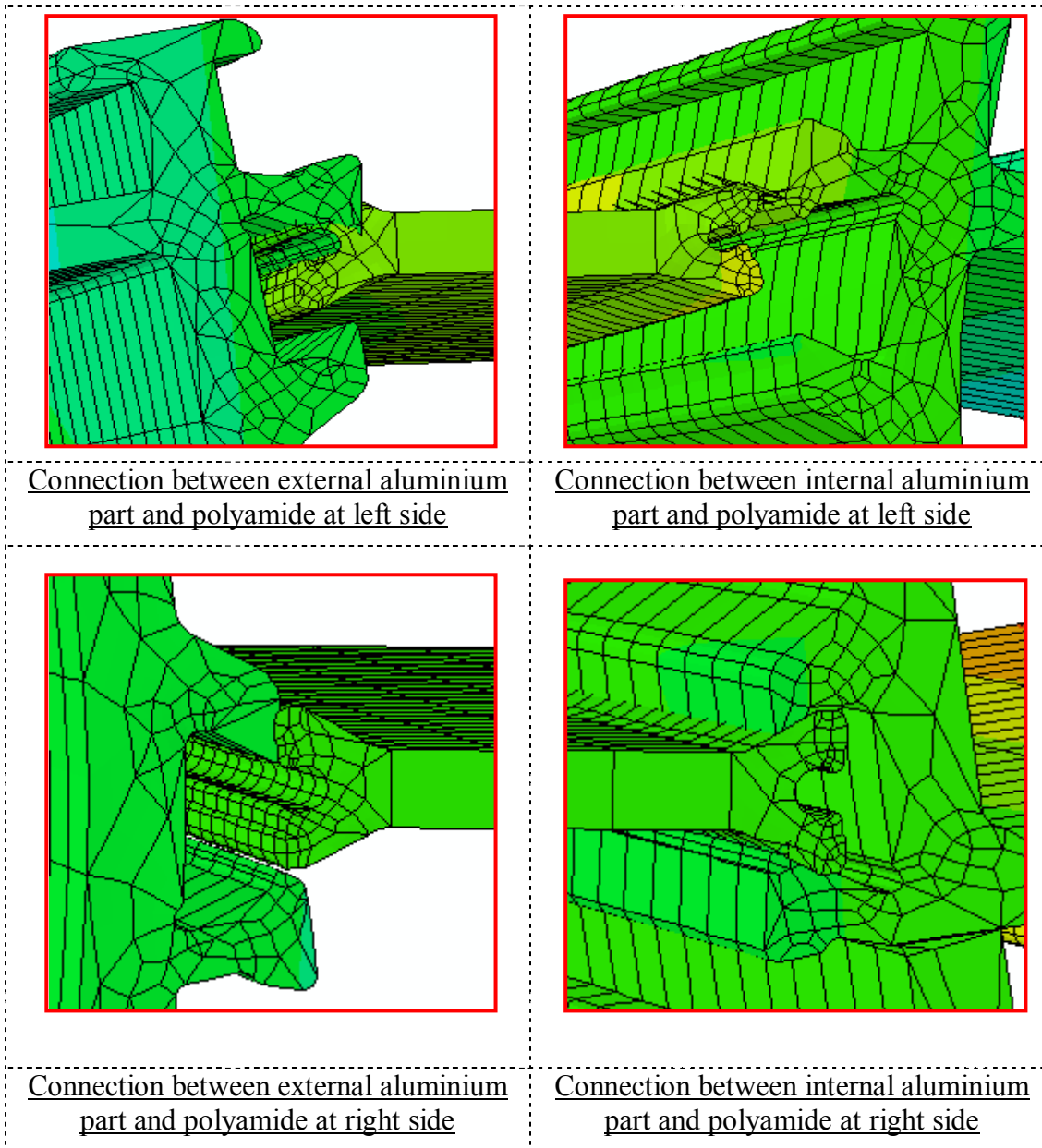


Figure 6.19 Enlarged details of failure mode

Figure 6.19 shows that the polyamide insert at the left side of the section and the polyamide insert at the right of the section, joining with external aluminium part, have been pulled out of the connection completely. However, the connection between internal aluminium part and polyamide insert at the right side of the section has kept some connectivity, i.e. the polyamide insert was semi-joined with the aluminium part. This behaviour is well expected as the section is not symmetrical. This failure mode is consistent with the failure mode of the typical section.

Load versus displacement graph is studied and plotted below. The graph shows similar trends as the one obtained from the typical section but with smaller load carrying capacity.

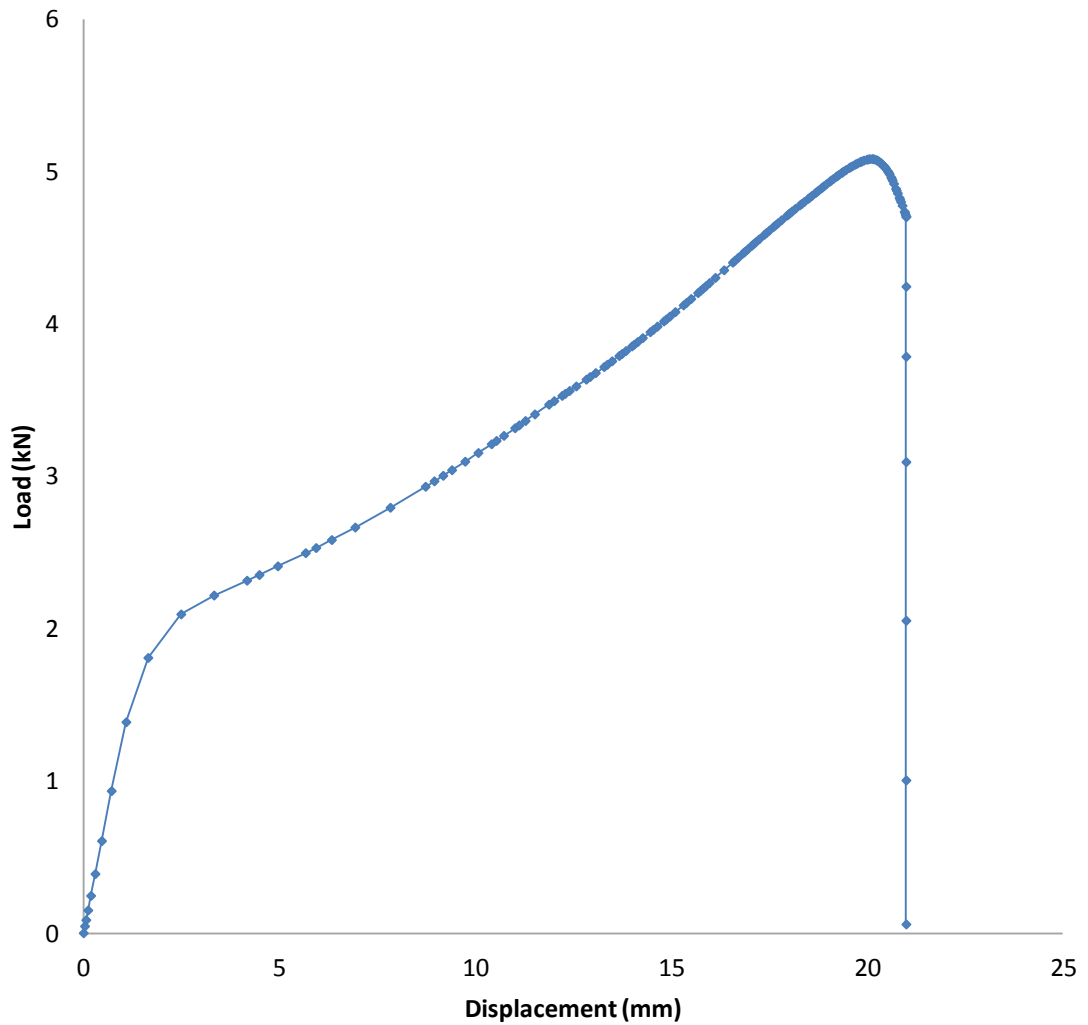


Figure 6.20 Load vs displacement diagram

Contact stresses were studied and listed in Table 6.3 and Table 6.4 below. The contact stresses at all interfaces increased with the loading and reached the peak value at the end of step one. They then dropped to zero in a second as the polyamide was pulled away from the connection. The contact stresses are consistent with the failure mode shown in Figure 6.19.

Table 6.3 Contact stresses at connection between internal aluminium part and polyamide

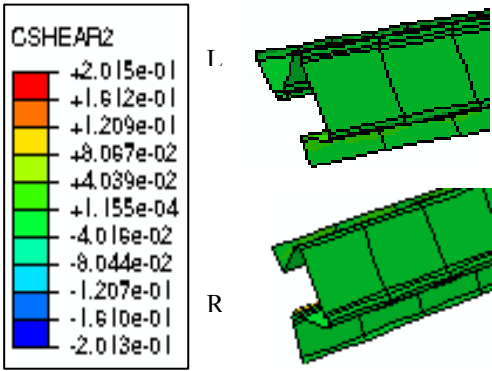
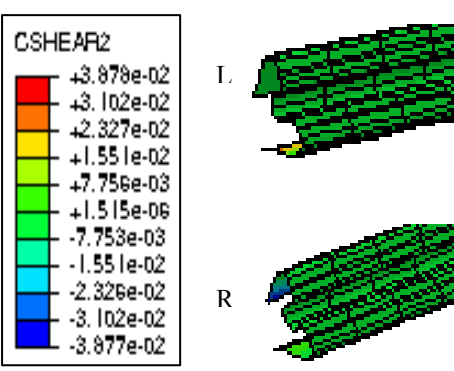
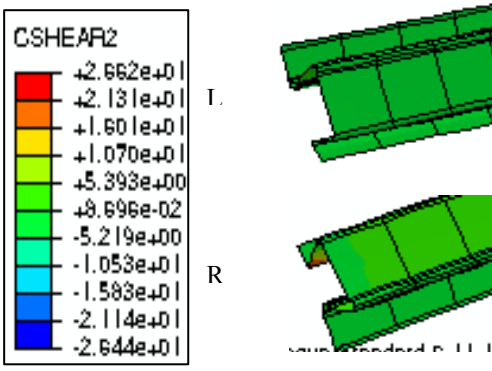
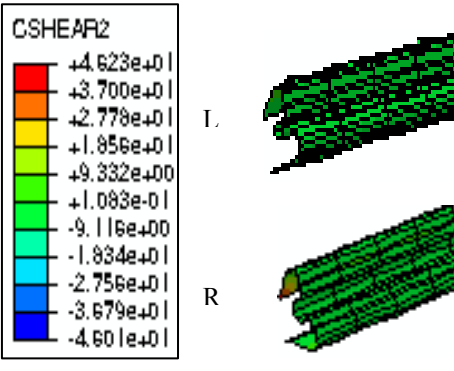
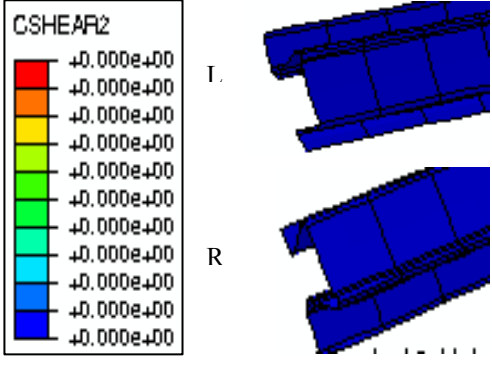
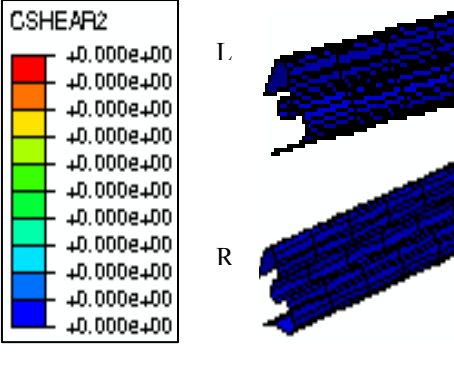
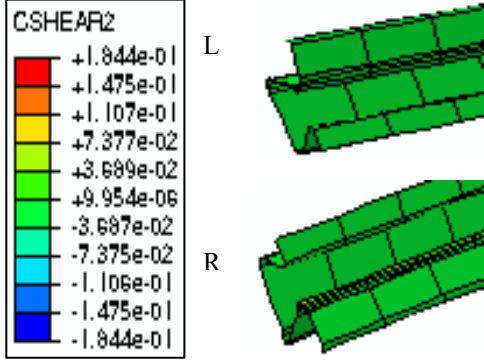
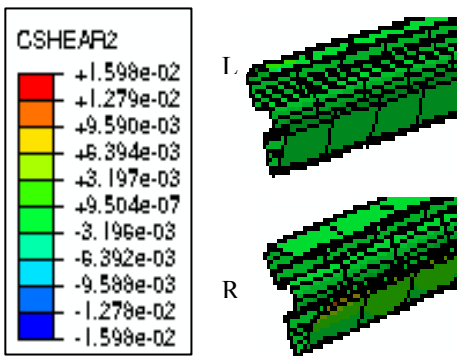
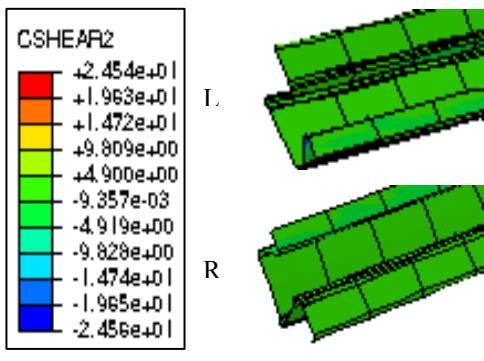
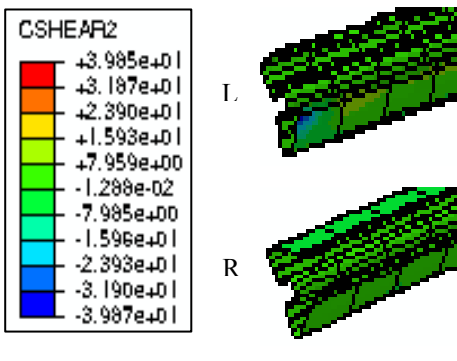
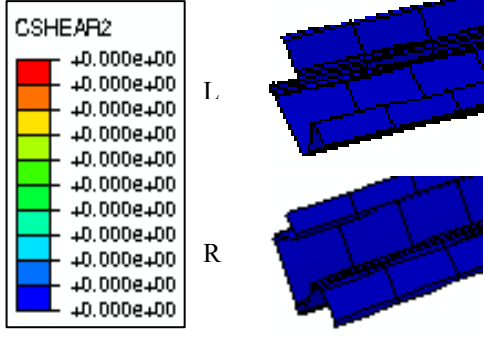
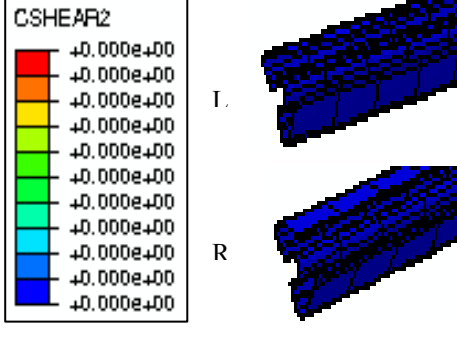
Analysis steps	Contact shear in aluminium (MPa)	Contact shear in polyamide (MPa)
Step 1 – increment 1 T=0.01s		
Step 1 – increment 8 T=1s		
Step 2 – increment 4 T=0.575s		

Table 6.4

Contact stresses at connection between external aluminium part and polyamide

Analysis steps	Contact shear in aluminium (MPa)	Contact shear in polyamide (MPa)
Step 1 – increment 1 $T=0.01s$		
Step 1 – increment 8 $T=1s$		
Step 2 – increment 4 $T=0.575s$		

In conclusion, deformed shape of this asymmetrical thermal break façade section showed both tensile and bending deformation, the same as the typical thermal break section. The failure mode was consistent with the one generated from the typical section, which is the polyamide pulled out of the connection. However, as the section is not symmetrical, the polyamide at the internal connection at the right side was still semi-connected with the aluminium part. Load versus displacement relationship also displayed a similar trend as the one of the typical section. However, the transverse tensile strength is weaker than the typical section. Contact stresses at internal and

external connections increased with loading and reached a peak value, respectively. They then dropped to zero as the connection failed. The contact stresses on the other hand reflected the failure mode. The good correlation of results between the typical symmetrical section and this asymmetrical section proves the validity of the finite element modelling technique for simulating the transverse tensile strength and its applicability to various thermal break façade sections.

6.4 Numerical investigation of four-point beam bending

The above numerical investigations have determined the characteristic strength of this asymmetrical façade section. To understand its behaviour as a façade mullion which bends under the lateral loads, a finite element model has been setup by using ABAQUS software. The model setup details and results will be discussed below.

6.4.1 Model setup

The geometry of the section shown in Figure 6.1 shows the area of external skin being more than twice of the internal skin. This is opposite to the typical façade section studied in this research. The geometry of external skin was determined by architectural requirements instead of by strength or thermal isolation requirements. This is a typical non-standard façade section. To build a finite element model of non-standard section, the modelling technique initiated by this research was adopted.

As the typical span of curtain wall is 3m to 3.5m between floors, the span length of this beam made of the asymmetrical section was chosen as 3.12m as the type D beam in Chapter 4. The same span length is to provide comparison between both sections. Due to its asymmetrical geometry, the full section was imported into the model. This section was also simplified as previously done for the typical symmetrical section to reduce computational cost. Since the four-point bending behaviour largely relates to the geometry of cross section and neutral axis of the beam as well as the contact interactions as explained in Chapter 4, the profile details make minimum contribution. The external and internal aluminium parts were then modified slightly to have minimum change of neutral axis location. As the interaction is based on the contact surface, therefore, the geometry of the contact interface was maintained as the actual shape to reflect the true interface behaviour similar to the typical section. The simplified section is shown in Figure 6.21 below.

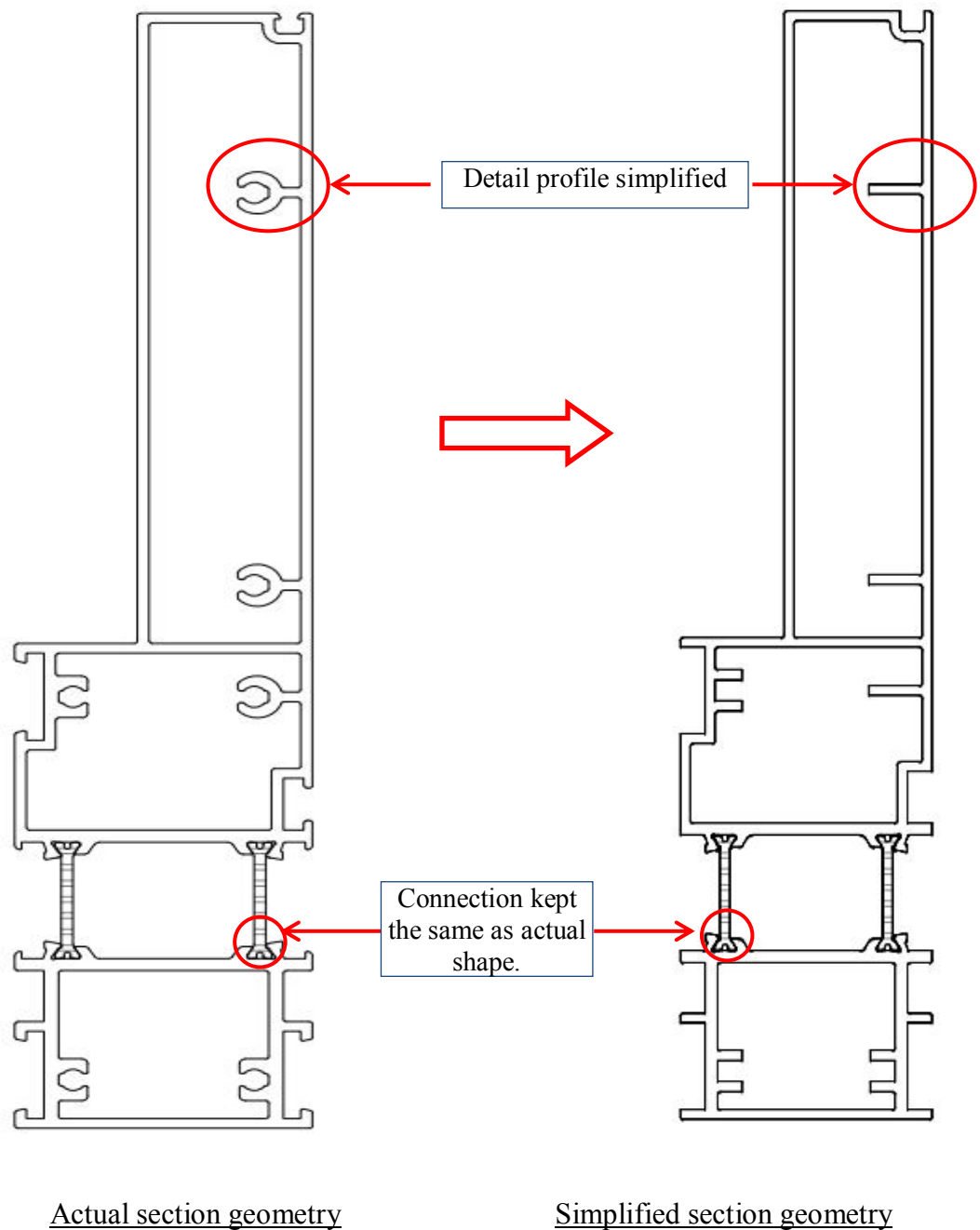


Figure 6.21 Details of simplified section

Similar to the typical section model, the geometry of the simplified section was drawn in Autocad drawing format and then converted to a standard ACIS text (SAT) file. The beam was imported as four separate parts. All four parts were assigned as deformable solids and then joined together by position constraint tools.

Material properties of aluminium alloy 6063T6 were assigned to external and internal aluminium parts. Middle polyamide parts were assigned the property of 25% reinforced polyamide PA66. Similar to shear and tension models, material model of aluminium discussed in Section 4.2.1 was applied. Aluminium Young's modulus, yield stress and ultimate stress defined in Section 4.2.1 were input into the models and aluminium was defined as an isotropic material. To determine the stress and strain relationship in the plastic range, Ramberg-Osgood continuous model was adopted. True stress and true plastic strain from Table 4.1 were used to define the plasticity.

As discussed in Section 4.7.1 regarding the FE model of the typical section, the material properties of the polyamide in longitudinal direction shall be adopted. Young's modulus of polyamide in longitudinal direction, discussed in Section 4.2.2, was adopted to define the elasticity of the material. True stress - true strain relationship of polyamide in longitudinal direction shown in Figure 4.6 was input into the model to define plasticity.

To be able to make comparison with the typical section model, locations of loadings and supports were assigned according to the type D model shown in Figure 6.22.

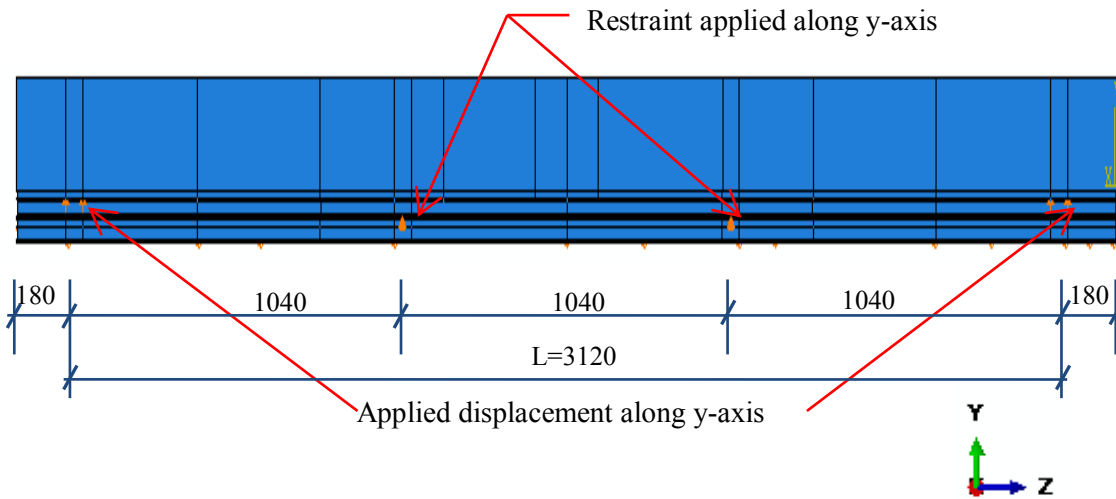
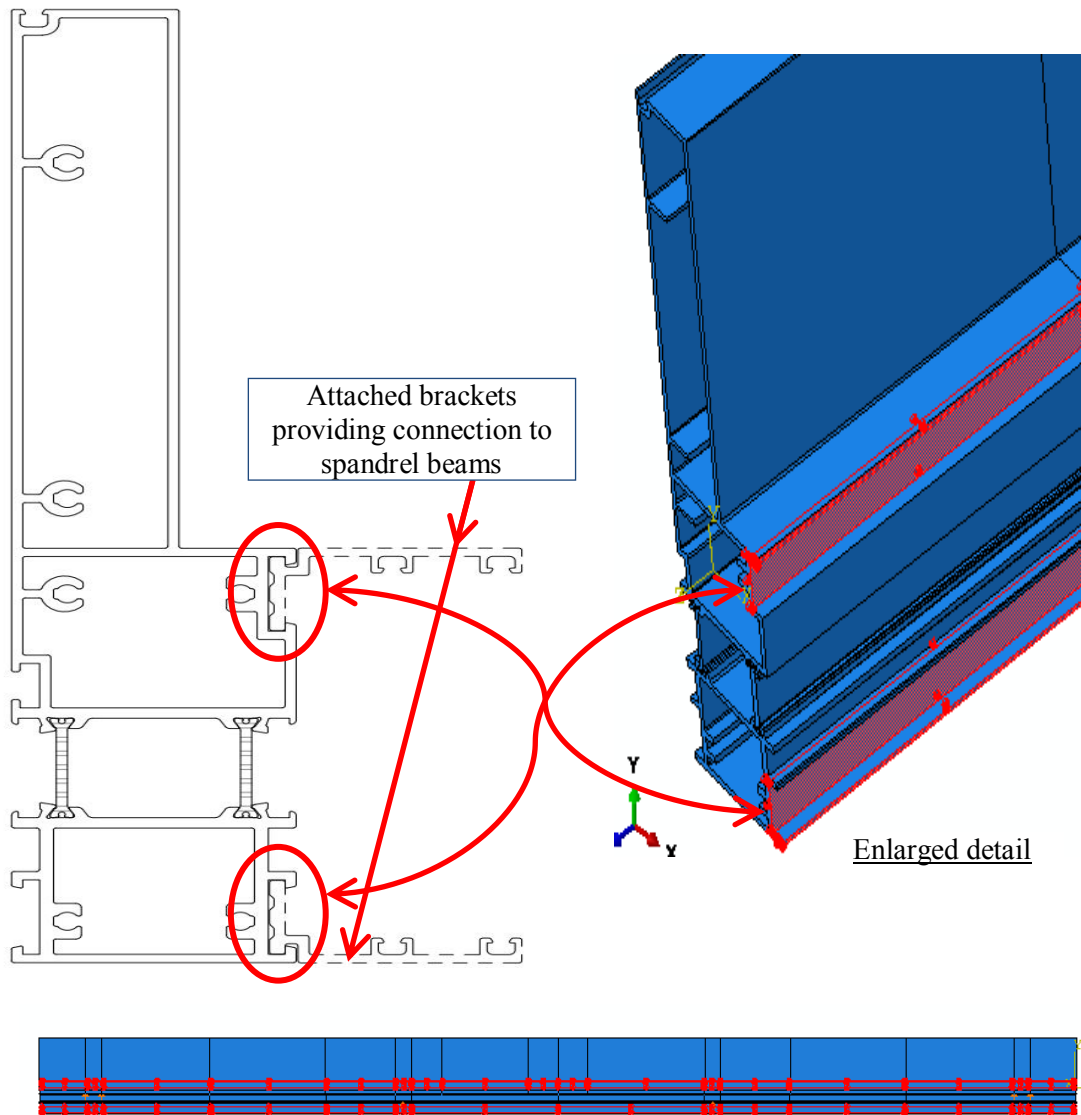


Figure 6.22 Model setup diagram

Figure 6.22 shows identical span, loading and support conditions as type D beam of the typical section. However, extra lateral supports had to be assigned to stop the section from losing balance due to the asymmetrical geometry of the section. Lateral supports were assigned to the locations where brackets were attached to connect the mullion section to the spandrel beams of the façade as the spandrel beams provide lateral restraint to the mullion. The assigned lateral supports, representing the lateral restraint

provided by spandrel beams, are shown in the figure below. The areas of support were defined according to the assembly diagram shown in Figure 6.23.



Lateral supports assigned along the whole span

Figure 6.23 Assignment of lateral support

Same partitioning techniques, used in building the typical section model, were also employed here. The beam model was divided into several regions according to Figure 4.42 and Figure 4.43 as well as Table 4.8 in Chapter 4. The setup dimensions of type D beam listed in Table 4.8 was adopted. As the beam model was partitioned into regions A1 to G1, boundary conditions and loadings can easily be applied as well as the contact interactions along the beam span. When assigning contact interactions between skin and

core, the multi-phase beam failure model initiated in Section 4.7.2, was applied to model the progressive failure process.

Fine meshes were assigned to all parts of the beam. Internal and external aluminium parts were assigned to hex dominated quadratic reduced integration solid element (C3D20R). The mesh size of the external aluminium is seed 9 while the internal one had to be assigned to finer mesh of seed 7 due to its geometrical character. Fine mesh of seed 7 was assigned to polyamide part (PA). According to the typical section model, hex dominated linear elements with incompatible mode (C3D8I) were assigned to polyamide part. Detailed mesh assignments are shown in Figure 6.24 to Figure 6.27 below.

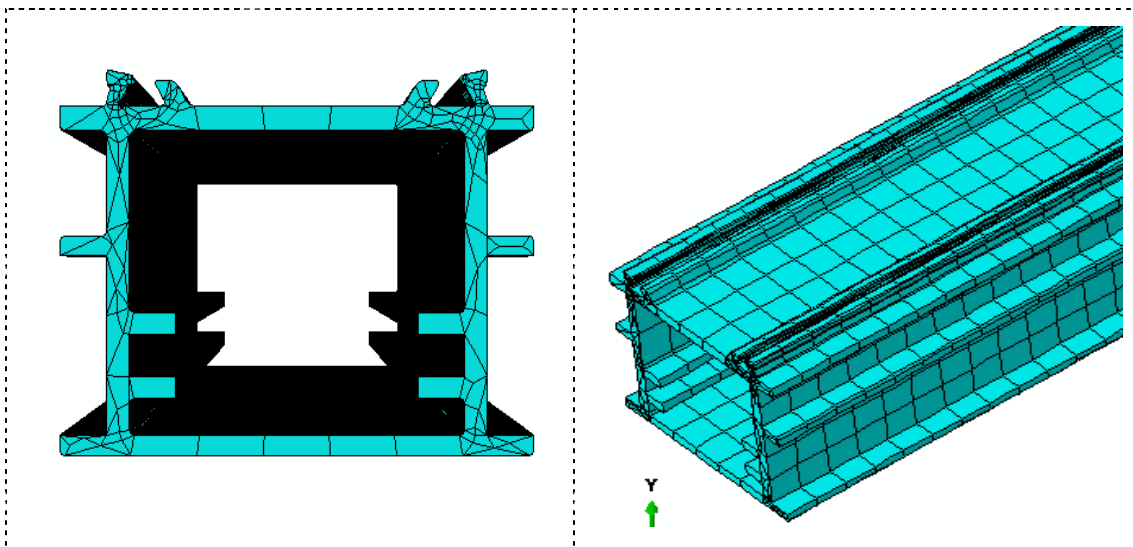


Figure 6.24 Mesh assignment of internal aluminium part

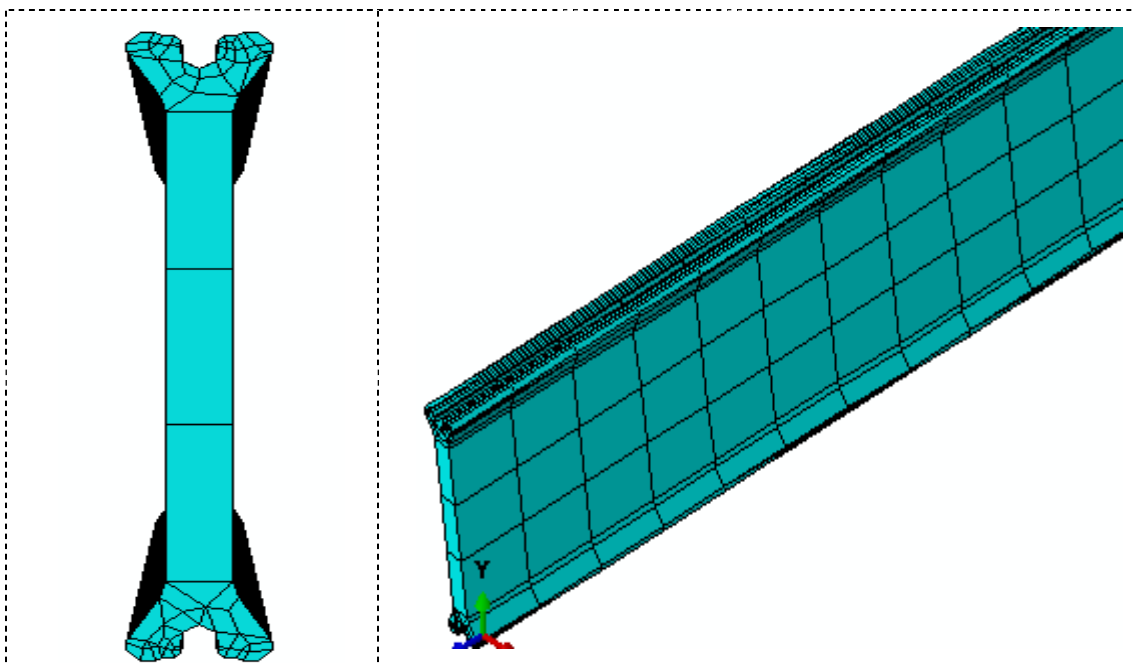


Figure 6.25 Mesh assignment of polyamide part

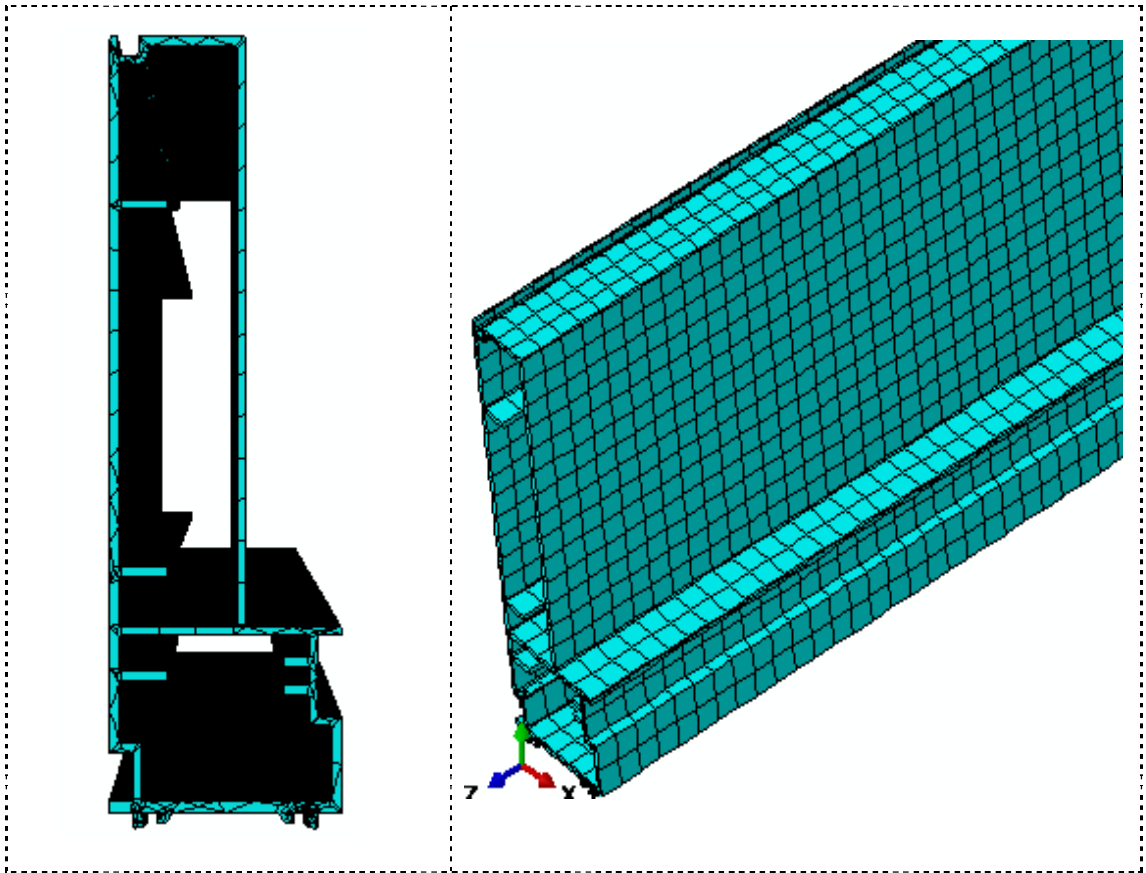


Figure 6.26 Mesh assignment of external aluminium part

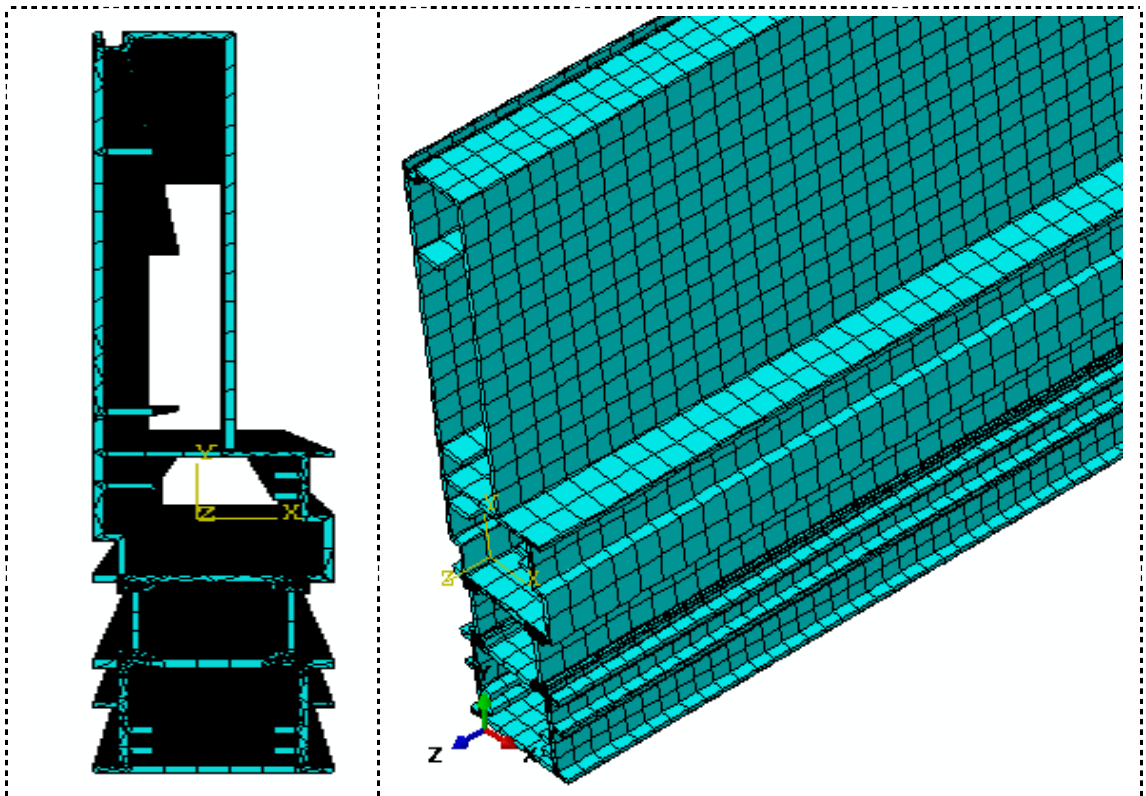


Figure 6.27 Mesh assignment of the whole section

Based on the methodology created during the modelling of the typical section, the mechanical contact property of tangential behaviour was assigned as interaction property. Penalty friction formulation was adopted for the contact bodies in the isotropic direction. Since experimental investigations have not been carried out for this asymmetrical profile, the initial friction co-efficient of the typical section of 0.7 was assigned based on the typical section.

“Surface to surface” discretization was again assigned to the interaction between aluminium and polyamide contact surfaces as the typical section. The aluminium interface was assigned as “master” surface while polyamide interface was assigned as “slave” surface. The details of master-slave surfaces are similar to the shear model shown in Figure 6.3. “Small sliding” tracking formulation was assigned for the tracking approach between master and slave surfaces. The assignment of external and internal interactions is visualized in Figure 6.28. Similar to the typical section model, interference fit option was chosen to remove minor degree of overclosures between the contact pairs.

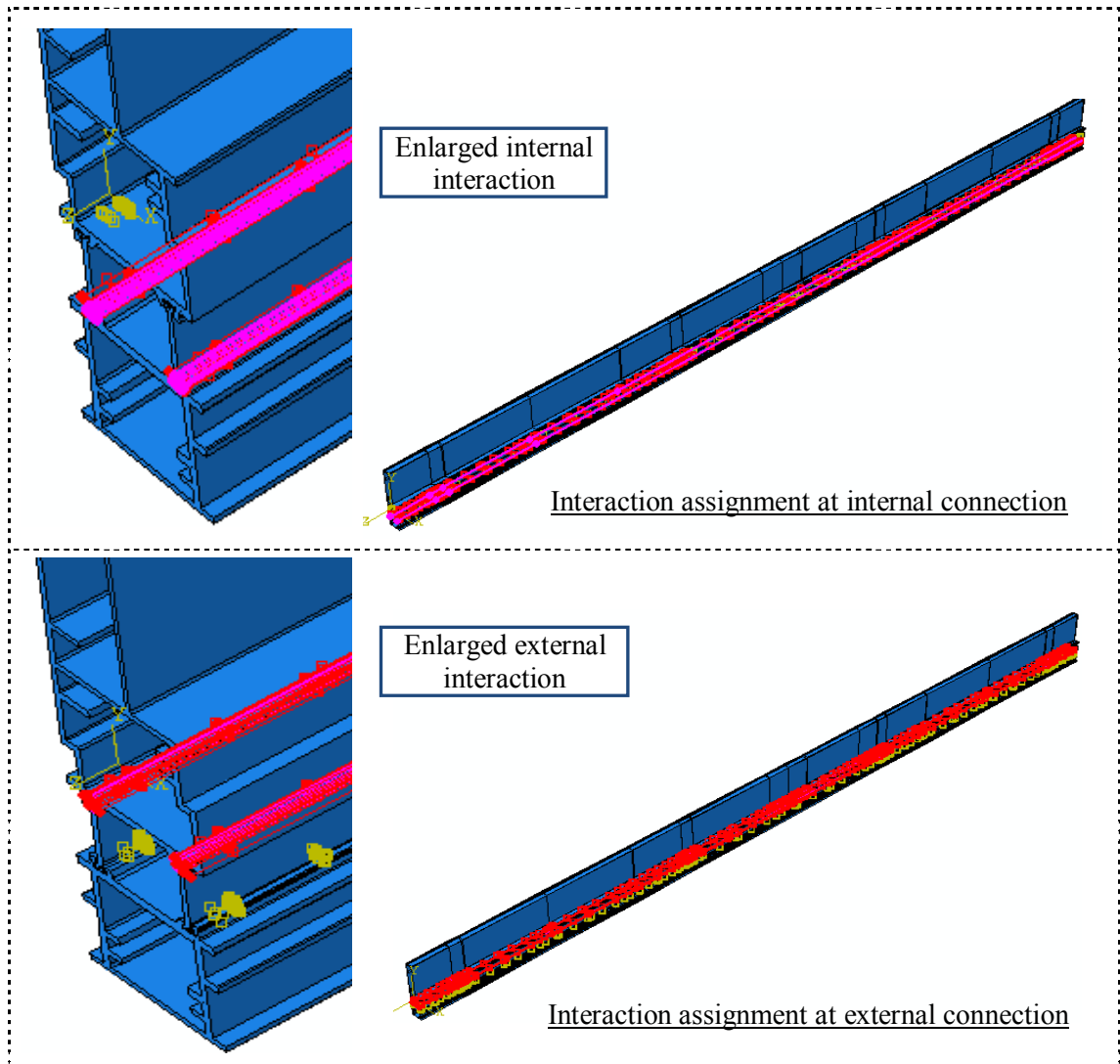


Figure 6.28 Interaction assignment

Loading was applied as displacement according to the typical section models. The applied displacement values of the typical section models were based on the observation of experiments. Unfortunately, there was no experimental data available for this asymmetrical section. Therefore, trial and error method was adopted to find the critical loading (applied displacement). To determine the critical applied displacement, the typical section model was used as a benchmark. As the displacement and bending capacity are related to the bending stiffness of the section and beam span, comparison was made between the asymmetrical section and the typical section of type D beam. Since the loading was applied on the internal aluminium part, the bending capacity comparison was based on the comparison between the bending stiffness of the internal aluminium parts. Since both have the same material properties, the second moment of inertia of the internal aluminium part, related to the neutral axis of the whole section, was compared. The second moment of inertial of internal part of the asymmetrical

section is about 60% of the typical section. Hence, the initial trial displacement for the first step was set at 30mm which is 60% of the applied displacement to type D of the typical section model. In the third step, corresponding to Table 4.9, the applied displacement was assigned as 50mm (approximately 60% of type D beam). The model ran for 70 hours and stopped when it finished 99.8% of the first step. The deflection at mid-span reached 30mm obtained from the load versus mid-span displacement graph (Figure 6.29). The stress concentration at external aluminium parts reached ten times their yield stresses. The contact penetration errors stopped the model to converge. As the interfacial actions between the contact bodies are complicated, they generated the highly non-linear behaviour under bending. The excessive deformation brought in high contact forces and, therefore, produced unresolvable contact penetration errors to prevent the model from converging. This implied that the beam might be overloaded as the loading history affected the loading capacity and loading path. The applied displacement caused geometrical non-linearity in the earlier loading increment determined the loading capacity and deformation in the next increment. Therefore, the applied displacement of 30mm caused excessively large deformation and contact forces, well beyond the capacity of this façade section, and had to be reduced to find an approximate match for its actual capacity.

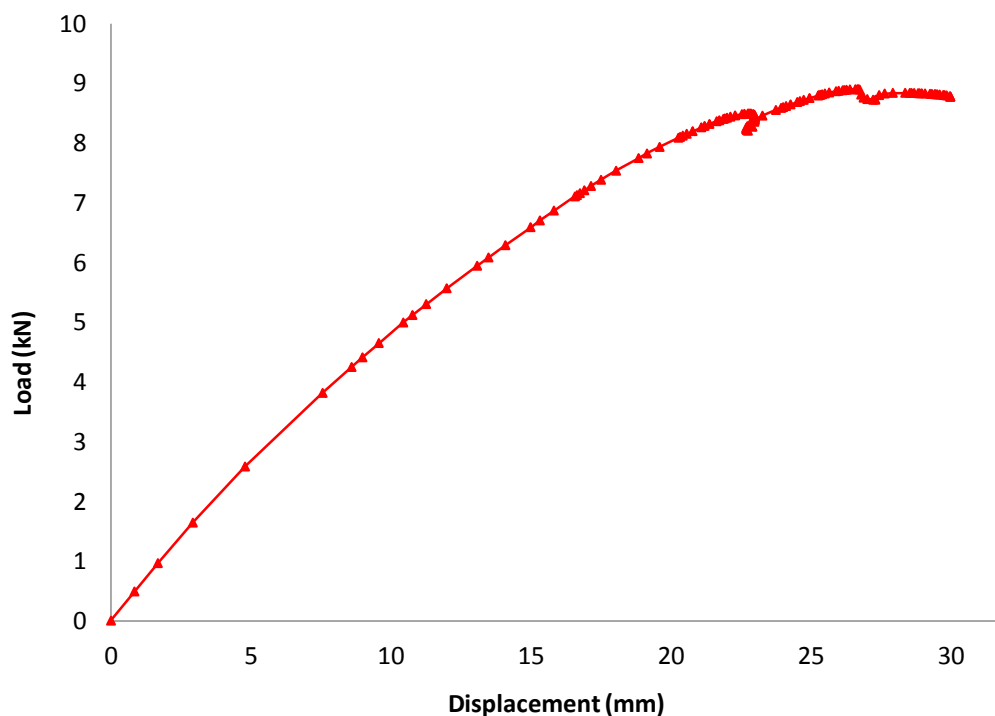


Figure 6.29 Load vs mid-span displacement – Trial 1

The applied displacement in step one was then gradually reduced to find the approximate critical loading, capable of generating realistic load-displacement pattern and making the model converge. A series of models were created to apply trial displacement in the first step. When the applied displacement reduced to 14mm, the model converged. The load versus mid-span displacement graphs for these trial models are plotted below in Figure 6.30.

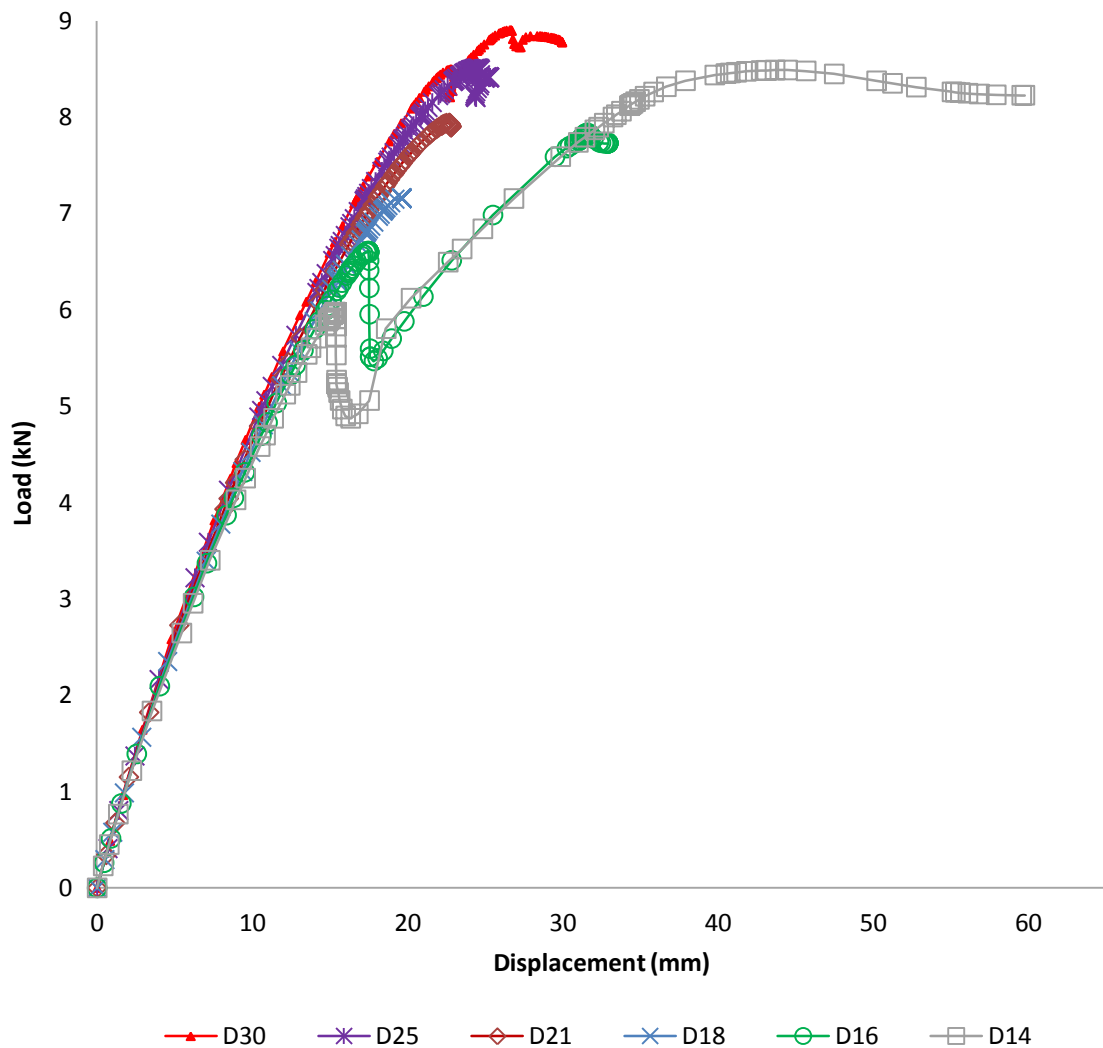


Figure 6.30 Load vs mid-span displacement – comparison of trial models

where,

D30 to D14 indicates the applied displacement in the first step varying from 30mm to 14mm, respectively.

Based on the observations in Figure 6.30, the load verse mid-span displacement graphs show a consistent trend for all models in the elastic range. The mid-span displacement

increased with applied loading for D30 to D18 graphs. However, the severe contact penetration errors made these models fail to advance through the first step.

For the graphs D14 and D16, both graphs show a dip in loadings when the connection slipped. The loads then picked up after reaching the lowest values. Although the peak load of D14 is lower than D16, the trends coincided after the dip. D14 graph was able to show the full loading duration as the model converged. This D14 model exhibited a similar behaviour to the typical section model and showed the hardening part after the connection slipped and re-engaged itself in the plastic range.

From the above load-displacement graphs, it can be concluded that the applied loading in the first step before slip occurring affected the overall behaviour of the beam. This is probably due to the non-linearity of the interactions existing in the connections. The beam behaviour at any loading increment relies on the previous increment. The frictional interaction between aluminium and polyamide is related to the applied normal pressure in the connection. Any loads higher than the beam capacity resulted in unrealistic stress concentrations and high degree of overclosure between the contact pairs. And, therefore, the applied high load caused convergence problems of the models and can be considered as not suitable for the beam. This trial and error process was based on the calculations done by the finite element method to find a realistic loading value for the beam model when there is no experimental data available. This method is able to provide a reasonable estimate of the section capacity with limited resources. For this asymmetrical section, the critical applied displacement was identified as 14mm in step 1. The detailed assignment of displacement and friction co-efficient are listed in Table 6.5 below.

Table 6.5 Assignment of displacement and friction co-efficient

Step 1 - Phase I		Step 2 - Phase II		Step 3 - Phase II	
Assigned displacement (mm)	Friction co-efficient	Assigned displacement (mm)	Friction co-efficient	Assigned displacement (mm)	Friction co-efficient
14	0.7 for all regions	Propagated from Step 1	0.7 for A1,D, G1; 0.1 for other regions	50	As step 2

6.4.2 Typical results and discussions

Results of the converged model D14 are discussed in this section. The beam bent under the two applied loading (displacement). The largest displacement is at mid-span of the beam. The deformed shape at the end of step 3 is shown in Figure 6.31 below.

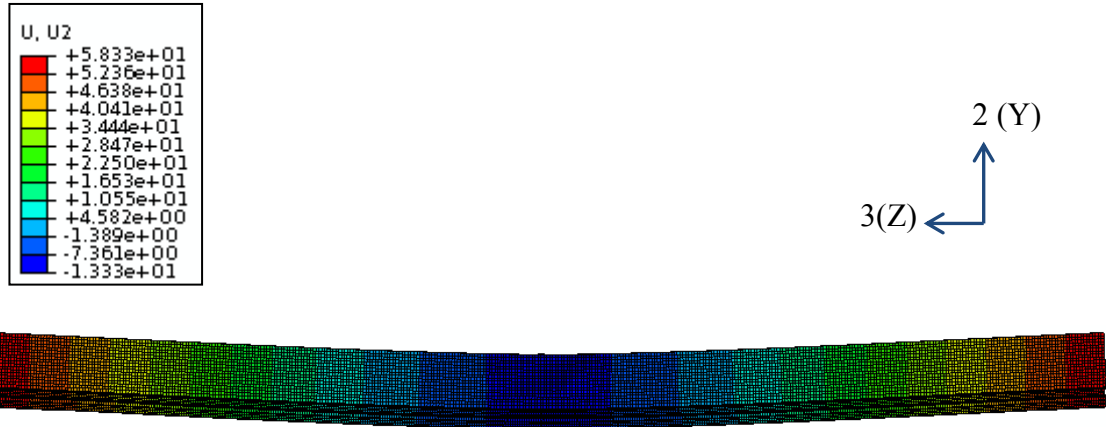


Figure 6.31 Deformed shape and displacement contour along 2-axis (vertical displacement)

The horizontal displacement (along 3-axis) is also plotted below in Figure 6.32 to show the differential movement between each part of the section. The region at mid-span of the beam shows no differential displacement at the connections which indicates no slippage is occurring. This confirmed the assumption of multi-phase beam failure model, initiated in Section 4.7.2, was also applicable to the asymmetrical sections. Connections at both ends of the beam show clear differential displacements which indicate the occurrence of slippage.

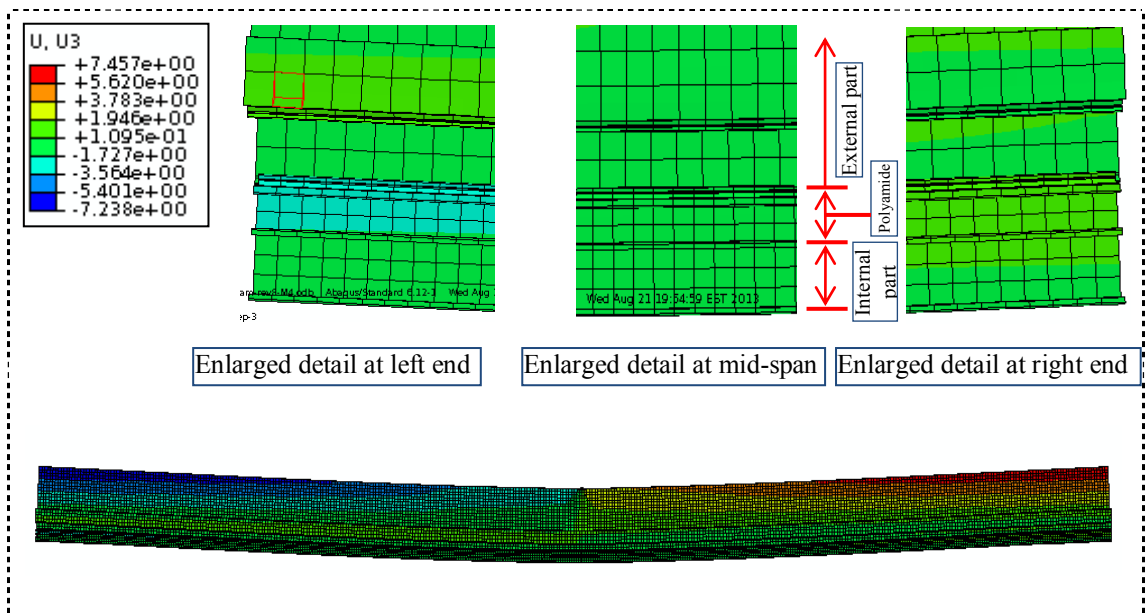


Figure 6.32 Displacement contour along 3-axis (horizontal displacement)

Load versus mid-span displacement graph shown in Figure 6.30 of D14 shows similar trend as the one obtained from the typical section model – type D beam model. When the loading capacity reached a peak value, it dropped down sharply due to the slippage of polyamide away from the connection. The loading capacity soon picked up and went up higher than the previous peak value, then trended flat as displacement increased. This phenomenon is different from the typical section results, as both experimental and numerical investigations of the typical section showed only one peak load. This is probably due to the re-engagement of the connections. Further investigation is required to confirm this assumption.

To study further into the bending behaviour, neutral axis location is investigated at the critical load points – elastic load, first peak and dip loads. Strain diagrams at mid-span location are plotted at these load stages, to show the neutral axis location, in Figure 6.33. In the elastic range, the neutral axis is located below the mid section height. It moved higher towards the middle of the section height when it reached the peak load. At the dip load, the neutral axis rested at middle of the section height. It indicated that the neutral axis location was no longer at the geometric centroid of the section after the slippage in the connection occurred. After slip, the external and internal aluminium parts partially separated and bent according to their own neutral axis rather than the neutral axis of the composite section. As the connections were formed by polyamide being rolled into the knurled aluminium extrusions, the polyamide bent together with the aluminium parts after slip. As the deformation increased, the interfacial action between them possibly re-connected the slipped joints and the composite action was restored again. As the sectional area of the external aluminium part is much larger than the internal one, the re-engaged section was able to reach the second peak load shown in the load versus mid-span displacement diagram. This is different from the typical section due to the different geometry and possible minor degree of re-engagement at the connection after slip. The section capacity of the typical section increased but was not able to create the second peak load.

The strain distribution diagrams also showed the connection failure after elastic loads. Point A and B are located at the top and bottom extreme fibre of the external part while point C is located at the bottom extreme fibre of internal part which is also the bottom extreme fibre of the whole section. The strain diagram in the elastic range is almost linear where point A, B and C are lying on a straight line. The point C moved away

from the linear line between points A and B in the peak and dip loads, which showed non-linear behaviour in these loading stages. This phenomenon is consistent with the experimental and numerical results of the typical section.

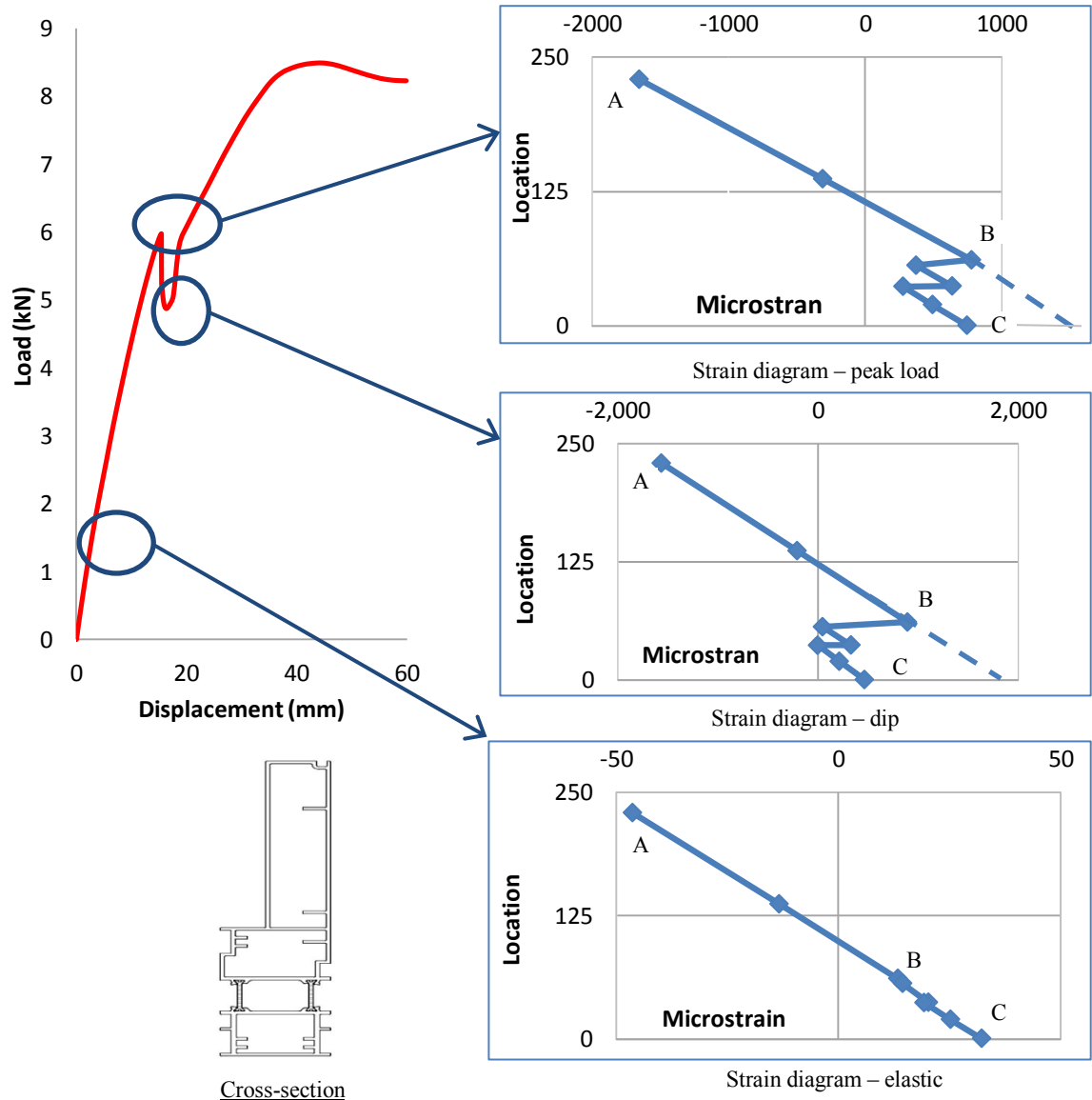


Figure 6.33 Strain distribution diagrams at mid-span location

Load versus curvature diagrams of top and bottom extreme fibres at mid-span location were plotted below for further understanding of the beam behaviour. The formulation used to calculate the curvatures given in Section 5.4.4 was adopted. The top and bottom curvatures of the external aluminium part (points A and B) together with the curvature of the internal part at bottom extreme fibre (point C) are plotted together in Figure 6.34.

The curvature of bottom extreme fibre (point C) is much smaller than the one at top extreme fibre (point A). After the loading reached the first peak value, the connection

slipped. The loading capacity dropped to the dip load and the curvature at top extreme fibre increased but the curvature at bottom extreme fibre decreased. This can be explained by the strain diagram shown in Figure 6.33. The strain at point C is similar to point B at peak load. It dropped to approximately half of the value at point B at dip load due to the partial separation of the connections after slip. Therefore, the curvature at point C decreased from the peak load to dip load stage. As both aluminium extrusions bent along their own neutral axes, the strain distribution between points A and B remained as a linear distribution and the load versus curvature graph of points A and B is mirrored between each other. Interestingly, the graph of load versus curvature at bottom extreme fibre of the section (point C) is similar to the one at top extreme fibre of the typical section.

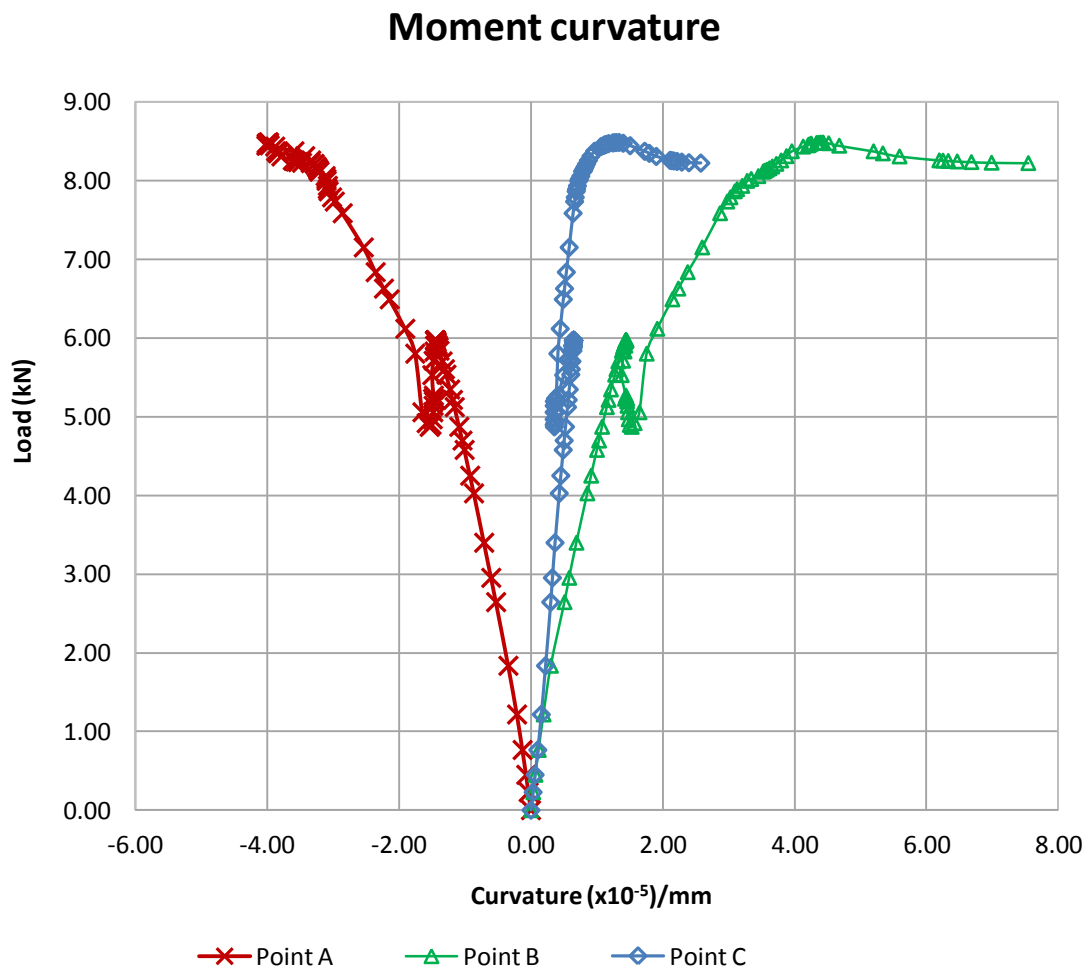


Figure 6.34 Load vs curvatures at various locations of the mid-span cross-section

In conclusion, the beam model shows similar behaviour between this asymmetrical section and the typical section. The proposed partitioned multi-phase beam failure

model was successfully applied. The beam deformed in a consistent way as the typical section. The connection slipped after reaching the peak load. As the polyamide slipped, the internal and external aluminium parts were separated partially. This caused the dip in loading capacity. After the drop, the connection was gradually re-engaged together and the loading capacity increased similar to the typical section models. However, due to the large bending stiffness of the external part, the loading capacity exceeded the previous peak to create the second peak load before the hardening stage started. This phenomenon is different from the typical section as the bending stiffness of the external part of the typical section is too small to generate the second peak load after slip.

6.5 Summary and conclusions

In summary, numerical investigation of an asymmetrical thermal break façade mullion section was presented in this chapter. Finite element models were created by using ABAQUS software to investigate the shear and transverse tensile capacities. FE model of four-point beam bending was built using ABAQUS software as well. Results were presented and discussed.

Basic principles of setting up the model and applying loading and boundary conditions were based on the principles initiated in Chapter 4. Mesh assignment, material modelling and contact interactions were defined according to Chapter 4. Fine meshes were adopted similar to the typical section model. Simplified assumptions for assigning material properties were made by applying isotropic material properties of polyamide in transverse direction to the whole part in shear and tensile models while polyamide material properties in longitudinal direction were applied as in isotropic case for the beam model. The interaction between aluminium and polyamide was assigned as frictional behaviour as for the typical section.

To simulate the failure mechanism under shear and bending, the two modelling techniques created in Chapter 4 were adopted for this asymmetrical section model. To model the shear failure, the proposed progressive failure model was applied while the proposed partitioned multi-phase beam failure model was adopted to simulate the failure mode under bending/shear combined action.

Similar to the typical section, the failure modes of shear and tension models were either the polyamide slipping away or being pulled away from the connections, respectively.

The beam model showed slippage of connection and the three-stage progressive failure mode.

The deformed shapes of all FE models were also presented and discussed. Contact stresses of shear and tensile models were plotted to provide an understanding of interaction between aluminium and polyamide at these loading conditions. Load-displacement relationships for both tension and beam models were plotted as well as load-slippage relationship for the shear model. Strain distribution diagrams at mid-span location of the beam model as well as load versus top and bottom extreme fibre curvature graphs were plotted to gain further knowledge of the beam bending behaviour.

In conclusion, the modelling techniques created to build the FE models of the typical section were successfully adopted to model this custom made asymmetrical façade section. This is a strong and supporting evidence that the two novel models proposed in Chapter 4, namely, proposed progressive failure model and proposed partitioned multi-phase beam failure model are suitable to be generalised for various thermal break façade sections.

The models of section shear and transverse tensile capacity generated a similar trend as the typical section. However, variations in the beam model were observed. The capacity of beam model made of asymmetrical section mainly depends on the contact forces, contact penetration errors and loading history and loading path. After slippage occurred in the connections, the internal and external aluminium extrusions were partially separated and bent along their own neutral axes. As the deformation increased, the interfacial action between them possibly re-connected the slipped joints and the composite action was restored again. As sectional area and bending stiffness of the external aluminium part are too large to be ignored, the re-engaged section was able to reach the second peak load. This phenomenon, revealed by the finite element simulation, needs to be confirmed by experimental investigation in future studies.

Chapter 7

Proposed Frame Work for Analytical Solution Based on Sandwich Theory

7. Proposed frame work for analytical solution based on sandwich theory

7.1 Introduction

Sandwich types of sections have been widely used in various industries, mainly aerospace and car industries, for years. They are also used in manufacturing large integral shell structures. A typical sandwich section consists of two thin stiff skins and a core which is stiff in vertical direction and very flexible in horizontal direction. The skins are either identical or different.

Early studies of sandwich theory are listed in (Plantema 1966) and then followed by Allen in (Allen 1969). Allen assumed the skins and the core are firmly bonded together. The core is anti-plane which makes no contribution to the flexural rigidity of the sandwich beam. However, it is stiff in transverse direction. Allen studied both thin and thick skinned sandwich beams. For the thick faced sandwich beam, he concluded that local bending stiffness of the skins has an effect on the shear deformation of the core. He also assumed that shear stress is constant through the core and the whole sandwich beam study is limited to the elastic range. Zenkert (Zenkert 1995) further developed Allen's sandwich theory by introducing transverse shear deformation.

Other researchers such as Monforton and Ibrahim (Monforton & Ibrahim 1977) studied sandwich plates with anti-plane core and two unequal thickness faces. Kemmochi and Uemura (K.Kemmochi 1980) proposed a multilayer-builtup theory to analyse a sandwich beam under four-point bending. They considered bending stiffness of face and core as well as the relative displacement between both faces. Gordaninejad and Bert (Gordaninejad & Bert 1989) included transverse shear deformation in the facings and stretching action in the core into their sandwich theory.

Several researches led by Frostig (Frostig & Baruch 1990), (Frostig 1991),(Y 1992), (Frostig 1992), (Y. Frostig 1992), (Frostig & Shenhar 1995), (Shenhar, Frostig & Altus 1996) and (Thomsen & Frostig 1997) studied the behaviour of sandwich beams with transversely flexible cores by using a superposition approach. They included the effects of transverse flexibility of the core and peeling stresses between the skin face and the core on the overall bending behaviour. They investigated sandwich beams with either identical or different skins. Their superposition approach is the basis of this proposed analytical solution.

A typical thermal break façade section comprises two aluminium extrusions joined by a polyamide core. Comparing with aluminium extrusions, the polyamide core is very flexible in horizontal direction due to the material properties and geometrical size. However, it is stiff in the vertical direction as it is often made short and stocky. It, therefore, can be classified as a special type of sandwich structure which has irregular thick skins.

Past studies of the thermal break façade profiles by Feldmeier in (Franz Feldmeier 1988) and Heinrich et, al. in (Heinrich, Schmid & Stiell 1980) were based on the sandwich theory. They took consideration of the shear deformation of the core. Shear deformation was obtained from the experiments to calculate elasticity constant of the polyamide core. Elasticity constant and section geometry were used as well as the span length to work out the effective stiffness of the section in the elastic range. The capacity of the composite section relies entirely on the experimental results to determine the elasticity constant. Their approach to include the composite action between aluminium and polyamide by defining the elasticity constant was adopted in European Standard EN14024:2004 (Standard 2004).

Although the above analytical investigation of the section capacity of the thermal break façade section provided analytical solutions to work out the section capacity, it is rather a semi-empirical analytical solution and has to rely on the outcomes of experimental investigation. This chapter proposes a new frame work for an analytical solution based on the sandwich theory and superposition approach to evaluate the bending capacity of any thermal break façade section in the elastic range. The original sandwich structures proposed by Frostig is under the assumption that the structure is formed by top and bottom thin skins with relative thick core in the middle, which is different from the thermal break façade sections in this research. The differences are listed below.

1. Geometrical difference – the typical sandwich structure is made of solid top and bottom face sheets/skins plus solid thick core in the middle while the thermal break façade section comprises top and bottom aluminium extrusions which are hollow sections and two thin pieces of polyamide joining them together.
2. Connection between the skin and core is different. The width of contact surface of the typical sandwich structure equals to the section width while the contact width of the thermal break façade section is only a fraction of the section width.

The interfacial action between the skins and core of the thermal break section is mainly frictional action with dependence on the manufacturing process as the polyamide is rolled into the pre-knurled aluminium extrusions. It is therefore complicated. However, the interfacial action for the typical sandwich structure is cohesion/friction against peeling stresses.

3. Loading conditions are different. This research focused on beam bending under multi-loading points rather than the simple three-point loadings/uniformly distributed loadings.
4. The failure mechanism is different. The failure of the typical sandwich structure is the separation of skin and core due to the peeling stresses while the failure mechanism of the thermal break section is much more complicated. The failure of the thermal break façade is mainly due to the slippage of the connection, i.e. polyamide slipped away from connection. However, peeling forces also make contributions. The failure mechanism of the thermal break section is the combination of slippage due to friction and separation due to peeling stresses. It is therefore much complicated than the typical sandwich structure.

These differences result in the fact that Frostig's formulations cannot be directly adopted in the current study, and therefore, it requires analytical development to derive new formulations to suit the thermal break section. Based on the superposition approach, the analytical formulations were re-developed and advanced for the thermal break façade mullion sections under four-point bending. The typical thermal break façade section studied in this thesis is used as an example.

7.2 Analytical formulations

Analytical formulations are based on the superposition approach by Frostig and his colleagues. Formulations for calculating deflection, shear stresses and peeling stresses as well as bending moment were derived based on the sandwich section with anti-plane core under either uniformly distributed load or concentrated load. Due to the differences between the typical sandwich structure studied by Frostig and the thermal break façade section, formulations were re-derived to suit. Boundary conditions of four-point bending were adopted to work out constants in the equations. The analytical formulations are based on the typical thermal break façade section studied in this research, which comprises asymmetrical top and bottom skins made of identical aluminium alloy and glass fibre reinforced polyamide core.

7.2.1 Superposition approach

Superposition approach is to separate the total loading conditions applied on the skins and core of the sandwich beam. The whole sandwich structure is divided into two sub-structures. The sub-structure I is assumed to be loaded in the same direction by either uniformly distributed load (UDL) or concentrated load (P). The core of sub-structure I is an anti-plane core where shear stresses exist, but the height of the core remains unchanged. Therefore, the deflections of both skins are identical. For sub-structure II, the height of the core is allowed to change. The core is loaded with self-equilibrating UDL or concentrated load P and, therefore, is free of shear stresses. The UDL or P applied on top and bottom skin is equally valued but in opposite direction. The demonstration of this superposition loading is shown in Figure 7.1.

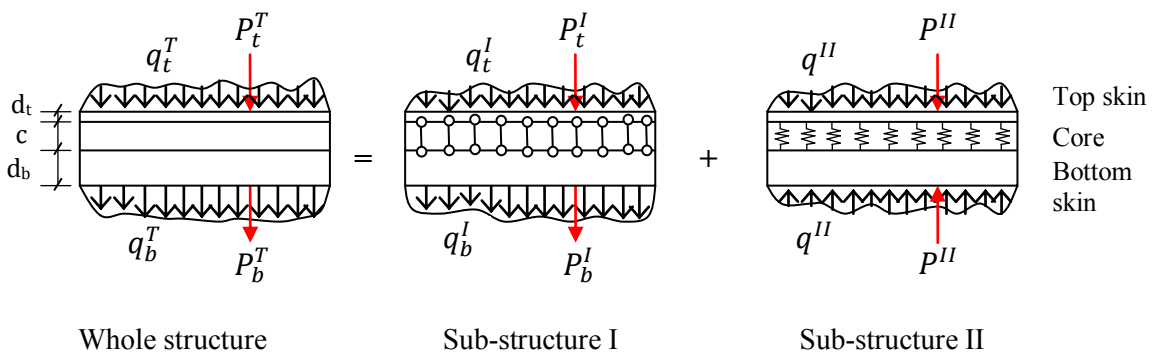


Figure 7.1 Illustration of superposition loadings

where:

d_t and d_b denote the height of top and bottom skin

c denotes the height of core

q_t^I and q_b^I denote UDL applied on sub-structure I at top and bottom skin

q^{II} denotes UDL applied on sub-structure II

q_t^T and q_b^T denote UDL applied on the whole structure at top and bottom skin

P_t^I and P_b^I denote concentrated load P applied on sub-structure I at top and bottom skin

P^{II} denotes concentrated load P applied on sub-structure II

P_t^T and P_b^T denote concentrated load P applied on the whole structure at top and bottom skin

As to Figure 7.1, it is, therefore, seen that,

$$q_t^I + q^{II} = q_t^T; \quad q_b^I + q^{II} = q_b^T \quad [7.1]$$

or

$$P_t^I + P^{II} = P_t^T; \quad P_b^I + P^{II} = P_b^T \quad [7.2]$$

and

$$q_t^I + q_b^I = q_t^T + q_b^T = q^T \quad \text{or} \quad P_t^I + P_b^I = P_t^T + P_b^T = P^T \quad [7.3]$$

7.2.2 Basic assumptions

Assumptions are made to work out governing equations and formulas. The assumptions are consistent with the assumptions made by Allen and Frostig. They are listed below.

1. The structure is assumed to behave in the elastic range.
2. The deflections and rotations of skins and core are small.
3. The cross-section of top and bottom skins remains plane and perpendicular to its longitudinal axis after bending.
4. The distance between the centroids of the skins is constant.
5. The shear strain in the skins is negligible.

6. The mechanical properties of top and bottom skins are identical.
7. The core is very stiff in transverse direction that can only resist shear stresses and transverse normal stresses, but has negligible normal stress resistance in horizontal direction. In other words, the core has little flexural stiffness.
8. The interface between skin and core carries shear and transverse normal stresses.
9. The sandwich beam is loaded on the bottom skin under four-point bending.

7.2.3 Sub-structure I

As mentioned in Section 7.2.1, sub-structure I consists of two asymmetrical skins and an anti-plane core. The skins are loaded by two different loads in the same direction whose sum is the applied load. The core can only resist shear stresses and has no flexural rigidity. As the core is very stiff in transverse direction, the shear stress is assumed uniform in the core. The interfaces between skins and core are subjected to shear and peeling stresses. As the core is not deformed vertically, the displacements of the top and bottom skin are identical.

Internal force equilibrium

Internal forces are studied by assuming the top and bottom skins loaded by two loads q_t^I and q_b^I as shown in Figure 7.1. If a small portion of sub-structure I at the length of dx is used to draw the free body diagram, the internal forces on the whole structure and on skins and core can be shown as below. The width of the sandwich beam is 'b'.

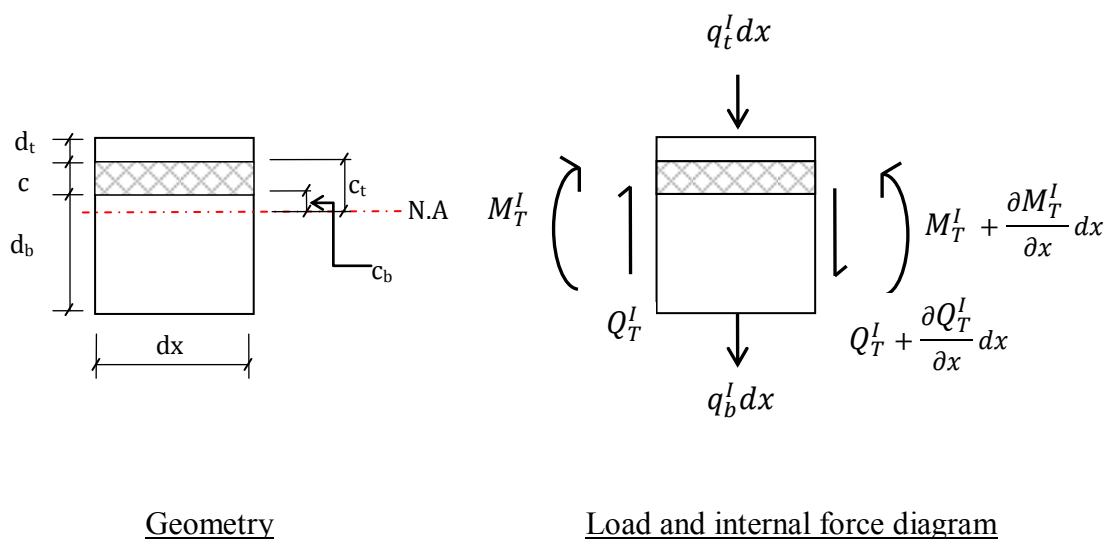


Figure 7.2 Geometry and free body diagram of overall sub-structure I

From Figure 7.2 above, the force equilibrium of overall sub-structure I can be expressed as,

$$N_T^I = 0 \quad [7.4]$$

$$\frac{\partial Q_T^I}{\partial x} + (q_t^I + q_b^I) = 0 \quad [7.5]$$

$$\frac{\partial M_T^I}{\partial x} - Q_T^I = 0 \quad [7.6]$$

where

N_T^I denotes axial force existing at the section

Q_T^I denotes total shear force existing at the section

M_T^I denotes total bending moment existing at the section

To understand the internal forces at skins and core, free body diagram is drawn below (Figure 7.3) to show internal forces separately on skins and core, based on the assumption that core takes a uniform shear stress ' τ '. The peeling stresses p_t^I and p_b^I are the normal stresses in the top and bottom interfaces between skin and core.

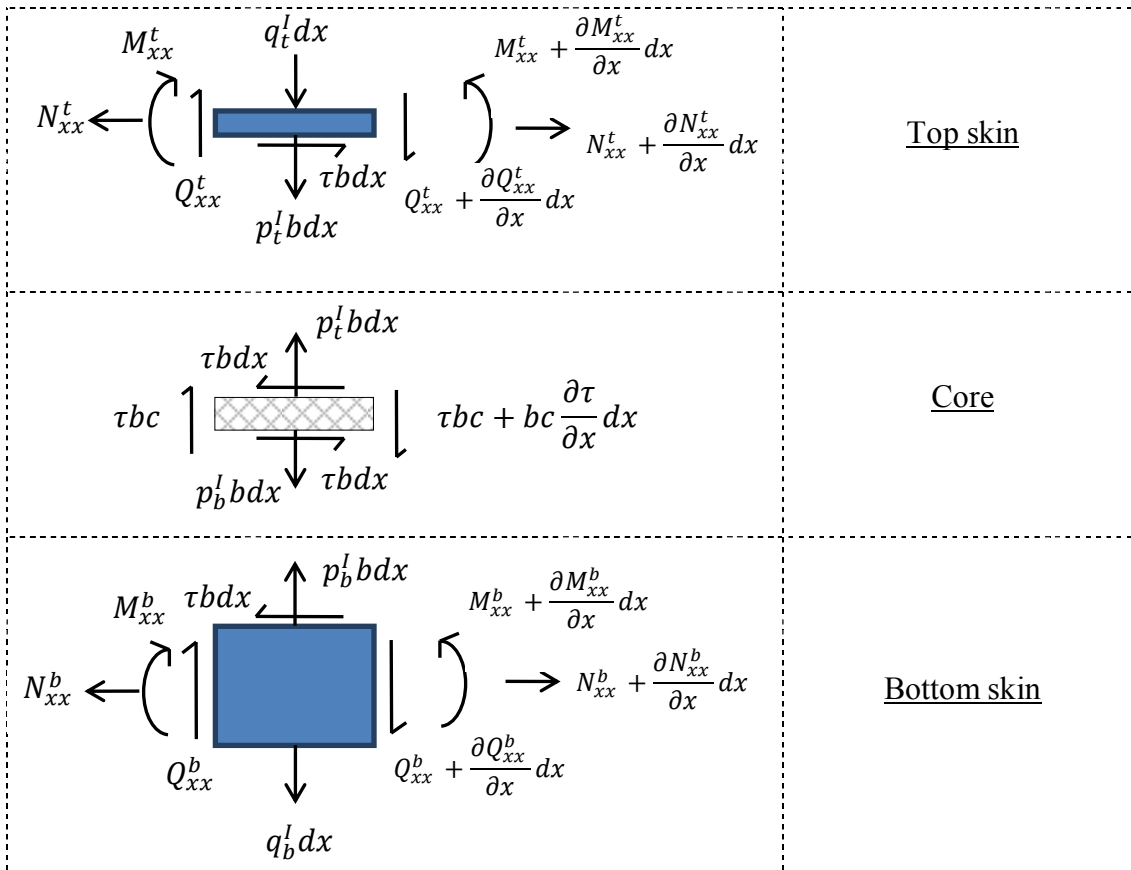


Figure 7.3 Loads and internal forces on skins and core of sub-structure I

From Figure 7.3 above, equations of force equilibrium of skins and core are:

Upper skin

$$\frac{\partial N_{xx}^t}{\partial x} + \tau b = 0 ; \frac{\partial Q_{xx}^t}{\partial x} + q_t^I - p_t^I b = 0 ; \frac{\partial M_{xx}^t}{\partial x} - Q_{xx}^t + \frac{\tau b d_t}{2} = 0 \quad [7.7]$$

Lower skin

$$\frac{\partial N_{xx}^b}{\partial x} - \tau b = 0 ; \frac{\partial Q_{xx}^b}{\partial x} + q_b^I - p_b^I b = 0 ; \frac{\partial M_{xx}^b}{\partial x} - Q_{xx}^b + \frac{\tau b d_b}{2} = 0 \quad [7.8]$$

Core

$$\frac{\partial \tau}{\partial x} c + (p_t^I + p_b^I) = 0 \quad [7.9]$$

where

N_{xx}^i denotes axial forces at top and bottom skins ($i = t, b$)

Q_{xx}^i denotes shear forces at top and bottom skins ($i = t, b$)

M_{xx}^i denotes bending moments at top and bottom skins ($i = t, b$)

b denotes the width of beam

p_t^I and p_b^I denotes the vertical normal stress at top and bottom contact layers, respectively.

Deformation diagram

Based on the definition of sub-structure I, the deflections at the top and bottom skins as well as the centre of rotation ‘O’ are identical. Assume w^I is the displacement at top and bottom skin and the centre of rotation which is located on neutral axis for sub-structure I. The corresponding deflection diagram is shown below in Figure 7.4.

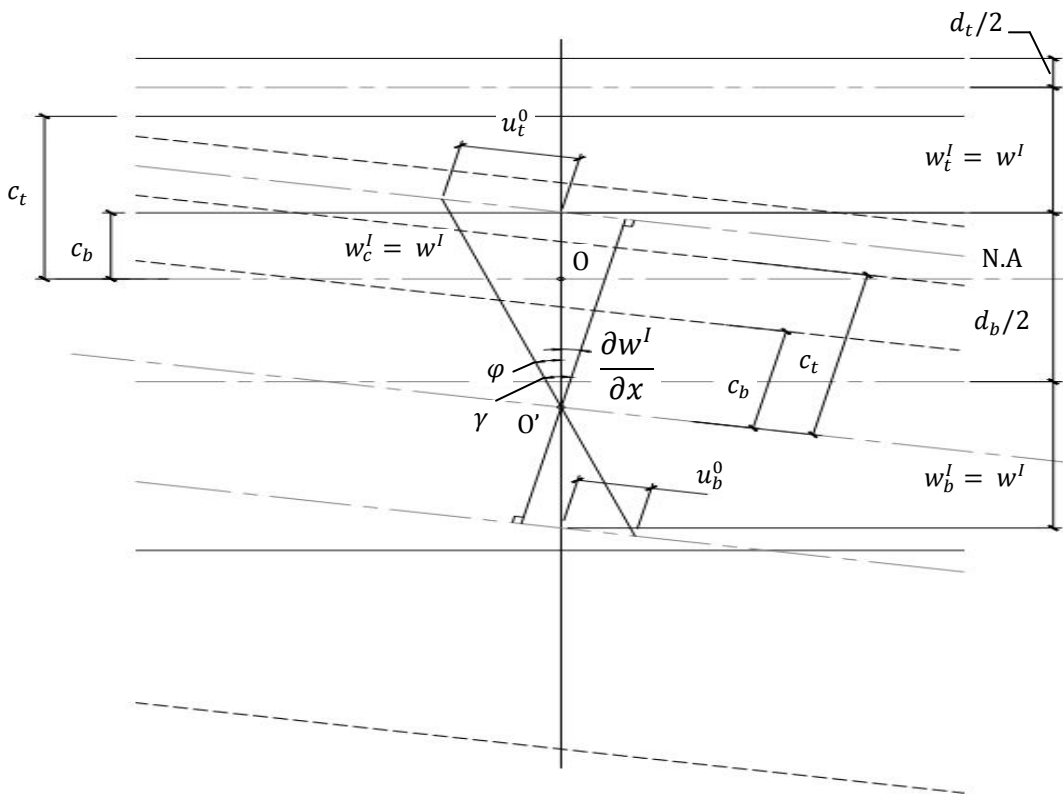


Figure 7.4 Deformation diagram of sub-structure I

In Figure 7.4 above, point O represents the centre of rotation while point O' represents deformed location of point O. The distance between point O to point O' is equal to the vertical displacement of skins and core - w^I . Based on the assumptions stated in Section 7.2.2, the centre of gravity is located on the neutral axis (N.A.) as the centre of rotation. The top and bottom skins have bending resistance, but not the core. The core only takes shear forces and has shear deformation. The maximum displacement caused by shear deformation is at the interface between the skin and core. Therefore, kinematic relationships can be worked out based on Figure 7.4.

The horizontal displacements along the centroidal axis of top and bottom skins are:

Top skin displacement

$$u_t^0 = \underbrace{-\gamma c_t}_{\text{Displacement by shear deformation of core}} + \underbrace{\frac{\partial w^I}{\partial x} (c_t + \frac{d_t}{2})}_{\text{Displacement by bending deformation of skins}} \quad [7.10]$$

Displacement by shear deformation of core Displacement by bending deformation of skins

$$u_b^0 = \gamma c_b - \frac{\partial w^I}{\partial x} \left(\frac{d_b}{2} - c_b \right) \quad [7.11]$$

Shear deformation of core

$$\gamma = \frac{\tau}{G_c} \quad [7.12]$$

where

w^I denotes the vertical displacement of the skins and core for sub-structure I.

u_t^0 and u_b^0 denote horizontal displacement at the neutral axis of top and bottom skin, respectively.

γ denotes shear strain of the core.

G_c denotes shear modulus of the core.

c_t and c_b denote distance from neutral axis to the centroidal axis of top and bottom skins, respectively.

The constitutive formulations for axial force and bending moment can be derived based on small deflection and linear elasticity assumption. They are

Axial forces at top and bottom skins

$$N_i^I = \Sigma E_i A_i \frac{\partial u_i^0}{\partial x}$$

$$\text{Top skin} \quad N_{xx}^t = EA_t \frac{\partial u_t^0}{\partial x} = EA_t$$

$$\text{therefore,} \quad N_{xx}^t = EA_t \left\{ -\frac{\partial \left[\left(-\frac{\partial w^I}{\partial x} + \gamma \right) c_t \right]}{\partial x} + \frac{d_t}{2} \frac{\partial^2 w^I}{\partial x^2} \right\} \quad [7.13]$$

$$\text{Bottom skin} \quad N_{xx}^b = EA_b \frac{\partial u_b^0}{\partial x} = EA_b \left\{ \frac{\partial \left[\gamma c_b - \frac{\partial w^I}{\partial x} \left(\frac{d_b}{2} - c_b \right) \right]}{\partial x} \right\}$$

$$\text{therefore,} \quad N_{xx}^b = EA_b \left\{ -\frac{\partial \left[\left(-\frac{\partial w^I}{\partial x} + \gamma \right) c_b \right]}{\partial x} - \frac{d_b}{2} \frac{\partial^2 w^I}{\partial x^2} \right\} \quad [7.14]$$

$$M_t^I = -EI_t \frac{\partial^2 w^I}{\partial x^2}; \quad M_b^I = -EI_b \frac{\partial^2 w^I}{\partial x^2} \quad [7.15]$$

where,

E denotes Young's modulus of top and skin material

I_t and I_b denotes second moment of inertia of top and bottom skin

Based on the internal force diagram shown in Figure 7.3 and nil axial resultant forces, the total internal forces can be expressed as:

$$N_{xx}^t = -N_{xx}^b \quad [7.16]$$

$$Q_T^I = Q_{xx}^t + Q_{xx}^b + \tau bc \quad [7.17]$$

$$M_T^I = M_{xx}^t + M_{xx}^b + N_{xx}^b \left(c + \frac{d_t}{2} + \frac{d_b}{2} \right) \quad [7.18]$$

After substituting Eqn. 7.13 and Eqn. 7.14 into Eqn. 7.16, Eqn. 7.16 becomes

$$N_{xx}^t = EA_t \left\{ -\frac{\partial \left[\left(-\frac{\partial w^I}{\partial x} + \gamma \right) c_t \right]}{\partial x} + \frac{d_t}{2} \frac{\partial^2 w^I}{\partial x^2} \right\} = -N_{xx}^b = EA_b \left\{ -\frac{\partial \left[\left(-\frac{\partial w^I}{\partial x} + \gamma \right) c_b \right]}{\partial x} - \frac{d_b}{2} \frac{\partial^2 w^I}{\partial x^2} \right\} \quad [7.19]$$

Eqn. 7.19 can be re-arranged into

$$A_t \left[-\frac{\partial(\varphi c_t)}{\partial x} + \frac{\partial^2 w^I}{\partial x^2} \frac{d_t}{2} \right] + A_b \left[\frac{\partial(\varphi c_b)}{\partial x} - \frac{\partial^2 w^I}{\partial x^2} \frac{d_b}{2} \right] = 0 \quad [7.20]$$

From Figure 7.4, geometrical relations can be obtained such as,

$$\varphi = -\frac{\partial w^I}{\partial x} + \gamma \quad \text{and} \quad c_t - c_b = c \quad [7.21]$$

By substituting Eqn. 7.21 into Eqn. 7.20, Eqn. 7.20 can be solved by integration and therefore,

$$\varphi c_t = \frac{A_b}{A_b - A_t} \varphi c - \frac{\partial w^I}{\partial x} \left(\frac{A_t \frac{d_t}{2} - A_b \frac{d_b}{2}}{A_b - A_t} \right) + A_1 \quad [7.22]$$

$$\varphi c_b = \frac{A_t}{A_b - A_t} \varphi c - \frac{\partial w^I}{\partial x} \left(\frac{A_t \frac{d_t}{2} - A_b \frac{d_b}{2}}{A_b - A_t} \right) + A_2 \quad [7.23]$$

Constants A_1 and A_2 were generated during integration where A_1 and A_2 can be taken as zero based on Eqn. 7.20.

Based on Eqn. 7.8, Eqn. 7.14 can be re-written as

$$N_{xx}^b = EA_b \frac{\partial}{\partial x} \left\{ -\frac{\partial \left[\left(-\frac{\partial w^I}{\partial x} + \gamma \right) c_b \right]}{\partial x} - \frac{d_b}{2} \frac{\partial^2 w^I}{\partial x^2} \right\} = \tau b \quad [7.24]$$

Substituting Eqn. 7.12, Eqn. 7.23 and Eqn. 7.21 into Eqn. 7.24, then Eqn. 7.24 can be re-arranged as

$$\frac{EA_t A_b c}{(A_b - A_t) G_c} \frac{\partial^2 \tau}{\partial x^2} - \frac{\partial^3 w^I}{\partial x^3} EA_b \left(-c_{2A} + \frac{d_b}{2} \right) - \tau b = 0 \quad [7.25]$$

where,

$$c_{2A} = \frac{A_b \frac{d_b}{2} + A_t \left(c - \frac{d_t}{2} \right)}{A_t - A_b}$$

With algebraic manipulations, Eqn. 7.25 is recast as the first governing equation below.

$$\frac{\partial^3 w^I}{\partial x^3} - \alpha \frac{\partial^2 \tau}{\partial x^2} + \beta \tau = 0 \quad [7.26]$$

where,

$$\alpha = \frac{A_t c}{(A_t - A_b) \left(-c_{2A} + \frac{d_b}{2} \right) G_c}; \beta = \frac{b}{\left(-c_{2A} + \frac{d_b}{2} \right) EA_b}$$

The second governing equation can be derived by first substituting Eqn. 7.15 into Eqn. 7.18.

$$M_{xx}^T = -EI_t \frac{\partial^2 w^I}{\partial x^2} - EI_b \frac{\partial^2 w^I}{\partial x^2} + N_{xx}^b \left(c + \frac{d_t}{2} + \frac{d_b}{2} \right)$$

Then, based on Eqn. 7.6 and Eqn. 7.17, the above expression can be written as

$$Q_T^I = -EI_t \frac{\partial^3 w^I}{\partial x^3} - EI_b \frac{\partial^3 w^I}{\partial x^3} + \tau b \left(c + \frac{d_t}{2} + \frac{d_b}{2} \right) \quad [7.27]$$

Based on Eqn. 7.5 and Eqn. 7.3, we get

$$\frac{\partial Q_{xx}^T}{\partial x} = -(q_t^I + q_b^I) = -q^T$$

Therefore, Eqn. 7.27 is cast into the second governing equation,

$$E(I_t + I_b) \frac{\partial^4 w^I}{\partial x^4} - b \left(c + \frac{d_t}{2} + \frac{d_b}{2} \right) \frac{\partial \tau}{\partial x} = q^T$$

By simplifying the above equation, we get

$$\frac{\partial^4 w^I}{\partial x^4} - \bar{\delta} \frac{\partial \tau}{\partial x} = \frac{q^T}{E(I_t + I_b)} \quad [7.28]$$

where,

$$\bar{\delta} = \frac{b \left(c + \frac{d_t}{2} + \frac{d_b}{2} \right)}{E(I_t + I_b)}$$

Eqn. 7.26 and Eqn. 7.28 are the two governing equations used to work out displacement and internal forces. The solutions of these two equations are

$$w^I = C_1 + C_2x + C_3x^2 + C_4x^3 + C_5e^{sx} + C_6e^{-sx} + w_p^I \quad [7.29]$$

$$\tau = -\frac{6C_4}{\beta} + \frac{s^3}{\delta}C_5e^{sx} - \frac{s^3}{\delta}C_6e^{-sx} + \tau_p \quad [7.30]$$

where,

$s = \sqrt{\frac{\delta+\beta}{\alpha}}$; coefficients C_1 to C_6 are to be determined by using appropriate boundary conditions and will be explained at the end of this section.

To find particular solutions of the governing equations, we first combine them together by subtracting Eqn. 7.28 from Eqn. 7.26. Therefore, the differential equation with one unknown is

$$\alpha \frac{\partial^3 \tau}{\partial x^3} - (\bar{\delta} + \beta) \frac{\partial \tau}{\partial x} = \frac{q^T}{E(I_t + I_b)} \quad [7.31]$$

Hence, one of the particular solutions of the above equation is

$$\frac{\partial \tau_p}{\partial x} = -\frac{q^T}{E(I_t + I_b)(\bar{\delta} + \beta)} \quad [7.32]$$

The above equation is the particular solution of Eqn.7.30. To find the particular solution of Eqn. 7.28, Eqn. 7.32 is to substituted into Eqn. 7.28, so

$$\frac{\partial^4 w_p^I}{\partial x^4} - \bar{\delta} \left(-\frac{q^T}{E(I_t + I_b)(\bar{\delta} + \beta)} \right) = \frac{q^T}{E(I_t + I_b)}$$

Hence,

$$\begin{aligned} \frac{\partial^4 w_p^I}{\partial x^4} &= \bar{\delta} \left(-\frac{q^T}{E(I_t + I_b)(\bar{\delta} + \beta)} \right) + \frac{q^T}{E(I_t + I_b)} \\ &= \left(\frac{\beta}{\bar{\delta} + \beta} \right) \frac{q^T}{E(I_t + I_b)} \end{aligned} \quad [7.33]$$

Loading function

As this research is focused on the four-point beam bending, the applied loading q^T is varied along the beam span instead of a uniformly distributed load. For the uniformly distributed load, the loading situation is simple and can be treated as a constant along the span. To represent the point loads applied at one-third and two-thirds of the span, Dirac Delta function was introduced. Therefore,

$$q_{(x)}^T = P^T [\delta_D(x - x_1) + \delta_D(x - x_2)] \begin{cases} 1, & x = x_1 \text{ or } x = x_2 \\ 0, & x \neq x_1 \text{ or } x \neq x_2 \end{cases} \quad [7.34]$$

where,

$$P^T = \int_{x_i - \varepsilon}^{x_i + \varepsilon} q_{(x)}^T dx, \quad \varepsilon \ll 1 \quad (i = 1, 2)$$

Eqn. 7.32 and Eqn. 7.33 shall be integrated to find the particular solutions for deflection w^I and shear stress τ . The integration process listed below is a process to derive relationships between shear force versus loading, slope versus loading, bending moment versus loading and deflection versus loading.

The first integration of Dirac Delta function can be represented by Heaviside function which can also represent the shear force along the beam span.

$$\int q_{(x)}^T = Q_{(x)} = P^T [H(x - x_i)] + D_1 \begin{cases} -1, & x \leq x_1 \\ 0, & x_1 < x < x_2 \\ 1, & x \geq x_2 \end{cases} \quad [7.35]$$

The second integration of Dirac Delta function can be represented by ramp function. This ramp function is equivalent to bending moment along the span as well.

$$\iint q_{(x)}^T = M_{(x)} = P^T [R(x - x_i)] + D_1 x + D_2 \begin{cases} -(x - x_1), & x \leq x_1 \\ 0, & x_1 < x < x_2 \\ (x - x_2), & x \geq x_2 \end{cases} \quad [7.36]$$

The third integration of Dirac Delta function can be represented by the first integration of ramp function. This can represent the slope along the beam span.

$$\iiint q_{(x)}^T = \theta_{(x)} = P^T [R_1(x - x_i)] + \frac{D_1}{2} x^2 + D_2 x + D_3 \begin{cases} -\frac{(x-x_1)^2}{2}, & x \leq x_1 \\ 0, & x_1 < x < x_2 \\ \frac{(x-x_2)^2}{2}, & x \geq x_2 \end{cases} \quad [7.37]$$

The fourth integration of Dirac Delta function can be represented by the second integration of ramp function which equals to the deflection multiplied by the flexural stiffness of the beam. This is the basic Euler-Bernoulli equation, also known as “static beam equation”.

$$\iiint \int q(x) = EIw(x) = P^T[R_2(x - x_i)] + \frac{D_1}{6}x^3 + \frac{D_2}{2}x^2 + D_3x + D_4$$

$$\begin{cases} -\frac{(x-x_1)^3}{6}, & x \leq x_1 \\ 0, & x_1 < x < x_2 \\ \frac{(x-x_2)^3}{6}, & x \geq x_2 \end{cases} \quad [7.38]$$

where,

x_1 and x_2 Denote the distance equal to one-third of span length and two-thirds of span length from left support, respectively.

D_1 to D_4 Denote integration constants which will be determined by appropriate loading and boundary conditions

To determine integration constants D_1 to D_4 , boundary conditions of simply supported beam loaded with two concentrated loads at one-third and two-thirds of the span (L) shown in

Figure 7.5 are considered. Based on the shear force diagram of this four-point bending beam in Figure 7.6, constant D_1 in Eqn. 7.35 shall equal to zero to be consistent with the diagram. To find the value of D_2 , boundary conditions of bending moment equal to zero at the supports were applied as illustrated below.

when $x = 0$, $M_{(0)} = 0$, also $D_1 = 0$,

therefore, from Eqn. 7.34,

$$P^T \left[\left(0 - \frac{L}{3} \right) \right] + 0 + D_2 = 0 \quad \Rightarrow \quad D_2 = -\frac{P^T L}{3}$$

Based on boundary conditions,

$$(i) \quad x = 0, \quad w_{(0)} = 0$$

$$(ii) \quad x = L, \quad w_{(L)} = 0$$

D_3 and D_4 are solved as below.

$$D_3 = \frac{P^T L^2}{6} \quad \text{and} \quad D_4 = -\frac{P^T L^3}{162}$$

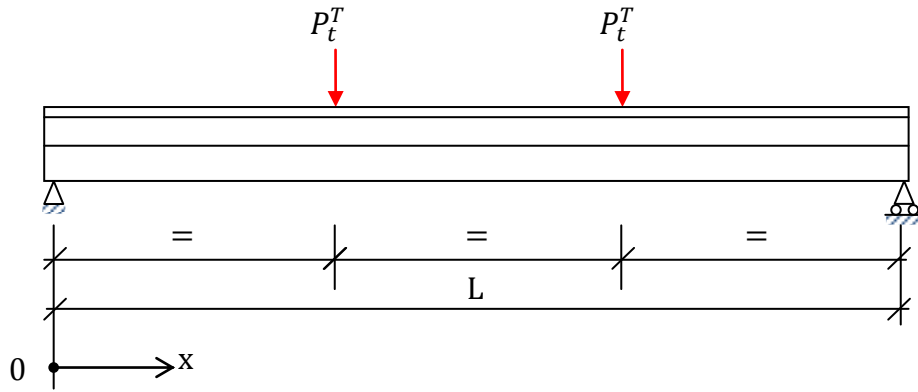


Figure 7.5 Loading diagram of four-point bending

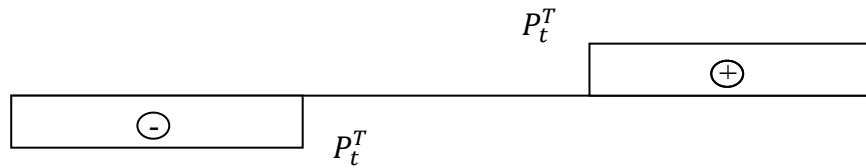


Figure 7.6 Shear force diagram

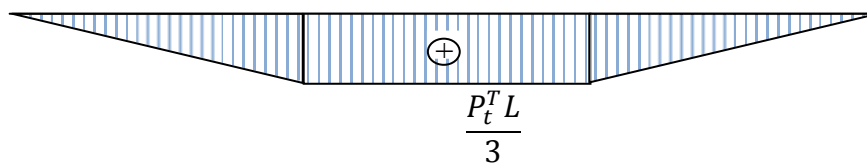


Figure 7.7 Bending moment diagram

Applying the constants D_1 to D_4 into Eqn. 7.35 to Eqn.7.38, the following equations are then derived and can be used to solve the particular solutions of Eqn. 7.29 and Eqn.7.30. The particular solution of Eqn.7.31 represented by Eqn. 7.32 can be solved by applying the Heaviside function in Eqn. 7.35 as

$$\tau_p = -\bar{A}P^T[H(x - x_i)] \begin{cases} -1, & x \leq x_1 \\ 0, & x_1 < x < x_2 \\ 1, & x \geq x_2 \end{cases} \quad [7.39]$$

$$\text{and } \bar{A} = \frac{1}{(\delta + \beta)E(I_t + I_b)}$$

The particular solution of Eqn.7.29 represented by Eqn. 7.33 by applying the second integration of Ramp function in Eqn.7.38 is

$$E(I_t + I_b)w_p^I = \left(\frac{\beta}{\delta + \beta}\right)P^T[R_2(x - x_i)] - \frac{P^T L}{6}x^2 + \frac{P^T L^2}{6}x - \frac{P^T L^3}{162}$$

$$\begin{cases} -\frac{(x-x_1)^3}{6}, & x \leq x_1 \\ 0, & x_1 < x < x_2 \\ \frac{(x-x_2)^3}{6}, & x \geq x_2 \end{cases} \quad [7.40]$$

To obtain the solution for deflection and shear stress, constants C_1 to C_6 shall be found. Constants C_1 to C_4 can be worked out by direct integration method. Based on Figure 7.5, the whole beam can be divided into three parts. Relationship between bending moment and deflection for a beam ignoring shear deformation is based on Euler-Bernoulli beam theory.

$$M = -EI \frac{\partial^2 w}{\partial x^2}$$

where, w is the vertical deflection of the beam.

To find out the relationship between M and w , direct integration method is used. The integration process is shown below.

$$\text{when } 0 \leq x \leq \frac{L}{3}, \quad M = -EI \frac{\partial^2 w}{\partial x^2} = P^T x$$

$$\text{therefore,} \quad w = -\frac{1}{EI} \left(\frac{P^T}{6} x^3 + Ax + B \right) \quad [7.41]$$

$$\text{when } \frac{L}{3} \leq x \leq \frac{2L}{3}, \quad M = -EI \frac{\partial^2 w}{\partial x^2} = \frac{P^T L}{3}$$

$$w = -\frac{1}{EI} \left(\frac{P^T L}{6} x^2 + A_1 x + B_1 \right) \quad [7.42]$$

$$\text{when } \frac{2L}{3} \leq x \leq L, \quad M = -EI \frac{\partial^2 w}{\partial x^2} = -P^T x + P^T L$$

$$w = -\frac{1}{EI} \left(-\frac{P^T}{6} x^3 + \frac{P^T L}{2} x^2 + A_2 x + B_2 \right) \quad [7.43]$$

The constants A , A_1 , A_2 , B , B_1 and B_2 can be worked out by using boundary conditions and compatibility conditions of the four-point bending.

(i) boundary conditions

$$x = 0, w = 0; \quad x = L, w = 0;$$

(ii) Compatibility conditions

$$x = \frac{L}{3}, \quad \theta_L = \theta_R = \frac{\partial w_L}{\partial x} = \frac{\partial w_R}{\partial x};$$

$$x = \frac{2L}{3}, \quad \theta_L = \theta_R = \frac{\partial w_L}{\partial x} = \frac{\partial w_R}{\partial x};$$

$$x = \frac{L}{3}, \quad w_L = w_R;$$

$$x = \frac{2L}{3}, \quad w_L = w_R;$$

Applying boundary and compatibility conditions into Eqn.7.41 to Eqn.7.43, six equations can be produced. It is, therefore, possible to determine the six constants can be solved.

$$A = -\frac{P^T L^2}{9}; \quad A_1 = -\frac{P^T L^2}{6}; \quad A_2 = -\frac{7P^T L^2}{18};$$

$$B = 0; \quad B_1 = \frac{P^T L^3}{162}; \quad B_2 = \frac{P^T L^3}{18};$$

Eqn.7.41 to Eqn.7.43 can, therefore, be re-written as

$$\text{when } 0 \leq x \leq \frac{L}{3}, \quad w = -\frac{1}{EI} \left(\frac{P^T}{6} x^3 - \frac{P^T L^2}{9} x \right) \quad [7.44]$$

$$\text{when } \frac{L}{3} \leq x \leq \frac{2L}{3}, \quad w = -\frac{1}{EI} \left(\frac{P^T L}{6} x^2 - \frac{P^T L^2}{6} x + \frac{P^T L^3}{162} \right) \quad [7.45]$$

$$\text{when } \frac{2L}{3} \leq x \leq L, \quad w = -\frac{1}{EI} \left(-\frac{P^T}{6} x^3 + \frac{P^T L}{2} x^2 - \frac{7P^T L^2}{18} x + \frac{P^T L^3}{18} \right) \quad [7.46]$$

With the loading versus deflection relationships listed in Eqn.7.44 to Eqn. 7.46 for classic beams ignoring shear deformation, constants C_1 to C_4 can be derived as below.

$$\text{when } 0 \leq x \leq \frac{L}{3}, \quad C_1 = C_3 = 0, \quad C_2 = -\frac{P^T L^2}{9E(I_t + I_b)}, \quad C_4 = \frac{P^T}{6E(I_t + I_b)};$$

$$\text{when } \frac{L}{3} \leq x \leq \frac{2L}{3}, \quad C_1 = \frac{P^T L^3}{162E(I_t + I_b)}, \quad C_2 = -\frac{P^T L^2}{6E(I_t + I_b)}, \quad C_3 = \frac{P^T L}{6E(I_t + I_b)}, \quad C_4 = 0;$$

$$\text{when } \frac{2L}{3} \leq x \leq L, \quad C_1 = \frac{P^T L^3}{18E(I_t + I_b)}, \quad C_2 = -\frac{7P^T L^2}{18E(I_t + I_b)},$$

$$C_3 = \frac{P^T L}{2E(I_t + I_b)}, \quad C_4 = -\frac{P^T}{6E(I_t + I_b)};$$

As constants C_5 and C_6 in Eqn. 7.29 and Eqn. 7.30 are the coefficients of the portions representing shear deformation, Eqn. 7.30 is used to find the value of them based on the loading conditions. With particular solution τ_p , Eqn. 7.30 can be re-written as

$$\tau = -\frac{6C_4}{\beta} + \frac{s^3}{\delta} C_5 e^{sx} - \frac{s^3}{\delta} C_6 e^{-sx} - \bar{A}P^T [H(x - x_i)] \begin{cases} -1, & x \leq x_1 \\ 0, & x_1 < x < x_2 \\ 1, & x \geq x_2 \end{cases} \quad [7.47]$$

The loading boundary conditions of $x = 0$, $\frac{\partial \tau}{\partial x} = 0$ and $x = L$, $\frac{\partial \tau}{\partial x} = 0$ are applied to Eqn. 7.47. The following two equations are then derived.

$$\begin{aligned} \text{(i)} \quad x = 0, \quad \frac{\partial \tau}{\partial x} &= \frac{s^4}{\delta} C_5 e^0 + \frac{s^4}{\delta} C_6 e^0 = 0 \\ \text{(ii)} \quad x = L, \quad \frac{\partial \tau}{\partial x} &= \frac{s^4}{\delta} C_5 e^{sL} + \frac{s^4}{\delta} C_6 e^{-sL} = 0 \end{aligned}$$

Therefore, $C_5 = C_6 = 0$

With all constants and particular solutions determined, the deflection and shear stress can be obtained by the following equations.

Deflection

$$\text{when } 0 \leq x \leq \frac{L}{3}, \quad w^I = \frac{1}{E(I_t + I_b)} \left(\frac{P^T L^2}{9} x - \frac{P^T}{6} x^3 \right) + w_p^I \quad [7.48]$$

$$\text{when } \frac{L}{3} \leq x \leq \frac{2L}{3}, \quad w^I = \frac{1}{E(I_t + I_b)} \left(-\frac{P^T L^3}{162} + \frac{P^T L^2}{6} x - \frac{P^T L}{6} x^2 \right) + w_p^I \quad [7.49]$$

$$\text{when } \frac{2L}{3} \leq x \leq L, \quad w^I = \frac{1}{E(I_t + I_b)} \left(-\frac{P^T L^3}{18} + \frac{7P^T L^2}{18} x - \frac{P^T L}{2} x^2 + \frac{P^T}{6} x^3 \right) + w_p^I \quad [7.50]$$

where

$$w_p^I = \begin{cases} \bar{A}\beta P^T \left[-\frac{(x-\frac{L}{3})^3}{6} - \frac{L}{6} x^2 + \frac{L^2}{6} x - \frac{L^3}{162} \right]; & x \leq \frac{L}{3} \\ \bar{A}\beta P^T \left[-\frac{L}{6} x^2 + \frac{L^2}{6} x - \frac{L^3}{162} \right]; & \frac{L}{3} \leq x \leq \frac{2L}{3} \\ \bar{A}\beta P^T \left[\frac{(x-\frac{2L}{3})^3}{6} - \frac{L}{6} x^2 + \frac{L^2}{6} x - \frac{L^3}{162} \right]; & \frac{2L}{3} \leq x \leq L \end{cases}$$

Shear stress

$$\text{when } 0 \leq x \leq \frac{L}{3}, \tau = -\frac{P^T}{\beta E(I_t + I_b)} - \tau_p \quad [7.51]$$

$$\text{when } \frac{2L}{3} \leq x \leq L, \tau = -\tau_p \quad [7.52]$$

$$\text{when } \frac{2L}{3} \leq x \leq L, \tau = \frac{P^T}{\beta E(I_t + I_b)} - \tau_p \quad [7.53]$$

where, τ_p is shown in Eqn. 7.39.

Internal forces

Based on the formulas derived above, slope, shear force and bending moment are given below.

Slope θ^I

Slope θ^I can be derived from Figure 7.4 and Eqn. 7.21,

$$\theta^I = \varphi = -\frac{\partial w^I}{\partial x} + \gamma = -\frac{\partial w^I}{\partial x} + \frac{\tau}{G_c}$$

$$\text{when } 0 \leq x \leq \frac{L}{3}, \theta^I = \frac{1}{E(I_t + I_b)} \left(\frac{P^T L^2}{9} - \frac{P^T}{2} x^2 \right) - \frac{\partial w_p^I}{\partial x} - \frac{1}{G_c} \left(\frac{P^T}{\beta E(I_t + I_b)} + \tau_p \right) \quad [7.54]$$

where $\frac{\partial w_p^I}{\partial x} = \bar{A}\beta P^T \left[-\frac{(x - \frac{L}{3})^2}{2} - \frac{L}{3}x + \frac{L^2}{6} \right]$, and τ_p is shown in Eqn. 7.39.

$$\text{when } \frac{L}{3} \leq x \leq \frac{2L}{3}, \theta^I = \frac{1}{E(I_t + I_b)} \left(\frac{P^T L^2}{6} - \frac{P^T L}{3} x \right) - \frac{\partial w_p^I}{\partial x} - \frac{\tau_p}{G_c} \quad [7.55]$$

where, $\frac{\partial w_p^I}{\partial x} = \bar{A}\beta P^T \left[-\frac{L}{3}x + \frac{L^2}{6} \right]$ and τ_p is shown in Eqn. 7.39.

$$\text{when } \frac{2L}{3} \leq x \leq L, \theta^I = \frac{1}{E(I_t + I_b)} \left(\frac{7P^T L^2}{18} - P^T L x + \frac{P^T}{2} x^2 \right) - \frac{\partial w_p^I}{\partial x} + \frac{1}{G_c} \left(\frac{P^T}{\beta E(I_t + I_b)} - \tau_p \right) \quad [7.56]$$

where, $\frac{\partial w_p^I}{\partial x} = \bar{A}\beta P^T \left[\frac{(x - \frac{2L}{3})^2}{2} - \frac{L}{3}x + \frac{L^2}{6} \right]$ and τ_p is shown in Eqn. 7.39.

Bending moment

Bending moment at top and bottom skins can be obtained from Eqn. 7.15 and total bending moment can be calculated by Eqn. 7.18 and Eqn. 7.19. Eqn. 7.19 can be re-

written as the following and substituted into Eqn. 7.18 to obtain total bending moment of the section.

$$N_{xx}^b = EA_b \left\{ -\frac{\partial \left[-\frac{\partial w^I}{\partial x} + \frac{\tau}{G_c} \right]}{\partial x} c_b - \frac{d_b}{2} \frac{\partial^2 w^I}{\partial x^2} \right\} = EA_b \left\{ -\left[-\frac{\partial^2 w^I}{\partial x^2} + \frac{1}{G_c} \frac{\partial \tau}{\partial x} \right] c_b - \frac{d_b}{2} \frac{\partial^2 w^I}{\partial x^2} \right\}$$

where

$$\frac{\partial \tau}{\partial x} = -\bar{A}P^T \left[\delta_D \left(x - \frac{L}{3} \right) + \delta_D \left(x - \frac{2L}{3} \right) \right] \begin{cases} 1, & x = \frac{L}{3} \text{ or } x = \frac{2L}{3} \\ 0, & x \neq \frac{L}{3} \text{ or } x \neq \frac{2L}{3} \end{cases}$$

$$\text{when } 0 \leq x \leq \frac{L}{3}, \frac{\partial^2 w^I}{\partial x^2} = \frac{1}{E(I_t + I_b)} (P^T x) + \frac{\partial^2 w_p^I}{\partial x^2}$$

$$\text{where, } \frac{\partial^2 w_p^I}{\partial x^2} = \bar{A}\beta P^T \left[-\left(x - \frac{L}{3} \right) - \frac{L}{3} \right]$$

$$\text{when } \frac{L}{3} \leq x \leq \frac{2L}{3}, \frac{\partial^2 w^I}{\partial x^2} = \frac{1}{E(I_t + I_b)} \left(\frac{P^T L}{3} \right) + \frac{\partial^2 w_p^I}{\partial x^2}$$

$$\text{where, } \frac{\partial w_p^I}{\partial x} = \bar{A}\beta P^T \left(-\frac{L}{3} \right)$$

$$\text{when } \frac{2L}{3} \leq x \leq L, \theta^I = \frac{1}{E(I_t + I_b)} (P^T L - P^T x) + \frac{\partial^2 w_p^I}{\partial x^2}$$

$$\text{where, } \frac{\partial w_p^I}{\partial x} = \bar{A}\beta P^T \left[\left(x - \frac{2L}{3} \right) - \frac{L}{3} \right]$$

Shear force

Shear forces at top and bottom skins can be calculated by Eqn. 7.7 and Eqn. 7.8 and total shear force can be calculated by Eqn. 7.17.

$$Q_{xx}^t = \frac{\partial M_{xx}^t}{\partial x} + \frac{\tau b d_t}{2} = -EI_t \frac{\partial^3 w^I}{\partial x^3} + \frac{\tau b d_t}{2}$$

$$Q_{xx}^b = \frac{\partial M_{xx}^b}{\partial x} + \frac{\tau b d_b}{2} = -EI_b \frac{\partial^3 w^I}{\partial x^3} + \frac{\tau b d_b}{2}$$

where $\frac{\partial^3 w^I}{\partial x^3}$ is calculated below

$$\text{when } 0 \leq x \leq \frac{L}{3}, \frac{\partial^3 w^I}{\partial x^3} = \frac{-P^T}{E(I_t + I_b)} + \frac{\partial^3 w_p^I}{\partial x^3}$$

$$\text{where, } \frac{\partial^3 w_p^I}{\partial x^3} = -\bar{A}\beta P^T$$

$$\text{when } \frac{L}{3} \leq x \leq \frac{2L}{3}, \frac{\partial^3 w^I}{\partial x^3} = \frac{\partial^3 w_p^I}{\partial x^3}$$

$$\text{where, } \frac{\partial^3 w_p^I}{\partial x^3} = 0$$

$$\text{when } \frac{2L}{3} \leq x \leq L, \frac{\partial^3 w^I}{\partial x^3} = \frac{p^T}{E(I_t + I_b)} + \frac{\partial^3 w_p^I}{\partial x^3}$$

$$\text{where, } \frac{\partial^3 w_p^I}{\partial x^3} = \bar{A}\beta P^T$$

Peeling stresses

Peeling stresses are the vertical contact stresses between interface of the core and the top and bottom skins to transfer the loads between the skins. Peeling stresses are related to the shear stress in the core which was defined in Eqn. 7.9. Based on the assumptions stated in Section 7.2.2, the anti-plane is rigid in vertical direction but slender in horizontal direction. The height of core is unchanged under the loading. The deflection of top and bottom skins and centre of rotation are kept identical. As the section is studied in elastic range, the normal stress distribution is assumed to be linear and can be plotted as below.

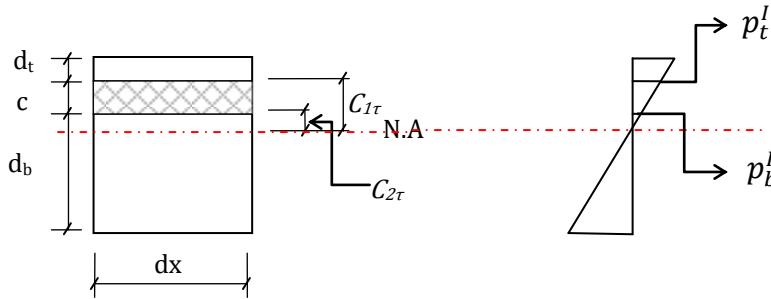


Figure 7.8 Peeling stress in the core

Combining Eqn. 7.7 and Eqn. 7.9 with Eqn. 7.15, the relationship formula between top and bottom peeling stresses can be formed as following.

$$\frac{q_t^I + b \frac{d_t \partial \tau}{2 \partial x} - p_t^I b}{E I_t} = \frac{q_b^I + b \frac{d_b \partial \tau}{2 \partial x} - p_b^I b}{E I_b} \quad [7.57]$$

Based on Figure 7.8, peeling stress can be expressed as

$$p_t^I = -\frac{\partial \tau}{\partial x} C_{1\tau}; \text{ and } p_b^I = -\frac{\partial \tau}{\partial x} C_{2\tau}; \quad [7.58]$$

$$c = C_{1\tau} - C_{2\tau} \quad [7.59]$$

Combining Eqns. 7.57 to Eqn. 7.59 and, peeling stresses at top and bottom interface for a four-point bending beam without any distributed loads can be obtained as below.

$$p_i^I = -\frac{\partial \tau}{\partial x} \left[\frac{I_i}{I_b - I_t} \left(\frac{d_t}{2} - \frac{d_b}{2} + c \right) + \frac{d_i}{2} \right], \quad i = t, b \quad [7.60]$$

Therefore,

$$C_{1\tau} = \frac{I_t}{I_b - I_t} \left(\frac{d_t}{2} - \frac{d_b}{2} + c \right) + \frac{d_t}{2}; \quad \text{and} \quad C_{2\tau} = \frac{I_b}{I_b - I_t} \left(\frac{d_t}{2} - \frac{d_b}{2} + c \right) + \frac{d_b}{2}; \quad [7.61]$$

As a beam under four-point bending, compatibility conditions at the point loads can be derived as the follows,

$$Q_T^I(L) - Q_T^I(R) = P^T; \quad \tau_{(L)} = \tau_{(R)} \quad [7.62]$$

Substituting Eqn. 7.7 and Eqn.7.8 into Eqn. 7.17, shear forces can be represented by the derivative of bending moment. Therefore, total shear force is

$$Q_T^I = -EI_t \frac{\partial^3 w^I}{\partial x^3} - EI_b \frac{\partial^3 w^I}{\partial x^3} + \tau b \left(\frac{d_b}{2} + \frac{d_t}{2} + c \right) \quad [7.63]$$

Substituting Eqn. 7.63 into Eqn. 7.62, Eqn. 7.62 is re-written as

$$-EI_t \left(\frac{\partial^3 w_{(L)}^I}{\partial x^3} - \frac{\partial^3 w_{(R)}^I}{\partial x^3} \right) - EI_b \left(\frac{\partial^3 w_{(L)}^I}{\partial x^3} - \frac{\partial^3 w_{(R)}^I}{\partial x^3} \right) = P^T \quad [7.64]$$

Also, peeling forces at top and bottom interfaces are the shear force increments at top and bottom interfaces and are defined as

$$P_t^I = -EI_t \left(\frac{\partial^3 w_{(L)}^I}{\partial x^3} - \frac{\partial^3 w_{(R)}^I}{\partial x^3} \right); \quad P_b^I = -EI_b \left(\frac{\partial^3 w_{(L)}^I}{\partial x^3} - \frac{\partial^3 w_{(R)}^I}{\partial x^3} \right) \quad [7.65]$$

Therefore,

$$P_i^I = \frac{I_i}{I_t + I_b} P^T, \quad i = t, b \quad [7.66]$$

7.2.4 Sub-structure II

Sub-structure II is similar to sub-structure I with asymmetrical skins. However, the core in sub-structure II is treated as an elastic core which is flexible in vertical direction, very flexible in longitudinal direction and free of shear stresses. The height of the core changes under compression. The self-equilibrated load system of sub-structure II is illustrated in Figure 7.1. The elastic core of sub-structure II works similar to an elastic foundation to transfer loads between the skins. To understand the behaviour of beam

supported by elastic foundation, Hetenyi's book, "Beams on elastic foundation" (Hetényi 1946) was studied. In this book, Hentenyi explored the two types of elastic foundations. The first type is based on the pressure in the foundation which is proportional at every point to the deflection occurring at that point but is independent of pressures or deflections elsewhere. This is a widely used assumption. However, it implies discontinuity in the supporting medium which is made of independent springs. The second type of elastic foundation considers the continuity of supporting medium. The supporting medium is an elastic continuum. In his book, Hetenyi discussed the beam with infinite length and finite length under concentrated load, and different shapes of uniformly distributed loads for the first type of elastic foundation. He worked out basic governing equations to solve for deflection and internal forces as well as presenting worked examples. His methodology is applied here to solve the deflection and internal forces in sub-structure II.

Internal force equilibrium

From the loading diagram shown in Figure 7.1, the top and bottom skins are loaded with two loads equal in value but applied in opposite directions. The internal force diagram can be drawn by adopting a small portion of the structure with length dx . The geometry of the sandwich beam is identical to sub-structure I. The free body diagram for the whole structure is shown below in Figure 7.9.

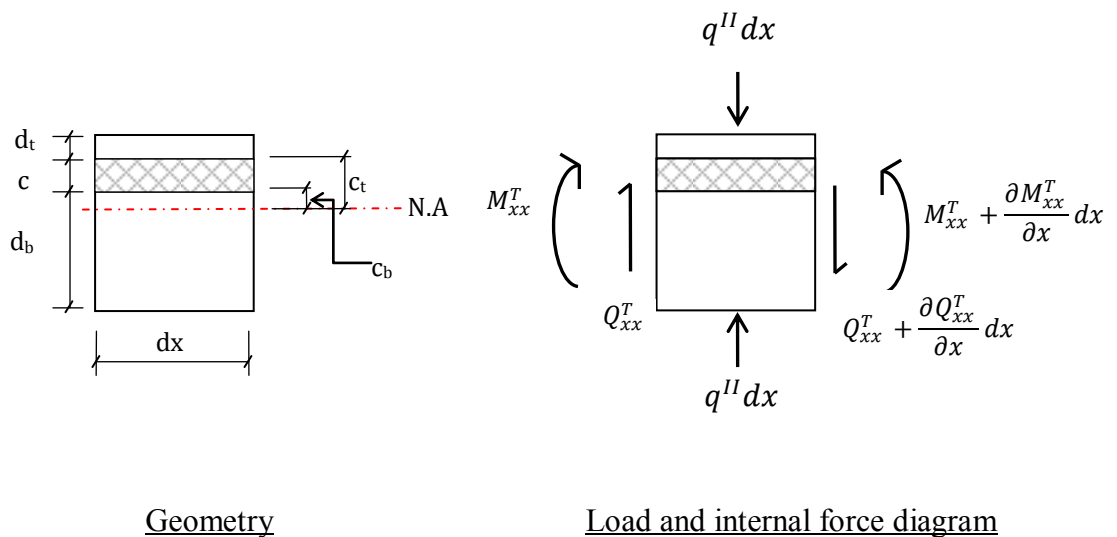


Figure 7.9 Free body diagram of overall sub-structure II

Overall internal force equilibrium can be derived based on the above diagram.

$$M_{xx}^t = M_{xx}^b; Q_{xx}^t = Q_{xx}^b; N_{xx}^t = N_{xx}^b = 0 \tag{7.67}$$

A free body diagram of internal forces at skins and core is also shown in Figure 7.10.

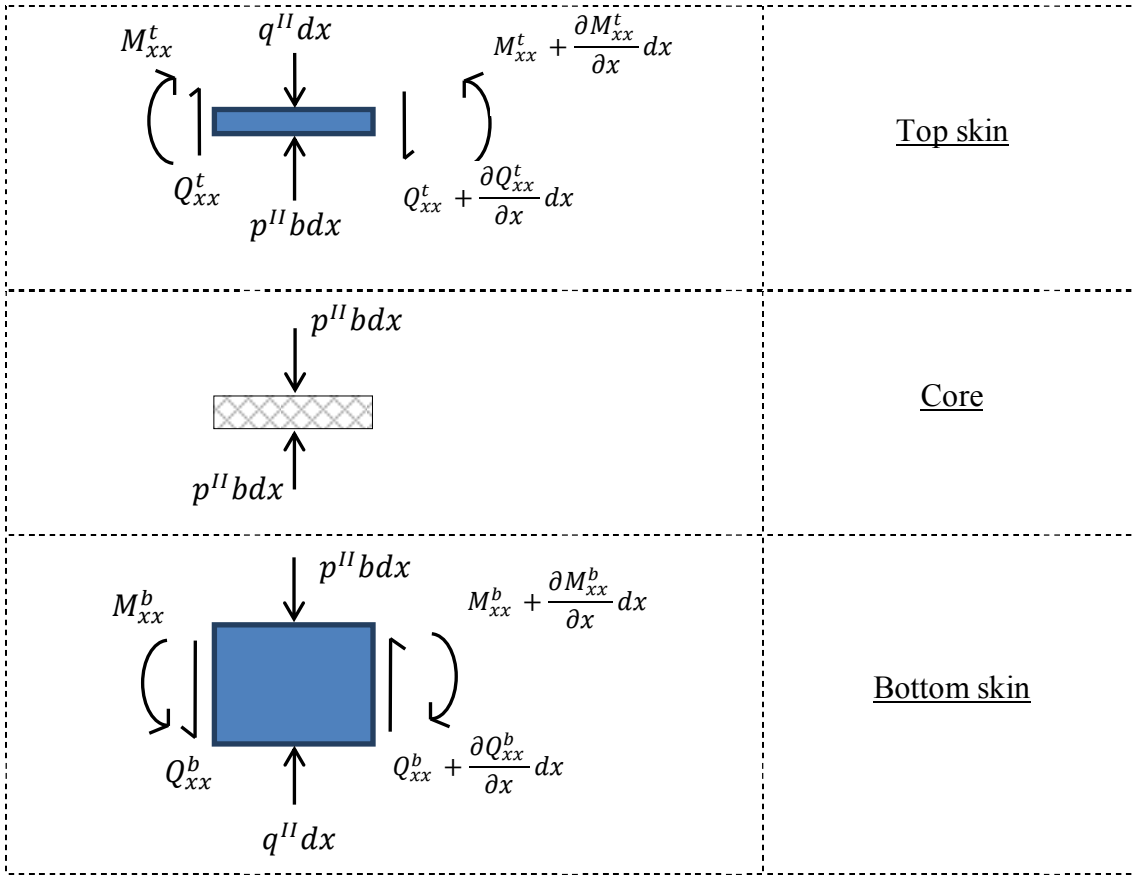


Figure 7.10 Loads and internal forces on skins and core of sub-structure II

From the internal force diagram and loading condition shown above in Figure 7.10, several equations can be derived as follows,

Upper skin

$$N_{xx}^t = 0 ; \frac{\partial Q_{xx}^t}{\partial x} + q^{II} - p^{II} b = 0 ; \frac{\partial M_{xx}^t}{\partial x} - Q_{xx}^t = 0 \quad [7.68]$$

Lower skin

$$N_{xx}^b = 0 ; \frac{\partial Q_{xx}^b}{\partial x} + q^{II} - p^{II} b = 0 ; \frac{\partial M_{xx}^b}{\partial x} - Q_{xx}^b = 0 \quad [7.69]$$

Core

$$Q_{xx}^c = 0 ; \quad \sigma_v^c = p^{II} \quad [7.70]$$

where,

σ_v^c denotes normal compressive stress in vertical direction in the core

p^{II} denotes vertical peeling stress at the interface between core and skins

The constitutive relations of the top and bottom skins are the same as those defined in sub-structure I in Eqn. 7.15. As the core is an assumed elastic core which is able to change in height under compression, it shall comply with Hooke's Law.

$$\sigma_v^c = E_c \varepsilon_v = E_c \frac{\partial w_c^{II}}{\partial x} \quad [7.71]$$

where,

E_c denotes Young's modulus of core material

w_c^{II} denotes the displacement of core

Deformation diagram

As the core of sub-structure II is an elastic core, it is able to change its height, the displacement of top and bottom skin cannot be kept identical to sub-structure I. The relationship between them relies on the height change of the core. To demonstrate the kinematic relation, the deformation diagram is drawn below in Figure 7.11.

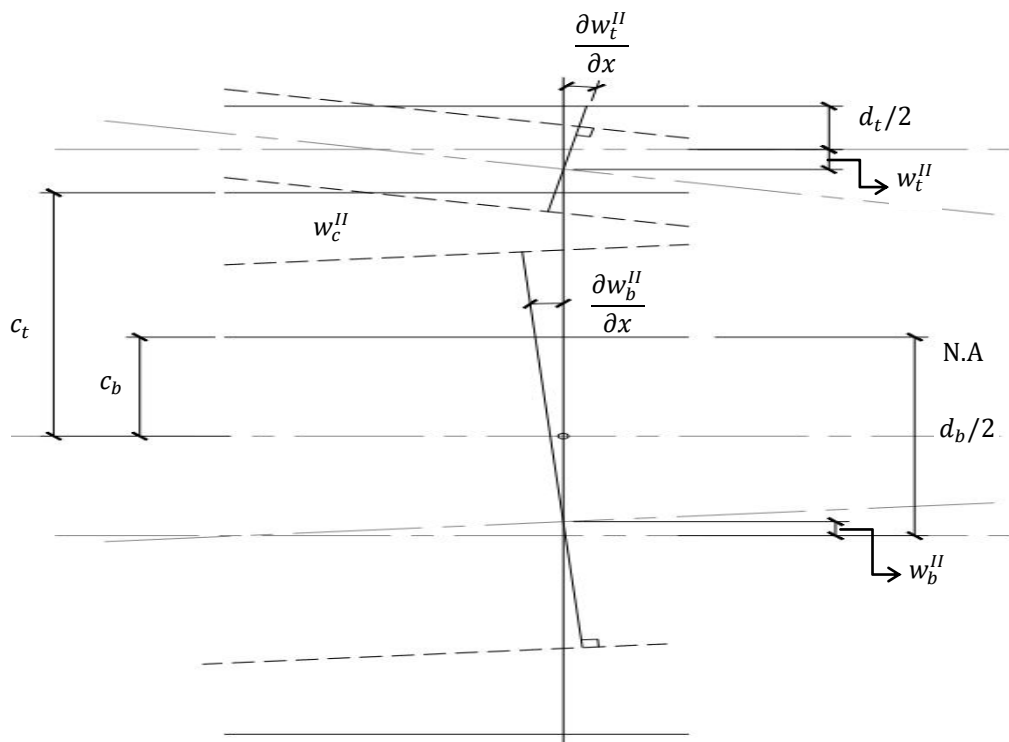


Figure 7.11 Deformation diagram of sub-structure II

To find out the relationship between the skins and the core, the elastic core can be treated as an elastic foundation (Hetenyi, (Hetényi 1946)). The top and bottom skins are assumed supported along their length by an elastic foundation which can deform

vertically. The interaction between them is opposite to the applied forces. As the top and bottom skins deflect, horizontal forces such as friction might be generated. In this study, the influence of horizontal friction is not considered to minimize complexity. However, it is worth to investigate the influence of friction in a future study.

The change of the core height determines the total displacement at top and bottom skins. As the vertical displacement of the core generated by the normal stress was ignored in sub-structure I, it shall be included in the displacement calculation of sub-structure II. Hence, the displacement of the core has two components: axial deformation due to axial compression p^{II} and the deformation caused by the vertical normal stresses from sub-structure I. It can therefore be expressed as,

$$w_t^{II} + w_b^{II} = w_c^{II} \quad [7.72]$$

According to Hooke's Law $\implies p^{II} b dx = E_c b dx w_c^{II} / c$

$$\implies w_c^{II} = \frac{p^{II} c}{E_c} \quad [7.73]$$

To determine the deformation of the core due to the normal stresses in sub-structure I, Eqn. 7.9 is evolved as below. The change of core height due to sub-structure I can be expressed as

$$\delta w = \frac{p_b^I c + \frac{\partial \tau}{\partial x} \left(\frac{c}{2}\right)}{E_c} \quad [7.74]$$

Substituting Eqn. 7.73 and Eqn.7.74 into Eqn. 7.72, the displacement in the skins are

$$w_t^{II} + w_b^{II} = \frac{p^{II} c}{E_c} - \frac{p_b^I c + \frac{\partial \tau}{\partial x} \left(\frac{c}{2}\right)}{E_c} \quad [7.75]$$

where,

w_t^{II} and w_b^{II} denote displacement in the top and bottom skin, respectively

As the top and bottom skins are bending under the same load, therefore, the bending moment applied to the top and bottom skin is identical. Therefore,

$$M_{xx}^t = M_{xx}^b \quad \implies \quad EI_t \frac{\partial^2 w_t^{II}}{\partial x^2} = EI_b \frac{\partial^2 w_b^{II}}{\partial x^2}$$

Let us integrate the above equation twice and apply the identical boundary conditions to the top and bottom skins. The integration constants cancel each other at either side of

the equation. The displacement relationship between top and bottom skins can be obtained as follows,

$$w_t^{II} = \frac{I_b}{I_t} w_b^{II} \quad [7.76]$$

Combining Eqn.7.75 and Eqn. 7.76 together, we get

$$p^{II} = w_b^{II} E_c \frac{(I_t + I_b)}{I_t c} + p_b^I + \frac{\partial \tau}{\partial x} \left(\frac{c}{2} \right) \quad [7.77]$$

Combining Eqn. 7.15 and Eqn. 7.69, we get

$$p^{II} = \frac{q^{II} - EI_b \frac{\partial^4 w_b^{II}}{\partial x^4}}{b} \quad [7.78]$$

The governing equation can be derived by combining Eqn. 7.77 and Eqn. 7.78 together.

$$\frac{q^{II} - EI_b \frac{\partial^4 w_b^{II}}{\partial x^4}}{b} = w_b^{II} E_c \frac{(I_t + I_b)}{I_t c} + p_b^I + \frac{\partial \tau}{\partial x} \frac{c}{2}$$



$$EI_b \frac{\partial^4 w_b^{II}}{\partial x^4} + w_b^{II} E_c b \frac{(I_t + I_b)}{I_t c} = q^{II} - b \left(p_b^I + \frac{\partial \tau}{\partial x} \frac{c}{2} \right)$$

Replacing p_b^I with Eqn. 7.58, the governing equation above can be re-written as

$$EI_b \frac{\partial^4 w_b^{II}}{\partial x^4} + w_b^{II} E_c b \frac{(I_t + I_b)}{I_t c} = q^{II} - \frac{\partial \tau}{\partial x} b \left(\frac{c}{2} - C_{2\tau} \right) \quad [7.79]$$

For a beam under four-point bending, the loading q^{II} applied on sub-structure II shall be solved as the following. The two concentrated loads are defined by Dirac Delta functions same as the ones in sub-structure I by Eqn. 7.34. When the concentrated loads are applied on the bottom skin, the load applied on sub-structure II (q^{II}) equals the load applied on the top skin ($p_t^I b$) at sub-structure I. Based on Eqn.7.66, peeling stress can be found as

$$p_t^I = \frac{I_i}{I_t + I_b} P^T = p_t^I b$$

Written for the four-point bending beam, concentrated loads applied on the sub-structure II at one-third and two-thirds of the span are

$$q_{(x)}^{II} = P^T \left(\frac{I_t}{I_t + I_b} \right) [\delta_D(x - x_1) + \delta_D(x - x_2)] \begin{cases} 1, & x = \frac{L}{3} \text{ or } x = \frac{2L}{3} \\ 0, & x \neq \frac{L}{3} \text{ or } x \neq \frac{2L}{3} \end{cases} \quad [7.80]$$

The governing equation, Eqn. 7.79, is re-written below with loading solved in Eqn. 7.80.

$$EI_b \frac{\partial^4 w_b^{II}}{\partial x^4} + k_c w_b^{II} = P^T \left(\frac{I_t}{I_t + I_b} \right) \left[\delta_D \left(x - \frac{L}{3} \right) + \delta_D \left(x - \frac{2L}{3} \right) \right] - \frac{\partial \tau}{\partial x} b \left(\frac{c}{2} - C_{2\tau} \right)$$

$$\begin{cases} 1, & x = \frac{L}{3} \text{ or } x = \frac{2L}{3} \\ 0, & x \neq \frac{L}{3} \text{ or } x \neq \frac{2L}{3} \end{cases} \quad [7.81]$$

where,

$$k_c = E_c b \frac{(I_t + I_b)}{I_t c} \quad \text{represents the spring stiffness of the core when acting as an elastic foundation}$$

The general solution of Eqn. 7.81 can be obtained from (Hetényi 1946) for a beam supported on elastic foundation under concentrated load as Eqn. 7.81 is similar to Eqn. 1 in (Hetényi 1946). The general solution is

$$w_b^{II} = e^{\lambda x} (m_1 \cos \lambda x + m_2 \sin \lambda x) + e^{-\lambda x} (m_3 \cos \lambda x + m_4 \sin \lambda x) \quad [7.82]$$

where constants m_1 to m_4 have been solved in (Hetényi 1946) and listed below.

$$m_1 = \frac{w^I}{2} + \frac{\theta^I}{4\lambda} + \frac{Q_T^I}{8\lambda^3 E (I_t + I_b)}$$

$$m_2 = \frac{\theta^I}{4\lambda} - \frac{M_T^I}{4\lambda^2 E (I_t + I_b)} - \frac{Q_T^I}{8\lambda^3 E (I_t + I_b)}$$

$$m_3 = \frac{w^I}{2} - \frac{\theta^I}{4\lambda} - \frac{Q_T^I}{8\lambda^3 E (I_t + I_b)}$$

$$m_4 = \frac{\theta^I}{4\lambda} + \frac{M_T^I}{4\lambda^2 E (I_t + I_b)} - \frac{Q_T^I}{8\lambda^3 E (I_t + I_b)}$$

where,

$$\lambda = \sqrt[4]{\frac{E_c b}{4E I_t c}}$$

w^I, θ^I, Q_T^I and M_T^I are internal forces from sub-structure I

To find particular solution, Eqn. 7.81 is re-written as

$$EI_b \frac{\partial^4 w_b^{II}}{\partial x^4} = -k_c w_b^{II} + P^T \left(\frac{I_t}{I_t + I_b} \right) \left[\delta_D \left(x - \frac{L}{3} \right) + \delta_D \left(x - \frac{2L}{3} \right) \right] - \frac{\partial \tau}{\partial x} b \left(\frac{c}{2} - C_{2\tau} \right)$$

$$\begin{cases} 1, & x = \frac{L}{3} \text{ or } x = \frac{2L}{3} \\ 0, & x \neq \frac{L}{3} \text{ or } x \neq \frac{2L}{3} \end{cases} \quad [7.83]$$

(i) One particular solution due to w_b^{II} is

$$w_{bp1}^{II} = -\frac{k_c}{EI_b} \quad [7.84]$$

(ii) One particular solution due to the sum of P^T and $\frac{\partial \tau}{\partial x}$ can be solved as below,

$$\begin{aligned} EI_b \frac{\partial^4 w_b^{II}}{\partial x^4} &= P^T \left(\frac{I_t}{I_t + I_b} \right) [\delta_D \left(x - \frac{L}{3} \right) + \delta_D \left(x - \frac{2L}{3} \right)] - b \left(\frac{c}{2} - C_{2\tau} \right) \bar{A} P^T [\delta_D \left(x - \frac{L}{3} \right) + \\ &\delta_D \left(x - \frac{2L}{3} \right)] \begin{cases} 1, & x = \frac{L}{3} \text{ or } x = \frac{2L}{3} \\ 0, & x \neq \frac{L}{3} \text{ or } x \neq \frac{2L}{3} \end{cases} \\ &= [P^T \left(\frac{I_t}{I_t + I_b} \right) - b \left(\frac{c}{2} - C_{2\tau} \right) \bar{A} P^T] [\delta_D \left(x - \frac{L}{3} \right) + \delta_D \left(x - \frac{2L}{3} \right)] \begin{cases} 1, & x = \frac{L}{3} \text{ or } x = \frac{2L}{3} \\ 0, & x \neq \frac{L}{3} \text{ or } x \neq \frac{2L}{3} \end{cases} \\ &= \bar{B} P^T [\delta_D \left(x - \frac{L}{3} \right) + \delta_D \left(x - \frac{2L}{3} \right)] \begin{cases} 1, & x = \frac{L}{3} \text{ or } x = \frac{2L}{3} \\ 0, & x \neq \frac{L}{3} \text{ or } x \neq \frac{2L}{3} \end{cases} \end{aligned} \quad [7.85]$$

where,

$$\bar{B} = \left(\frac{I_t}{I_t + I_b} \right) - \bar{A} b \left(\frac{c}{2} - C_{2\tau} \right)$$

To find out the solution of w_b^{II} , an integration process similar to Eqn.7.35 to Eqn.7.38 were carried out. The solution is,

$$w_{bp2}^{II} = \begin{cases} \frac{\bar{B} P^T}{EI_b} \left[-\frac{(x-\frac{L}{3})^3}{6} - \frac{L}{6} x^2 + \frac{L^2}{6} x - \frac{L^3}{162} \right]; & x \leq \frac{L}{3} \\ \frac{\bar{B} P^T}{EI_b} \left[-\frac{L}{6} x^2 + \frac{L^2}{6} x - \frac{L^3}{162} \right]; & \frac{L}{3} \leq x \leq \frac{2L}{3} \\ \frac{\bar{B} P^T}{EI_b} \left[\frac{(x-\frac{2L}{3})^3}{6} - \frac{L}{6} x^2 + \frac{L^2}{6} x - \frac{L^3}{162} \right]; & \frac{2L}{3} \leq x \leq L \end{cases} \quad [7.86]$$

Combining the two particular solutions together, the particular solution of Eqn.7.83 is

$$w_{bp}^{II} = \begin{cases} \frac{\bar{B}P^T}{EI_b} \left[-\frac{(x-\frac{L}{3})^3}{6} - \frac{L}{6}x^2 + \frac{L^2}{6}x - \frac{L^3}{162} \right] - \frac{k_c}{EI_b} e^x; & x \leq \frac{L}{3} \\ \frac{\bar{B}P^T}{EI_b} \left[-\frac{L}{6}x^2 + \frac{L^2}{6}x - \frac{L^3}{162} \right] - \frac{k_c}{EI_b} e^x; & \frac{L}{3} \leq x \leq \frac{2L}{3} \\ \frac{\bar{B}P^T}{EI_b} \left[\frac{(x-\frac{2L}{3})^3}{6} - \frac{L}{6}x^2 + \frac{L^2}{6}x - \frac{L^3}{162} \right] - \frac{k_c}{EI_b} e^x; & \frac{2L}{3} \leq x \leq L \end{cases} \quad [7.87]$$

The Eqn. 7.83 is solved with a general solution and a particular solution. Therefore, deflection and internal forces for sub-structure II can be derived as following,

Deflection

$$w_b^{II} = e^{\lambda x}(m_1 \cos \lambda x + m_2 \sin \lambda x) + e^{-\lambda x}(m_3 \cos \lambda x + m_4 \sin \lambda x) - w_{bp}^{II} \quad [7.88]$$

Bending moment

Top and bottom skins:

$$M_t^{II} = -EI_t \frac{\partial^2 w_b^{II}}{\partial x^2}; \quad M_b^{II} = -EI_b \frac{\partial^2 w_b^{II}}{\partial x^2} \quad [7.89]$$

where,

$$\frac{\partial^2 w_b^{II}}{\partial x^2} = -\lambda^2 [e^{\lambda x}(m_1 \cos \lambda x + m_2 \sin \lambda x) + e^{-\lambda x}(m_3 \cos \lambda x + m_4 \sin \lambda x)] + \frac{\partial^2 w_{bp}^{II}}{\partial x^2}$$

and,

$$\frac{\partial^2 w_{bp}^{II}}{\partial x^2} = \frac{\bar{B}P^T}{EI_b} \left[R(x - x_i) - \frac{L}{3} \right] - \frac{k_c}{EI_b} e^x \begin{cases} -(x - \frac{L}{3}), & x \leq \frac{L}{3} \\ 0, & \frac{L}{3} < x < \frac{2L}{3} \\ (x - \frac{2L}{3}), & \frac{2L}{3} \leq x \leq L \end{cases}$$

Total bending moment at section is,

$$M_T^{II} = M_t^{II} + M_b^{II} \quad [7.90]$$

Shear force

Top and bottom skin shears are,

$$Q_t^{II} = \frac{\partial M_t^{II}}{\partial x} = -EI_t \frac{\partial^3 w_b^{II}}{\partial x^3}; \quad Q_b^{II} = \frac{\partial M_b^{II}}{\partial x} = -EI_b \frac{\partial^3 w_b^{II}}{\partial x^3}; \quad [7.91]$$

where,

$$\frac{\partial^3 w_b^{II}}{\partial x^3} = \lambda^3 [e^{\lambda x}(m_1 \sin \lambda x - m_2 \cos \lambda x) - e^{-\lambda x}(m_3 \sin \lambda x - m_4 \cos \lambda x)] + \frac{\partial^3 w_{bp}^{II}}{\partial x^3}$$

and

$$\frac{\partial^3 w_{bp}^{II}}{\partial x^3} = \frac{\bar{B}P^T}{EI_b} \left[H(x - x_i) - \frac{L}{3} \right] - \frac{k_c}{EI_b} e^x \begin{cases} -1, & x \leq \frac{L}{3} \\ 0, & \frac{L}{3} < x < \frac{2L}{3} \\ 1, & \frac{2L}{3} \leq x \leq L \end{cases}$$

Peeling stresses

$$p_t^{II} = \frac{w_b^{II} k_c}{b}; \quad p_b^{II} = -\frac{w_b^{II} k_c}{b} \quad [7.92]$$

7.2.5 Overall structure behaviour

Overall structure behaviour is determined by both sub-structures. Internal forces, apart from axial forces, and deflection, are the sum of both sub-structures. As the axial force does not exist in sub-structure II, it is only generated by sub-structure I. The deflection and internal forces are listed below.

Deflection

- (i) Total deflection at top skin

$$w_{t,tot} = w^I + \frac{I_b}{I_t} w_b^{II}$$

- (ii) Total deflection at bottom skin

$$w_{b,tot} = w^I + w_b^{II}$$

Bending moments

- (i) Total bending moment at top skin

$$M_{t,tot} = M_{xx}^t + M_t^{II}$$

- (ii) Total bending moment at bottom skin

$$M_{b,tot} = M_{xx}^b + M_b^{II}$$

Shear forces

- (i) Total shear force at top skin

$$Q_{t,tot} = Q_{xx}^t + Q_t^{II}$$

- (ii) Total shear force at bottom skin

$$Q_{b,tot} = Q_{xx}^b + Q_b^{II}$$

Axial force – Eqn. 7.13 and Eqn. 7.14

Peeling stresses

- (i) Total peeling stress at top skin

$$p_{t,tot} = \frac{w_b^{II} k_c}{b} - \frac{\partial \tau}{\partial x} \left[\frac{I_t}{I_b - I_t} \left(\frac{d_t}{2} - \frac{d_b}{2} + c \right) + \frac{d_t}{2} \right]$$

- (ii) Total peeling stress at bottom skin

$$p_{b,tot} = -\frac{w_b^{II} k_c}{b} - \frac{\partial \tau}{\partial x} \left[\frac{I_b}{I_b - I_t} \left(\frac{d_t}{2} - \frac{d_b}{2} + c \right) + \frac{d_b}{2} \right]$$

7.3 Equivalent section

The above analytical formulations are based on a solid composite section. Unfortunately, the thermal break façade mullion section is a thin walled hollow section which comprises top and bottom aluminium extrusions and glass fibre reinforced polyamide inserts. To be able to calculate the forces and responses in a thermal break façade section by the analytical solutions, the typical thermal break section studied in this research has to be transformed into an equivalent solid composite section.

As the analytical solution is to determine the capacity of the section under four-point bending, the sectional bending and shear capacities and deflection along the span are sought after. The bending and shear capacities and deflection are related to bending stiffness and neutral axis location of the section. The cross-sectional area is not as critical as the bending stiffness. Therefore, the basic principle to transfer the hollow thermal break section into a solid section is to keep the bending stiffness relatively similar to the original one. To work out the equivalent section, trial and error method was introduced and applied. Based on the section geometry, the bottom skin has major contribution to the section bending stiffness due to its larger size whose area is almost four times bigger than the top skin. As both skins are made of identical material, the transformation relies on the second moment of inertia of the top and bottom skins. To start the trial and error process, the geometry of the original section is investigated. The geometry and properties of the typical thermal break section are shown below.

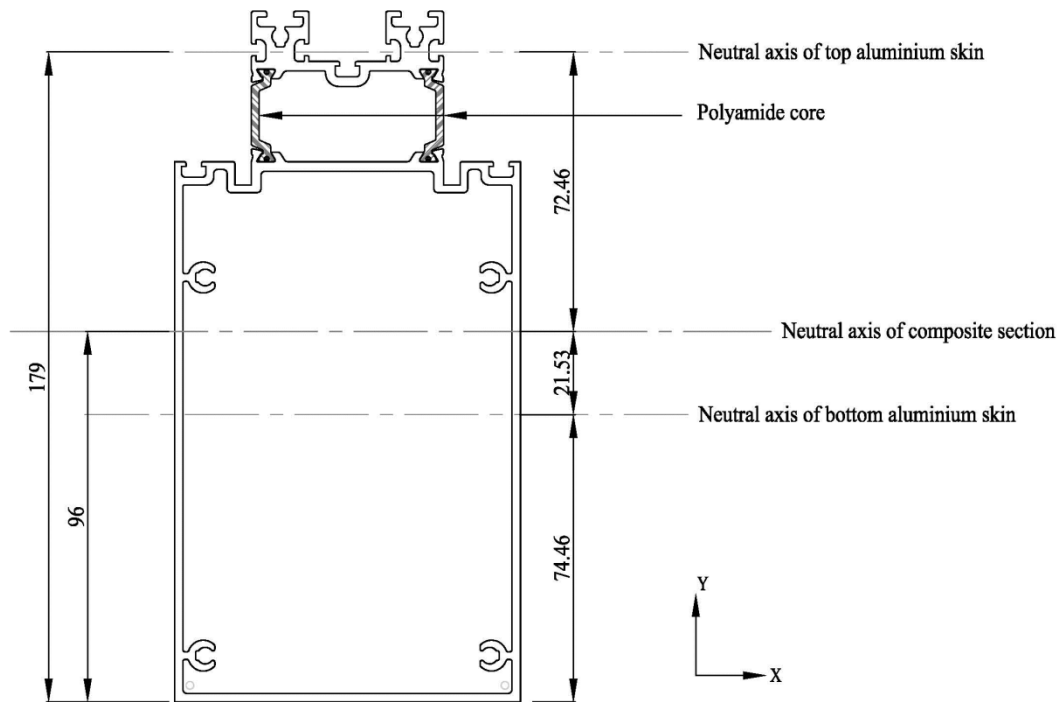


Figure 7.12 Geometry of the typical thermal break façade section

The section properties are

$$I_t = 1.92 \times 10^6 \text{ mm}^4, \quad I_b = 4.13 \times 10^6 \text{ mm}^4$$

$$A_t = 364.11 \text{ mm}^2, \quad A_b = 1225.67 \text{ mm}^2, \quad A_c = 119.7 \text{ mm}^2$$

where,

I_t and I_b represent the second moment of inertia of top and bottom skins with respect to the neutral axis of the whole section

A_t and A_b denotes the area of top and bottom skins, respectively

A_c denotes the total areas of polyamide inserts

Based on the geometry and section properties of the typical thermal break façade section, an equivalent solid composite section was derived by applying trial and error method to match the second moment of inertia of both top and bottom skins. The neutral axis location is also taken into consideration during calculation. As the bottom skin is much larger than the top section, its geometry provides a starting point for the trial and error process. After several trials and errors, the geometry of the equivalent section was determined. The equivalent section is shown in the figure below.

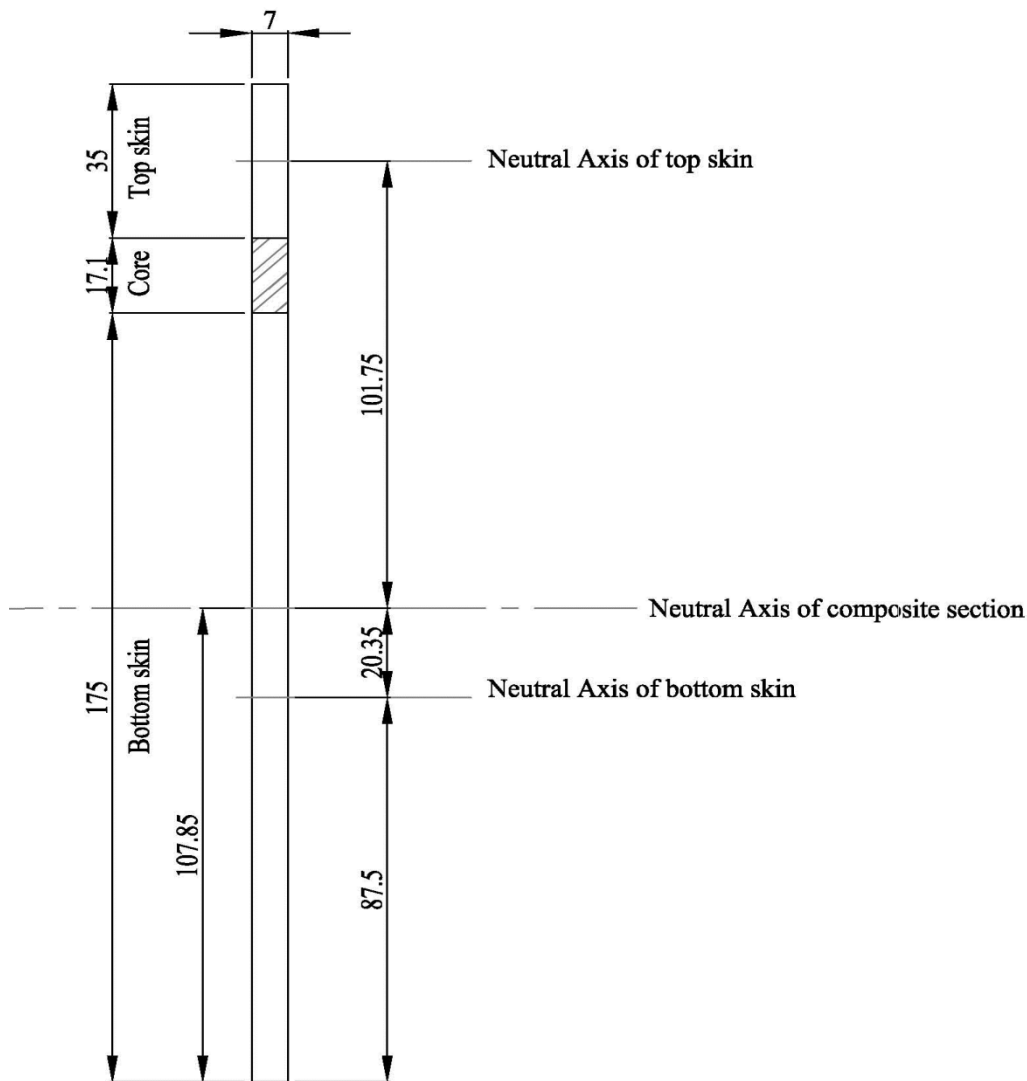


Figure 7.13 Geometry of equivalent solid section

The section properties of the equivalent section are

$$I_t = 2.56 \times 10^6 \text{ mm}^4, \quad I_b = 3.63 \times 10^6 \text{ mm}^4$$

$$A_t = 245 \text{ mm}^2, \quad A_b = 1225 \text{ mm}^2, \quad A_c = 119.7 \text{ mm}^2$$

Comparing with the original section, the areas of bottom skin and core are identical to the original one. However, the area of the top skin is smaller than the original one. Although the individual second moment of inertia of top and bottom skin differs from the original one, the sum of I_t and I_b almost equals to the original one. During the trial and error process, it is impossible to match every section property between the equivalent and the original one. As the overall section behaviour is based on the overall section properties, the conversion was, therefore, focused to match the total second

moment of inertia with least discrepancy of the neutral axis locations between them. For this conversion, the distance of the neutral axis location from the extreme fibre of bottom skin is increased by 12% with the section height increasing by 17%. Therefore, the neutral axis location is matching the original section. Hence, the equivalent solid section provides similar section properties comparing with the original one and, therefore, can be used in the calculations by applying the analytical solutions.

7.4 Summary and conclusions

The proposed frame work for analytical solution for four-point bending of a beam is based on the superposition approach with modifications to suit the thermal break façade section. Due to the difference between typical sandwich structure and the thermal break façade section, formulations were re-derived and advanced. Based on the sandwich theory, some basic assumptions were made to start deriving relevant formulations. The sandwich beam was divided into two sub-structures. The first sub-structure was assumed to be loaded in the same direction by either a uniformly distributed load or concentrated loads. The core is an anti-plane core which is stiff in the vertical direction but slender in the horizontal direction. The height of the core was kept unchanged under loading. The deflections of top and bottom skins were identical. The second sub-structure was loaded by self-equilibrating loads which are either uniformly distributed or concentrated loads. The core in the second sub-structure is an elastic core which changed its height under loading.

Internal force diagrams of both sub-structures were drawn to assist the analysis. Kinematic relationships of sub-structure I and II were also derived and plotted in graphs. Governing equations were derived based on these relationships. Boundary and loading conditions as well as continuous conditions based on a four-point bending beam were adopted to solve the differential equations for particular solutions and integration constants. The second sub-structure was assumed as a beam supported by elastic foundation. The core of the sub-structure II was assumed to act as an elastic foundation. Its vertical stiffness affected the load transfer between the top and bottom skins. Governing equations of the second sub-structure were solved by Hetenyi's methodology. The overall structural behaviour of the sandwich beam is a combination of first and second sub-structures. Deflection and internal forces, such as bending moment, shear

forces and peeling stresses, are the sum of those for the first and second sub-structure. As there is no axial force in the second sub-structure, axial forces are only related to the first sub-structure.

To be able to apply the formulations derived to calculate the deflection and internal forces of a thermal break façade section, the façade section had to be transformed into a solid sandwich section. Trial and error method was recommended to solve the problem. The typical thermal break façade section was used as an example to explain the principle of transformation.

The analytical solution proposed in this thesis needs to be verified by experimental and numerical work before design tables can be derived for industry applications. Unfortunately, these works require extra funding and time which is beyond the scope of this study. However, it is recommended that experimental and numerical investigation based on the analytical frame work provided in this chapter to be carried out to verify the analytical solution and apply them to the industry applications in future studies.

Chapter 8

Summary, Conclusions and Recommended Future Works

8. Summary, conclusions and recommended future works

8.1 Summary and conclusions

In summary, a typical thermal break façade mullion section was studied in this research. Experimental and numerical investigation was carried out to gain thorough understanding of the section behaving under shear, tension and bending loads. A proposed frame work was carried out as well to work out an analytical solution for beam bending of a typical thermal break section.

Rigorous laboratory tests were carried out to determine shear, transverse tensile and bending capacity of the typical section at the beginning of the research. These experiments were performed at various temperatures and under various loading rates at room temperature. Beam tests of four-point bending were carried out at room temperature under quasi-static loading. Experimental setup and process were demonstrated and the results discussed.

All section capacity tests show similar failure modes under either quasi-static loadings at various temperatures or high strain rate loadings at room temperature. For shear capacity tests, shear failure of the polyamide, due to it slipping away from connection, was observed for all shear tests regardless of testing environment and loading rates. In terms of the transverse tensile tests, polyamide was observed to either pull away from the connection or break. Test results show both shear and tensile section capacities, as well as elasticity constant, are temperature sensitive. However, the section shear and tensile tests under various loading rates showed mixed trend of strain rate sensitivity. The section shear and tensile capacity demonstrated no clear trend of strain rate sensitivity, but the elasticity constant was clearly increased with the strain rate.

The four-point bending beam tests confirmed a good ductility of this type of façade mullion section. The failure mechanism of three-stage progressive failure mode was observed. The bending capacity of the section after slippage occurring was re-gained to some extent based on the capacity of bottom aluminium part with partial connection to the top aluminium part.

Finite element models were created by using ABAQUS software to gain further insight into the typical thermal break section. The FE models were built to simulate the shear and transverse tensile tests as well as four-point beam tests. Modelling details including

mesh and partition assignments, boundary and loading conditions as well as contact interactions were discussed. Material modelling of aluminium and polyamide materials was shown. Isotropic material properties of aluminium alloy were applied to the aluminium extrusions. Ramberg-Osgood material model was adopted to describe the elastic, plastic and hardening relations of the aluminium alloy. As the glass-fibre reinforced polyamide is an orthotropic material, simplified assumptions were made to treat it as an isotropic material. According to the loading direction and deformed shape, isotropic material properties of polyamide in transverse direction was assigned to shear and tensile models while polyamide material properties in longitudinal direction was applied as an isotropic case for the beam models.

The contact interaction between aluminium and polyamide was assigned as friction. As the interfaces between them are geometrically complicated and the interfacial actions between them largely depend on the manufacturing process, it is a challenge to simulate the failure mode of the connections. To solve this problem, two new modelling techniques were developed and applied to the models to simulate the progressive failure process under pure shear force and under bending/shear combined action. These two new models are

- Proposed progressive failure model – under pure shear force
- Proposed partitioned multi-phase beam failure model – under bending/shear combined action

By applying the proposed failure models, failure modes of shear and bending models were showing good correlation with experimental investigations. The polyamide slipped away from the connection in shear model. The beam models showed the slippage of polyamide and the three-stage progressive failure mode. In terms of tension model, the polyamide was pulled away completely from the top connection while it rotated half out of the bottom connection but remained connected by the other half of interface.

The deformed shapes of all FE models were presented and discussed. Stress distributions were plotted to provide further understanding of this typical section in all three loading conditions. Load-displacement relationships for both tension and beam models were plotted as well as load-slip relationship for the shear model.

As the two proposed progressive failure models were derived for the typical symmetrical thermal break section, it is important to test them on different thermal

break façade mullion sections which have similar connections to the typical one. Therefore, an asymmetrical thermal break façade mullion section was modelled using ABAQUS software to investigate the shear and transverse tensile capacities. The FE model of four-point beam bending was also built using ABAQUS software.

Basic principles of setting up the model and applying loading and boundary conditions were based on the principles for the typical section. Mesh assignment, material modelling and contact interaction were also defined according to the typical section models. The two proposed progressive failure models were successfully applied to the shear and four-point bending models, respectively.

Similar to the typical section, the failure modes of shear and tension models were either the polyamide slipping away or being pulled away from the connections, respectively. The beam model showed slippage of connection and the three-stage progressive failure mode. Results of these FE models were presented and discussed were carried out.

To extend the research into the analytical domain, a frame work for analytical solution for four-point bending was proposed based on the sandwich theory and superposition approach with modifications to suit the thermal break façade section.

Due to the differences between typical sandwich structure and the thermal break façade section, formulations were re-derived and extended. The sandwich beam was divided into two sub-structures. Internal force diagrams of both sub-structures were drawn to assist the analysis. Kinematic relationships of sub-structure I and II were also derived and plotted in graphs. Governing equations were derived based on these relationships. Boundary and loading conditions as well as compatibility conditions based on a four-point bending beam were adopted to solve the differential equations for particular solutions and integration constants.

The overall structural behaviour of the sandwich beam is a combination of first and second sub-structure. Deflection and internal forces, such as bending moment, shear forces and peeling stresses, are the sum of the first and second sub-structure. As there is no axial force in the second sub-structure, axial forces are only related to the first sub-structure.

To be able to apply the formulations derived to calculate the deflection and internal forces of a thermal break façade section, the façade section had to be transformed into a solid sandwich section. Trial and error method was recommended to solve the problem.

The typical thermal break façade section was used as an example to explain the principle of transformation.

In conclusion, a comprehensive and rigorous experimental investigation was carried out. The investigation showed that the shear and transverse tensile strength increased with temperature under quasi-static loadings. However, it showed no clear relationship between shear and tensile capacity with strain rate loadings at room temperature except the elasticity constant which increased with increasing strain rate.

The four-point beam tests displayed a three-stage progressive failure mode. This failure mode applied to all beam specimens at various span lengths. The specimens showed ductile behaviour.

The FE models were built to simulate the experimental works on shear, tension and beam bending. Two new models, namely, a proposed progressive failure model and proposed partitioned multi-phase beam failure model were successfully applied to the FE models.

Comparing with the experimental results, the FE model provided good correlation to the experiments, generally. The deformed shape generated from the FE model for shear capacity provided idealised slippage location which was confirmed by the experiments. The load-slippage curve obtained from the FE model matched the experimental results very well. The consistency between the FE model and experiments clearly indicated that the proposed progressive failure model created to simulate the shear tests was appropriate.

The deformed shape between the FE model and tensile tests showed a reasonable correlation. Both deformed shapes showed not only tensile deformation but also bending deformation. The failure model generated by the FE model matched the experimental one. Comparing the load-displacement graphs between FE model and the experiments, some discrepancies were observed. Equivalent material properties of aluminium were adopted to rectify the FE model. After applying the equivalent material properties of aluminium, the relationship of load-displacement obtained from the FE model showed good agreement to the results from the experimental ones.

The results generated by the FE models were consistent with the experimental ones. After successfully applying the proposed partitioned multi-phase failure model, the FE model generated a three-stage progressive failure mode similar to the experimental ones.

Slippage was observed between the top aluminium part and polyamide core. Comparisons were made for load-displacement relationship, moment-curvature relationship and mid-span strain distribution diagrams between experimental results and FE models for all beam types. In general, the FE models presented consistent results with the experiments. This finding proved that the proposed partitioned multi-phase failure model is appropriate for numerical simulation.

The numerical investigation of the asymmetrical thermal break mullion section showed general consistency with the typical section. The modelling techniques created to build the FE models of the typical section were successfully adopted to model this custom made asymmetrical façade section. This is a strong supporting evidence that the two proposed novel models, namely, the proposed progressive failure model and proposed partitioned multi-phase beam failure model are suitable to be generalised for various thermal break façade sections.

Analytical formulations were derived based on sandwich theory and superposition approach. These formulations were developed and extended to suit the thermal break façade mullion sections.

8.2 Recommended future works

Due to the limitation of current research scope and funding, the analytical solution proposed in this thesis has not been verified by experimental and numerical work. Future experimental investigation is recommended to confirm the validity of the formulation. The numerical investigation is also recommended to transfer the formulation into computational codes to generate numerical results which can be then used to compare with experimental ones. The combined numerical and experimental investigation will determine the application of the analytical formulation. Design tables then can be derived for industry applications. The methodology to transform thermal break section into a uniform rectangular section shall also be verified in future study.

Analytical formulation can be refined to include frictional interfacial actions in sub-structure II. By assuming a continuous elastic supporting medium, frictional contact forces can be adopted and developed in future study.

As the experimental investigation for the strain rate sensitivity in this thesis gave uncertain results due to limited numbers of tests performed, future experimental investigation involving large quantities of specimens under various strain rate tests are recommended to carry out.

Although the asymmetrical thermal break mullion section studied in this thesis shows similar behaviour as the typical symmetrical section based on finite element modelling, it is important to prove the correlation by experimental investigation in future study. Discrepancies discovered in this study from FE models can also be verified as well in future work.

Appendix – Polyamide Material Properties in transverse direction

Bayer MaterialScience AG / BMS-Thermoplastics Testing Center Uerdingen
Zugversuch nach VA 5.1.3.1 (in Anlehnung an DIN EN ISO 527)

03.07.2008

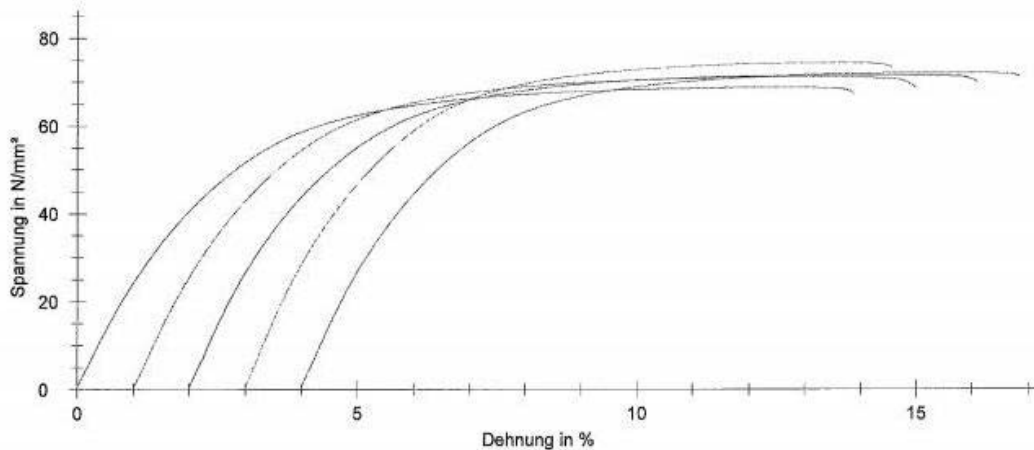
18:19

Parametertabelle:

Auftragsnummer	: KUEXT02667	v-Prüf	: 2,5 mm/min
Auftraggeber	: H.Ousios	LE	: 55 mm
Materialtyp	:	L0 SW	: 25 mm
Ansatz	:	Probekörper	: Typ 1BA EN ISO 527-2:1996
Partie	:	Prüftemperatur	: 23°C/50%r.F.
Prüfer	: Deben	Lagerbedingungen	: konditioniert
Bemerkung	: Prüfkörper gefräst.	Prüfmaschine	: ZwickZ020/148385
V- E-Modul	: 1 mm/min		

Ergebnisse:

Nr	B mm	H mm	SST N/mm ²	DST %	SB N/mm ²	SR N/mm ²	DR %	E-Mod. N/mm ²	NDR %	Rp 0.1 N/mm ²	D.b.Rp0.1 %	Rp1 N/mm ²	D.b.Rp1 %
1	5,18	2,02	68,73	12,71	68,7	67,4	13,9	2493	10,3	28,32	1,2	52,2	3,1
2	5,18	2,02	71,09	11,60	71,1	68,7	14,0	2593	10,5	31,10	1,3	55,5	3,1
3	5,18	2,02	71,50	12,33	71,5	69,8	14,1	2654	10,5	32,47	1,3	55,9	3,1
4	5,18	2,02	74,35	10,53	74,4	73,1	11,6	2915	9,2	32,91	1,2	59,0	3,0
5	5,17	2,02	72,08	11,73	72,1	71,0	12,9	2749	9,8	31,73	1,2	56,5	3,0



Statistik:

Serie	B mm	H mm	SST N/mm ²	DST %	SB N/mm ²	SR N/mm ²	DR %	E-Mod. N/mm ²	NDR %	Rp 0.1 N/mm ²	D.b.Rp0.1 %	Rp1 N/mm ²	D.b.Rp1 %
n = 5													
\bar{x}	5,18	2,02	71,55	11,78	71,5	70,0	13,3	2681	10,0	31,30	1,3	55,8	3,1
s	0,01	0,00	2,02	0,83	2,0	2,2	1,1	161	0,6	1,81	0,0	2,4	0,0
v	0,11	0,17	2,82	7,06	2,82	3,13	8,03	6,00	5,72	5,77	3,22	4,34	1,44

SST: Streckspannung ; DST: Streckdehnung ; SB: Zugfestigkeit
SR: Bruchspannung ; DR: Bruchdehnung ; NDR : nominelle Reißdehnung
E-Modul : Zugmodul
Rp0.1 : Spannung b. 0,1% Dehngrenze ; D.b.Rp0.1 : Dehnung b. Rp0.1
Rp 1 : Spannung b. 1% Dehngrenze ; D.b.Rp1 : Dehnung b. Rp 1

Prüfergebnisse werden nach den gültigen Prüfnormen und Verfahrensanweisungen der Prüfeinrichtung generiert.
Hinweis gemäß DIN EN 17025 :
- Die Prüfergebnisse beziehen sich ausschließlich auf die Prüfgegenstände.
- Ohne schriftliche Genehmigung des Prüflaboratoriums darf der Bericht nicht auszugsweise vervielfältigt werden.
- Weitere Prüfparameter entnehmen Sie bitte der Auftragsbestätigung.
Eine Verwendung der gelieferten Prüfergebnisse für weitere Auswertungen seitens des Auftraggebers ist gestattet.

Bibliography:

- Adekola, A.O. 1968, 'Partial interaction between elastically connected elements of a composite beam', *International Journal of Solids and Structures*, vol. 4, no. 11, pp. 1125-35.
- Akay, M. & O'Regan, D.F. 1995, 'Fracture behaviour of glass fibre reinforced polyamide mouldings', *Polymer Testing*, vol. 14, no. 2, pp. 149-62.
- Allen, H.G. 1969, *Analysis and design of structural sandwich panels*, Pergamon Press.
- Allix, O., Ladevéze, P. & Corigliano, A. 1995, 'Damage analysis of interlaminar fracture specimens', *Composite Structures*, vol. 31, no. 1, pp. 61-74.
- Barlow, J. 1976, 'Optimal stress locations in finite element models', *International Journal for Numerical Methods in Engineering*, vol. 10, no. 2, pp. 243-51.
- Belouettar, S., Abbadi, A., Azari, Z., Belouettar, R. & Freres, P. 2009, 'Experimental investigation of static and fatigue behaviour of composites honeycomb materials using four point bending tests', *Composite Structures*, vol. 87, no. 3, pp. 265-73.
- Bitzer, T. 1997, 'Honeycomb Technology - Materials, Design, Manufacturing, Applications and testing'.
- Blau, P.J. 2001, 'The significance and use of the friction coefficient', *Tribology International*, vol. 34, no. 9, pp. 585-91.
- Cao, H.C. & Evans, A.G. 1989, 'An experimental study of the fracture resistance of bimaterial interfaces', *Mechanics of Materials*, vol. 7, no. 4, pp. 295-304.
- Chang, W.-R., Etsion, I. & Bogy, D. 1988, 'Static friction coefficient model for metallic rough surfaces', *J. Tribology(Trans. ASME)*, vol. 110, no. 1, pp. 57-63.
- Chaudhary, A.B. & Bathe, K.-J. 1986, 'A solution method for static and dynamic analysis of three-dimensional contact problems with friction', *Computers & Structures*, vol. 24, no. 6, pp. 855-73.
- Cheng, Q.H., Lee, H.P. & Lu, C. 2006, 'A numerical analysis approach for evaluating elastic constants of sandwich structures with various cores', *Composite Structures*, vol. 74, no. 2, pp. 226-36.
- Cook, R.D., Malkus, D.S. & Plesha, M.E. 1989, *Concepts and applications of finite element analysis*, 3rd edn, John Wiley & Sons, New York.
- Cooke, T. 2007, 'The Effect of Thermal Breaks on Structural Performance ', *The Journal of the society of Facade Engineering*.
- Corigliano, A., Rizzi, E. & Papa, E. 2000, 'Experimental characterization and numerical simulations of a syntactic-foam/glass-fibre composite sandwich', *Composites Science and Technology*, vol. 60, no. 11, pp. 2169-80.
- Cui, W.C. & Wisnom, M.R. 1992, 'Contact finite element analysis of three- and four-point short-beam bending of unidirectional composites', *Composites Science and Technology*, vol. 45, no. 4, pp. 323-34.
- Curtis, P., Bader, M. & Bailey, J. 1978, 'The stiffness and strength of a polyamide thermoplastic reinforced with glass and carbon fibres', *Journal of Materials Science*, vol. 13, no. 2, pp. 377-90.

- Daniel, I.M. & Abot, J.L. 2000, 'Fabrication, testing and analysis of composite sandwich beams', *Composites Science and Technology*, vol. 60, no. 12-13, pp. 2455-63.
- Feldmeier, F. 1987, 'Statische Nachweise bei Metall-Kunststoff-Verbundprofilen', *Fenster und fassade*.
- Ferdinand P.Beer and E.Russell Johnston, J. 1992, *Mechanics of Materials*, Metric Edition edn, McGraw-Hill Book Company Europe UK.
- Foo, C., Seah, L. & Chai, G. 2008, 'Low-velocity impact failure of aluminium honeycomb sandwich panels', *Composite Structures*, vol. 85, no. 1, pp. 20-8.
- Franz Feldmeier, J.S. 1988, *Statische Nachweise bei Metall-Kunststoff-Verbundprofilen*.
- Frostig, Y. 1992, 'Behavior of delaminated sandwich beam with transversely flexible core — high order theory', *Composite Structures*, vol. 20, no. 1, pp. 1-16.
- Frostig, Y. & Baruch, M. 1990, 'Bending of sandwich beams with transversely flexible core', *AIAA Journal*, vol. 28, no. 3, pp. 523-31.
- Frostig, Y., Baruch, M., Vilnay, O., and Sheinman, I. 1991, 'Bending of Nonsymmetric Sandwich Beams with Transversely Flexible Core.', *Journal of Engineering Mechanics*, vol. 117, no. 9, pp. 1931-52.
- Frostig, Y. & Shenhar, Y. 1995, 'High-order bending of sandwich beams with a transversely flexible core and unsymmetrical laminated composite skins', *Composites Engineering*, vol. 5, no. 4, pp. 405-14.
- Fu, S.Y., Lauke, B., Mäder, E., Yue, C.Y. & Hu, X. 2000, 'Tensile properties of short-glass-fiber- and short-carbon-fiber-reinforced polypropylene composites', *Composites Part A: Applied Science and Manufacturing*, vol. 31, no. 10, pp. 1117-25.
- Gardner, L. & Ashraf, M. 2006, 'Structural design for non-linear metallic materials', *Engineering Structures*, vol. 28, no. 6, pp. 926-34.
- Gordaninejad, F. & Bert, C.W. 1989, 'A new theory for bending of thick sandwich beams', *International Journal of Mechanical Sciences*, vol. 31, no. 11-12, pp. 925-34.
- Haslinger, J., Kučera, R., Vlach, O. & Baniotopoulos, C.C. 2012, 'Approximation and numerical realization of 3D quasistatic contact problems with Coulomb friction', *Mathematics and Computers in Simulation*, vol. 82, no. 10, pp. 1936-51.
- Heinrich, P., Schmid, J. & Stiell, W. 1980, 'Static Stress Calculations for Aluminum-Composite Sections With a Thermal Break. Pt. 1', *Aluminium*, vol. 56, no. 4, pp. 269-73.
- Hetényi, M. 1946, *Beams on elastic foundation: theory with applications in the fields of civil and mechanical engineering*, University of Michigan Press.
- Hibbeler, R.C. 2008, *Mechanics of Materials*, 7th edn, Pearson Prentice Hall.
- Hu, H., Belouettar, S., Potier-Ferry, M. & Daya, E.M. 2008, 'Multi-scale modelling of sandwich structures using the Arlequin method Part I: Linear modelling', *Finite Elements in Analysis and Design*, vol. 45, no. 1, pp. 37-51.
- Inc, H. 2001, *Coulomb Friction in User Subroutine FRIC Using the Penalty Method*.

- Institution, B.S. 2007, 'Eurocode 9: Design of aluminium structures', *Part 1-1: General structural rules*, vol. BS EN1999, no 1, British Standards Institution, London, U.K., p. 207.
- Johnson, A.F. & Holzapfel, M. 2006, 'Influence of delamination on impact damage in composite structures', *Composites Science and Technology*, vol. 66, no. 6, pp. 807-15.
- Johnson, A.F., Pickett, A.K. & Rozycki, P. 2001, 'Computational methods for predicting impact damage in composite structures', *Composites Science and Technology*, vol. 61, no. 15, pp. 2183-92.
- K.Kemmochi, M.U. 1980, 'Measurement of stress distribution in sandwich beams under four-point bending'.
- Kee Paik, J., Thayamballi, A.K. & Sung Kim, G. 1999, 'The strength characteristics of aluminum honeycomb sandwich panels', *Thin-Walled Structures*, vol. 35, no. 3, pp. 205-31.
- Kogut, L. & Etsion, I. 2004, 'A static friction model for elastic-plastic contacting rough surfaces', *TRANSACTIONS-AMERICAN SOCIETY OF MECHANICAL ENGINEERS JOURNAL OF TRIBOLOGY*, vol. 126, no. 1, pp. 34-40.
- Lagunegrand, L., Lorriot, T., Harry, R. & Wagnier, H. 2006, 'Design of an improved four point bending test on a sandwich beam for free edge delamination studies', *Composites Part B: Engineering*, vol. 37, no. 2-3, pp. 127-36.
- Li, W., Li, Q.-n. & Jiang, W.-s. 2012, 'Parameter study on composite frames consisting of steel beams and reinforced concrete columns', *Journal of Constructional Steel Research*, vol. 77, no. 0, pp. 145-62.
- Meriam, J.L. & Kraige, L.G. 2008, *Engineering Mechanics, SI Version: Statics*, John Wiley & Sons.
- Mines, R.A.W. & Alias, A. 2002, 'Numerical simulation of the progressive collapse of polymer composite sandwich beams under static loading', *Composites Part A: Applied Science and Manufacturing*, vol. 33, no. 1, pp. 11-26.
- Monforton, G.R. & Ibrahim, I.M. 1977, 'Modified stiffness formulation of unbalanced anisotropic sandwich plates', *International Journal of Mechanical Sciences*, vol. 19, no. 6, pp. 335-43.
- Mouhmid, B., Imad, A., Benseddiq, N., Benmedakhène, S. & Maazouz, A. 2006, 'A study of the mechanical behaviour of a glass fibre reinforced polyamide 6,6: Experimental investigation', *Polymer Testing*, vol. 25, no. 4, pp. 544-52.
- Nik Vigener, P.a.M.A.B. 2011a, 'Building Envelope Design Guide - Curtain Wall', *WBDG - Whole building Design Guide - A program of the National Institute of Building Sciences*.
- Nik Vigener, P.M.A.B. 2011b, 'Building Envelope Design Guide - Windows', *WBDG - Whole building Design Guide - A program of the National Institute of Building Sciences*.
- Osgood, W. & Ramberg, W. 1943, 'Description of stress-strain curves by three parameters', *Tech. Notes Nat. Adv. Comm. Aeronaut*, vol. 1943, p. 13.
- Padhi, G.S., Shenoi, R.A., Moy, S.S.J. & Hawkins, G.L., 'Progressive failure and ultimate collapse of laminated composite plates in bending', *Composite Structures*, vol. 40, no. 3-4, pp. 277-91.

- Plantema, F.J. 1966, *Sandwich construction: the bending and buckling of sandwich beams, plates, and shells*, Wiley New York.
- Ramberg, W. & Osgood, W.R. 1943, 'Description of stress-strain curves by three parameters'.
- Sadighi, M. & Saadati, M. 2010, 'Unequal faces effect on fracture of composite sandwich beam with flexible core', *Applied Composite Materials*, vol. 17, no. 2, pp. 111-20.
- Sato, N., Kurauchi, T., Sato, S. & Kamigaito, O. 1984, 'Mechanism of fracture of short glass fibre-reinforced polyamide thermoplastic', *Journal of Materials Science*, vol. 19, no. 4, pp. 1145-52.
- Shenhar, Y., Frostig, Y. & Altus, E. 1996, 'Stresses and failure patterns in the bending of sandwich beams with transversely flexible cores and laminated composite skins', *Composite Structures*, vol. 35, no. 2, pp. 143-52.
- Sheri D. Sheppard, B.H.T. 2004, *Statics: Analysis and Design of Systems in Equilibrium*, 1 edn, John Wiley & Sons Inc, United states of America.
- Sokolinsky, V.S., Shen, H., Vaikhanski, L. & Nutt, S.R. 2003, 'Experimental and analytical study of nonlinear bending response of sandwich beams', *Composite Structures*, vol. 60, no. 2, pp. 219-29.
- Stamm, K. & Witte, H. 1974, *Sandwichkonstruktionen: Berechnung, Fertigung, Ausführung*, vol. 3, Springer.
- Standard, E. 2004, 'Metal profiles with thermal barrier-Mechanical performance-Requirements, proof and tests for assessment', European committee for standardization.
- Standardization, I.O.f. 1993a, 'Plastics - Determination of tensile properties ', *Part 1: General principles*, vol. ISO 527, no 1, International Organization for Standardization, Geneve, Switzerland, p. 9.
- Standardization, I.O.f. 1993b, 'Plastics - Determination of tensile properties', *Part 2: Test conditions for moulding and extrusion plastics*, vol. ISO 527, no 1, International Organization for Standardization, Geneve, Switzerland, p. 5.
- Steeves, C.A. & Fleck, N.A. 2004a, 'Collapse mechanisms of sandwich beams with composite faces and a foam core, loaded in three-point bending. Part I: analytical models and minimum weight design', *International Journal of Mechanical Sciences*, vol. 46, no. 4, pp. 561-83.
- Steeves, C.A. & Fleck, N.A. 2004b, 'Collapse mechanisms of sandwich beams with composite faces and a foam core, loaded in three-point bending. Part II: experimental investigation and numerical modelling', *International Journal of Mechanical Sciences*, vol. 46, no. 4, pp. 585-608.
- Straalen, I.J.V. 2000, 'comprehensive overview of theories for sandwich panels'.
- Systemes, D. 2010, 'Abaqus Theory Manual', V6.10 edn.
- Systemes, D. 2011a, 'Abaqus Analysis User's Manual', V6.11 edn.
- Systemes, D. 2011b, 'Abaqus Theory Manual', V6.11 edn.
- Thomsen, O.T. & Frostig, Y. 1997, 'Localized bending effects in sandwich panels: photoelastic investigation versus high-order sandwich theory results', *Composite Structures*, vol. 37, no. 1, pp. 97-108.
- Urbakh, M., Klaffer, J., Gourdon, D. & Israelachvili, J. 2004, 'The nonlinear nature of friction', *Nature*, vol. 430, no. 6999, pp. 525-8.
- Welo, T., Paulsen, F. & Brobak, T. 1994, 'The behaviour of thin-walled, aluminium alloy profiles in rotary draw bending—A comparison between

- numerical and experimental results', *Journal of materials processing technology*, vol. 45, no. 1, pp. 173-80.
- Y, F. 1992, 'Behavior of delaminated sandwich beam with transversely flexible core — high order theory', *Composite Structures*, vol. 20, no. 1, pp. 1-16.
- Y. Frostig, M.B., O.Vilnay, I.Sheinman 1992, 'High-order theory for sandwich-beam behaviour with transversely flexible core', *Engineering mechanics*, vol. 118, no. 5.
- Yasunori, A., Sumio, H. & Kajita, T. 1981, 'Elastic-plastic analysis of composite beams with incomplete interaction by finite element method', *Computers & Structures*, vol. 14, no. 5–6, pp. 453-62.
- Zenkert, D. 1995, *An Introduction to Sandwich Construction*, Engineering Materials Advisory Services.